Crustal Structure of the Central Nova Scotia Margin and the Transition from Volcanic to Non-Volcanic Rifting off Eastern Canada

by

Yue Wu

Submitted in partial fulfillment of the requirements for
the degree of Doctor of Philosophy

at

Dalhousie University
Halifax, Nova Scotia
November 2007

Distribution License

DalSpace requires agreement to this non-exclusive distribution license before your item can appear on DalSpace.

NON-EXCLUSIVE DISTRIBUTION LICENSE

You (the author(s) or copyright owner) grant to Dalhousie University the non-exclusive right to reproduce and distribute your submission worldwide in any medium.

You agree that Dalhousie University may, without changing the content, reformat the submission for the purpose of preservation.

You also agree that Dalhousie University may keep more than one copy of this submission for purposes of security, back-up and preservation.

You agree that the submission is your original work, and that you have the right to grant the rights contained in this license. You also agree that your submission does not, to the best of your knowledge, infringe upon anyone's copyright.

If the submission contains material for which you do not hold copyright, you agree that you have obtained the unrestricted permission of the copyright owner to grant Dalhousie University the rights required by this license, and that such third-party owned material is clearly identified and acknowledged within the text or content of the submission.

If the submission is based upon work that has been sponsored or supported by an agency or organization other than Dalhousie University, you assert that you have fulfilled any right of review or other obligations required by such contract or agreement.

Dalhousie University will clearly identify your name(s) as the author(s) or owner(s) of the submission, and will not make any alteration to the content of the files that you have submitted.

If you have questions regarding this license please contact the repository manager at dalspace@dal.ca.

Grant the distribution license by signing and dating below.

_____ _____

Name of signatory Date

DALHOUSIE UNIVERSITY

DEPARTMENT OF EARTH SCIENCES

The undersigned hereby certify that they have read and recommend to the Faulty of Graduate studies for acceptance a thesis entitled "Crustal Structure of the Central Nova Scotia Margin and the Transition from Volcanic to Non-Volcanic Rifting off Eastern Canada" by Yue Wu in partial fulfillment of the requirements for the degree of Doctor of Philosophy.

Date: _____

External Examiner: _____

Research Supervisor: _____

Examining Committee: _____

_____

Department Representative: _____

Dalhousie University

Date of defence: _____

AUTHOR: Yue Wu

TITLE: Crustal Structure of the Central Nova Scotia Margin and the Transition fromVolcanic to Non-Volcanic Rifting off Eastern Canada

DEPARTMENT OR SCHOOL: Department of Earth Sciences

DEGREE: Ph.D. CONVOCATION: May YEAR: 2008

Permission is herewith granted to Dalhousie University to circulate and to have copied for non-commercial purposes, at its discretion, the above title upon the request of individuals or institutions.

_____

Signature of the Author

For

My Dearest Father

who had empowered me to pursue a university education. My father encouraged me to start my Ph.D. studies in Canada but, unfortunately, he could not see the end.

Table of Contents

List of Figures

List of Tables

Abstract

The central Nova Scotia margin is located at a transition from a volcanic rifted margin in the south to a non-volcanic margin in the north. New seismic results are presented to elucidate the crustal structure of the transitional region of the margin. A velocity model derived from wide-angle seismic data show three major crustal zones. The continental crust consists of three layers with velocities of 5.5-6.9 km/s with a maximum thickness of ~36 km. The rifted continental crust extends to a region of the faulted basement blocks. Oceanic crust immediately seaward of continental breakup consists of layer 2 and a high-velocity lower crustal layer which is interpreted as a composite layer of serpentinized peridotite and gabbroic layer 3. The ocean-continent transition zone contains a ~170-km-wide partially serpentinized mantle layer with velocities of 7.6-7.95 km/s, overlain by highly faulted continental crust in the northwest and thin oceanic crust in the southeast. No evidence of underplating or excessive extrusion is observed, suggesting that the central Scotian margin is non-volcanic. NovaSpan Project MCS data show that excessive rift volcanism disappears ~100 km north of the SW Scotian margin.Therefore, the major part of Scotian margin is non-volcanic except for the southwest-most part, and the East Coast Magnetic Anomaly with reduced amplitude along the major part of Scotian margin is not caused by an igneous wedge. The volcanic to non-volcanic margin transition takes place across a ~100-km-wide zone, which is characterized by rugged basement topography and relatively deeper depths. Based on the seismic results, magnetic anomaly and salt distribution from both sides of the Scotian/Moroccan margin pair, reconstructions to continental breakup and pre-rift positions are proposed. Two types of asymmetrical crustal structures are presented along this margin pair. Across the northern segment, rifting and breakup are symmetrical; but post-rift compression of the High Atlas Mountains caused uplift and erosion on the Morocco side, resulting in a shallow Essaouira Basin with thin sediment offshore Morocco, in contrast to a deeper Sable Subbasin with thicker sediment off Nova Scotia. Across the central segment, uplift and erosion occurred off Nova Scotia at the early stage of rifting. The absence of syn-rift uplift and erosion off Morocco produced asymmetrical initial extension. However, the Jurassic breakup and subsequent seafloor spreading became more symmetric.

List of Abbreviations and Symbols Used

1D	One dimensional
2D	Two dimensional
3D	Three dimensional
86-5A, 5B	Reflection profiles across the Orpheus Graben and along the eastern coast off Cape Breton Island, shot in 1986
88-1,1A	Reflection profiles across the central Nova Scotia margin, shot in 1988
88-2,3,4	Reflection profiles across the Bay of Fundy and along the western coast off Nova Scotia, shot in 1988
89-1	Reflection profiles across the northern Nova Scotia margin, shot in 1989
89-3,4,5	Reflection profiles across the southwest coast of Nova Scotia, shot in 1989
89-11	An unpublished reflection profile across the Jurassic magnetic quiet zone off the central Nova Scotia, shot in 1989
89-12	An unpublished reflection profile across the slope and the Jurassic magnetic quiet zone off the northern Nova Scotia, shot in 1989
β	The ratio of original crustal thickness divided by present thickness after stretching
δ	The ratio of original subcrustal lithosphere thickness divided by present thickness after stretching
γ	Equivalent thinning factors $(1-1/\beta)$ or $(1-1/\delta)$
χ^2	Normalized misfit
BB	Bay of Biscay
BGR	German Federal Agency of Geosciences and Natural Resources
BH	Basement high
BTJ	Biscay Triple Junction
CAMP	Central Atlantic Magmatic Provinces
CBF/CBF-2	Continental breakup front

CCFZ	Cobequid Chedabucto fault zone
CDP	Common depth point
CMP	Common midpoint
COB	Continent-ocean boundary
CSP	Common scatter point
CTD	Conductivity, temperature and depth measurement
DMO	Dip moveout
ECMA	East Coast Magnetic Anomaly
EOM	Equivalent offset migration
FB	Faulted basement blocks
FC	Flemish Cap
FD	Finite difference
FZ	Fracture zone
GAL	Galicia Bank
GB	Georges Bank
GBs	Grand Banks
GFZ	Charlie-Gibbs Fracture Zone
GPS	Global Positioning System
GS	Goban Spur
GT	Gander Terrane
HVLC	High-velocity lower crust
HSM	Exhumed and highly serpentinized upper mantle
IAP	Iberia-Abyssal Plain

JMQZ	Jurassic Magnetic Quiet zone
L_2	Oceanic layer 2
L_3	Oceanic layer 3
LaS	Labrador Sea
Line 1,2,3	Refraction profiles across the northern, central and southwestern Nova Scotia margin acquired during Cruise Hudson-2001
LITHOPROBE	A special national research project designed to probe the earth's crust and understand the geological evolution of Canada
Ma	Million year
MCS	Multi-channel seismic
NEC	Northeast Channel
NFZ	Newfoundland Fracture Zone
MO	Morocco
NB	Newfoundland Basin
NMB	North Mountain Basalt
NMO	Normal moveout
NS	Nova Scotia
OBS	Ocean bottom seismometers
OCT	Ocean-continent transition
ODP	Ocean Drilling Program
P_bP	P-wave reflection from the basement surface
P_{c1}, P_{c2} and P_{c3}	Refractions from the upper, middle and lower continental crust
$P_{c1}P$ and $P_{c2}P$	Midcrustal reflections from the bottom of the upper and middle continental crust
P_{HVLC}	Refraction from the high-velocity lower crust (HVLC)

$P_{HVLC}P$	Reflection from the high-velocity lower crust (HVLC)
P_{L2}	Refraction from the oceanic layer 2
$P_{L2}P$	Reflection from the oceanic layer 2
$P_{m1}P$ and P_mP	Reflections from the top boundaries of the serpentinized and unserpentinized mantle
P_n	Refraction from the "normal" (*i.e.* unserpentinized) mantle
P_{n1}	Refraction from the serpentinized mantle layer
P_{sn}	P-wave refracted phase through the n^{th} sedimentary layer
$P_{sn}P$	P-wave refleccted phase through the n^{th} sedimentary layer
PSM	Partially serpentinized mantle
RMS	Root mean square
R_{MO}	Crustal refection off Morocco
R_{NS}	Crustal refection off Nova Scotia
SB	Southern Baltimore Canyon Trough
SC	Southern Carolina
SDP	Slope diapiric province
SDR	Seaward dipping reflection
SISMAR/SIS	Sismique Maroc marine seismic survey
SLCC/SLCC'	The seaward limit of the continental crust
SMART	Scotian MARgin Transects refraction seismic experiment
SP	Shot point
SWG	Southwest Greenland
TWT/TWTT	Two-way traveltime
VNT	Volcanic to non-volcanic transition

v_p	P-wave velocity
VSP	Vertical seismic profiling
WACMA	The West African Coast Magnetic Anomaly
WAR/R	Wide-angle refraction/reflection

Acknowledgements

The completion of this thesis is attributed to the support of many individuals. First of all, I wish to thank my supervisor, Dr. Keith E. Louden, for giving me the opportunity to work on the seismic data off Nova Scotia and his many years' financial support towards this thesis. I am thankful for Keith's great efforts leading me into this research area and his fresh ideas in interpreting seismic data and in writing my thesis. As an international student, whose first language is not English, I am very grateful that Keith showed immense patience in reading and commenting on my writings.

I would like to acknowledge my thesis supervisory committee—Dr. Patrick J.C. Ryall, Dr. Grant Wach, and Dr. Ruth Jackson—for their patient instruction, constructive comments and suggestions, and insightful criticisms on each chapter of my thesis. I appreciate their encouragement and kindness in helping me overcome all sorts of difficulties in completing of this thesis.

I would like to thank my co-workers in the SMART experiment Dr. Thomas Funck and Dr. Sonya A. Dehler. Thomas has helped me in learning velocity modeling. Sonya has provided a lot of support in presenting the magnetic anomalies off Nova Scotia. I also thank Thomas and Sonya for their comments on the manuscript of chapter 2.

I thank Dr. Mladen Nedimovic for reviewing the results of pre-stack migration and providing valuable comments.

I would like to thank Dr. Helen Lau. When she was a Ph.D. student at Dalhousie University, she gave me tremendous assistance in seismic data processing and velocity modeling. Her instruction in using various seismic processing softwares and generosity in lending me her scripts for reference are much appreciated.

I am thankful to Dr. Deping Chian who modified his seismic processing software SeisWide to meet my particular needs. I will not forget the days when we exchanged ideas on the fundamentals of margin formation. I am grateful to him for his personal support in the past years.

I extend my gratitude to Patrick Potter for his support for downloading the early LITHOPROBE and BGR data from old tapes. I also thank John Shimeld for his insightful ideas of how to interpret the diapiric structure. I wish to thank Dr. Nick Culshaw and Dr. Anne-Marie Ryan, who provide the geology information of Nova Scotia. I would like to thank Charlie and Guang Yang for their technical support in the GIS lab and plot room.

I thank the GX Technology Corporation for allowing me to use some seismic sections of the NovaSpan Project data for comparison in this study. I also thank Christopher LeBlanc, Derek Woodward, Guy Maslen and Jonathan Ravens for their technical support of GLOBE Claritas seismic processing software.

CHAPTER 1

INTRODUCTION

This thesis aims to provide a better characterization of the rifting mechanism and tectonic structure of the rifted Scotian margin. The data used in this thesis include wide-angle seismic refraction data and coincident multi-channel seismic reflection data across the central Nova Scotia margin. Regional gravity and magnetic data have also been integrated with seismic data to constrain the crustal structure. The crustal structure across the central Nova Scotia margin has been correlated with other existing margin transects off Morocco and Nova Scotia, from which this conjugate margin pair is reconstructed to the continental breakup and pre-rift position. The rifting geometry across the conjugate margin pair and the volcanic to non-volcanic margin transition along the North Atlantic passive margin system are elucidated in the breakup reconstruction.

1.1 Rifted Continental Margins

1.1.1 Formation of Rifted Continental Margins

Rifted continental margins are formed during the extension and breakup of continents. As rifting begins, the continental crust thins and extends. A rift valley appears as the thinned continental crust subsides through faulting and stretching. As the continental crust thins, the reduced pressure allows the underlying lithosphere and hot asthenosphere to rise and partially melt to form magma. The magma may intrude into the extended crust or solidify and underplate at the base of crust. The magma may also find its way through faults and rise to surface, forming volcanoes and basaltic lava flows. As rifting proceeds, the increasingly thinned continental crust becomes entirely brittle (Perez-Gussinye and

Reston 2001) and eventually breaks up, resulting in the formation of continental margins and opening of oceans. The North Atlantic passive margins were formed during the opening of the North Atlantic Ocean between the North American, African and European continents (Figure 1.1). Recent studies of the crustal structures along this margin system have shown many complications compared to the above simple view for the formation of rifted continental margins (e.g. Louden and Chian 1999; Wu et al. 2006).

1.1.2 Volcanism of Rifted Continental Margins

Rifted continental margins can be divided into two major categories: volcanic and non-volcanic. Volcanic margins are those that have been extensively affected by syn-rift volcanism, which has modified or obscured the extensional fabric within the crust. The crustal structure of volcanic margins is characterized by the large quantities of volcanic rocks. Figure 1.2a shows a typical crustal structure for a volcanic margin—the southern Baltimore Canyon Trough along EDGE 801 (SB, Figure 1.1; Holbrook and Kelemen 1993; Talwani and Abreu 2000), where seaward dipping reflections (SDR), indicative of volcanic extrusives, are observed in the basement across the ocean-continent transition (OCT), and a thick high-velocity lower crustal (HVLC) layer of intrusives underplates at the base of the rifted crust. The existence of extrusive rocks has been confirmed by drilling on the Outer Vøring Plateau of the Norwegian Sea margin (Eldholm et al. 1986) and the SE Greenland margin (Fitton et al. 1995), while the presence of underplated rocks was interpreted from seismic refraction data based on the characteristic lower crustal velocity (v_p=7.2-7.5 kms^{-1}), and anomalous thickness of igneous rocks (e.g. 15 km, but up

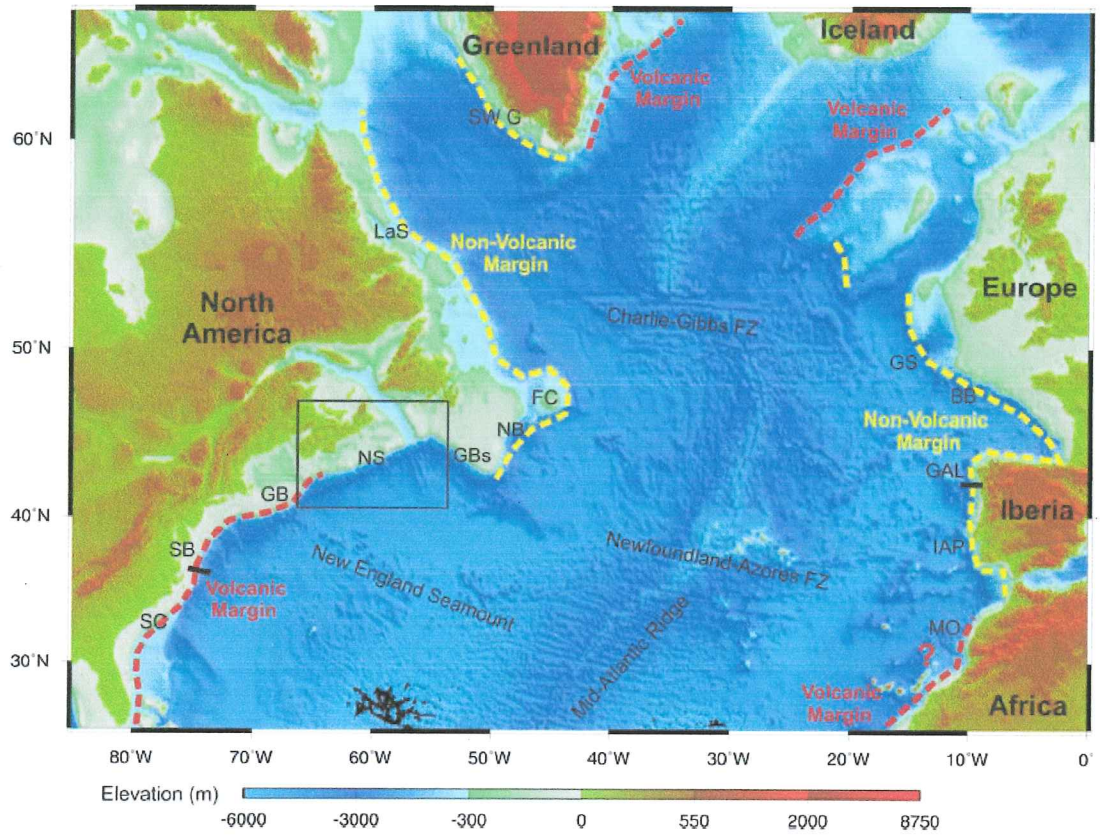

Figure 1.1. The distribution of continental margins along the North Atlantic. The red-dashed lines mark the volcanic margins, while the yellow lines non-volcanic margins. The area for this study is indicated by the rectangle. Abbreviations: SC: South Carolina; SB: southern Baltimore Canyon Trough; GB: Georges Bank; NS: Nova Scotia; GBs: Grand Banks; NB: Newfoundland Basin; FC: Flemish Cap; LaS: Labrador Sea; MO: Morocco; IAP: Iberia-Abyssal Plain; GAL: Galicia Bank; BB: Bay of Biscay; GS: Goban Spur; SWG: southwest Greenland; FZ: fracture zone. The crustal structure of the southern Baltimore Canyon Trough margin (SB) and Galicia Bank margin (GAL), marked by black lines, is compared in Figure 1.2.

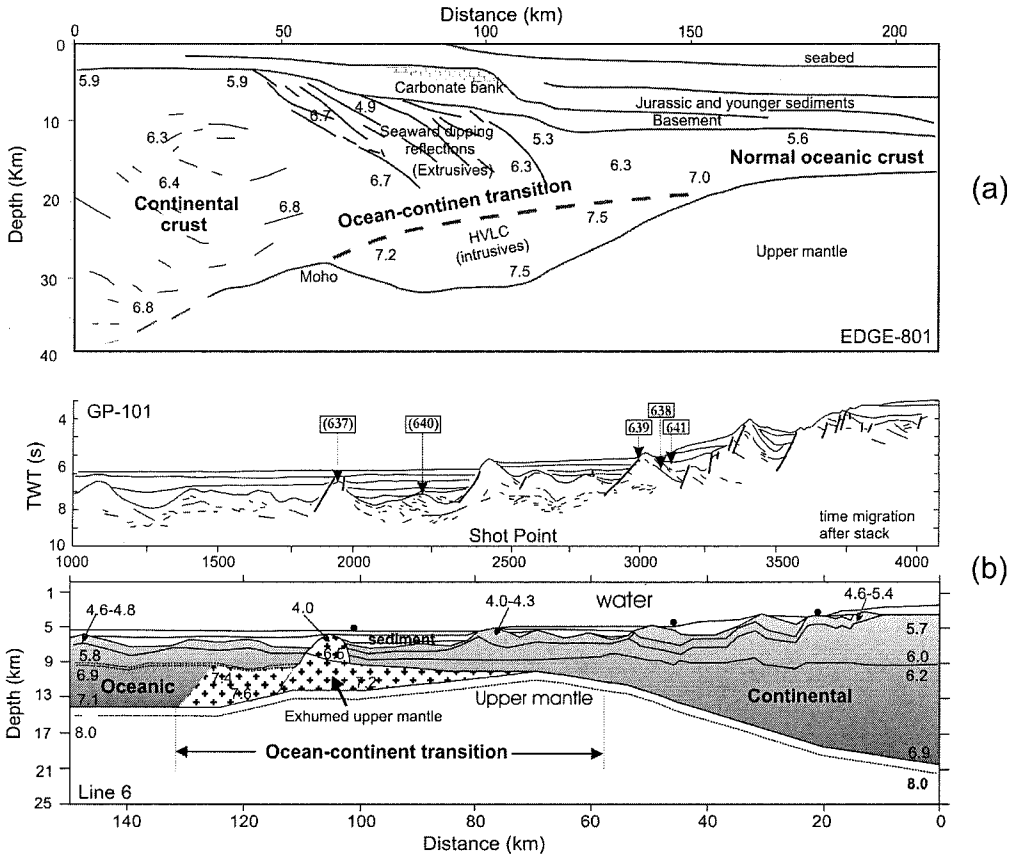

Figure 1.2. (a) A crustal section along line EDGE 801 across the southern Baltimore Canyon Trough. Major crustal layers are labeled with *P*-wave velocities (unit: kms^{-1});. SP: shot point. Area highlighted with pattern indicates a high-velocity lower crust (HVLC) layer. After Talwani and Abreu (2000). (b) A crustal section consisting of the line drawing of reflection travel time profile GP101 (Mauffret and Montadert 1987) and the velocity model for coincident refraction line 6 (Whitmarsh et al. 1996) in the west of the Galicia Bank. Boxes with arrows give locations of Ocean Drilling Program borehole sites (Shipboard Scientific Party, 1987); receiver locations (filled circles) and layer velocities (kms^{-1}) are shown in the velocity model. The boundary between the oceanic crust and exhumed upper mantle is not well defined due to lack of seaward refraction receivers. After Louden and Chian (1999).

to 20-25 km; e.g. Holbrook and Kelemen 1993). The distribution of volcanic margins along the North Atlantic is shown in Figure 1.1.

The excessive volcanism (including extrusion and intrusion) has been attributed to the rising decompressional melting of anomalously hot asthenosphere during the formation of rifted continental margins. White and McKenzie (1989) showed that the amount of observed magmatism across the Hatton Bank margin could result if the potential temperature of the asthenosphere under the rifted continental margin was raised by ~100-150°C from the normal temperature (1300°C) at the oceanic spreading center. Along the North Atlantic margin system, the southwestern-most of the Scotian margin and the entire US East Coast margins are largely classified into this category (e.g. Holbrook and Kelemen 1993; Keen and Potter 1995a; Talwani and Abreu 2000). Holbrook and Kelemen (1993) estimated that a total volume of 3.2×10^6 km^3 of igneous rocks was produced by magmatism during the formation of the US East Coast margin. A mantle plume was proposed to have been situated off present day Florida at ~200 Ma, which may have initiated the continental rifting of the North American and African continents and wide-spread volcanism along the North Atlantic margin system (Sleep 1996; Ernst and Buchan 2001). Previously de Boer et al. (1988) had proposed a weak mantle plume that moved southward from New England to Florida. Non-plume models were also suggested to create voluminous volcanism, which require shallow thermal anomalies or rapid upwelling of the mantle material (e.g. Vogt 1991; Anderson et al. 1992). Mutter et al. (1988) suggested that small scale mantle convection at the continental edges, possibly due to lateral and vertical temperature gradients between colder lithosphere and warmer

upwelling lithosphere could enhance magmatic activity in the absence of elevated mantle potential temperatures. Similar studies were also conducted by Anderson (1994), King and Anderson (1995), King and Ritsema (2000), and Foulger and Anderson (2005).

Non-volcanic margins, on the other hand, are often characterized by limited melt generation, which may be a result of slow extension rates or cold upper mantle (Sleep and Barth 1997; Reston et al. 2003). In this case, a relatively thin layer with velocity of v_p =7.2-7.6 kms^{-1} is observed across the transition zone (Figure 1.2b). Such velocity layers are associated with basement highs on the Galicia Bank/Iberia Abyssal Plain, which have been evidenced by drilling at ODP (Ocean Drilling Program) Sites 637 (Shipboard Scientific Party, 1987; Figure 1.2), 897, 899 and 1068 as peridotite ridges, indicative of exhumed upper mantle (Sawyer et al. 1994). The exhumed mantle presents *P*-wave velocity anisotropy of 5-7 % at depth of 3-7 km below the top of acoustic basement (Cole et al. 2002). Most models of *P*-wave azimathal seismic anisotropy suggest that the fast velocity direction is parallel to the direction of stretching, normal to the rift (e.g. Vauchez et al. 2000). This is an indicator of initial stretching direction in a region adjacent to oceanic crust where no fracture zones have been identified, as well as an indicator for exhumed mantle due to stretching instead of underplated rocks with similar velocities. In contrast to the volcanic margins, the non-volcanic margins are devoid of surface volcanic activity. Along the North Atlantic margin, margins north of Nova Scotia, from the Grand Banks/Newfoundland-Iberia Abyssal Plain conjugates (e.g. Reid 1994; Dean et al. 2000; Funck *et al.* 2003; Lau et al. 2006a) to the Labrador Sea-SW Greenland margins, also have similar crustal structures (Chian and Louden 1994; Chian et al. 1995a).

The limited melt generation for the northern North Atlantic margins may be a result of one or several of the following factors in the course of rifting. The temperature anomaly of hot asthenosphere for the volcanic US East Coast margins, which was suggested to ~~be~~ have originated from a mantle plume located off Florida (Sleep 1996), may be diminishing toward the northern passive margins, which are thousands of kilometers away from the anomaly center. Secondly, the rifting rates for the northern North Atlantic margins should be lower than that of the southern US East Coast margins because the Mesozoic rotation poles were located north or northeast of Iceland (Klitgord and Schouten 1986; Roest et al. 1992). Reduced rifting rates will affect the thermal regime by allowing more time for vertical diffusion to reduce the thermal anomaly associated with rifting. In addition, compared to the sharp necking of the US margins, the wider zones of lithospheric thinning of the Scotian margin, the Galicia Bank margin (Whitmarsh and Miles, 1995; González *et al.*, 1999), and the Labrador Sea margin (Chian et al. 1995a; Louden and Chian 1999), may result in reduced melt production. As shown by the melt generation models of Bown and White (1995), melt production can be completely suppressed if rifting lasts 15-20 m.y., despite extreme continental thinning. Minshull et al. (2001) also suggested that melt production at the time of continental breakup may have been reduced by effects of lateral heat conduction, depth-dependent stretching or reduced mantle temperature.

1.1.3 Volcanic to Non-Volcanic Transition

Based on the above characterization, the Nova Scotia margin is located at the transition along the North Atlantic from volcanic margins to the south to non-volcanic margins to

the north (Figure 1.1). The southwestern-most Scotian margin near Georges Bank is volcanic, evidenced by the SDR sequences on multi-channel seismic (MCS) reflection lines 89-3, 4 (Figure 1.3; Keen and Potter 1995a), similar to the volcanic US East Coast margins (e.g. Holbrook and Kelemen 1993). The northern Nova Scotia margin has been classified as a non-volcanic rift margin based on the absence of SDR sequences along MCS line 89-1 (Figure 1.3; Keen and Potter 1995b). Hence, the volcanic to non-volcanic transition should have occurred somewhere along the central Scotian margin.

Figure 1.3 shows the regional magnetic anomaly offshore Eastern Canada and US. Along the volcanic margin from the US Atlantic coast to the southwestern-most margin of Nova Scotia near Georges Bank, a strong, linear magnetic anomaly, referred to as the East Coast Magnetic Anomaly (ECMA), is well developed and coincident with a ~100 km wide zone of thick igneous wedge (e.g. Holbrook and Kelemen 1993; Keen and Potter 1995a). Magnetic models showed that the high-amplitude ECMA is attributed to the extrusive rocks or the entire igneous wedge (Alsop and Talwani 1984; Talwani and Abreu 2000; Dehler et al. 2003). The ECMA progressively weakens northward and eventually disappears within the northern Scotian margin, which has been identified as a non-volcanic rifted margin without evidence of excessive volcanism (Keen and Potter 1995b). However, along the central portion of the Nova Scotia margin, the magnetic anomaly is still pronounced. There is no evidence for a SDR sequence on MCS line 88-1A (Keen *et al.* 1991b), although it may be obscured by prominent diapiric salt structures. The concurrence of magnetic and seismic signatures leads to an ambiguous character for the central margin segment. A series of questions is raised, such as "is the

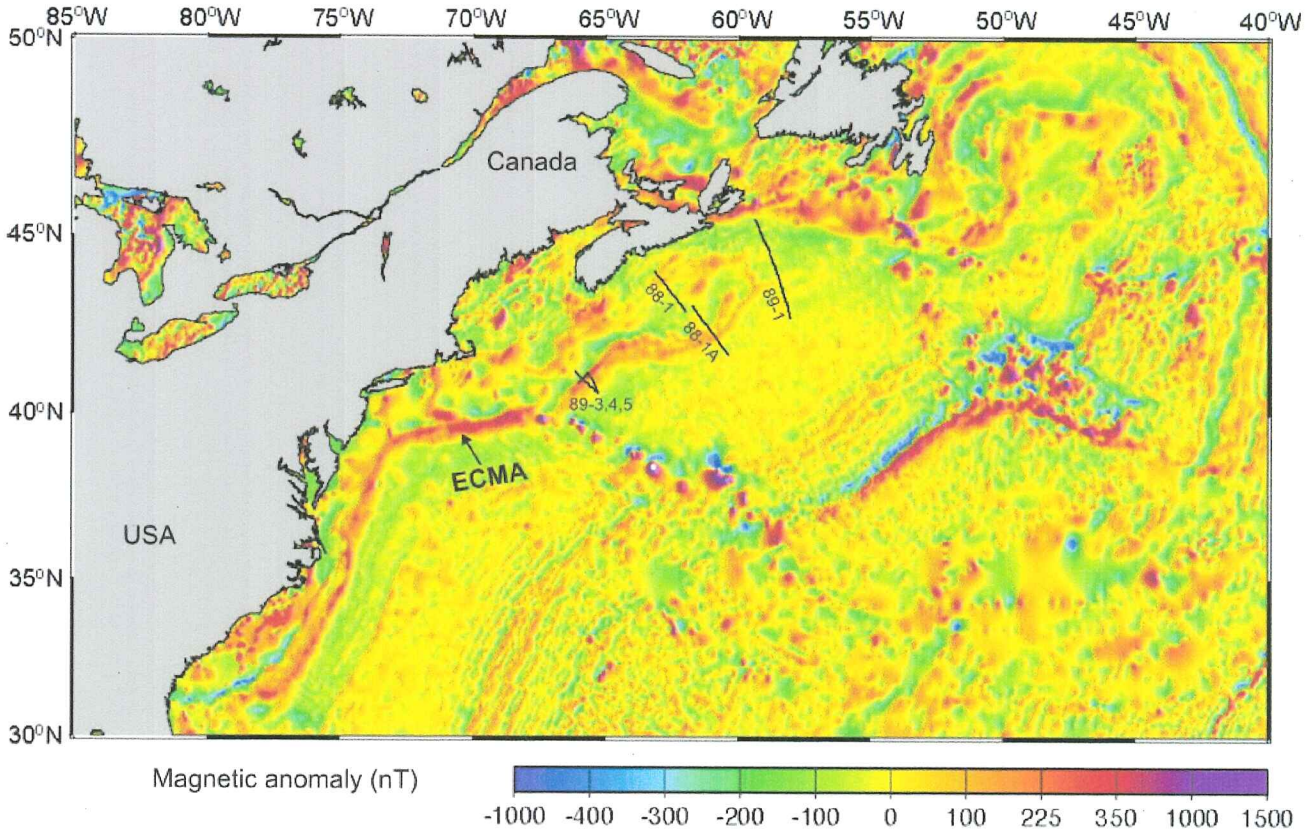

Figure 1.3. Regional magnetic anomalies offshore the east coast of the US and Canada. MCS lines are indicated for reference: 88-1, 1A (Keen et al. 1991b), 89-1 (Keen and Potter 1995b), 89-3, 4, 5 (Keen and Potter 1995a). ECMA: east coast magnetic anomaly.

central Nova Scotia margin volcanic or non-volcanic?", "is the volcanic to non-volcanic margin transition smooth or a sharp boundary?" and "where does the volcanic to non-volcanic margin transition take place?" This thesis will focus on these questions, which are important to understanding of the formation of the Nova Scotia margin.

1.2 Geological Setting of Eastern Canada

1.2.1 The Appalachian Orogen

Figure 1.4 is the geological map of eastern Canada, including the coastal area (after Wheeler et al. 1997). The basement rocks have recorded the history of late Precambrian rifting and the development of a Palaeozoic passive continental margin during the opening of the Iapetus Ocean, a Palaeozoic equivalent of the Atlantic Ocean (Keen et al. 1990). The Iapetus Ocean was closed in the Ordovician (Williams 1979), which produced the Appalachian Orogen after subduction and accretion of oceanic crust (Colman-Sadd 1982). The continental crust of eastern Canada, including the Nova Scotia, New Brunswick and Newfoundland, was formed during the Appalachian Orogen.

Closing of the Iapetus destroyed the Palaeozoic continental margin and several large exotic terranes were added to North America. Starting from the south, the basement of southern and central Nova Scotia consists of rocks of the Meguma Terrane, intruded by granitoid rocks (William 1979; Keppie 1989; Clarke and Chatterjee 1992). The Meguma terrane is composed of fine-grained siliciclastic turbidites and is of Gondwanan affinity based on its dispersal pattern (Schenck 1970). Keppie and Dallmeyer (1995) suggested that the basement rocks are Precambrian. Palaeozoic intrusions occurred during 380-370 Ma

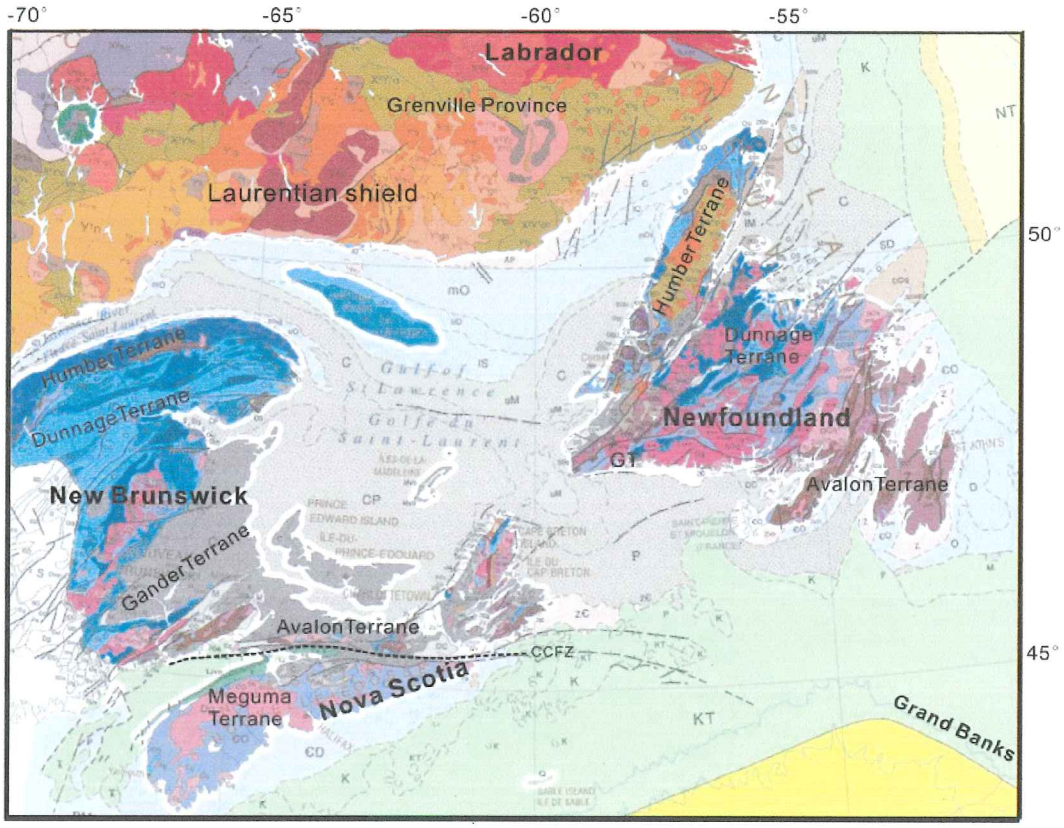

Figure 1.4. Geological map of eastern Canada (modified from Wheeler *et al.* 1997). GT-Gander Terrane. Legend can be downloaded from http://gdr.nrcan.gc.ca/mirage/mirage_list_e.php?id=208175.

Ma (Keppie and Dallmeyer 1995) and the South Mountain Batholith is the largest in the Appalachian Orogen (Benn et al. 1997). Hotspot activity may have caused the intrusion of granites and less mafic rocks (Murphy et al. 1999). The northern Nova Scotia shore, Cape Breton Island, and the eastern Grand Banks and southeastern Newfoundland belong to the Avalon Terrane (Williams and Hatcher 1982; Barr and Baeside 1989), which is separated from the Meguma Terrane to the south along the Cobequid Chedabucto fault zone (CCFZ, Figure 1.4; Withjack et al. 1995). The fault is steep from surface to ~6 km depth (Webster et al. 1998). Off Cape Breton, the Meguma-Avalon contact dips southward (Marillier et al. 1989; Jackson et al. submitted). Farther to the north, the Gander Terrane, the Dunnage Terrane and Humber Terrane are east to northeast trending (Figure 1.4). North of the Appalachian Orogen is the Laurentian Shield (Figure 1.4), which was not involved in the Palaeozoic opening and closing of Iapetus Ocean.

1.2.2 Episodes of Mesozoic Rifting

Mesozoic rifting and the subsequent seafloor spreading created the North Atlantic Ocean and the contemporary Atlantic passive margin system. Figure 1.5 shows plate reconstructions for the primary Mesozoic rifting episodes between North America and Africa, Europe, and Greenland. The Nova Scotia margin was formed by separation of Africa from North America in the middle Triassic to Early Jurassic (230-175 Ma; Welsink et al. 1989). The rifted margin east of the Grand Banks, and the rifted margin northeast of Newfoundland Flemish Cap margin, the Labrador Sea margin, and their conjugates were all formed during the following episodes of Mesozoic rifting (Figure 1.5), starting in early Cretaceous (~130 Ma) and ending in late Cretaceous (~80 Ma;

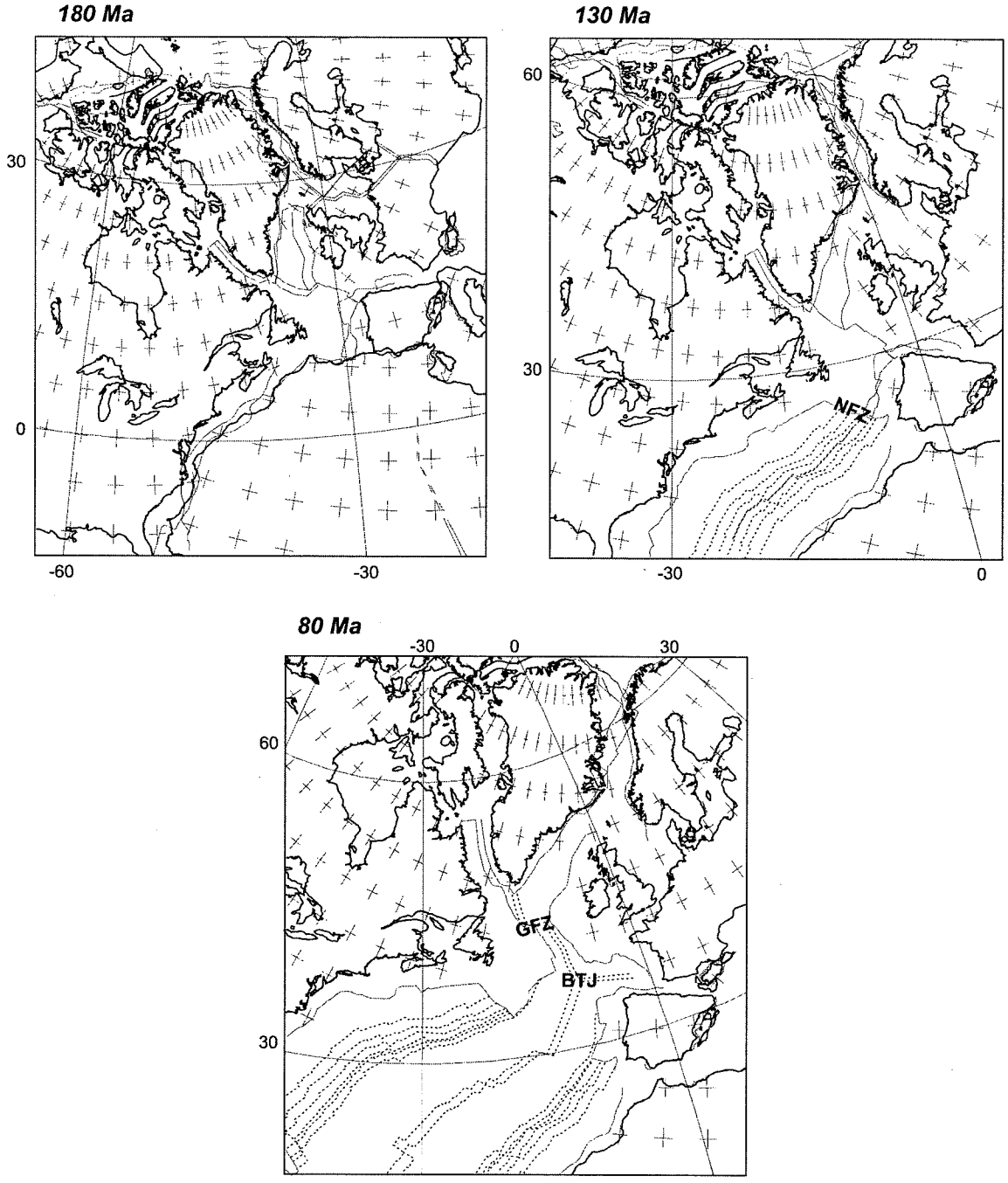

Figure 1.5. Plate reconstructions of the North Atlantic at 180 Ma, 130 Ma, and 80 Ma, respectively. Dashed lines are magnetic anomalies of oceanic crust. NFZ–Newfoundland Fracture Zone; GFZ–Charlie-Gibbs Fracture Zone; BTJ–Biscay Triple Junction. Reconstructions from Coffin *et al.* (1992), after Louden and Chian (1999).

Hiscott et al. 1990; Watt 1969; Moullade et al. 1988; Louden and Chian 1999). The Scotian/Moroccan margin conjugates, including the US East Coast margins and their conjugates (Figure 1.1), represent the earliest episode of Mesozoic rifting along the North Atlantic (Figure 1.5; Klitgord and Schouten 1986).

1.2.3 Volcanism during Mesozoic Rifting

Two periods of magmatism were associated with early Mesozoic continental rifting of eastern Canada (Figure 1.6; Pe-Piper et al. 1990). The earlier igneous activity on the Nova Scotia margin occurred during the earliest stage of Mesozoic rifting by intrusion, which is represented by alkaline dikes in the Northumberland Strait F-25 well and in southwest Nova Scotia. The former consists of rocks of sodic high-alumina olivine tholeiites, with a whole-rock K/Ar date of 214 ± 9 Ma or older date of 239 ± 10 Ma on removal of pyroxene phenocrysts (Pe-piper and Jansa 1986). The latter contains mafic dikes of similar age (Rogers, 1985). One dike from the Wedgeport (Figure 1.6) was about 225 Ma defined by $^{39}Ar/^{40}Ar$ (Reynolds et al. 1987).

The younger period of igneous activity is associated with the main phase of Mesozoic rifting (Pe-piper et al. 1990). The igneous rocks are tholeiitic basalts, represented by both dikes and extensive multiple lava flows. Large igneous dikes include the Shelburne dike (Papezik and Barr 1981) and the Caraquet dike (Burke et al. 1973; Greenough and Papezik 1986). These dikes show multiple injections of magma and are tens of meters wide and more than 100 km long. The Shelburne dike extends more than 450 km along

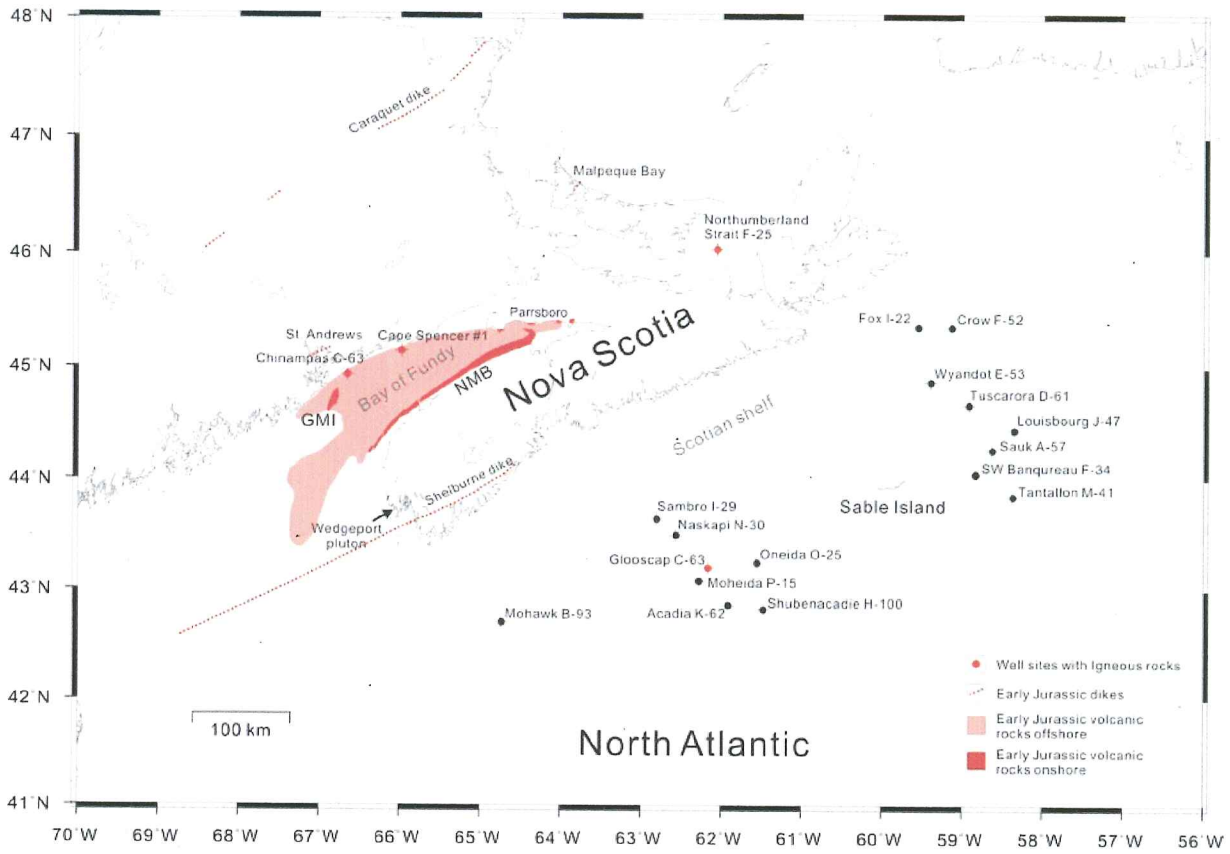

Figure 1.6. Mesezoic volcanism onshore and offshore Nova Scotia. Red areas denote the onshore igneous province of late Triassic and early Jurassic lava surface flows; dotted lines the dikes onshore and offshore. The Pink area indicates the subsurface basalt in the Bay of Fundy. Filled circles overprinted on crosses mark the location of deep exploration wells on the Scotian shelf (BASIN database, Geological Survey of Canada, Dartmouth, Nova Scotia, Canada). Igneous rocks are also presented at well sites offshore (red ones), which are described in the text. NMB: North Mountain Basalt; GMI: Grand Manan Island. The distribution of igneous rocks is based on Pe-Piper et al. (1992).

the southern shore of Nova Scotia and into offshore region indicated by its magnetic signature (Figure 1.6). Short dikes are also exposed on Minister Island (near St. Andrews, New Brunswick) and at Malpeque Bay, north of Summerside, Prince Edward Island (Figure 1.6). Precise dates of these dikes tend to cluster into two groups, one about 191 Ma and the other about 201 Ma (Pe-Piper et al. 1992). Basaltic lava flows from this stage of igneous activity form the landscape features in and around the Bay of Fundy. Onshore, the North Mountain of Nova Scotia extends from Cape Blomidon to Brier Island. Basaltic flows also cover much of the Grand Manan Island, New Brunswick (Pringle et al. 1974), and appear along the northern shore of the Minas Basin in Nova Scotia, at Cape d'Or near Advocate Harbour in the west, around Parrsboro-Five Islands-Bass River area (Greenough et al. 1989), and at Economy Mountain in the east. K/Ar dates of the North Mountain Basalt range from 195 ± 4 Ma (Armstrong and Besancon 1970) to 200 ± 10 Ma (Carmichael and Palmer 1968). Offshore, the North Mountain Basalt underlies most of the Bay of Fundy (Pe-Piper et al. 1992; Figure 1.6), which has been sampled in two wells, the Chinampas N-37 (Greenough and Papezik 1987) and the Cape Spencer #1 (Pe-Piper et al. 1992). Radiometric dating suggested an age of 191 Ma for the North Mountain Basalt (Hyatsu, 1979), which is consistent with the age of the onshore North Mountain Basalt.

On the Nova Scotia shelf, basalt rocks of a total thickness of 153 m appear in the Glooscap C-63 well (Pe-Piper et al. 1992; Figure 1.6). This well is located at the center of Triassic Mohican rift graben (Given 1977), with 7 km southward dipping sediments. The volcanic rocks appear at the depths of 3893-3935 m, 3935-3998 m, and 3998-4046 m.

Whole-rock K/Ar dating suggested an age of 176 ± 7 Ma. The upper layer is overlain by Toarcian and the lower unit underlain by Carnian-Norian strata with a sharp contact by red beds intercalated with thick salt layers. Basement was not reached in the well.

The two periods of magmatism are related with two phases of rifting. The earlier one occurred with the onset of Mesozoic rifting when basins formed by extension and normal dip-slip faults, and were filled by thick terrigenous clastics and evaporites. However, the associated igneous activity is of such a limited extent that rifting is lacking in volcanic rocks in most areas around eastern Canada (Pe-Piper et al. 1992) and the remaining Central Atlantic Margins (Olsen et al. 1981; Marzoli et al. 1999). The younger phase of magmatism involved flexural uplift along and landward of the hinge zone and subsidence seaward (Jansa and Wade 1975). The igneous activity in this period contains extensive extrusion, which is not only observed as outcrops onshore and in wells offshore Nova Scotia (Pe-Piper et al. 1992), but also prevailed in all the Central Atlantic Magmatic Provinces (CAMP; Figure 1.7), including once-contiguous parts of North America, South America, Africa and Europe associated with the breakup of Pangea (e.g. Sutter and Smith 1979; Olsen et al. 1981; Sutter 1985; Pe-Piper et al. 1992; Olsen 1997; Marzoli et al. 1999). However, the total volume of observed magmatic material in the circum-Atlantic region is small and most of this wide-spread magmatism event was consistently emplaced over a short time interval, within a few million years with a peak at ~200 Ma (Olsen et al. 1981; Sutter 1985; Pe-Piper et al. 1992; Olsen 1997; Marzoli et al. 1999; Hames et al. 2000). The main magmatic phase took place ~25 m.y. before the separation of continental crust and the first formation of oceanic crust (Pe-Piper et al. 1992).

Figure 1.7. Mesozoic volcanism in the Central Atlantic Magmatic Province (CAMP). The base map is the pre-Atlantic reconstruction modified from Klitgord and Schouten (1986). The paleo-equator is from Olsen (1997). The SDR wedge basalt location is from Holbrook and Kelemen (1993). Dikes, sills and basalts in Africa are mainly as shown by Deckart et al. (1997). Basaltic rocks in Atlantic Canada were from Pe-Piper et al. (1992) and Pe-Piper et al. (1990). Volcanic features in Eastern USA were from Sutter and Smith (1979) and Sutter (1985). CAMP features in South America were collected mainly from Marzoli et al. (1999), Baksi and Archibald (1997), Montes-Lauar et al. (1994), and Oliveira et al. (1990). Labels are WA = West Armoricain dike swarm, France (Caroff et al., 1995); ME = Messejana dike, Portugal and Spain (Schermerhorn et al., 1978); A = Avalon dike, Newfoundland (Papezik and Hodych, 1980); C = Caraquet dike, New Brunswick and Maine (Greenough and Papezik, 1986); S = Shelburne dike, Nova Scotia (Papezik and Barr, 1981); X = Christmas Cove dike, Maine (McHone et al. 1995); H = Higganum-Holden-Onway dike system, Connecticut-Massachusetts-New Hampshire (Philpotts and Martello, 1986); Z = Foum Zguid dike, Morocco (Bertrand, 1991); KK = Ksi-Ksou dike, Algeria (Bertrand, 1991); CE = Ceara alkali basalt, northern Brazil (Marzoli et al., 1999); MA = Maranhao dikes and basalts, Brazil (Fodor et al., 1990); MO = Mosquito basalt, western part of the Maranhao province (Baksi and Archibald, 1997); RO = Roraima dike swarm, Brazil (Marzoli et al., 1999); AM = Amazon Basin sill province (Marzoli et al., 1999); AN = Anari basalt, western Brazil (Montes-Lauar et al., 1994); TP = Tapirapua basalt, western Brazil (Montes-Lauar et al., 1994); BP = Blake Plateau area, western Atlantic; FL = Florida, southern USA; SGR = South Georgia Rift terrane (basalts described by Sundeen, 1989; Gohn et al., 1978; Arthur, 1988; McBride, 1991); MS = Mississippi Embayment (basalt dated by Baksi, 1997). This CAMP map is adapted from Hames et al. (2002) and McHone (2000).

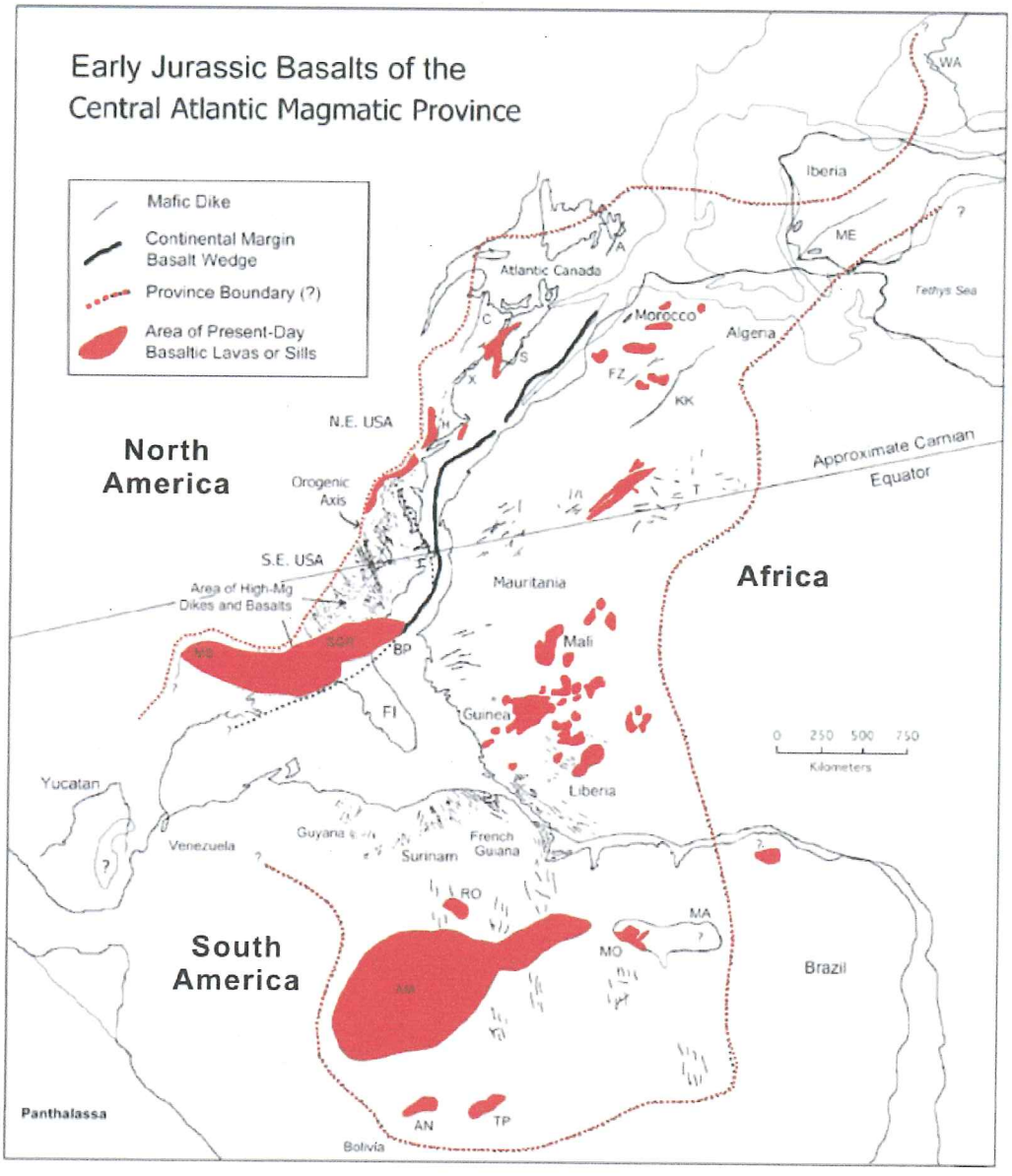
Early Jurassic Basalts of the
Central Atlantic Magmatic Province
Mafic Dike
Continental Margin Basalt Wedge
Province Boundary (?)
Area of Present-Day Basaltic Lavas or Sills
North America
South America
Africa
Iberia
Atlantic Canada
Morocco
Algeria
Tethys Sea
N.E. USA
S.E. USA
Orogenic Axis
Approximate Carnian Equator
Area of High-Mg Dikes and Basalts
Mauritania
Mali
Guinea
Liberia
Yucatan
Venezuela
Guyana
Surinam
French Guiana
Brazil
Panthalassa
Bolivia
0 250 500 750
Kilometers

1.3 Previous Geophysical Observations

1.3.1 Seismic Refraction Surveys

Offshore Nova Scotia, a large amount of seismic refraction data was collected in the past half century. The early seismic refraction experiments were carried out by Officer and Ewing (1954), Barrett et al. (1964), Jackson et al. (1975), Keen et al. (1975) and Keen and Cordsen (1981). Location of the selected previous profiles is shown in Figure 1.8. Officer and Ewing (1954) noticed that the rifted continental crust offshore southern Nova Scotia subsides from 5,000 feet to 20,000 feet under the continental slope. Barrett et al. (1964) measured velocities of 5.5 km/s, 6.1 km/s and 8.1 km/s for upper crust (Meguma rocks), lower crust and upper mantle, respectively. A high velocity layer was identified underlying the Meguma terrane, which was attributed to rocks of mafic underplating or Avalon terrane (Barrett et al. 1964). An expendable sonobuoy wide-angle reflection and refraction survey was also carried out offshore Nova Scotia, from which detailed sediment velocities were obtained (Jackson et al. 1975). Jackson et al. (1975) suggested that the continent-ocean transition off Nova Scotia may be limited to a 75-km-wide zone based on refraction data. Keen et al. (1975) reported that a 10-km-wide layer south of Sable Island with velocity of ~7.4 km/s was directly overlain by sediment.

These early seismic refraction surveys laid the framework for future research. However, the velocity models obtained are not detailed enough for understanding the rifting process of the Scotian margin. The reasons are due to a number of factors. One is that most of the previous profiles only had a few recording stations with large spacing, some of which were deployed on the coast while shooting offshore (e.g. Barrett et al. 1964). The shot spacing was also very large (e.g. 15 km for explosive shooting) such that the detailed

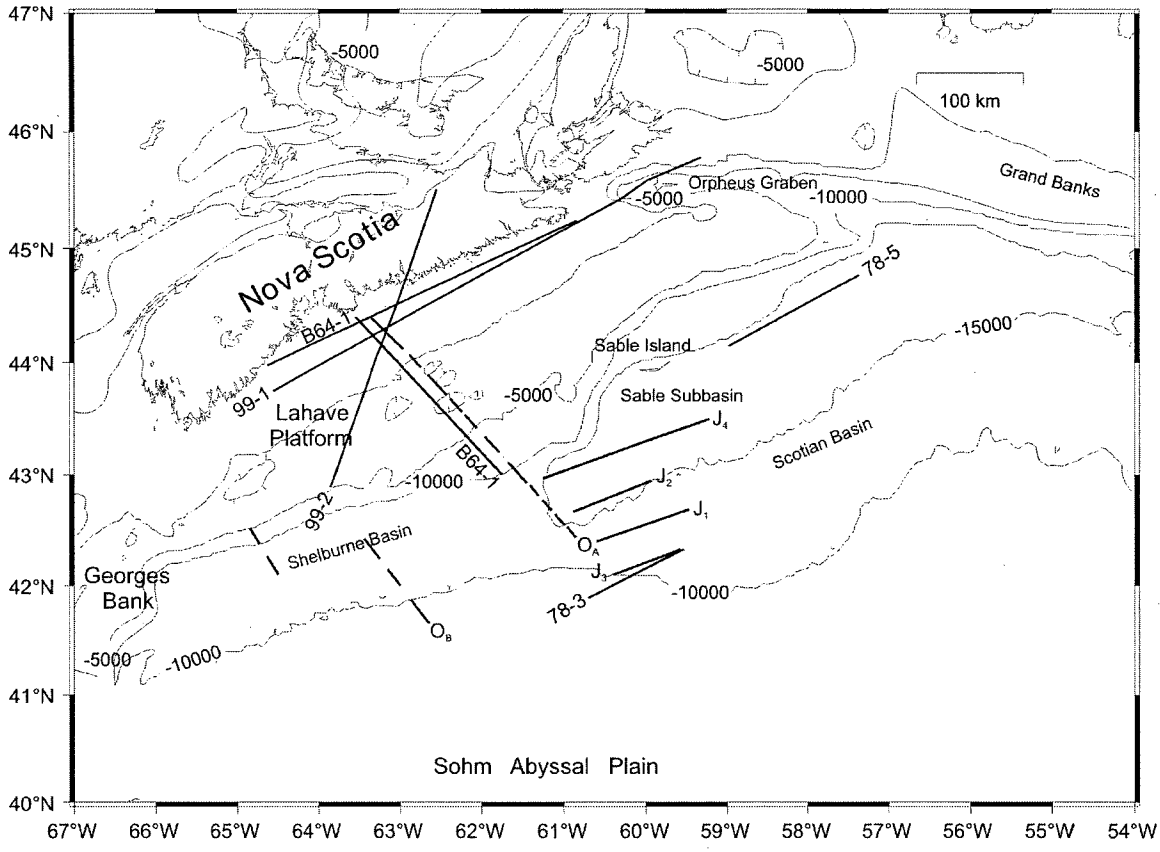

Figure 1.8. Previous refraction profiles onshore and offshore Nova Scotia: O_A and O_B (Officer and Ewing 1954), which were carried out in short sections indicated as broken lines, B64-1 and B64-2 (Barrett et al. 1964), J_1-J_4 (Jackson et al. 1975), 78-3 and 78-5 (Keen and Cordsen 1981), 99-1 (Jackson et al. submitted) and 99-2 (Jackson et al. 2000). Basement depth contours offshore are shown as thin lines (Oakey and Start 1995), with contours -5,000 m, -10,000 m, and -15,000 m labeled.

crustal structure was not recorded by the acquisition system. This contrasts to recent studies where tens of ocean bottom seismometers (OBS) are deployed on the seabed at much narrow spacing along the survey track and with airgun shooting at about 100 m intervals coincident with the track of OBS deployment. The details of present techniques of instrumentation, positioning and interpretation are described in chapter 2. It is expected that modern instrument and techniques will be able to avoid the shortcomings of previous studies. The other limiting factor to early studies is that all of the previous profiles were short (see Figure 1.8), and none of them crossed the entire margin from un-stretched continental crust to unequivocal oceanic crust. The longest the refraction profile offshore O_A is also composed of many short sections (Officer and Ewing 1954; Figure 1.8). Other refraction profiles are carried out along the strike, e.g. 78-3, 78-5 (Keen and Cordsen 1981), and they are short as well. Therefore, it is difficult to derive the full crustal structure for the rifting process across the entire margin from such limited data. In addition, it is hard to demonstrate the along strike variation of crustal structure with a number of short but scattered refraction profiles conducted along the margin.

Two long refraction profiles (99-1 and 99-2) were acquired recently (Jackson et al. 2000; Jackson et al. submitted). The refraction data along these lines provide detailed velocity constraint for the Meguma Supergroup and the internal structures of Mesozoic terranes, such as the geometry of the suture between the Avalon and Meguma Terranes (CCFZ, Figure 1.4). However, 99-1 is parallel and very close to the shoreline and 99-2 is partly onshore and partly on the Scotian shelf. These long profiles were not intended to investigate the crustal structure across the continent to ocean transition of this margin. To

study the crustal structural variation, including the varying volcanism along the margin, a series of across-margin refraction transects are required to be carried out along the entire margin.

1.3.2 Seismic Reflection Surveys

Reflection seismic surveys for studies of crustal structure started as early as the refraction surveys (e.g. Jackson et al. 1975; Keen et al. 1975; Barrett and Keen 1976). Early seismic reflection profiles were acquired across the refraction lines so as to allow layers in the refraction survey to be related to particular reflectors (e.g. Jackson et al. 1975). Based on seismic reflection images offshore Nova Scotia, Barrett and Keen (1976) identified Mesozoic magnetic anomalies M26-M28 in the Jurassic Magnetic Quiet zone (JMQZ). However, the deep structures beneath the basement surface were barely recognizable in the early seismic reflection profiles due to limited hydrophone group channels and short streamer array (e.g. Barrett and Keen 1976). A number of seismic reflection profiles were carried out to define the internal structures of Meguma and Avalon terranes or the crustal structure of early stage of Mesozoic rifting, e.g. MCS lines 88-2, 3, 4 (Keen et al. 1991a) and 86-5A and 5B (Marillier et al. 1989). Numerous seismic reflection lines were acquired offshore Nova Scotia by industries for petroleum exploration (e.g. TGS, GSI; Figure 1.9). These lines have densely covered the Scotian slope area; but most of them are short and were intended to investigate the sedimentary structure.

In order to study the crustal extension and varying volcanism along the Nova Scotia margin, a number of across-margin MCS profiles were acquired in late 1980s (Figure

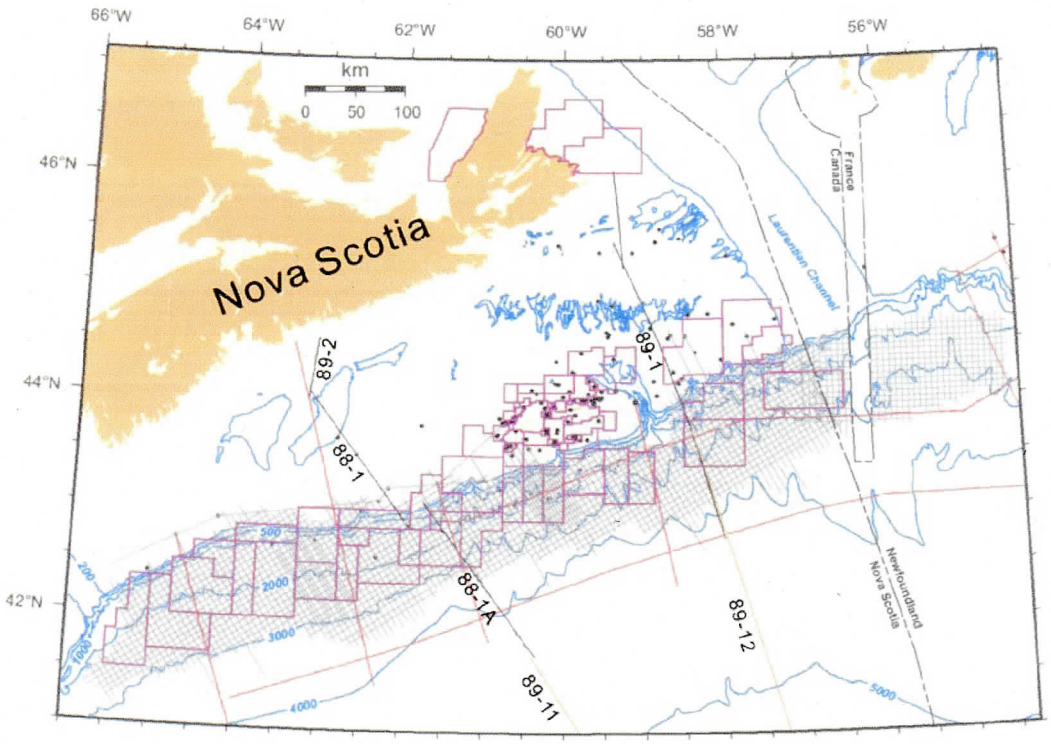

Figure 1.9. Location map showing areas for exploration off Nova Scotia. Seismic exploration datasets include TGS-Nopec (1998/1999) in grey and GSI (1972) in red. LITHOPROBE 1988/1989 lines are also denoted in black, including 88-1,1A (Keen et al. 1991a) and 89-1 (Keen and Potter 1995a). BGR lines 89-11 and 89-12 (unpublished, data courtesy the German Federal Agency of Geosciences and Natural Resources) are shown in brown. Wells drilled in the Scotian Basin are marked by dots. Bathymetry contours 200 m, 500 m, 1,000 m, 2,000 m, 3,000 m, 4,000 m, and 5,000 m are labeled. After Shimeld (2004).

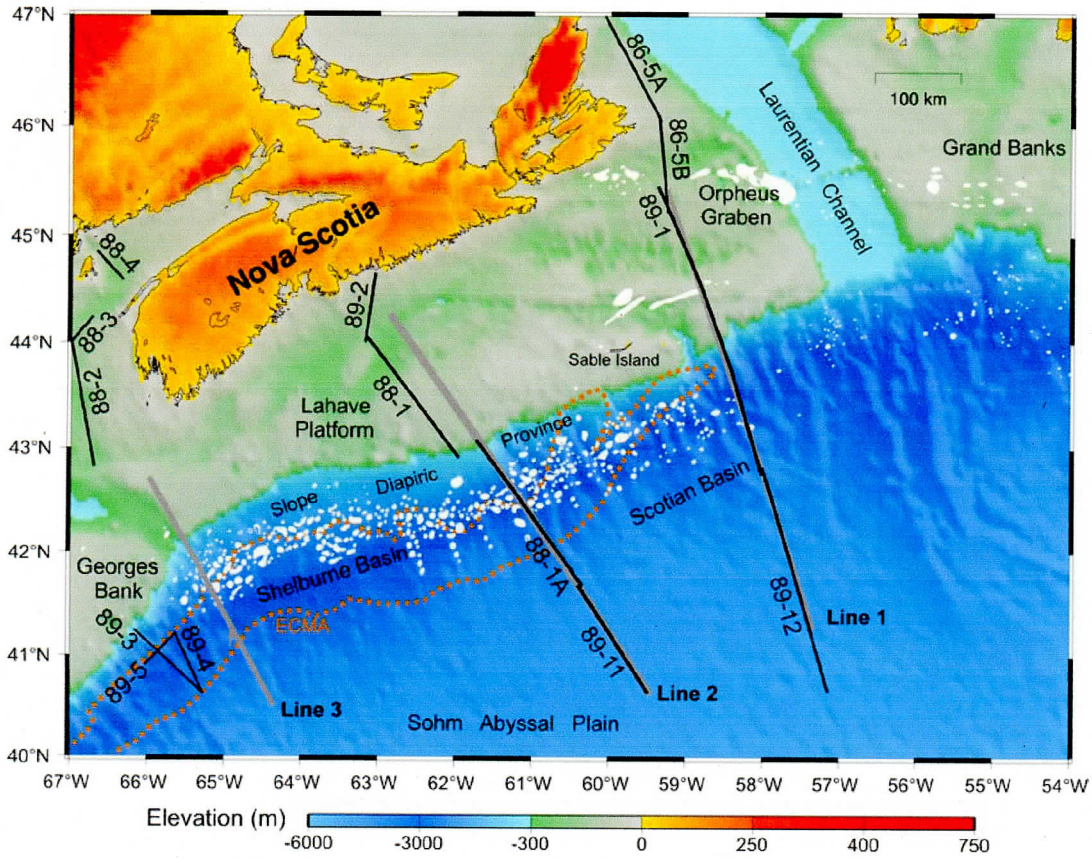

Figure 1.10. Previous seismic reflection profiles across the Nova Scotia margin. Previous seismic reflection profiles include 88-1,1A (Keen et al. 1991b), 88-2 (Keen et al. 1991a), 89-1 (Keen and Potter 1995a), 89-3, 4, 5 (Keen and Potter 1995b) and BGR lines 89-11 and 89-12 (unpublished, data courtesy the German Federal Agency of Geosciences and Natural Resources). The wide-angle refraction/reflection (WAR/R) profiles acquired during the SMART experiment Lines 1-3 are also shown as grey lines. The orange-doted region denotes the East Coast Magnetic Anomaly (ECMA), which is shown in Figure 1.3. The white-dotted area indicates the salt distribution along slope diapiric province (Wade and MacLean 1990).

1.10), such as MCS lines 89-3, 4, 5 (Keen and Potter 1995a), 88-1,1A (Keen et al. 1991b), and 89-1 (Keen and Potter 1995b). MCS lines 89-3, 4, 5 to the southwest of Nova Scotia cross the ECMA that parallels much of the margin of eastern North America, including the southwest of Nova Scotia. Studies along the US Atlantic coast margin suggest that the ECMA may be related to the emplacement of a large thickness of late rift-stage or early drift-stage igneous wedge which is characterized by SDRs at the basement surface and by HVLC layers underneath (Austin et al. 1990; Sheridan et al. 1993; Holbrook and Kelemen, 1993). The seismic image of 89-3 (Figure 1.11) shows that the SDR are still observed southwest of Nova Scotia, indicating that the area of the southwestern Nova Scotia margin is volcanic.

MCS lines 88-1, 1A span the central Nova Scotia margin across the LaHave Platform, the Naskapi Graben Complex, and the Mohican Graben (Given 1977). In the upper crust, Mesozoic extension is reflected by normal faults (NF, Figure 1.12), which flatten and end at mid-crust. In the lower crust and upper mantle, Mesozoic rifting produced dipping reflectors, which are interpreted to be major detachment faults (DF, Figure 1.12; Keen et al. 1991b). According to Keen et al. (1991b), there are some landward dipping reflections that may be correlated with igneous rocks beneath the thinned continental crust (I, Figure 1.12). These landward dipping reflections appear roughly underneath the ECMA, which is located at the seaward edge of the slope diapiric structure (Figure 1.10), indicating that the central margin may be volcanic in character. However, the seemingly landward dipping reflections observed beneath the salt might be artifacts caused by the irregular geometry of the salt/shale diapers. Such artifacts have been observed along recent seismic

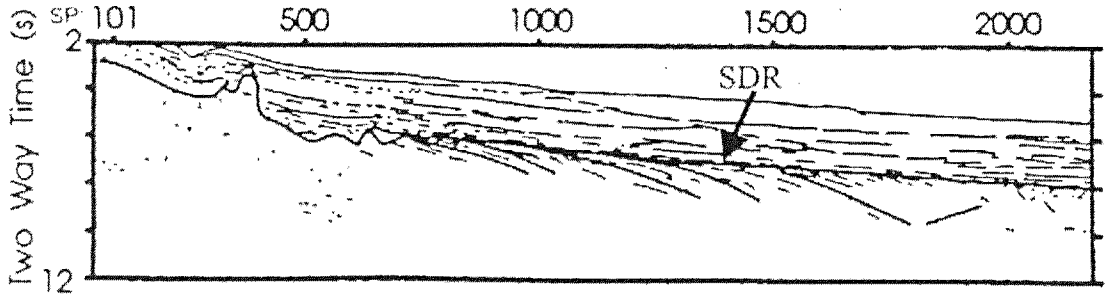

Figure 1.11. Line drawing of MCS profile 89-3. SDR: seaward dipping reflections. After Keen and Potter (1995a). See Figure 1.10 for location.

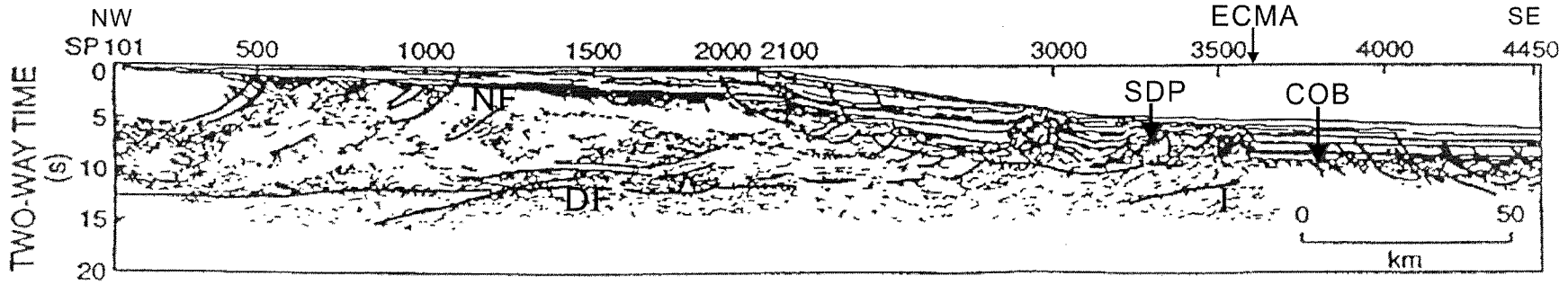

Figure 1.12. Line drawing of the composite profile of 88-1 and 88-1A. SDP: slope diapiric province; COB: continent-ocean boundary; NF: normal faults; DF: detachment faults; I: intrusives; ECMA: East Coast Magnetic Anomaly. After Keen et al. (1991b). See Figure 1.10 for location.

profiles offshore Nova Scotia (e.g. NovaSpan profile 1600 shown in chapter 3). In addition, it is not clear if SDR sequences exist beneath the salt/shale diapirs. The problem is that the slope diapiric salts along line 88-1A may have masked the deep structure. It is possible that large-scale volcanism has occurred beneath the diapiric salts but that the overlying salt has obscured the SDR produced by extrusive rocks. Therefore, the absence of the SDR is not sufficient to conclude that seaward dipping reflectors associated with volcanism do not exist along 88-1A. The Glooscap C-63 well on the outer shelf did show 153 m of basalt in sediment but the well did not penetrate the basement rocks.

These facts leave uncertainties about the nature of the margin along 88-1A and the location of the volcanic/non-volcanic transition. In this case, the MCS data alone are not able to address these problems. To identify whether the central Nova Scotia margin is volcanic or non-volcanic, will rely on the following evidences: 1) whether or not a thick layer of underplated rocks exists beneath the rifted continental crust, and 2) whether or not large-scale volcanic rocks appear at the basement surface beneath the ECMA. The first problem will depend on whether a thickened layer of anomalously high velocity exists. This requires cross-margin transects of wide-angle refraction seismic experiments. To solve the second problem requires using recent migration techniques to improve the seismic reflection image such that we may be able to verify whether or not SDR sequences, indicative of volcanic lava flows, exist beneath the salt structure. These issues will be addressed in chapters 2 and 3, respectively.

The extreme seaward end of the profile 88-1A is characterized by increasing basement relief associated with listric normal faults and linear landward-dipping intrabasement reflections. Wade and MacLean (1990) mapped the landward limit of oceanic crust at shot point (SP) 3800, as that position marked the landward extent of the diagnostic hyperbolic character of oceanic basement on unmigrated MCS sections. Keen et al. (1991b) interpreted the smooth zone (SP 3650-3800) seaward of the slope diapiric structure as basaltic rocks that extruded upon continental rocks, and used this interpretation to assign a continent-ocean boundary (COB) between the smooth and rough zones. However, this is also questionable because the deep crustal structure beneath the slope diapiric salts was masked such that the character of the basement across this region is unclear.

For the continental margins further north along the North Atlantic, the continent to ocean transition appears to be a wide transition zone with a thin upper layer of unclear character overlying partially sperpentinized mantle, such as the Newfoundland Basin continental margin (Lau et al. 2006a) and the Labrador Sea margin (Chian et al. 1995a). Such is also the case for the northern Scotian margin along 89-1 (Keen and Potter 1995b; Figure 1.13), where the OCT zone is characterized by a ~70-km-wide zone of flat basement topography (B, Figure 1.13) and a constant thickness (~2 km) of the upper basement layer. The landward limit of this zone appears to be blurred by overlying salt structures or synkinematic wedge on top of salt (shaded area, Figure 1.13; Ings and Shimeld 2006). Further seaward of this zone, which will be presented in chapters 2 and 5, anomalously thin (~4 km) oceanic crust is imaged along BGR 89-12 (see Figures 5.1 and 5.9 in

chapter 5; data courtesy German Federal Agency of Geosciences and Natural Resources). This OCT zone was interpreted as consisting of a ~70-km-wide zone of exposed mantle which separates the rifted continental crust and the oceanic crust (Funck et al. 2004).

Across the central Nova Scotia margin, the question is whether a sharp COB or a wide OCT zone exists between the continental crust and normal oceanic crust. To reveal the characteristic transition from continental crust to normal ocean crust will require a detailed velocity structure, which can be derived from coincident wide-angle refraction seismic data. An additional problem is that the existing reflection profile is not long enough to fully image the differences between continental and oceanic crust. Processing and interpreting additional MCS data seaward of this line (e.g. BGR 89-11) will provide a full width of reflection geometry across this margin.

In addition, the diminishing magnitude of the ECMA (Figure 1.3) along the major part of the Nova Scotia margin indicates the transition from a volcanic margin in the south to a non-volcanic margin in the north may take place between the southern and northern part of the Nova Scotia margin. However, no seismic profiles are available between MCS lines 89-3, 4, 5, and lines 88-1,1A, which provide firm evidence where the SDRs, indicative of extrusive rocks, disappear within this ~500 km offshore region. To demonstrate where the SDR sequences disappear along the margin requires additional strike profiles or a number of dip profiles that across the margin between MCS lines 88-1,1A and lines 89-3, 4, 5. This thesis will show such a strike profile that covers the full length of the Nova Scotia margin.

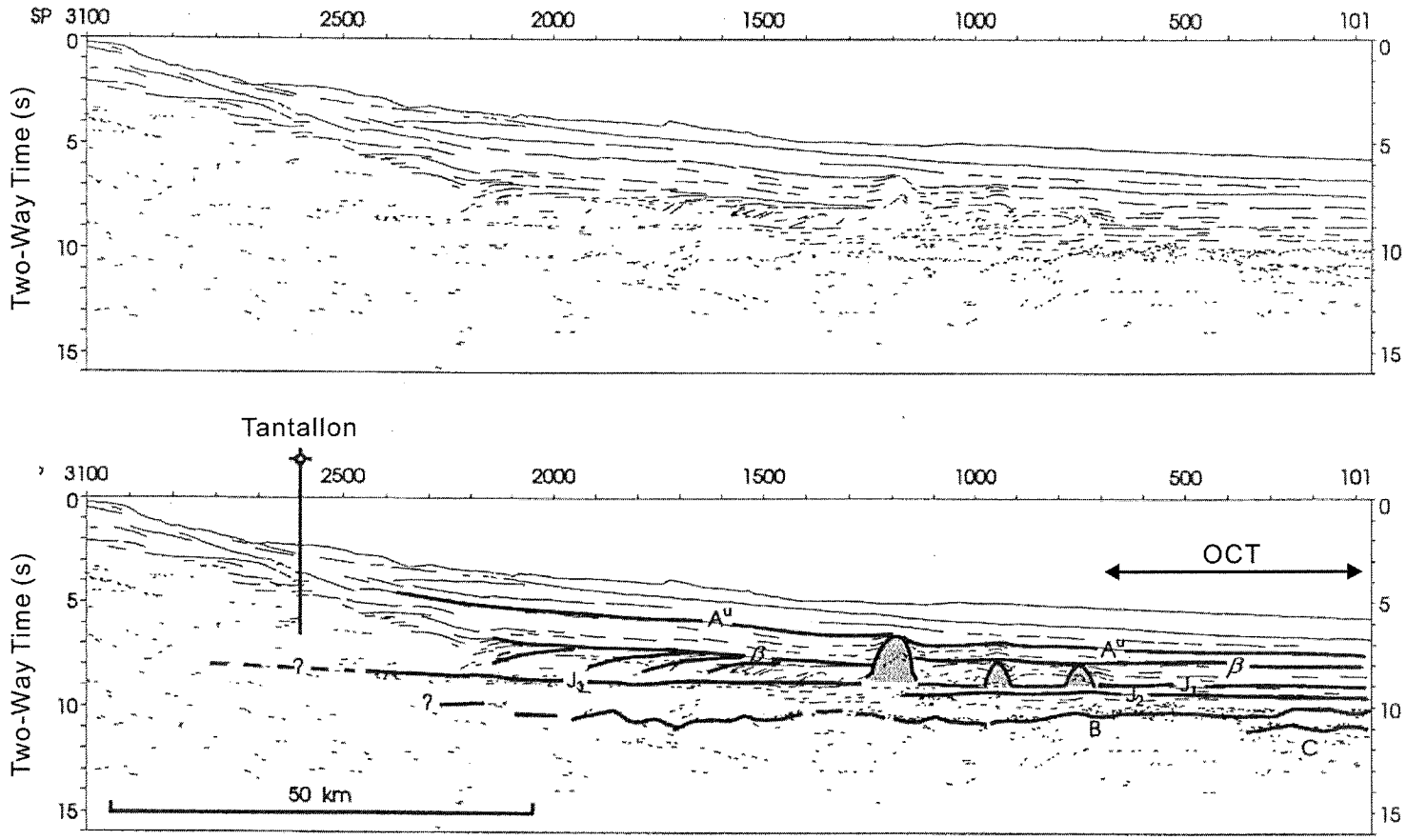

Figure 1.13. Line drawing (upper panel) and interpretation (lower panel) of MCS profile of 89-1 shot point 101-3100. Heavy lines and letters in the lower panel are the interpretation. B: top of basement; C: subbasement reflector. The ages of the sedimentary horizons are indicated by A^u (Oligocene), β (Barremian), J_1 (Top Jurassic), J_2 (Callovian-early Oxfordian) and J_3 (Upper/Middle Jurassic). Shaded regions are salt diapirs. After Keen and Potter (1995b). OCT: ocean-continent transition. The location of the well Tantallon is indicated in Figure 1.6.

1.4 Objectives and Methodology

1.4.1 Objectives

Previous refraction profiles were mostly short and none of them crossed the entire margin. A more detailed study of the crustal structure and varying volcanism can be achieved by acquiring new refraction profiles coincident with existing MCS profiles. The Scotian MARgin Transects (SMART) refraction seismic experiment was designed offshore Nova Scotia to image the along-strike variation in crustal structure from a volcanic to a non-volcanic style of rifting. Three wide-angle seismic refraction profiles (Lines 1-3) were acquired in 2001 (Figure 1.10). Line 1 is parallel to two deep MCS lines (89-1, BGR 89-12) and extends 490 km seaward off Cape Breton Island. Line 2 runs parallel to a MCS line 88-1 and farther seaward it coincides with MCS line 88-1A (Keen *et al.* 1991b) and an unpublished BGR line 89-11, forming a 500-km-long composite profile from the continental shelf to the deep ocean basin. Line 3 crosses the southwest-most part of the Nova Scotia margin near MCS lines 89-3, 4, 5. The crustal structure for these three transects will be constrained by both refraction and coincident reflection data. This thesis focuses on the analyzing and interpreting available geophysical and geological data along Line 2. The specific objectives for this thesis include:

1) Create a detailed velocity model across the central Scotian margin through analyzing and interpreting the wide-angle reflection/refraction (WAR/R) data along a 2D transect SMART Line 2 together with coincident MCS data and gravity data.

2) Improve the seismic reflection images across the OCT zone, beneath the salt/shale diapiric structures, so as to verify whether or not volcanic rocks (indicated by SDR sequences) that are related with ECMA exist at the basement surface.
3) Compare the velocity model of the central margin segment with those of the northern and southern segments if available, to investigate the along-strike crustal structural variation, including the varying volcanism along the Nova Scotia margin.
4) Combine the seismic results on the Scotian margin with those of the conjugate transects on the Morocco margin so as to conceptualize the rifting style of the Scotian/Moroccan margin conjugates.

1.4.2 Methodology

The main method to achieve the objectives will be velocity modeling of WAR/R data and interpreting the resultant velocity model across the central Nova Scotia margin. The WAR/R data were acquired during cruise Hudson-2001. The seismic source was a tuned airgun array, which was fired once a minute with an average shot spacing of 134 m. 21 OBS were deployed to the seafloor for recording seismic signals from shots. A 2D velocity model will be developed by forward modeling of observed travel times using the program RAYINVR (Zelt and Smith 1992; Zelt and Forsyth 1994). The forward model will be refined by using the inversion algorithm of the program.

In addition, bathymetry data, well log data and other existing geophysical data will be utilized to constrain the velocity model. Bathymetry obtained by the ship's echosounder,

and seismic reflection images along the coincident MCS lines 88-1, 88-1A (Keen *et al.* 1991b) and BGR 89-11 will be used to constrain the seafloor, sedimentary layer boundaries, the detailed basement surface and Moho boundaries, where the OBS data are not sufficient to determine the detailed geometry. Gravity data will be used to refine the Moho depth in regions where seismic data (WAR/R and MCS) provide only weak constraint. The sonic well-log data for four wells over the shelf and shallow slope of the central Nova Scotia margin are available and will also be used to constrain the sediment and uppermost basement velocities. The detailed methodologies will be described in chapter 2.

In order to improve the seismic reflection image of the complex structures across the OCT zone, for instance to improve the basement image beneath the salt/shale diapirs, pre-stack migration techniques will be used to reprocess the MCS data, which were previously migrated using post-stack algorithms. Post-stack migration can provide accurate images in regions with horizontal and gently dipping strata (e.g. < 10-15 degrees). For complex structure across the OCT zone where larger dips and irregular reflection geometry are present, however, the subsurface structure can not be accurately imaged due to mid-point smearing (e.g. Yilmaz 2001). This can be circumvented by migrating the unstacked seismic data. Available resources for pre-stack migration techniques at Dalhousie Seismic Group will be used, including equivalent offset migration (EOM; Bancroft and Geiger 1994) and common offset migration (e.g. Yilmaz 2001).

Velocity information plays a key role in migration. For the study of crustal structure, the velocity model derived from OBS data will be used in the pre-stack migrations. The reason for this is that the velocities constrained by OBS data are determined independently by larger offset refraction phases and are often constrained by multiple adjacent OBS instruments; therefore, the velocity field is more accurate for the deep structures compared to that converted from stacking velocities. Chapter 3 will demonstrate that by utilizing the velocities constrained by OBS data, pre-stack migration techniques significantly improved the basement image underneath the salt/shale diapiric structure compared to that of post-stack migration. The depth control of this technique approaches that of pre-stack depth migration.

1.5 Organization

Chapter 1 (this chapter) gives a general introduction of the rifted Scotian margin, including the fundamental concepts, the major evidences of volcanism, the previous geological and geophysical observations, and the objectives and methodologies of this thesis.

Chapter 2 presents the results of the WAR/R profile across the central segment of the Scotian margin, which have been published in the Geophysical Journal International (Wu et al. 2006; see Appendix E for copyright permission).

In chapter 3, the MCS data across the central margin segment are reprocessed using pre-stack time migration techniques based on the velocity model derived from seismic refraction data in chapter 2.

In chapter 4, the seismic results of MCS and WAR/R data and the existing magnetic anomalies and salt distributions from both sides of the Scotian/Moroccan margin conjugates are correlated with each other. This results in reconstructions of the conjugate margin pair at the breakup and pre-rift positions.

Chapter 5 analyzes the characteristic crustal structures in the reconstruction map of the conjugate margin pair, upon which the rifting geometries across the conjugate margins and varying volcanism along the conjugates are synthesized into conceptual models.

Chapter 6 summarizes the major observations and interpretations of this thesis. Possible implication and future work are also pointed out in the last chapter.

CHAPTER 2

CRUSTAL STRUCTURE OF THE CENTRAL NOVA SCOTIA MARGIN OFF EASTERN CANADA (PART I)—RESULTS OF WIDE-ANGLE REFRACTION DATA

2.1 Manuscript Information

2.1.1 Author's Contribution

The author of this thesis prepared all of the components of this manuscript, participated in data acquisition onboard Hudson, performed all of data processing except the generation of data files from recording instruments, all of data analyzing, and all of data interpreting. Coauthors have participated in the formulation of the Scotian MARgin Transects (SMART) program, data acquisition and the reviewing of this manuscript.

2.1.2 Citation

Wu, Y., Louden, K.E., Funck, T., Jackson, H.R., and Dehler, S.A., 2006. Crustal structure of the central Nova Scotia margin off Eastern Canada, *Geophy. J. Int.*, 166, 878–906.

2.1.3 Authors' Names and Addresses

Yue Wu[1], Keith E. Louden[2], Thomas Funck[3], H. Ruth Jackson[4] and Sonya A. Dehler[4]

[1]Department of Earth Sciences, Dalhousie University, Halifax, Nova Scotia, B3H 3J5, Canada, phone: (902) 494-3673, fax: (902) 494-3877, email: wuyue@phys.ocean.dal.ca

[2]Department of Oceanography, Dalhousie University, Halifax, Nova Scotia, B3H 4J1, Canada, phone: (902) 494-3452, fax: (902) 494-3877, email: Keith.Louden@dal.ca

[3]Department of Geophysics, Geological Survey of Denmark and Greenland (GEUS), Øster Voldgade 10, DK-1350 Copenhagen K, Denmark, phone: +45–3814 2652, fax: +45–3814 2050, Email: tf@geus.dk

[4]Geological Survey of Canada (Atlantic), Bedford Institute of Oceanography, P.O. Box 1006, Dartmouth, Nova Scotia, B2Y 4A2, Canada, phone: (902) 426-3791, fax: (902) 426-6152, email: rujackso@nrcan.gc.ca (H. Ruth Jackson) and sdehler@nrcan.gc.ca (Sonya A. Dehler).

2.1.4 Summary

The central Nova Scotia margin off Eastern Canada is located at a transition from a volcanic margin in the south to a non-volcanic margin in the north. In order to study this transition, a wide-angle refraction seismic line with dense airgun shots was acquired across the central Nova Scotia margin. The 500-km-long transect is coincident with previous deep reflection profiles across the Lahave Platform and extending into the Sohm Abyssal Plain. A *P*-wave velocity model was developed from forward and inverse modeling of the wide-angle data from 21 ocean bottom seismometers and coincident normal-incidence reflection profiles. The velocity model shows that the continental crust is divided into three layers with velocities of 5.5-6.9 km/s. The maximum thickness is 36 km. A minor amount (~5 km) of thinning occurs beneath the outer shelf, while the major

thinning to a thickness of 8 km occurs over the slope region. The seaward limit of the continental crust consists of 5-km-thick highly faulted basement. There is no evidence for magmatic underplating beneath the continental crust. On the contrary, a 4-km-thick layer of partially serpentinized mantle (7.6-7.95 km/s) begins beneath the highly faulted continental crust, and extends ~200 km seaward, forming the lower part of the ocean-continent transition zone. The upper part of the transition zone consists of the highly faulted continental crust and 4- to 5-km-thick initial oceanic crust. The continent-ocean boundary is moved ~50 km farther seaward compared to an earlier interpretation based only on reflection seismic data. The oceanic crust in the transition zone consists of layer 2 and a high-velocity lower crustal layer. Layer 2 is 1-3 km thick with velocities of 5.6-6.0 km/s. The high-velocity lower crustal layer is 1-2 km thick with velocities of 7.25-7.4 km/s, suggesting a composite layer of serpentinized peridotite and gabbroic layer 3. Oceanic crust with normal thickness of 5-7 km and more typical layer 3 with velocities of 6.95-7.3 km/s is observed at the seaward end of the profile.

Key words: crustal structure, Nova Scotia margin, continental margins, refraction seismology.

2.2 Introduction

Rifted continental margins typically are classified into two major categories, volcanic and non-volcanic. Volcanic margins are characterized by seaward dipping reflections (SDR) in the basement and thick underplated igneous rocks in the lower part of the thinned continental crust and initial oceanic crust, such as the U.S. East Coast margins (Holbrook and Kelemen 1993; Talwani and Abreu 2000). Non-volcanic margins, on the other hand, are characterized by limited melt generation, which may be a result of slow extensional rates and cooling of the asthenospheric mantle during the long period of continental extension prior to breakup (Bown and White 1995). In this case, an ocean-continent transition (OCT) zone consists of either thin oceanic crust or exposed and serpentinized mantle (Louden and Chian 1999). Such serpentinized mantle rocks have been evidenced by drilling on the Iberia-Galicia Bank (Sawyer *et al.* 1994).

The Nova Scotia margin (Figure 2.1) is located at the transition from volcanic margins to the south, *e.g.* the southern Baltimore Canyon Trough (Talwani and Abreu 2000), to non-volcanic margins to the north, *e.g.* the Grand Banks and Newfoundland Basins (Reid 1994; Funck *et al.* 2003). At the southern margin of Nova Scotia near Georges Bank, a strong, linear magnetic anomaly (~300 nT), referred to as the East Coast Magnetic Anomaly (ECMA), is well developed. Deep marine seismic reflection profiles show SDR sequences on lines 89-3, 4 (Keen and Potter 1995a) coincident with the high-amplitude ECMA. The ECMA progressively weakens northward and eventually disappears within the northern margin offshore Sable Island. The northern margin has been classified as a non-volcanic rifted margin without SDR sequence on line 89-1 (Keen and Potter 1995b).

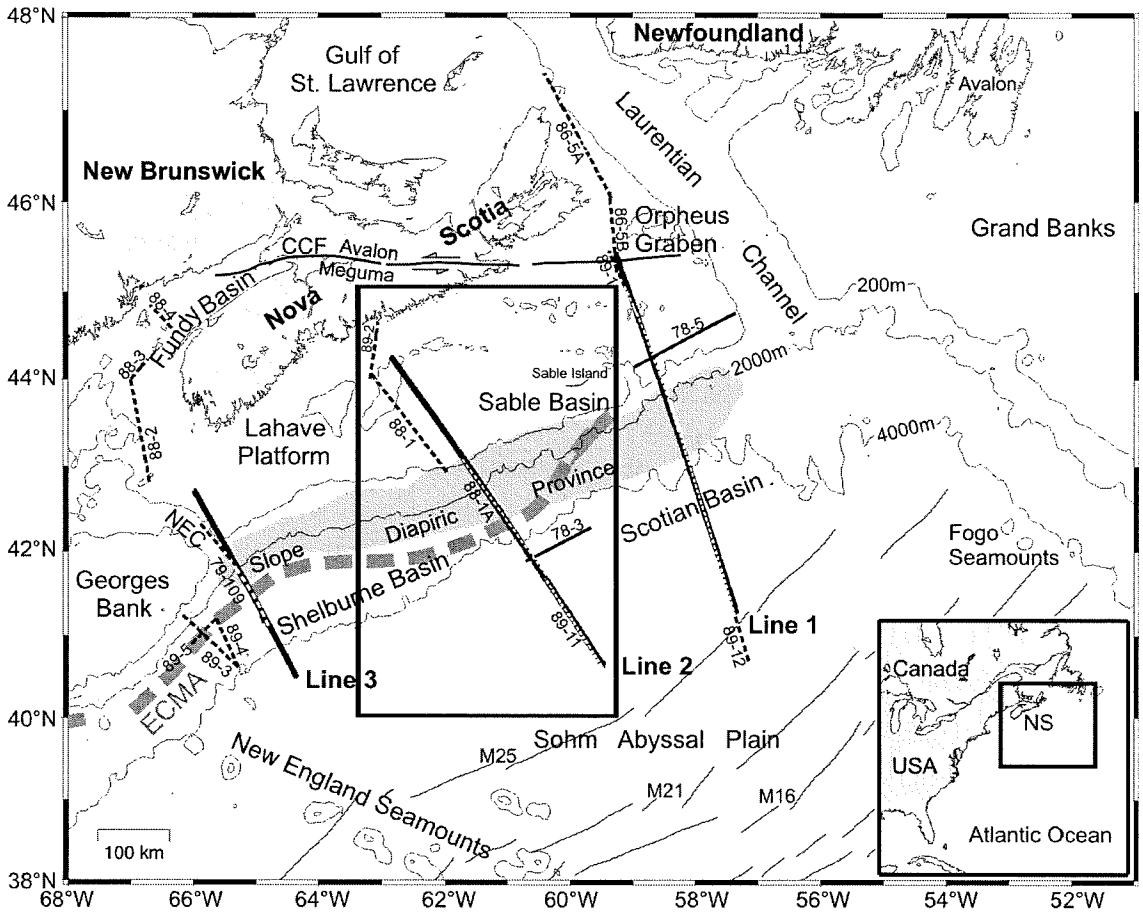

Figure 2.1. Location map of the Nova Scotia margin. The three refraction seismic lines of the SMART experiment are marked by bold solid lines. The rectangle outlines the area shown in Figure 2.2. The inset shows the study region relative to eastern North America. The 200 m bathymetric contour is shown as a thin solid line; the 2000 m and 4000 m contours are indicated by solid lines (National Geophysical Data Center 1988). The centre of the East Coast Magnetic Anomaly (ECMA) is marked by a dashed grey line (after Keen *et al.* 1995b). Shaded area indicates the location of the Jurassic salt of the Slope Diapiric Province (after MacLean 1991). Magnetic lineations are shown as solid lines (Klitgord and Schouten 1986). Earlier seismic refraction lines 78-3, 5 (Keen and Cordsen 1981) are indicated by thin solid lines. Relevant multi-channel seismic reflection lines in the study area are shown as dashed lines: lines 86-5A, 5B (Marillier *et al.* 1989); lines 88-1, 1A (Keen *et al.* 1991b), lines 88-2, 3, 4 (Keen *et al.* 1991a), lines 79-109, 89-11 and 89-12 (unpublished data by the German Federal Agency of Natural Resources and Geosciences, BGR), lines 89-3, 4, 5 (Keen and Potter 1995a); line 89-1 (Keen and Potter 1995b). The Cobequid Chedabucto fault (CCF) is shown as bold solid lines and arrows indicate the sense of displacement. Abbreviations are NS, Nova Scotia; NEC, Northeast Channel.

However, in the central segment of the Nova Scotia margin, the magnetic anomaly is still pronounced (~200 nT), but there is no evidence for a SDR sequence on line 88-1A (Keen *et al.* 1991b) unless it is obscured by salt. The concurrence of magnetic and seismic signatures leads to an ambiguous character for the central margin segment.

In order to understand what controls the transition from volcanic margins to non-volcanic margins, the SMART (Scotian MARgin Transects) refraction seismic experiment (Figure 2.1) was designed to image the along-strike variation in crustal structure at the transition from a volcanic to a non-volcanic style of rifting. Three wide-angle seismic refraction profiles (Lines 1-3) were acquired in 2001. Line 1 shows that the northern margin segment has an OCT zone of a highly serpentinized upper layer overlying a partially serpentinized lower layer, separating the highly thinned continental crust and oceanic crust by over ~70 km of exposed mantle rocks (Funck *et al.* 2004). The results indicate that the northern Nova Scotia margin is non-volcanic. However, it is unknown if this is still valid for the central part of the margin.

This paper presents the results of Line 2 (Figure 2.1). This line crosses the Lahave Platform and extends into the Sohm Abyssal Plain. Close to the coast, Line 2 runs parallel to a multi-channel seismic (MCS) reflection line 88-1 and farther seaward it coincides with MCS line 88-1A (Keen *et al.* 1991b) and an unpublished line 89-11 acquired by the German Federal Agency of Geosciences and Natural Resources (BGR), forming a 500-km-long composite profile from the continental shelf to the deep ocean

basin. The velocity model constrained by the wide-angle refraction data and the coincident MCS reflection profiles provides detailed information about crustal thinning and the ocean-continent transition. In this paper, we will show that the resulting velocity model also indicates a non-volcanic character across the central margin segment and therefore, that most of the Nova Scotia margin is primarily non-volcanic.

2.3 Geological Setting

The Nova Scotia margin off Eastern Canada was formed within the Appalachian Orogen by the separation of Africa from North America during the Mesozoic breakup of Pangaea (Klitgord and Schouten 1986; Wade and Maclean 1990). Onshore, the basement of southern and central Nova Scotia consists of the Meguma terrane, intruded by granitoid rocks (Williams 1979; Keppie 1989). The Cobequid Chedabucto fault (CCF, Figure 2.1) through the central Nova Scotia peninsula separates the Meguma terrane from the Avalon terrane to the north (Barr and Raeside 1989). Rifting of the Nova Scotia margin began in the Middle Triassic to Early Jurassic (230-175 Ma) (Welsink *et al.* 1989), followed by Jurassic seafloor spreading (Klitgord and Schouten 1986). The spreading rate for the initial opening until magnetic anomaly M21 is ~20 mm/year (Klitgord and Schouten 1986). Across the southern and central Nova Scotia margin, the Lahave Platform occupies the outer shelf and continental slope area, with the Shelburne Basin located on the continental slope. In contrast, across the northern margin segment, the Sable Basin with a thick wedge of both syn- and post-rift sediments is situated beneath the outer shelf. The oldest syn-rift deposits in the Sable Basin are nonmarine Triassic redbeds, which are generally found between fault blocks (Wade and MacLean 1990). These are overlain by

shallow marine sediments of Late Triassic-Early Jurassic age, including the extensive salt diapirs (Argo Formation) in the Slope Diapiric Province (Figure 2.1; Welsink *et al.* 1989). The continent-ocean boundary is generally located seaward of the salt front (Keen *et al.* 1991b; Keen and Potter 1995a; Keen and Potter 1995b), except for the northern Nova Scotia margin where the salt front moved seaward (Sahabi *et al.* 2004; Shimeld 2004) during the upper Jurassic in response to Avalon uplift (Wade, 1981).

2.4 Seismic Experiment

2.4.1 Data Acquisition and Processing

The wide-angle reflection/refraction seismic experiment was carried out onboard CCGS Hudson in 2001. Three lines were acquired across the Nova Scotia margin (Figure 2.1). The northern profile (Line 1) transects the Scotian Basin off Cape Breton Island. The middle profile (Line 2) extends from the Lahave Platform into the Sohm Abysmal Plain. The southern profile (Line 3) crosses the southwestern part of the margin near Georges Bank.

The seismic source was a tuned airgun array with a total volume of 104 liters, consisting of 12 individual guns whose volumes range from 2.6 to 16.4 liters. The airgun array was fired once a minute at an average ship's speed of 4.3 knots, resulting in an average shot spacing of 134 m. Twenty-one ocean bottom seismometers (OBS) were deployed along Line 2 (Figure 2.2). All the OBS were equipped with one hydrophone and three 4.5-Hz geophones. Instrument spacing varies from 32-40 km on the shelf (OBS 1-5) to 18-26 km farther seaward (OBS 6-21).

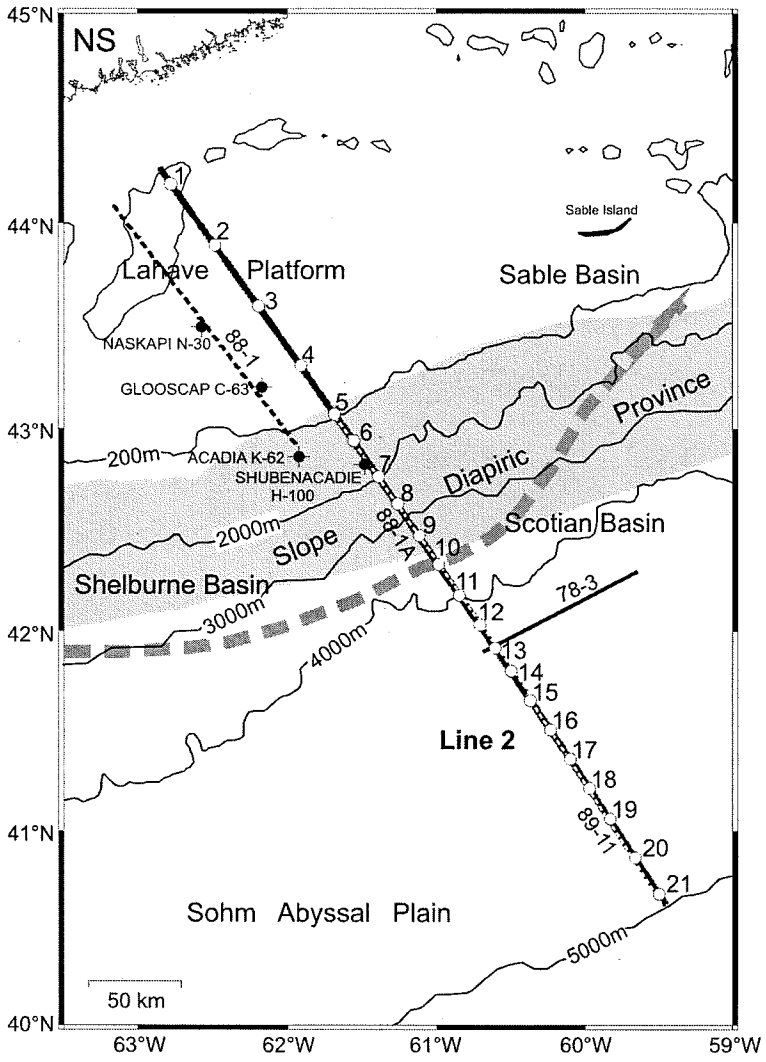

Figure 2.2. Location map for Line 2 (bold solid line). Positions of ocean bottom seismometers are denoted as open circles and labeled with the instrument number. Filled circles overprinting on crosses mark the location of deep exploration wells in the vicinity of Line 2 (BASIN database, Geological Survey of Canada, Dartmouth, Nova Scotia, Canada). MCS lines 88-1, 1A (Keen *et al.* 1991b) and BGR line 89-11 (unpublished) are shown as dashed lines. Seismic refraction line 78-3 (Keen and Cordsen 1981) is shown as thin solid line. Bathymetric contours for 200 m, and 2000-5000 m with an interval of 1000 m are shown as solid lines. Other features as described in Figure 2.1. NS, Nova Scotia.

OBS and shot locations were determined by the Global Positioning System (GPS). Water depths along the profile were recorded by the ship's echosounder. A velocity-depth profile was derived from a conductivity, temperature and depth (CTD) measurement at 40° 30.86' N, 59° 41.42' W, near the southeastern end of Line 2. The CTD measurement was only conducted down to a depth of 2 km; downward extrapolation of the depth-velocity function was applied for greater depths (see Figure A.1 in Appendix A).

Raw OBS data were downloaded and converted to SEGY format. Corrections for gun offset, gun delay, and OBS clock drift were applied. The OBS positions at the seafloor are recalculated to fit the observed direct wave arrivals (see Appendix B). All the data were debiased and filtered by a 5-10 Hz band-pass filter.

2.4.2 Methodology

A 2D velocity model was developed using the program RAYINVR (Zelt and Smith 1992; Zelt and Forsyth 1994). Initially, a model was developed by forward modeling of observed travel times (see Appendix A). Later, the forward model was refined by using the inversion algorithm of the program. The velocity model was primarily constrained by the OBS data. The bathymetry obtained by the ship's echosounder was used to define the seafloor geometry in the velocity model. The coincident MCS lines 88-1, 88-1A (Keen *et al.* 1991b) and 89-11 have been used to constrain the sedimentary layer boundaries and the detailed basement surface where the OBS data were not sufficient to determine the small-scale geometry. Sonic well-log data over the shelf and shallow slope were also used to constrain the sediment and uppermost basement

velocities. A total of four wells (BASIN database, Geological Survey of Canada, Dartmouth, Nova Scotia, Canada) were used for comparison and calibration, with the maximum depth of 5.8 km at Acadia K-62 (Figure 2.2).

The baseline for the 2D velocity model was defined by the shooting line. The northwestern-most shot marks the start of the model and the southeastern-most shot defines the seaward end of the model. All the OBS locations and MCS sections (lines 88-1, 88-1A, and 89-11) have been projected onto the baseline.

2.4.3 Data Analysis

Record sections for OBS 1, 6, 11, 14 and 18 are shown in Figures 2.3-2.7, representative of the wide-angle data acquired along Line 2. Additional record sections are also included in Appendix 2.A, including OBS 2, 5, 7, 8, 10, 15, 17, and 21. The horizontal distances in all these figures are relative to the starting point of the model.

The phase nomenclature is based on the interpretation of individual layers in the velocity model. Refractions from the sedimentary layers S_1 through S_7 are named P_{s1} through P_{s7}. The reflections from the base of each of the sedimentary layers are denoted as $P_{s1}P$ through $P_{s7}P$, except for the reflection from the basement, which is labeled P_bP. P_{c1}, P_{c2} and P_{c3} are refractions from the upper, middle and lower continental crust, respectively; $P_{c1}P$ and $P_{c2}P$ are the midcrustal reflections. Refraction and reflection from the oceanic layer 2 are labeled P_{L2} and $P_{L2}P$, respectively. The layer beneath layer 2 has anomalously high velocities. This layer is referred to as high-velocity lower crust (HVLC); its refraction and reflection are specifically named P_{HVLC} and $P_{HVLC}P$, respectively. A layer underneath

both continental and oceanic crust is later interpreted as partially serpentinized mantle (PSM); its refraction is labeled P_{n1}. Refraction from the "normal" (*i.e.* unserpentinized) mantle is named P_n. The reflections from the top boundaries of the serpentinized and unserpentinized mantle are marked as $P_{m1}P$ and P_mP, respectively.

On the landwardmost station OBS 1 (Figure 2.3), P_{c1} is imaged, but P_{c2} and P_{c3} are weak and difficult to identify. Moho reflection (P_mP) and mantle refraction (P_n) are also observed, although the latter is less clear.

OBS 6 (Figure 2.4) is located ~20 km seaward of the shelf edge. On this record section, P_{c1}, P_{c2} and the corresponding reflections $P_{c1}P$ and $P_{c2}P$ are observed. Moho reflection (P_mP) is imaged at far offsets. Mantle refraction (P_n) is less clear but identifiable at far offsets around -120 km.

OBS 11 is located at the seaward edge of the salt diapir structure (Figure 2.5). Refractions from the salt units (P_{s6}) are observed. The P_{c1} phase is disturbed by the irregular geometry of the salt diapirs (S_6). The P_{c2} phase is not imaged on this section. The P_{c3} phase is imaged but on the SSE side it suddenly terminates at offset ~50 km. Mantle refractions (P_n) are observed at far offsets.

OBS 14 (Figure 2.6) is sited at the seaward edge of a series of faulted basement blocks (FB) imaged by coincident MCS data (Keen *et al.* 1991b). On the NNW side, P_{c1} appears as first arrivals between offsets -18 km and -25 km with phase velocities of ~5.0 km/s. In

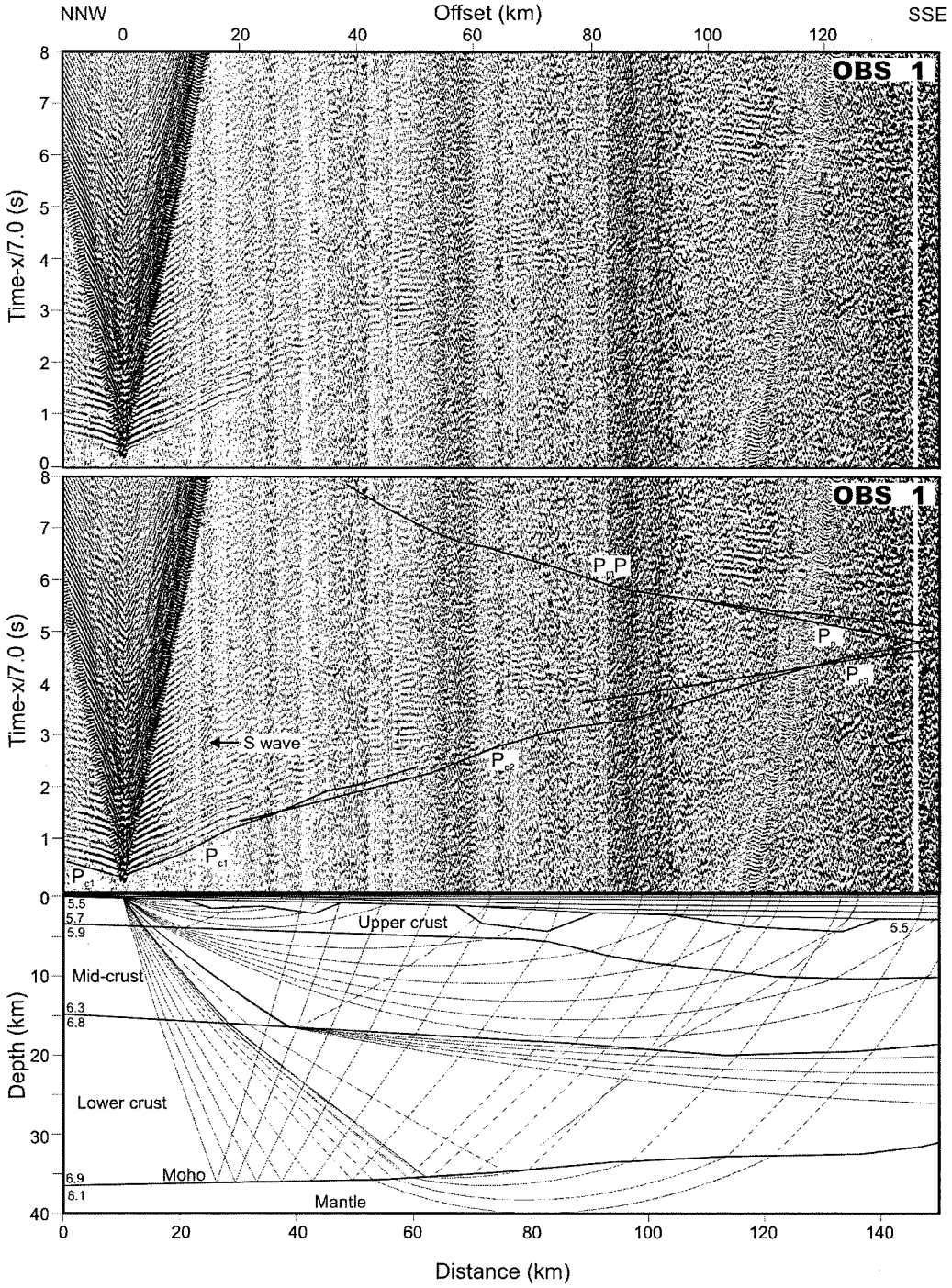

Figure 2.3. Record section (top), record section with calculated travel times (middle) and ray path diagram (bottom) for OBS 1 (hydrophone component). The horizontal scale of the record sections and the ray path diagram is distance along the velocity model (Figure 2.8). Shot-receiver distance (offset) is also shown above the record section. The vertical scale in the record section is travel time in seconds, displayed with a reduction velocity of 7.0 km/s. Numbers in the ray path diagram are *P*-wave velocity in km/s. Labels are defined in the text. The noise band in the data section at offset ~120 km is noise from previous shots.

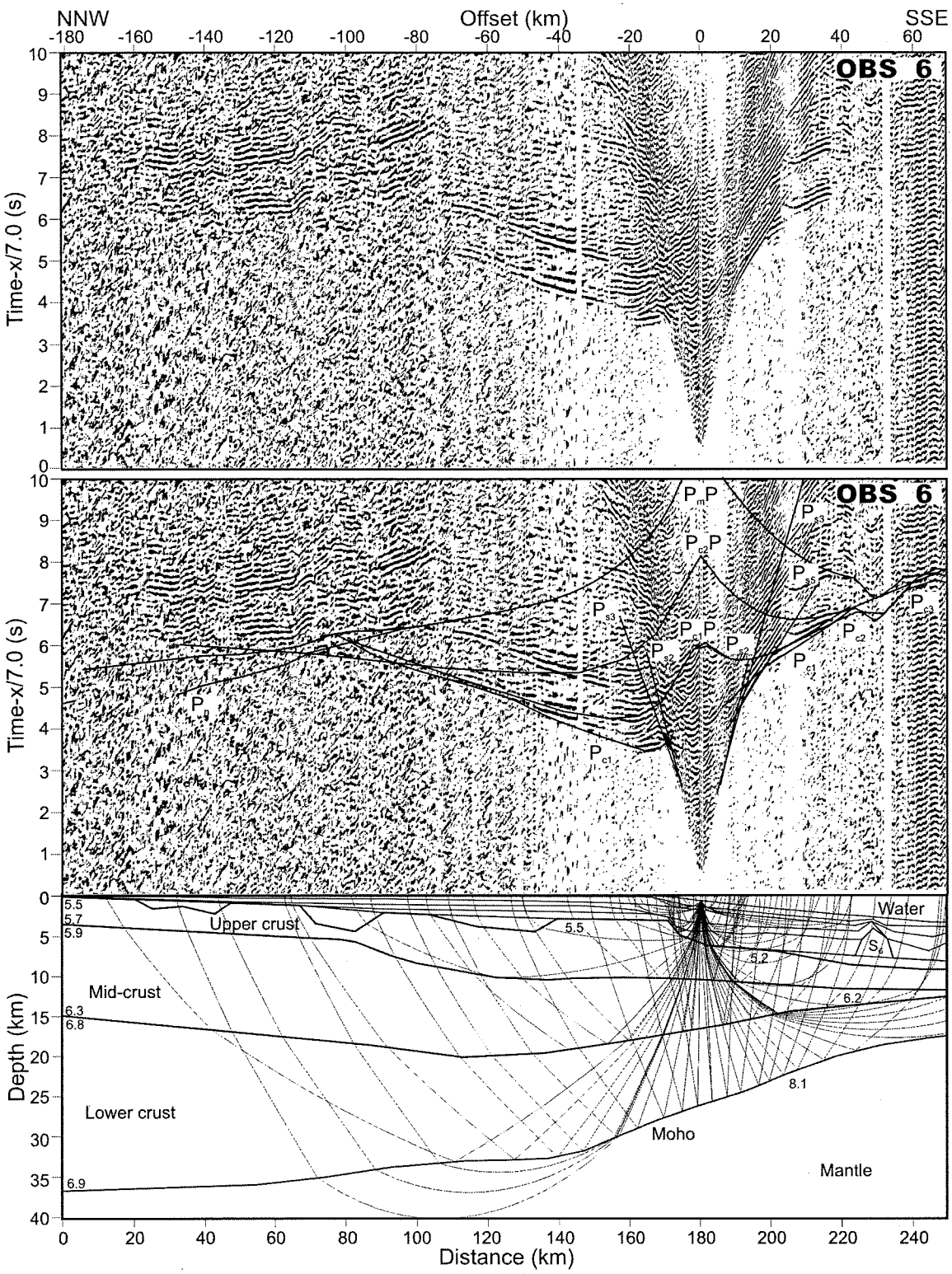

Figure 2.4. Record section (top), record section with calculated travel times (middle) and ray path diagram (bottom) for OBS 6 (hydrophone component). Features refer to Figure 2.3.

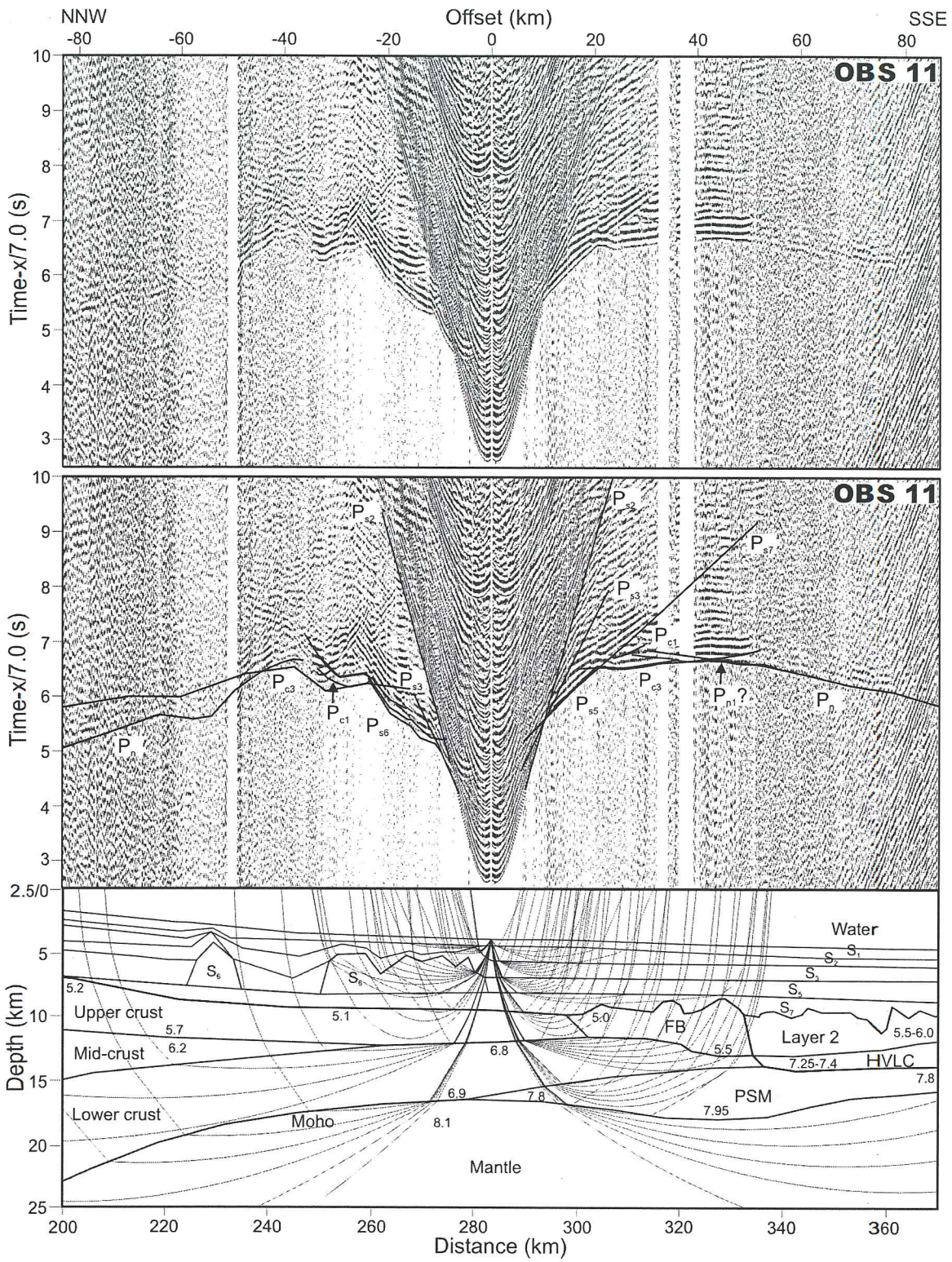

Figure 2.5. Record section (top), record section with calculated travel times (middle) and ray path diagram (bottom) for OBS 11 (vertical geophone component). Features refer to Figure 2.3.

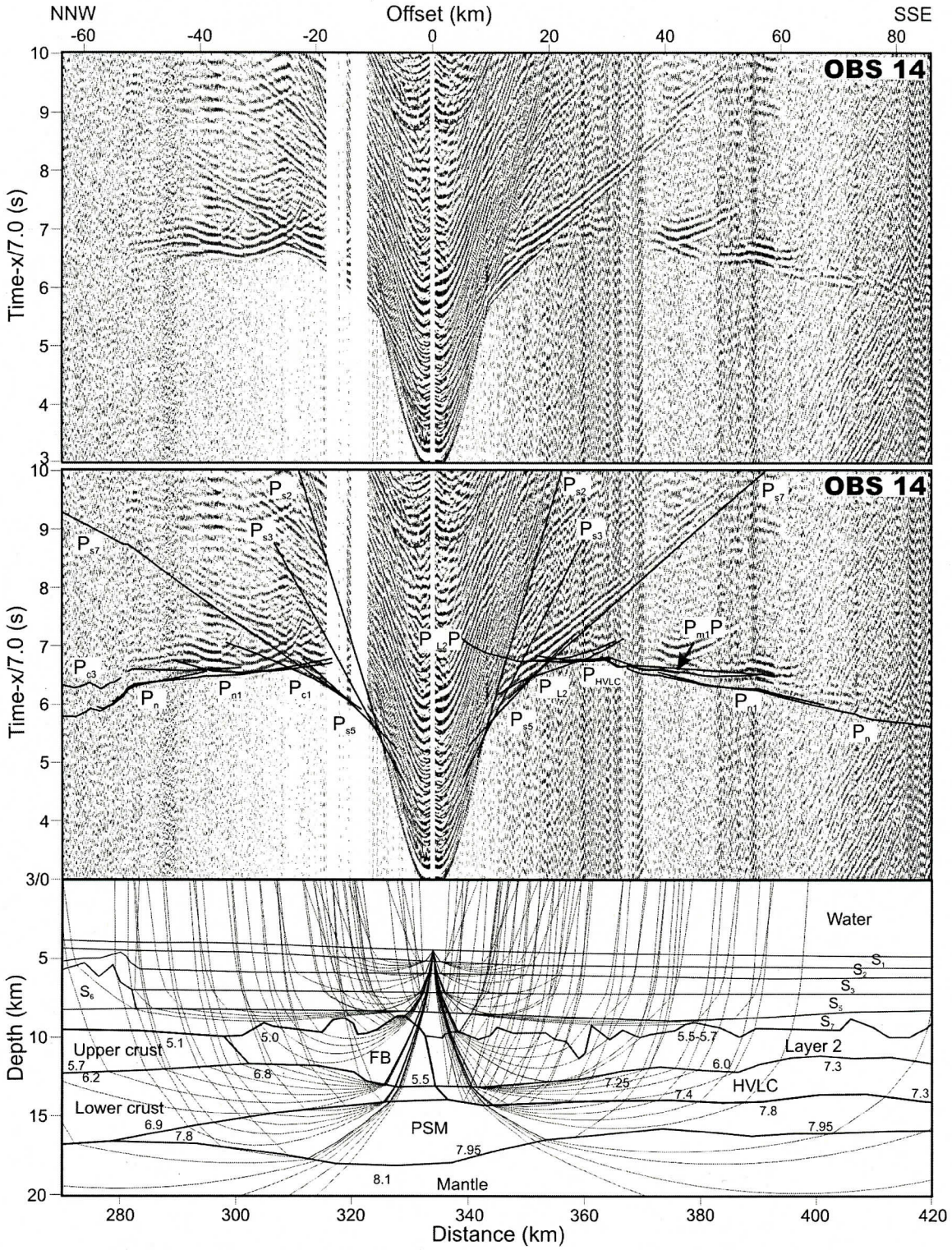

Figure 2.6. Record section (top), record section with calculated travel times (middle) and ray path diagram (bottom) for OBS 14 (vertical geophone component). Features refer to Figure 2.3.

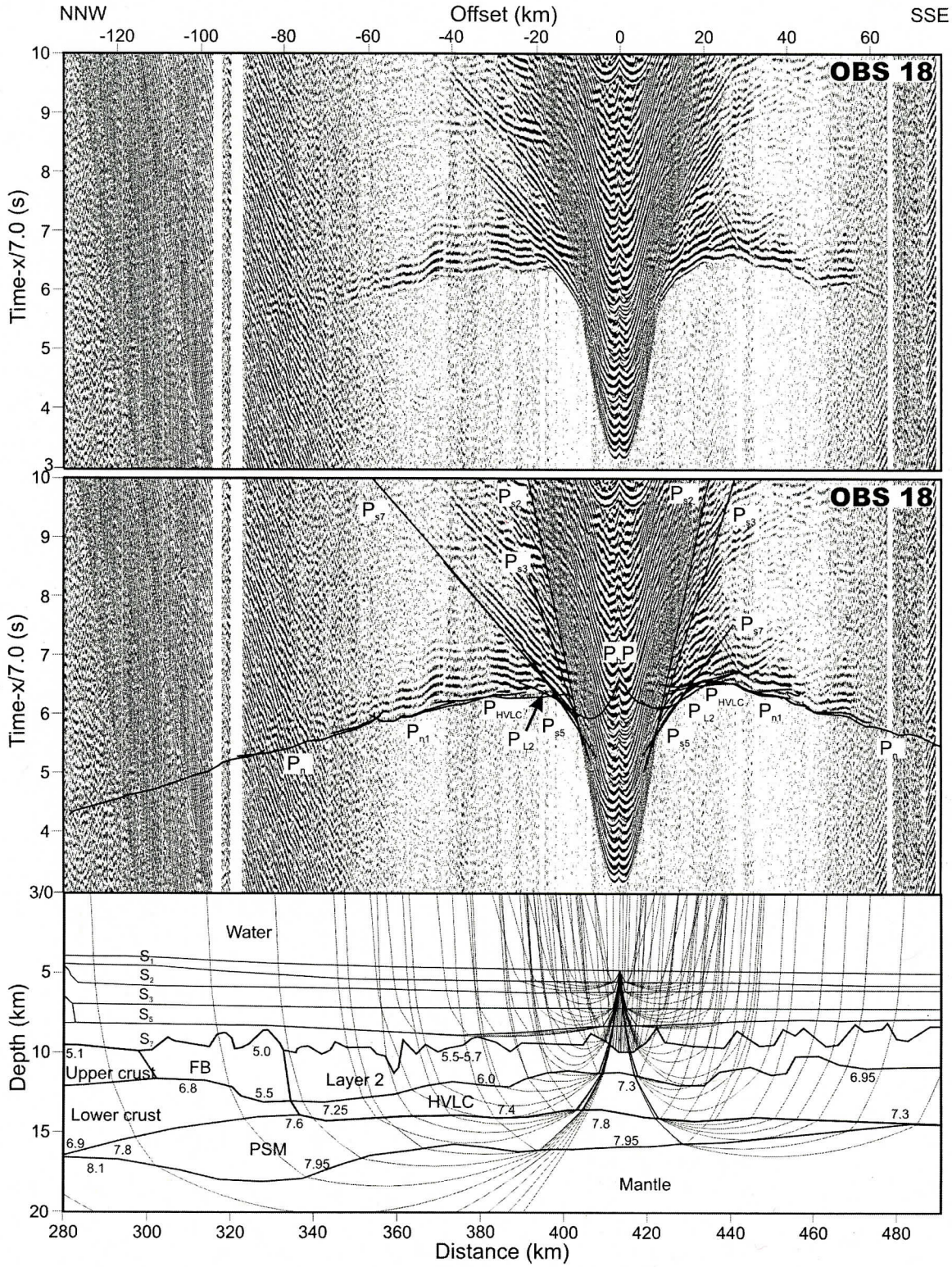

Figure 2.7. Record section (top), record section with calculated travel times (middle) and ray path diagram (bottom) for OBS 18 (hydrophone component). Features refer to Figure 2.3.

contrast, P_{L2} is imaged on the SSE side with phase velocities of 5.5-5.7 km/s (also see Figure 2.A6). In addition, P_{HVLC} appears on the SSE side with *P*-wave velocities (v_p) of 7.25 km/s but it is not observed on the NNW side. Furthermore, the P_{n1} phase is first observed as high amplitude signals, indicating a relatively high velocity gradient layer. The high-amplitude signals disappear at NNW side at offset -50 km, and they are not observed on stations further landward, indicating that this layer terminates somewhere between distances 280-300 km. The reflection from its top boundary, which is termed $P_{m1}P$, is imaged on the SSE side. Phase P_n is observed at far offsets.

On OBS 18 (Figure 2.7), phases P_{L2}, P_{HVLC}, P_{n1} and P_n are imaged on both sides as first or recognizable second arrivals. For P_{HVLC}, there is a change in velocity from 7.25-7.4 km/s in the NNW side to 6.95-7.3 km/s in the SSE side. The P_{n1} phase is observed on the SSE side at offset 60 km, but it no longer appears on the instruments farther seaward. This indicates that the layer producing the high-amplitude signals terminates seaward of OBS 18 at a distance of ~480 km.

2.5 Results

2.5.1 Velocity Model

The *P*-wave velocity model for Line 2 is shown in Figure 2.8. Sediments are divided into seven layers: S_1 to S_7. Velocities within the sediments vary from 1.7 to 4.6 km/s. Layers S_2, S_3, S_5, and S_7 are relatively flat layers over the deep sea basin with a total thickness of ~6 km, but they thin and pinch out on the continental slope and shelf. The average velocity of 4.5 km/s for the salt diapirs (S_6) is constrained by the OBS data (Figure 2.5) and is consistent with well-log results in Scotian Basin wells that penetrate the Argo Formation

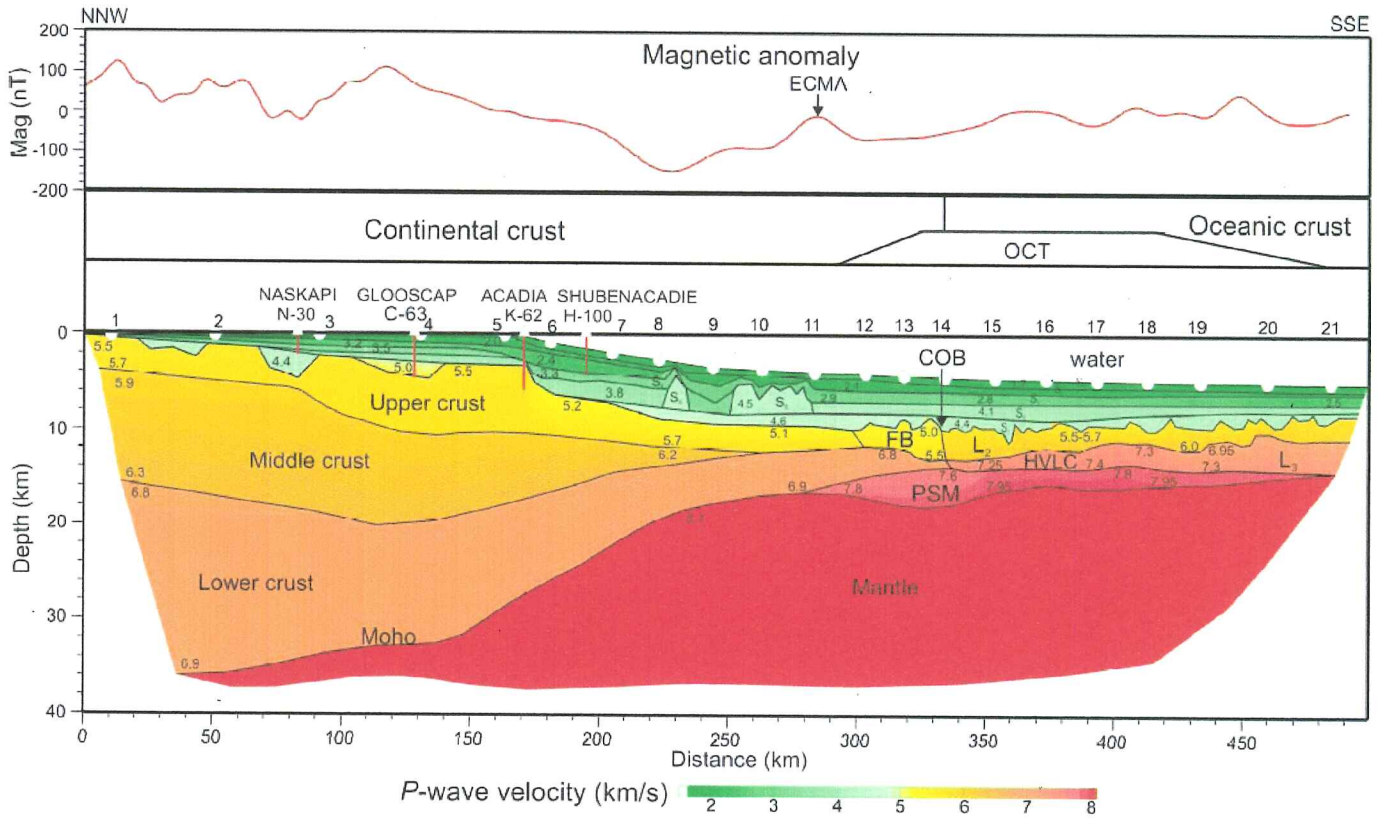

Figure 2.8. P-wave velocity model with color scale (bottom) and coincident magnetic anomaly (top). A simplified interpretation of the crustal units is also illustrated (middle). Numbers within the velocity model are *P*-wave velocity in km/s. White circles mark the OBS locations with station numbers indicated above the velocity model. S_1 through S_7 are sedimentary layers 1 through 7. White triangles mark the location of deep exploration wells in the vicinity of Line 2 and the vertical red lines show their depths. The magnetic profile (top) is taken from Oakey and Dehler (2004). Abbreviations COB: continent-ocean boundary; ECMA: East Coast Magnetic Anomaly; FB: faulted blocks; OCT: ocean-continent-transition; L_2: layer 2; L_3: layer 3; HVLC: high-velocity lower crustal layer; PSM: partially serpentinized mantle.

(Shimeld 2004). The boundary of the salt units is taken from coincident MCS line 88-1A (Keen *et al.* 1991b).

The continental crust has a maximum thickness of 36 km and is divided into upper, middle and lower crust with velocities of 5.5-5.7 km/s, 5.9-6.3 km/s, and 6.8-6.9 km/s, respectively. The continental crust thins gradually from the landward end of the line over a distance of 140 km. Most of the thinning occurs in the lower crust, while the total thickness of upper and middle crust is nearly constant. The upper crust may have included 1-3 km of carbonate rocks at the shelf break, based on results from Acadia K-62. Farther seaward, the continental crust thins rapidly from ~30 km thick at distance of ~140 km to ~8 km thick at distance of ~240 km. Seaward of ~220 km, the upper crust has a fairly constant thickness of ~4 km and its v_p is reduced to 5.1 km/s. The FB between distance 290 and 330 km have v_p of 5.0-5.5 km/s. The middle crust disappears beneath the salt diapir. The lower crust terminates beneath the FB.

Seaward of the FB, oceanic layer 2 (L_2) is first encountered with v_p of 5.6-6.0 km/s. The variable basement topography is defined by the coincident MCS profiles 88-1A (Keen *et al.* 1991b) and 89-11. Below layer 2, a thin layer (~1 km thick) is initially observed with v_p of 7.25-7.4 km/s. This layer is referred to as high-velocity lower crust (HVLC) because the velocity is anomalously high, compared to that of a normal oceanic layer 3 (White *et al.* 1992). Its possible interpretations are discussed in section 2.6.2.3. This layer thickens to ~3.5 km at the seaward end of the model where its v_p decreases to 6.95-7.3 km/s, which is more typical of layer 3 (L_3, Figure 2.8).

A layer with v_p of 7.6-7.95 km/s beneath highly thinned continental crust and oceanic crust extends from 280 to 480 km (Figure 2.8). The maximum thickness of this layer is ~4 km at the continent-ocean boundary (COB) with a velocity gradient of ~0.1 s^{-1}. Farther seaward, this layer thins as the overlying basement thickens seaward. The nature of this layer is discussed in section 2.6.2.4. Normal upper mantle appears at depths of 16.5-18 km with a velocity of 8.1 km/s.

2.5.2 Error Analysis

The error analysis for individual phases is summarized in Table 2.1. The model is constrained with a total RMS misfit of 82 ms between the calculated and picked traveltime arrivals. The normalized χ^2 of 1.015 is close to the optimum value 1.0 where the travel times are fit within the pick uncertainty. The pick uncertainties were assigned according to the signal-to-noise ratio and varied typically between 30 and 200 ms, with a few uncertainties up to 400 ms. The "resolution" parameter of the model is shown Figure 2.9. A value of 1 indicates the model is perfectly parameterized, while a value of 0 suggests an uncontrolled model. Matrix diagonal values of > 0.5 generally indicate reasonably well constrained model parameters (Lutter and Nowack 1990). Although the method fits the traveltime, the slope of the phases is also well determined for phases that can be identified over a significant lateral extent. The sedimentary layers S_2-S_5 are well parameterized for both velocity and boundary nodes. The salt and uppermost sediment layer S_1 are poorly parameterized due to lack of ray coverage. Velocities for the upper continental crust, the serpentinized mantle and most of the normal mantle are

Table 2.1. Number of observations *(n)*, RMS misfit between calculated and picked travel times (t_{rms}), and normalized χ^2 for individual phases.

Phase	n	t_{rms},(ms)	χ^2
P_{s2}	663	44	1.291
P_{s3}	609	53	1.139
P_{s4}	206	64	0.476
P_{s5}	417	45	1.286
P_{s6}	37	174	2.212
P_{s7}	839	69	1.127
P_{c1}	744	72	0.839
P_{c2}	447	89	0.913
$P_{c2}P$	253	131	1.261
P_{c3}	379	72	0.940
P_{L2}	266	69	1.459
$P_{L2}P$	13	52	0.294
P_{L3}	343	53	0.743
$P_{m1}P$	36	146	2.207
P_{n1}	503	61	1.049
P_mP	830	134	0.763
P_n	1093	87	0.790
All phases	7678	82	1.015

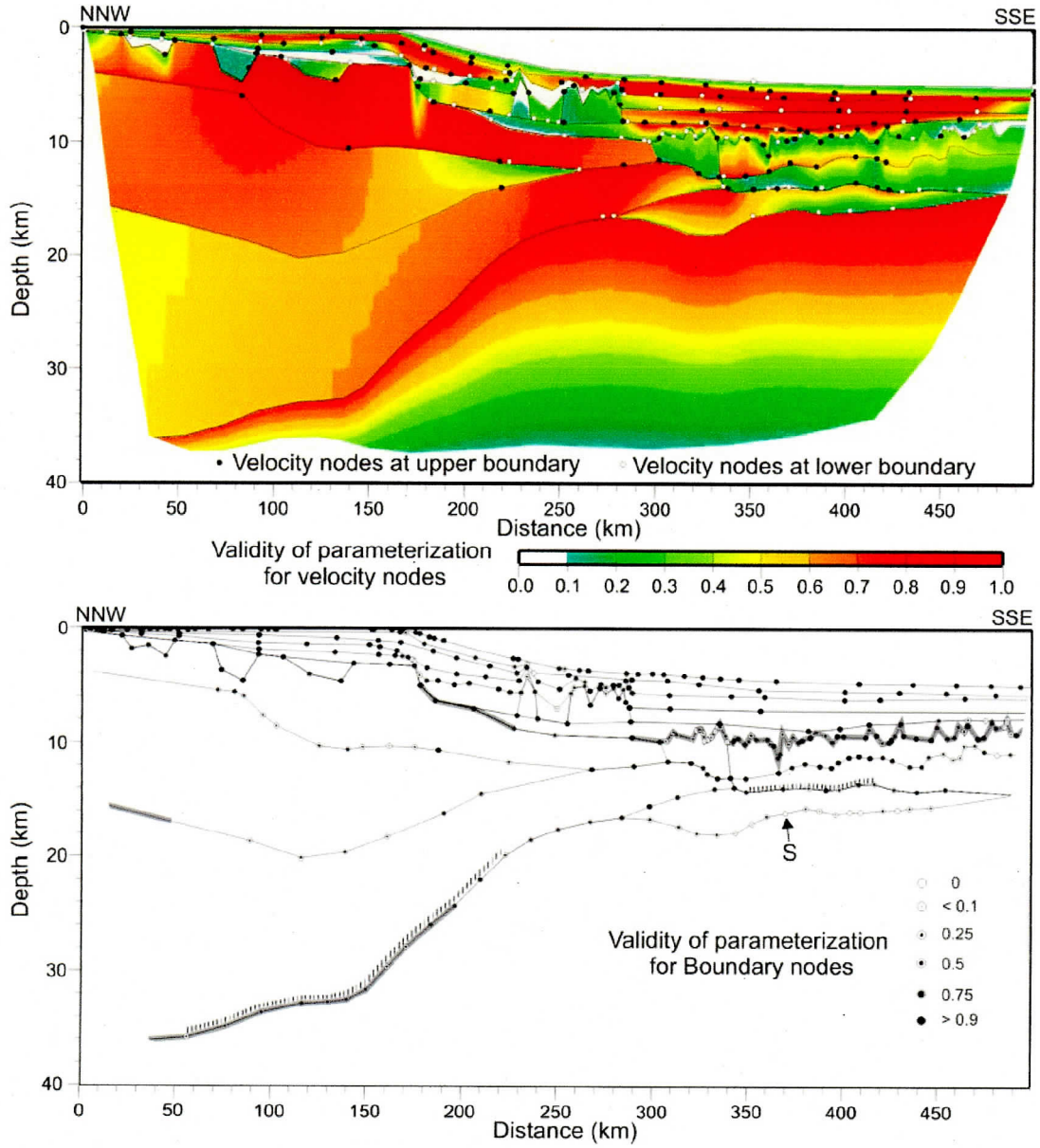

Figure 2.9. Resolution parameter of the *P*-wave velocities (upper) and boundaries (lower) for the model shown in Figure 2.8. The validity of velocity nodes is represented by colors (upper). The velocity nodes for each layer are denoted as solid and open circles for upper and lower boundaries, respectively. To keep the velocity model as simple as possible, velocity nodes are placed only where the data indicate a velocity variation. The validity of the boundary nodes is represented as the percentage of fill in circles (bottom). Blanked area marks zones unconstrained by OBS data. Boundaries constrained by mantle reflections (P_mP or $P_{m1}P$) are indicated by hatched bars. Boundaries overprinted by thick shaded lines are also constrained by reflections in the coincident MCS sections. S marks the boundary from the serpentinized mantle to the unaltered mantle discussed in text.

well constrained. Some areas are less well constrained, such as the middle continental crust beneath the shelf edge and the landward part of the lower continental crust, where only limited refraction phases appear as clear arrivals. The velocities for the oceanic layer and the faulted blocks are also poorly parameterized due to the reduced ray coverage over this area caused by rough basement topography. The boundaries for upper continental crust and layer 2 and the HVLC layer are well parameterized while the middle and lower continental crust and Moho are less well constrained. These results were only based on the refraction data. However, the velocity model boundaries are better defined because the major reflections (*e.g.* basement and Moho) within the coincident MCS sections were used to constrain the model (lower panel, Figure 2.9), but were not included in the error analysis.

2.5.3 Gravity Modeling

To verify the consistency of the velocity model with the observed gravity data, 2D gravity modeling (algorithm of Talwani *et al.* 1959) was performed along Line 2. The observed gravity data are the satellite-derived free-air gravity anomaly (Sandwell and Smith 1997). The initial density model (Figure 2.10b) was derived from conversion of *P*-wave velocity to density by using the empirical formula of Ludwig *et al.* (1970). To fit the regional gravity background, a density of 3.33 Mg/m^3 was used for the sub-continental mantle up to a distance of 249 km, whereas a mantle density of 3.31 Mg/m^3 was used farther seaward. This is consistent with the gravity model for Line 1 (Funck *et al.* 2004). The density of the salt units was reduced from 2.4 Mg/m^3 to 2.15 Mg/m^3, which is consistent with measurements from Scotian Basin wells (Shimeld 2004). With

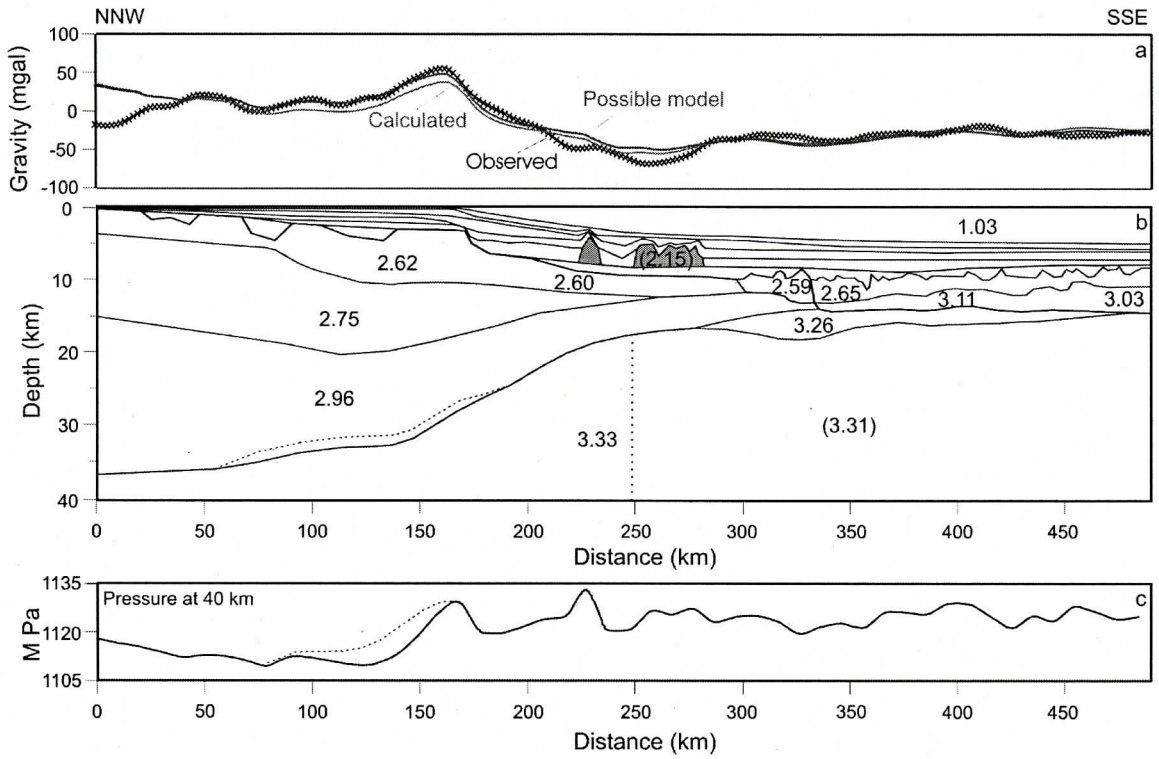

Figure 2.10. 2D gravity modeling for Line 2. Top section (a) is the comparison of the observed and computed gravity anomalies shown by cross-hatched and green lines, respectively. The red line is the computed gravity anomaly from an alternative model shown by dashed line in (b). Middle section (b) is the density model directly converted from the P-wave velocity model (Figure 2.8) by using the velocity-density relationship of Ludwig *et al.* (1970). To fit the observed gravity anomaly in (a), the density for the upper mantle beneath the oceanic crust and highly thinned continental crust is reduced from 3.33 Mg/m^3 to 3.31 Mg/m^3 across the dotted line, and salt density is reduced from 2.4 Mg/m^3 to 2.15 Mg/m^3 (indicated by the shaded region). Modifications are shown in parenthesis. Densities for sedimentary layers vary from 1.82 Mg/m^3 to 2.5 Mg/m^3. Densities in the model are given in Mg/m^3. To improve the fit at the shelf edge, an alternative model with the mantle 1.5 km shallower in this region (indicated by the dashed line) reduces the misfit of gravity anomaly (red line in panel a), but it decreases the fit of OBS data in this region (see Figures 2.4, 2.A3 and 2.A4). Bottom section (c) is the lithostatic pressure (solid line) at the base of the model at depth of 40 km, with a dashed line indicating the lithostatic pressure of the alternative model.

these adjustments, the calculated gravity fits the observed data with an overall misfit of ~9 mGal (Figure 2.10a). Some larger misfit (~20 mGal) occurs over the shelf edge and slope. Due to the fact that a larger region of salt is located just to the south and north of Line 2 than imaged along this profile (MacLean 1991), the local misfit between distances 250-280 km is probably related to additional local salt mass deficiency. The lithostatic pressure over the slope region at the depth of 40 km is slightly elevated to 1130 MPa, compared to an average of 1125 MPa for this profile (Figure 2.10c). To improve the fit over the shelf edge, an alternative model with the mantle 1.5 km shallower in this region (indicated by the dashed line in Figure 2.10b) reduces the misfit of gravity anomaly but it causes misfits of the OBS data (see Figures 2.4, 2.A3 and 2.A4). Other models that reduce the depths of upper or middle crust also improve the gravity fit but they also decrease the fit of OBS data in a similar way. Therefore, these models are not preferred. The misfit at the landward end of the model was not investigated further because there are no seismic constraints landward of the line. Several granitic intrusions are known onshore (Benn *et al.* 1997) and in the near offshore (Loncarevic *et al.* 1994). Hence, some of the mass deficit at the landward end of the line might be related to lower density granites within the mid-crustal layer.

2.6 Discussions

2.6.1 The Rifted Continental Crust

The composite profile of MCS 88-1 and 88-1A converted from travel time to depth using the velocity model shows that the velocity structure is consistent with the reflectivity (Figure 2.11). Landward of the shelf break, the upper and middle crust is less reflective except for a few northwest dipping reflections (*e.g.* W_1 and W_2) which flatten and

terminate at the top of the lower crust. These reflections could represent pre-rift or post-rift normal faults within the Meguma terrane (Keen *et al.* 1991b). The velocity model indicates only minor crustal thinning coincident with the normal faults. This suggests that the northwest dipping fabric is more likely to be associated with the prerift structural grain although they may have been reactivated during rifting. While only a few reflections are observed in the middle crust, the lower crust is characterized by increased reflectivity, with the Moho following the base of a strong reflection band (M, Figure 2.11). The initial crustal thinning seems to be mainly confined to the lower crust. The gently rising Moho reflection suggests that the crustal thinning begins at the northwestern end of the model, about 100 km farther landward than previously predicted by subsidence analysis (Keen and Beaumont 1990). This will be discussed further in section 2.6.3.2.

Seaward of the shelf break, the continental crust underwent an abrupt thinning beneath the hinge zone and southeast dipping reflections predominate (*e.g.* E_1, E_2). Unlike the preexisting fabric beneath the shelf, the abrupt thinning of the continental crust is accommodated along the seaward dipping faults, penetrating through the crustal layers and terminating at the Moho boundary. The Moho reflection is weak but still recognizable in this area, indicating that the continental crust extends at least to the landward edge of the salt. Beyond this point, the Moho reflections become ambiguous and the crustal thinning in the reflection section can not be traced further seaward. The reflectivity below the Moho boundary is obscure in this region, but the velocity model shows that there is no addition of a high-velocity (7.0-7.8 km/s) layer to the base of the abruptly thinned crust.

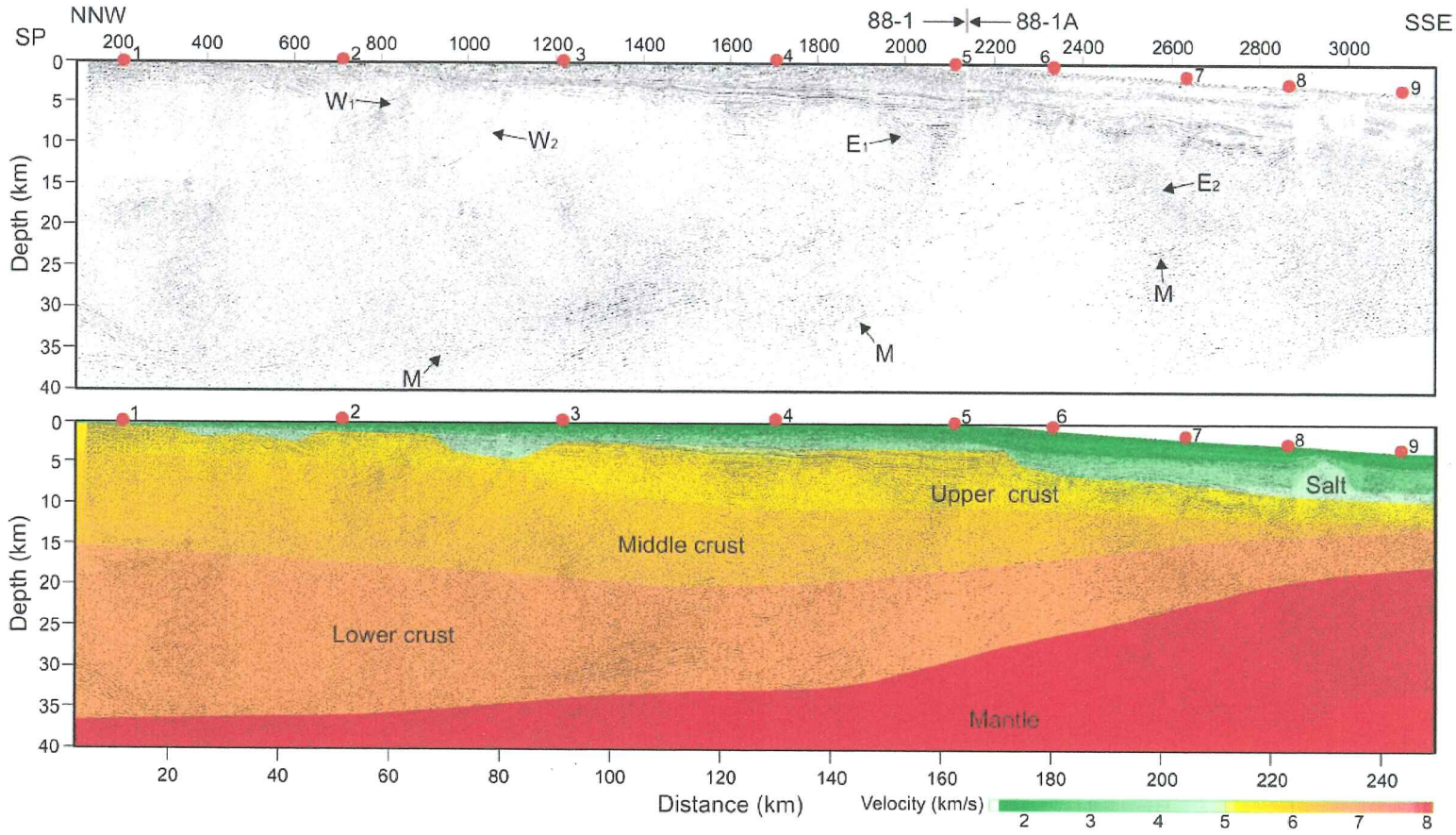

Figure 2.11. (Top) A composite MCS depth section of line 88-1 and part of line 88-1A (Keen *et al.* 1991b) converted from the two-way travel time using the velocity model shown in Figure 2.8. (Bottom) the same depth section shown together with the velocity model (color scale). The horizontal scale is distance along the velocity model with the shot point (SP) number shown on top of the section. OBS positions are marked by red circles on the seafloor and labeled with numbers. Features marked by letters are W_1 and W_2, northwest dipping reflections; E_1 and E_2, southeast dipping reflections; M, Moho reflection. Vertical exaggeration: 1.5.

2.6.2 The Ocean-Continent Transition (OCT) Zone

The OCT zone in the velocity model extends from ~280 km to ~480 km. Within the OCT, two anomalous velocity layers HVLC and PSM are overlain by continental crust in the NNW and oceanic crust in the SSE (Figure 2.8). The various layers are discussed below.

2.6.2.1 Thinned Continental Crust

The two upper layers in the OCT zone up to a distance of ~330 km are highly thinned continental crust (Figure 2.8). This interpretation is based on the *P*-wave velocities derived from the OBS data and the characteristic basement reflectivity of the FB compared with basement structures elsewhere.

The OBS data indicate that the FB have a velocity of 5.0 km/s, which is almost the same as observed for the highly thinned continental crust beneath the slope (5.1 km/s). In contrast, it is ~0.6 km/s lower than that of the upper basement layer seaward. The velocity for the FB is less well constrained because only a limited number of refraction first-arrivals are observed due to the rough basement topography across this region. However, this velocity is consistent with earlier observations of 4.62-5.27 km/s along refraction line 78-3 (Keen and Cordsen 1981) passing through the same region (Figure 2.2). The velocities for the FB are more consistent with an interpretation of continental crust.

This interpretation is further supported by reflectivity of the FB (top, Figure 2.12). Fanning reflectors against normal faults may indicate that layers are built up over a long period, while the pre-existing strata are being faulted and rotated, as for deposition in a subsiding half-graben. The half-grabens are bounded by rotated fault blocks and show similar geometry and reflectivity to those formed within rift-related depositional basins (*e.g.* Barents Sea; Prosser 1993). These features support the interpretation based on the OBS data and suggest that the onset of seafloor spreading is located seaward of the faulted basement structure (discussed in section 2.6.2.2).

This revises previous interpretations based on MCS profiles 88-1A (Salisbury and Keen 1993; Keen and Potter 1995a; b). In their interpretations, the FB, based on the basement reflectivity and faulting, are interpreted as volcanic episodes at a slow-spreading ridge modified by tectonic rotation, and the COB lies at the seaward edge of the salt (Salisbury and Keen 1993). However, it is unlikely for slow spreading seafloor to retain long-lasting off-axis volcanism for sufficiently long periods. The basement features of the FB are also different from those observed elsewhere on oceanic crust. In Figure 2.12, the FB blocks along 88-1A (Keen *et al.* 1991b) are compared with those observed on the Newfoundland rifted margin (Hopper *et al.* 2004) and mid-Labrador Sea (Srivastava and Keen 1995). The basement blocks observed on Line 2 (top, Figure 2.12) are segmented and rotated by uniformly seaward dipping faults (F_2-F_4, Figure 2.12), creating half-grabens up to ~10 km across. Within the FB, landward dipping reflectors (L, Figure 2.12) fan against the listric faults with the steepest dip angle greater than 40°. Across the Newfoundland rifted margin off Flemish Cap, Hopper *et al.* (2004) identified a region where volcanism

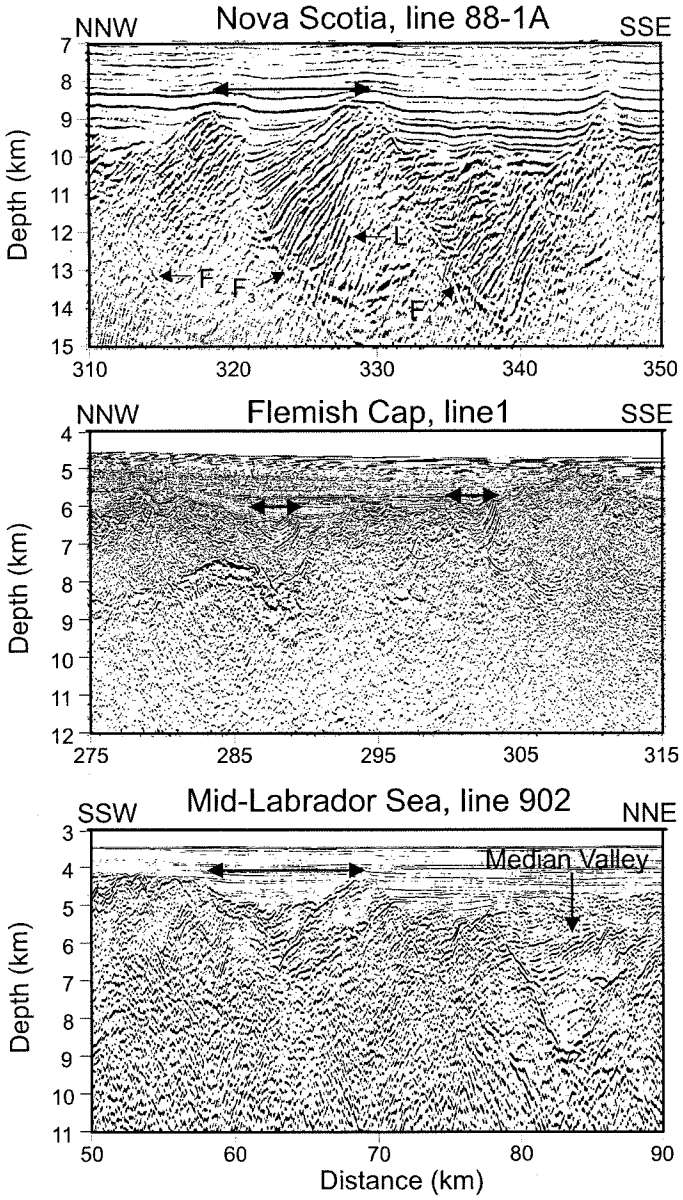

Figure 2.12. Basement topography and internal reflectivity of the faulted basement blocks along 88-1A (upper panel, after Keen *et al.* 1991b) compared with line 1 on the Newfoundland rifted margin (middle panel, after Hopper *et al.* 2004) and mid-Labrador Sea MCS profile 902 (bottom, after Srivastava and Keen 1995; Louden *et al.* 1996). Distances are referenced to the coincident velocity models. Double-arrows mark the location and horizontal region of basement structures, discussed in the text. Features marked by letters are F_2-F_4, listric normal faults bounding the highly faulted basement blocks; L, landward dipping reflectors.

dominated seafloor spreading. However, this example shows no faulting pattern bounding the oceanic basement blocks, and no fanning sequences of volcanic overflows within the separate volcanic episodes (middle, Figure 2.12). Across the abandoned median valley of the Mid-Labrador Sea (Srivastava and Keen 1995), which is rifting-dominated oceanic crust, even though the horizontal scale of the individual overflows (bottom, Figure 2.12) is close to that observed on Line 2, no fanning reflectors are imaged within the volcanic units. This distinguishes the basement structures observed along Line 2 from those observed on oceanic crust across the Newfoundland rifted margin off Flemish Cap and the extinct spreading center of the mid-Labrador Sea.

2.6.2.2 Oceanic Crust

The upper basement layer seaward of the FB is interpreted to be oceanic crust (Figure 2.8). The *P*-wave velocities of 5.6-6.0 km/s are within the global velocity range for layer 2 (White *et al.* 1992). In addition, a series of faults are imaged on MCS line 89-11, penetrating into the basement (F_5-F_9, Figure 2.13). These faults result in a variable crustal thickness and irregular basement relief (*e.g.* H and N in Figure 2.13), which is a typical representation of oceanic basement created by slow seafloor spreading (White *et al.* 1994). The initial thickness just seaward of the FB is 3-3.5 km; it reduces to 2-3 km at the seaward end of the model. The thickness variation suggests that this layer may have been affected by faulting (see faults F_5 and F_6 in Figure 2.13) and small-scale fracturing that would reduce the velocities at depth.

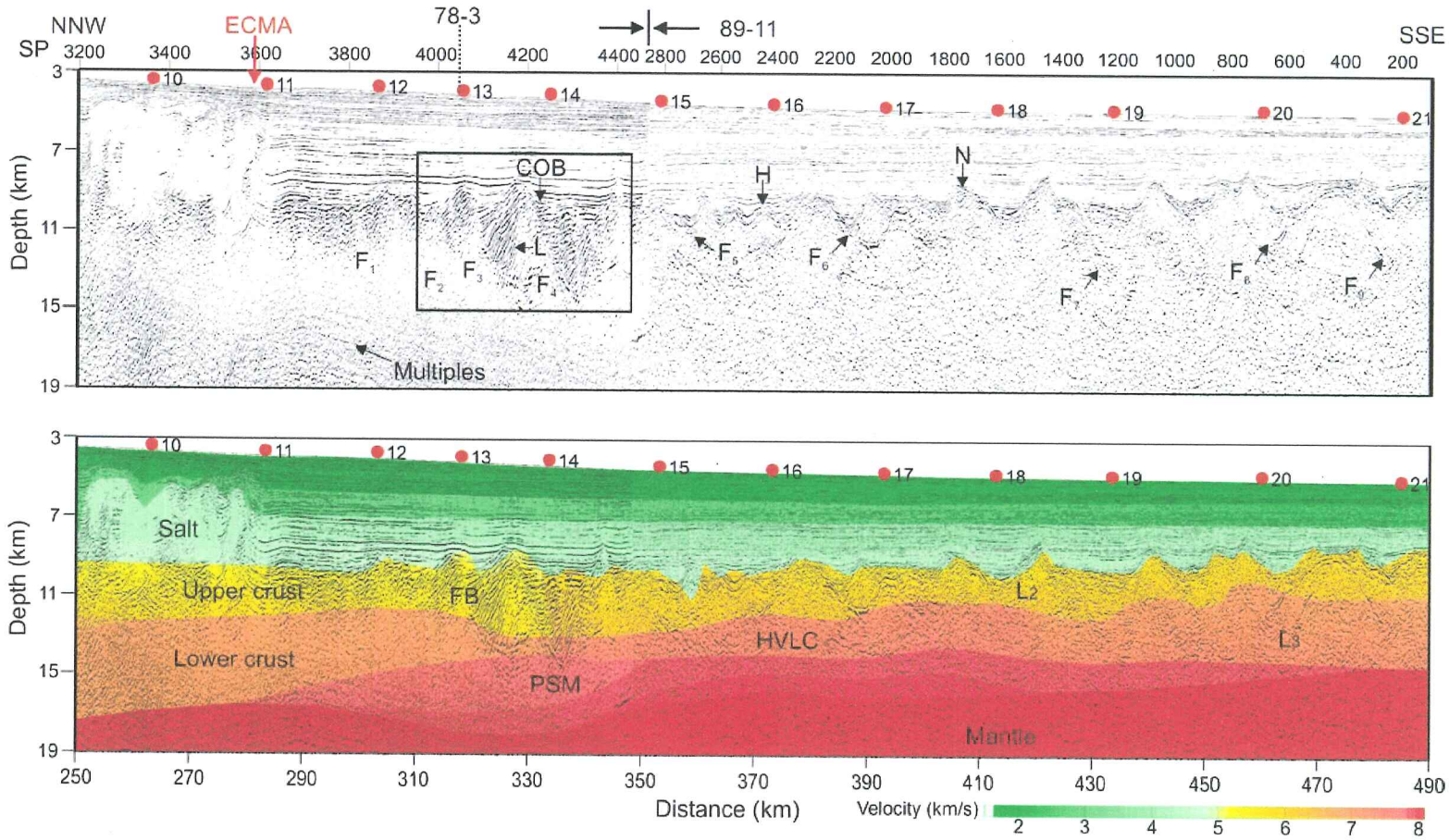

Figure 2.13. (Top) A combined MCS depth section of lines 88-1A (Keen *et al.* 1991b) and 89-11 (BGR). Features marked by letters are: F_1-F_9, faults; H and N, topographic basement "high" mentioned in the text; L, landward dipping reflectors. Other features refer to Figures 2.8 and 2.11. The cross point of seismic refraction profile 78-3 (Keen and Cordsen 1981) is marked by a dashed line. The image within the rectangle is shown in Figure 2.12.

An alternative interpretation is that this layer could be exhumed upper mantle. Such a layer was observed on Line 1 across the northern Nova Scotia margin (Funck *et al.* 2004). However, the exposed serpentinized mantle layer on Line 1 is characterized by flat basement topography and constant thickness without major faults. The rough basement relief and the presence of major faults in the basement do not support an interpretation of an exposed mantle layer for the central Nova Scotia margin. In summary, initial oceanic crust accretes seaward of the highly thinned continental crust, with a sharp COB (Figure 2.13) in the upper part of the OCT zone.

2.6.2.3 High-Velocity Lower Crustal (HVLC) Layer

The HVLC layer beneath the interpreted oceanic basement described above has velocities of 7.25-7.4 km/s, which decrease to 6.95-7.3 km/s at the seaward end of the model. The initially ~1 km thick layer thickens gradually seaward to about 3.5 km. The seaward portion has velocities within the global range of 6.7-7.2 km/s for oceanic layer 3 (White *et al.* 1992). The observed velocities at the landward side do not fall into the normal range of layer 3, although similar velocities are interpreted as layer 3 across the Labrador Sea (Osler and Louden 1995).

The atypically high velocities suggest that the HVLC layer may consist of a mixture of mantle with some frozen mafic melt. Such a mix may result from incomplete separation of rising melt from mantle when surface cooling freezes the upwelling melt in the mantle. This is consistent with the mafic and ultramafic mix models where mantle material is incorporated within the lower oceanic crust at slow-spreading rates (Cannat 1993; Sleep

and Barth 1997). The incomplete separation of rising melt reduces the bulk velocity of the upper mantle or seismically determined "lower crust". The seaward reduction of velocity is attributed to the increasing amount of separation of upwelling melt from ultramafic mantle.

Subsequent serpentinization may have further reduced the velocities and increased the velocity gradient as the amount of serpentinization reduces with depth. The faults through the episodic volcanic flows (F_5-F_9, Figure 2.13) enable seawater to penetrate into and serpentinize the uppermost mantle. Provided the velocity reduction is entirely due to mantle serpentinization, the degree of serpentinization inferred from the observed *P*-wave velocities is < 25 % (Miller and Christensen 1997).

Another possible hypothesis for the origin of the anomalous velocities is a high temperature of partial melting followed by fractionation. However, this interpretation is not consistent with the reduced thickness of the HVLC layer. To create the anomalously high velocity (7.25-7.4 km/s), a temperature anomaly of ~300° C would be required in the mantle, and more than 20 km thickness of igneous crust would be expected due to passive upwelling (White and McKenzie 1989; Korenaga *et al.* 2000). In addition, the depth (< 5 km beneath basement surface) of the HVLC layer is much shallower than the estimated depth of 20-35 km for the top of partial melting and fractionation below slow spreading mid-ocean ridge (Herzberg, 2004).

2.6.2.4 PSM Layer

The bottom layer of the OCT zone is also an anomalous velocity layer. Its velocities (7.6-7.95 km/s), compared to measurement of rock samples (Holbrook et al. 1992; Christensen and Mooney 1995), fall into a range of possible rocks such as serpentinized peridorite, underplated material, or a mix of intrusion and mantle material. The observations discussed below, however, are more consistent with an interpretation of partially serpentinized upper mantle.

The PSM layer is first observed beneath the highly thinned continental crust where a series of faults penetrate through the overlying crust (F_1-F_4, Figure 2.13). Rheological models show that mantle serpentinization occurs when the entire overlying crust lies within the brittle regime (Pérez-Gussinyé and Reston 2001), which is evidenced here by the major faults. These major faults allow circulation of seawater down to the uppermost mantle, by which the mantle rocks become serpentinized. Further seaward, an increasingly thinner PSM layer coincides with an increasingly thicker overlying basement (F_5-F_9, Figure 2.13). The PSM layer pinches out eventually at ~480 km when the overlying basement layer thickens to ~6 km. Such a PSM layer underneath oceanic basement has been documented along the Flemish Cap margin (Funck *et al.* 2003).

The reduced velocities (7.6-7.95 km/s) in the PSM layer indicate < 12 % of serpentinization (Miller and Christensen 1997). The *P*-wave velocities of the PSM in the OCT zone are well constrained, but its boundary with the underlying unaltered mantle is poorly parameterized (S, Figure 2.9). This indicates that the boundary more likely

represents a transition in the upper mantle from a relatively higher velocity gradient to a lower gradient with no velocity discontinuity.

We compare the PSM layer with similar layers elsewhere. The velocities and gradients of this layer are similar to those of the bottom layer in the OCT zone across the southern Iberia Abyssal Plain, which are 7.6 km/s and ~0.1 s^{-1} for velocity and gradient, respectively (Chian *et al.* 1999; Dean *et al.* 2000). The width and thickness of the lower layer are comparable, about 170 km and 4 km, respectively, for these two margins. The velocities (6.4-7.7 km/s) for the Labrador Sea-SW Greenland conjugates are lower than that observed along Line 2, and the thickness of the former (4-5 km; Chian and Louden 1995a) is relatively greater than that of Line 2 (~4 km). However, a higher velocity gradient (~0.3 s^{-1}) occurs for the Labrador Sea-SW Greenland margin conjugates, suggesting a higher degree of serpentinization; the overlying basement is also thinner (< 2 km; Chian *et al.* 1995a; Chian *et al.* 1995b).

Since the velocities also fall within the range of magmatically underplated material observed on volcanic margins, an alternative interpretation might be an underplated layer. This hypothesis is not favored by comparing the velocity model and magnetic anomalies observed here with those for volcanic margins elsewhere. Firstly, the extremely high velocities of 7.6-7.95 km/s, if attributed to underplating, would require an extremely high melting temperature. The high temperature would produce a large amount of magmatic intrusion and underplating, such as the 12- to 15-km-thick underplated layer beneath the U.S. East Coast margins (Holbrook and Kelemen 1993; Kelemen and Holbrook 1995). In

contrast, the PSM layer on Line 2 is only ~4 km thick. In addition, this layer is ~200 km across and its location is more than 100 km away from the hinge line. Both of these observations contradict crustal models for the U.S. East Coast margins where a 100-km-wide layer of underplated rocks is located underneath the outer shelf (Holbrook and Kelemen 1993). Furthermore, the underplated layer associated with SDR sequence along the U.S. margin is observed beneath the ECMA (Talwani *et al.* 1995; Talwani and Abreu 2000), while the PSM layer on Line 2 begins seaward of the ECMA and there are no observations of SDR sequences (Figure 2.13). Thus, the bottom layer along this margin segment is not related to the ECMA as it is on the U.S East Coast. Paleomagnetic data also suggest that the Triassic magmatism on land is only a brief coeval magmatic event which ceased well before continental breakup (Marzoli *et al.*. 1999). Based on the above comparisons, we conclude that the bottom layer observed along Line 2 is not produced by underplated rocks.

Another hypothesis is that the PSM layer could be a mix of mafic intrusion and unserpentinized mantle. This would occur if melt is frozen in the mantle by surface cooling, similar to the explanation of the HVLC layer. However, thermal models suggest that frozen melt due to surface cooling mostly occurs at shallow depths (*e.g.* $\leq$ 5 km) below the seafloor (Sleep and Barth 1997). Furthermore, ultraslow mid-ocean ridge, such as the Gakkel Ridge (Jokat *et al.* 2003) and Southwest Indian Ridge (Minshull and White 1996; Muller *et al.* 1999), do not demonstrate a reduced velocity in the off-axis mantle. Therefore, such a hypothesis does not explain the reduced mantle velocities in the PSM layer.

2.6.3 Along-Strike Variations of Margin

Figure 2.14 compares the velocity model along Line 2 with that for Line 1 (Funck *et al.* 2004). Both models indicate a non-volcanic character for the northeastern part of the Nova Scotia margin. Nonetheless, significant differences occur during the continental extension and the transition to seafloor spreading along the two margin segments. In the following sections, variations in crustal structure during the rift-to-drift transition and syn-rift crustal thinning are compared between the two velocity models and correlated with regional magnetic anomalies.

2.6.3.1 Rift-to-Drift Transition

The velocity models for Lines 1 and 2 show that both margin segments contain an OCT zone. The OCT zone of Line 2 consists of a PSM layer, overlain by highly faulted continental crust in the northwest and oceanic crust in the southeast. Thin oceanic crust forms immediately seaward of continental breakup. In contrast, the OCT zone of Line 1 comprises a 70-km-wide upper layer of exhumed and highly serpentinized mantle (HSM) overlying a PSM layer. This suggests that at the time of breakup, limited magma was generated across the central margin segment while no melt was created across the northern Nova Scotia margin. The PSM layer in the OCT zone of Line 1 is ~6 km thick with velocities of 7.2-7.6 km/s; the corresponding layer for Line 2 is less than 4 km thick with higher velocities of 7.6-7.95 km/s. This suggests a relatively low degree of mantle serpentinization along Line 2, and an increasingly higher percentage of serpentinized mantle toward Line 1. The oceanic crust for Line 1 is only ~4 km thick compared with 7.1±0.8 km for normal oceanic crust (White *et al.* 1992), indicating a magma-starved

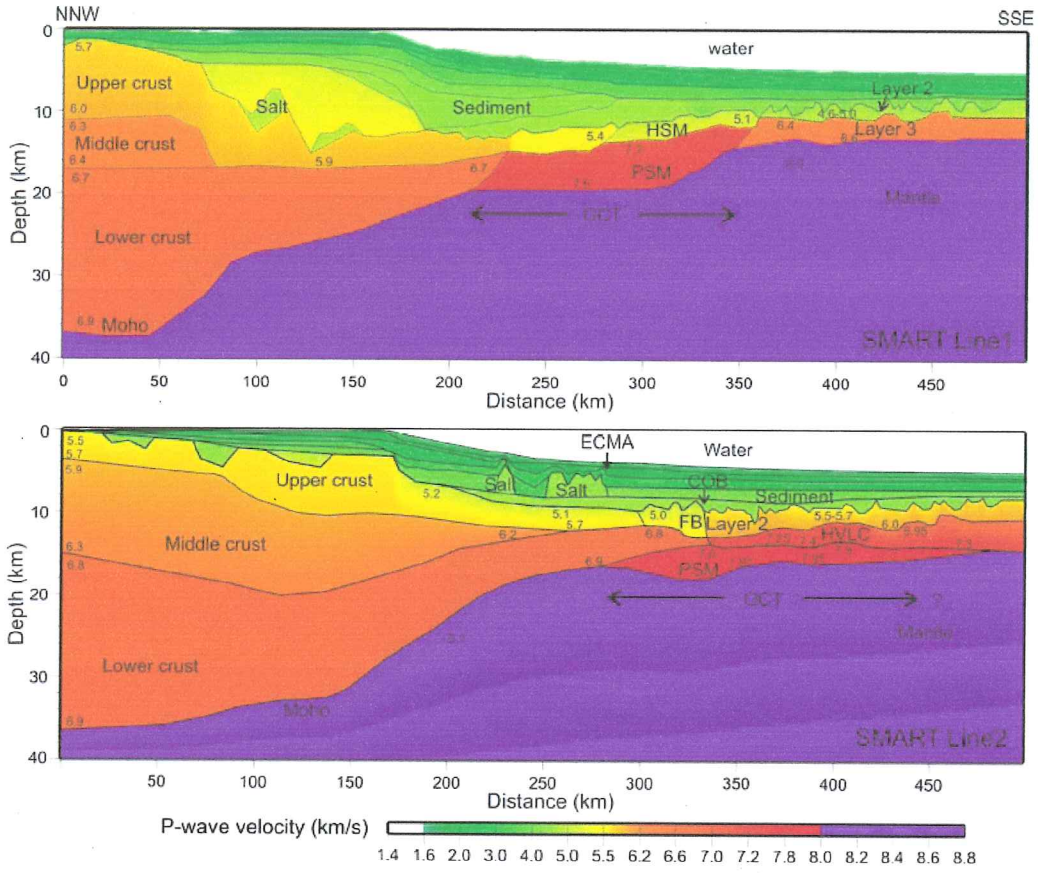

Figure 2.14. A comparison of velocity models along Line 1 (upper panel, Funck *et al.* 2004) and Line 2 (lower panel). *P*-wave velocities are indicated by a color scalar and numbers in the models (in km/s). Abbreviation: HSM, exhumed and highly serpentinized upper mantle. Other features refer to Figure 2.8.

margin after initiation of seafloor spreading. Along Line 2, although the initial oceanic crust could be ~4 km thick considering the mantle material incorporated to the HVLC layer, the oceanic crust at the seaward end has a more normal thickness of 5-7 km, which is 2-3 km thicker than on Line 1. The thickness variation also implies an increase of magma supply from the northern margin to the central margin. The preliminary results for Line 3 show an underplated lower crustal layer (Dehler *et al.* 2004) coinciding with the SDR sequence that is observed nearby on MCS profiles 89-3 and 4 (Keen and Potter 1995a). This further suggests a continuing increase of volcanism towards the southern Nova Scotia margin, where the margin eventually changes its character from a non-volcanic margin to a volcanic margin.

2.6.3.2 Syn-Rift Crustal Thinning

The thinning of the continental crust calculated from the velocity models in Figure 2.15 also presents different features across the two margin segments. For Line 2, the continental crust underwent a few kilometers (~5 km) of gradual thinning over the outer continental shelf, followed by a rapid thinning across the continental slope into the ocean basin (lower panel, Figure 2.15). The limited initial crustal thinning for the Lahave Platform was not able to counteract the uplift resulting from the thinning of subcrustal lithosphere predicted by subsidence analysis (Keen and Beaumont 1990) and therefore, there was no space beneath the shelf edge area to accommodate thick sediments. In contrast, the continental crust along Line 1 is dramatically thinned right from the onset of rifting, followed by a gradual thinning to the ocean basin (upper panel, Figure 2.15). The

abrupt crustal thinning across the northern margin has given rise to a rapid subsidence and formation of the deep Sable Basin seaward of the hinge line.

The results are basically in agreement with estimates of thermal-mechanical modeling for this margin (Keen and Beaumont 1990). The thermal-mechanical models are primarily based on subsidence analysis of exploratory well data. These models predict a non-uniform thinning of crustal and subcrustal lithosphere across the Lahave Platform, which produced uplift and erosion, and a more uniform thinning across the Scotian Basin, which created subsidence at the onset of rifting (Figure 2.15). However, the velocity model shows that the crustal thinning along Line 2 occurs about 100 km farther landward compared to the results of the thermal-mechanical models (lower panel, Figure 2.15). Provided that the result of the subcrustal lithospheric thinning (δ) is correct, we use the δ value and the crustal thinning (β) obtained from this experiment to calculate the subsidence through the non-uniform extension model of Royden and Keen (1980). The resulting maximum uplift of ~0.75 km across the central Nova Scotia margin is significantly less than estimates of ~2 km from the thermal-mechanical model (Keen and Beaumont 1990). In comparison, the crustal thinning for Line 1 starts 20-30 km further seaward and appears to be more rapid and abrupt over the slope area (upper panel, Figure 2.15), indicating a deeper basin seaward of the hinge line compared to analysis of Keen and Beaumont (1990).

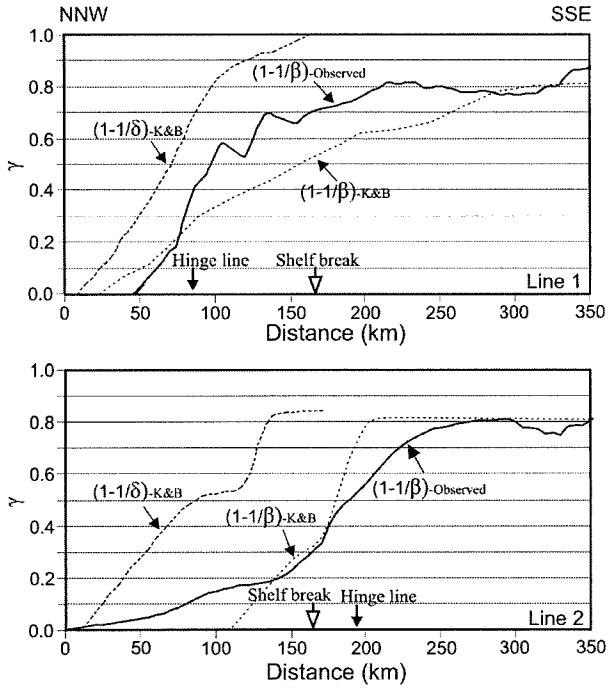

Figure 2.15. Comparison of model results with estimates of the thermal-mechanical models (Keen and Beaumont 1990) for Line 1 (upper panel) and Line 2 (lower panel). β and δ are the equivalent crustal and subcrustal thinning factors (1-1/β) and (1-1/δ), respectively. γ refers to either (1-1/β) or (1-1/δ) indicated by arrows. K&B, thermal-mechanical model of Keen and Beaumont (1990). Solid thick arrows mark the location of hinge lines. Open arrows indicate the location of shelf break.

2.6.3.3 Comparison with Regional Magnetic Anomaly

Selected magnetic profiles from the U.S. East Coast to the northern Nova Scotia margin are shown in Figure 2.16. The ECMA along the U.S. East Coast margin is a broad anomaly of ± 300 nT, which is thought to mark an igneous wedge created by voluminous magma intrusion and extrusion at the COB (Kelemen and Holbrook 1995; Talwani *et al.* 1995). This anomaly becomes narrower and sharper as it approaches the southwest Nova Scotia margin (Figure 2.16e-i), suggesting a narrower zone of volcanism. Further north of this region, the magnetic anomaly becomes broader and the amplitude decreases (Figure 2.16a-d). The along-strike magnetic signature implies that the anomaly source changes its character between Line 3 and profile NS 2-3 (Figures 2.16 and 2.17). The weak anomalies north of this region suggest that igneous material was not emplaced. This is consistent with the velocity models for Line 2 and Line 1 where no underplated material was identified within the transition zones.

The ECMA with reduced amplitude may be caused by the transition from highly thinned continental crust to serpentinized mantle rocks with different degrees of serpentinization. The ECMA along most of the margin up to MCS line 89-1 is roughly coincident with the distribution of the autochthonous salt (Shimeld 2004), suggesting that the underlying basement should be continental. The velocity models show that the landward extent of the OCT zone on Lines 1 and 2 is roughly consistent with the seaward limit of the ECMA (Figure 2.17). Further offshore, a "speckled" magnetic pattern correlates with oceanic crust. This suggests that the onset of the serpentinized transition zone is consistent with regional magnetic patterns. The subdued longer wavelength anomalies between the

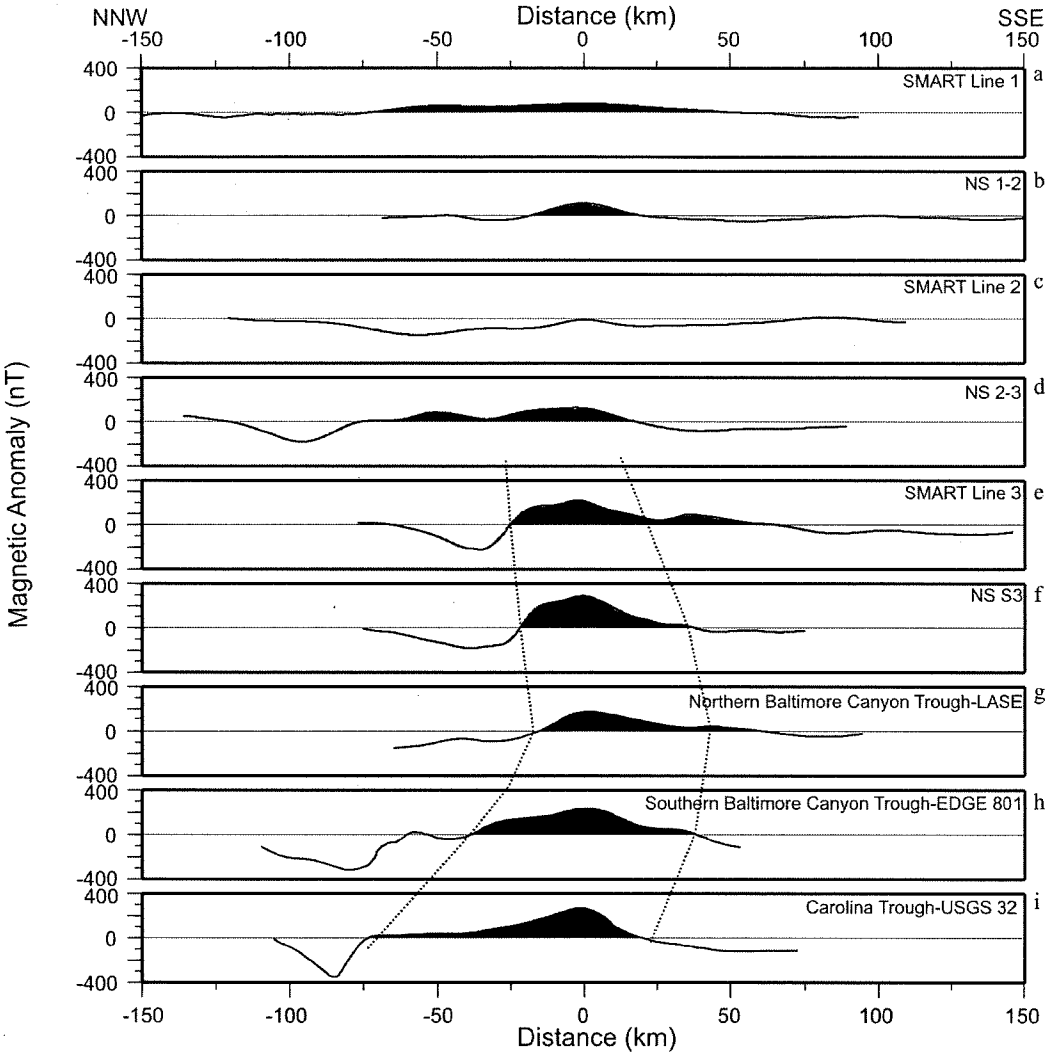

Figure 2.16. Selected magnetic profiles across the East Coast margin of North America. The upper six profiles (a-f) are taken from Oakey and Dehler (2004) and their locations are shown in Figure 2.17. The lowest three sections (g-i) are after Talwani *et al.* (1995). The distances are with respect to the peak anomaly of ECMA (0 km). The positive anomalies are filled with black. The relative widths of the ECMA are defined by two dotted lines.

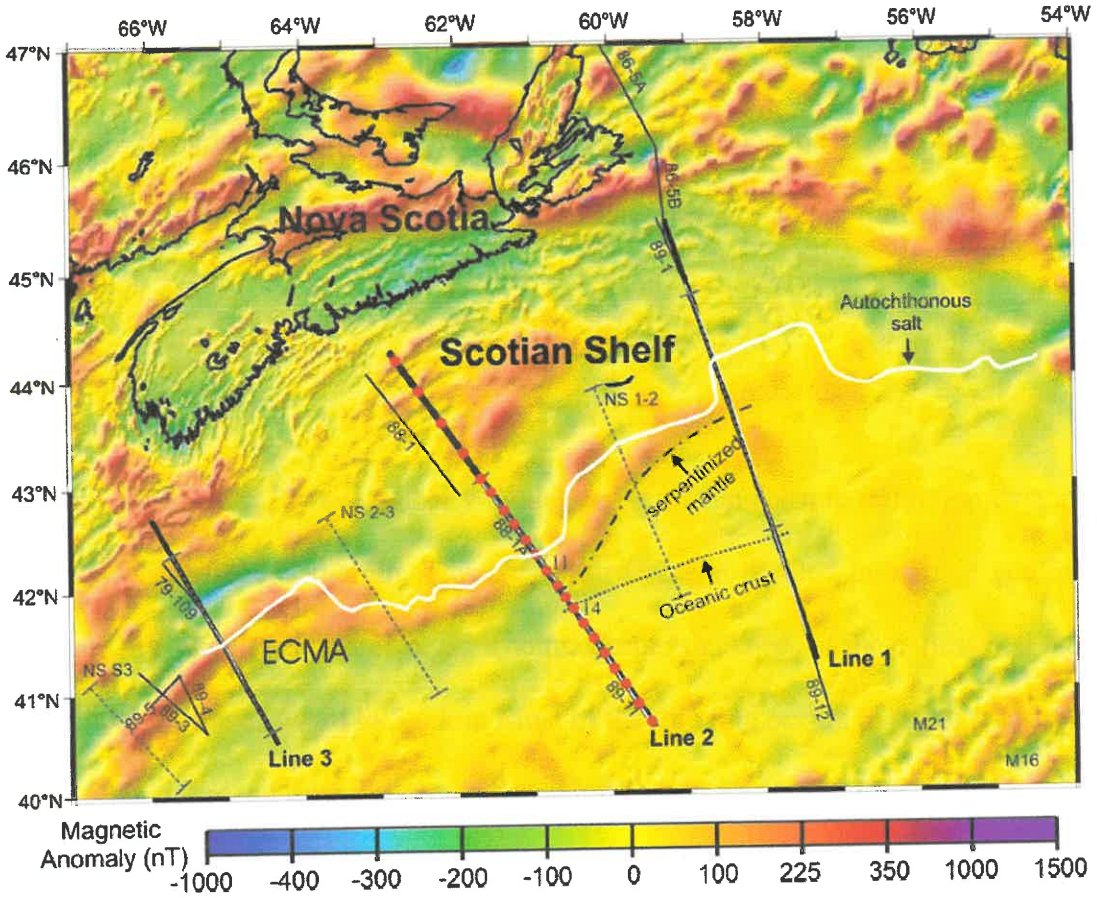

Figure 2.17. Magnetic anomaly map for the Nova Scotia margin and surrounding areas. Magnetic data are taken from Oakey and Dehler (2004). Bold solid lines represent the shot lines of the experiment with red circles indicating the location of OBS along Line 2. Other reflection seismic lines in the area are shown as thin black lines (see Figure 2.1 for references). Dashed lines are magnetic profiles extracted from the magnetic map and shown in Figure 2.16. OBS 11 and OBS 14 are annotated for reference. The thick white line marks the seaward boundary of the autochthonous salt (Shimeld 2004). The dot-dashed line marks the landward limit of the serpentinized mantle. The dotted line marks the landward limit of the "speckled" magnetic anomaly pattern, which is roughly coincident with the onset of the oceanic crustal accretion in this area. The magnetic lineation at the right lower corner represents magnetic anomalies M21 and M16 (Barrett and Keen 1976; Klitgord and Schouten 1986).

ECMA and the "speckled" pattern are associated with either highly thinned continental crust (Line 2) or exposed and highly serpentinized upper mantle (Line 1, Funck *et al.* 2004). Southwest of Line 2, the magnetic anomaly between the ECMA and the "speckled" pattern is dominantly negative. A preliminary model for Line 3 indicates oceanic crust underlies most of the negative anomaly at the seaward end of the line (Dehler *et al.* 2004).

2.7 Conclusions

We have presented a *P*-wave velocity model derived from seismic refraction data across the central Nova Scotia margin. The crustal structure is divided into rifted continental crust, an OCT zone and oceanic crust. The maximum thickness of the continental crust is ~36 km and it thins seaward to 5-6 km. Most of the thinning occurs over the slope region, while ~5 km of crustal thinning occurs beneath the outer shelf. The FBs are interpreted as the seaward-most continental fragments. The OCT zone contains a PSM layer, which extends from beneath the FB and ~200 km farther seaward beneath initial oceanic crust. Oceanic crust with normal thickness of 5-7 km is observed at the seaward end of the line.

The results suggest several modifications to earlier interpretations. First of all, the thinned continental crust extends up to a highly faulted basement structure, which was previously interpreted to be oceanic. With the new interpretation, the COB is moved ~50 km farther seaward. Furthermore, the velocity model shows that the initial continental thinning along Line 2 occurs ~100 km farther landward, compared to results of earlier thermal-mechanical models.

The velocity model shows no evidence for a magmatic underplated layer beneath the continental crust, suggesting primarily non-volcanic rifting across the central Nova Scotia margin. The high-amplitude of the magnetic anomaly related to the excessive volcanism south of the Nova Scotia margin does not extend further north along most of the margin. Compared to the magma-starved margin segment along Line 1 to the northeast, the results on Line 2 indicate a normal melt supply after continental break up. Although the melt generation along these margin segments farther to the south may have been affected by extensive volcanism, we suggest that the entire Nova Scotia margin, except for the southernmost part near Georges Bank, is non-volcanic in character.

2.8 Acknowledgments

We thank the scientists, technicians and all individuals onboard the CCGS HUDSON who helped carry out the seismic experiment in 2001. The experiment was funded by the Natural Sciences and Engineering Research Council of Canada (NSERC), the Geological Survey of Canada and the Danish National Research Foundation. Seismic line 89-11 was collected as part of a collaborative program between the Geological Survey of Canada and the German Federal Agency of Geosciences and Natural Resources (BGR). We are grateful to Tim Minshull, Tim Reston and Isabelle Contrucci for their comments and valuable suggestions on the manuscript. This is Geological Survey of Canada contribution number 2005124.

2.9 References

Barr, S. M. and Raeside R. P., 1989. Tectono-stratigraphic terranes in Cape Breton Island, Nova Scotia: Implications for the configuration of the northern Appalachian orogen, *Geology,* 17, 822-825.

Barrett, D. L. and Keen, C. E., 1976. Mesozoic magnetic lineations, the magnetic quiet zone, and sea floor spreading in the northwest Atlantic, *J. Geophys. Res.*, 81, 4875-4884.

Benn, K., Horne, R. J., Kontak, D. J., Pignotta, G. S. and Evans, N. G., 1997. Syn-Acadian emplacement model for the South Mountain batholith, Meguma Terrane, Nova Scotia: Magnetic fabric and structural analyses, *Geological Society of America Bulletin*, 109, 1279-1293.

Bown, J. W. and White, R. S., 1995. Effect of finite extension rate on melt generation at rifted continental margins, *J. Geophys. Res.,* 100, 18011-18029.

Cannat, M., 1993. Emplacement of mantle rocks in the seafloor at mid-ocean ridges, *J. Geophys. Res.,* 98, 4163-4172.

Chian, D., Louden, K. E. and Reid, I., 1995a. Crustal structure of the Labrador Sea conjugate margin and implications for the formation of nonvolcanic continental margins, *J. Geophys. Res.,* 100, 24239-24253.

Chian, D., Keen, C., Reid, I. and Louden, K. E., 1995b. Evolution of non-volcanic rifted margins: new results from the conjugate margins of the Labrador Sea, *Geology*, 23, 589-592.

Chian, D., Louden, K.E., Minshull, T.A. and Whitmarsh, R.B., 1999. Deep structure of the ocean-continent transition in the southern Iberia Abyssal Plain from seismic refraction profiles: Ocean Drilling Program (Legs 149 and 173) transect, *J. Geophys. Res.,* 104, 7443-7462.

Christensen, N. I. and Mooney, W. D., 1995. Seismic velocity structure and composition of the continental crust: A global view, *J. Geophys. Res.*, 100(B6), 9761–9788.

Dean, S. M., Minshull, T.A., Whitmarsh, R. B. and Louden, K. E., 2000. Deep structure of the ocean-continent transition in the southern Iberia Abyssal Plain from seismic refraction profiles: The IAM-9 transect at 40°20'N, *J. Geophys. Res.,* 105, 5859-5885.

Dehler, S. A., Keen, C. E., Funck, T., Jackson, H. R. and Louden, K. E., 2004. The limit of volcanic rifting: A structural model across the volcanic to non-volcanic transition off Nova Scotia. Eos Trans. AGU, 85(17), Jt. Assem. Suppl., Abstract T31D-04.

Funck, T., Hopper, J. R., Larsen, H. C., Louden, K. E., Tucholke, B. E. and Holbrook, W. S., 2003. Crustal structure of the ocean-continent transition at Flemish Cap: Seismic refraction results, *J. Geophys. Res.*, 108(B11), 2531, doi: 10.1029/2003JB002434.

Funck, T., Jackson, H. R., Louden, K. E., Dehler, S. A. and Wu, Y., 2004. Crustal structure of the northern Nova Scotia rifted continental margin (Eastern Canada), *J. Geophys. Res.*, 109, B09102, doi: 10.1029/2004JB003008.

Herzberg, C., 2004. Partial crystallization of mid-ocean ridge basalts in the crust and mantle, *J. Petrol.*, 45, 2389-2405.

Holbrook, W. S. and Kelemen, P. B., 1993. Large igneous province on the US Atlantic margin and implications for magmatism during continental breakup, *Nature*, 364, 433-436.

Holbrook, W.S., Mooney, W.D. and Christensen, N.I., 1992. The seismic velocity structure of the deep continental crust, in *Continental lower crust. Edited by* Fountain, D.M., Arculus, R. and Kay, R., Elsevier, Amsterdam, pp. 1-43.

Hopper, J. R., Funck, T., Tucholke, B. E., Larsen, H. C., Holbrook, W. S., Louden, K. E., Shillington, D. and Lau, H., 2004. Continental breakup and the onset of ultraslow seafloor spreading off Flemish Cap on the Newfoundland rifted margin, *Geology*, 32(1), 93-96, doi:10.1130/G19694.1.

Jokat, W., Ritzmann, O., Schmidt-Aursch, M. C., Drachev, S., Gauger, S. and Snow, J., 2003. Geophysical evidence for reduced melt production on the Arctic ultraslow Gakkel mid-ocean ridge, *Nature,* 423, 962-965.

Keen, C. E. and Beaumont, C., 1990. Geodynamics of rifted continental margins, in *Geology of the Continental Margin of Eastern Canada*, Edited by Keen, M. J. and Williams, G. L., Geological Survey of Canada, Geology of Canada, No. 2, 393-472.

Keen, C. E. and Cordsen, A., 1981. Crustal structure, seismic stratigraphy, and rift processes of the continental margin off eastern Canada: ocean bottom seismic refraction results off Nova Scotia, *Can. J. Earth Sci.*, 18, 1523-1538.

Keen, C. E., Kay, W. A., Keppie, D., Marillier, R., Pe-Piper, G. and Waldron, J. W. F., 1991a. Deep seismic reflection data from the Bay of Fundy and marine: tectonic implication for the northern Appalachian, *Can. J. Earth Sci.*, 28, 1096-1111.

Keen, C. E., MacLean, B. C. and Kay, W. A., 1991b. A deep seismic reflection profile across the Nova Scotia continental margin, offshore eastern Canada, *Can. J. Earth Sci.*, 28, 1112-1120.

Keen, C. E. and Potter, P., 1995a. The transition from a volcanic to nonvolcanic rifted margin off eastern Canada, *Tectonics,* 14, 359-371.

Keen, C. E. and Potter, P., 1995b. Formation and evolution of the Nova Scotian rifted margin: Evidence from deep seismic reflection data, *Tectonics,* 14, 918-932.

Kelemen, P. B. and Holbrook, W. S., 1995. Origin of thick, high-velocity igneous crust along the U.S. East Coast Margin, *J. Geophys. Res.*, 100, B7, 10,077-10,094.

Keppie, J. D., 1989. Northern Appalachian terranes and their accretionary history, in *Terranes in the circum-Atlantic Paleozoic Orogens,* edited by Dallmeyer, R. D., Geological Society of America, Special Paper, 230,159-192.

Klitgord, K. D. and Schouten, H., 1986. Plate kinematics of the central Atlantic, in *The Geology of North America, Volume M, The Western North Atlantic Region*, edited by Vogt P. R. and Tucholke, B. E., 351-378, Geological Society of America, Boulder, Colo.

Korenaga, J., Holbrook, W.S., Kent, G.M., Kelemen, P.B., Detrick, R.S., Larsen, H. C., Hopper, J.R. and Dahl-Jensen, T., 2000. Crustal structure of the Southeast Greenland margin from joint refraction and reflection seismic tomography, *J. Geophys. Res.*, 105, 21, 591–21, 614.

Loncarevic, B. D., Courtney, R. C., Fader, G. B. J., Giles, P. S., Piper, D. J. W., Costello, G., Clarke, J. E., Hughes and Stea, R. R., 1994. Sonography of a glaciated continental shelf, *Geology*, 22, 747-750.

Louden, K. E. and Chian, D., 1999. The deep structure of non-volcanic rifted continental margins, *Phil Trans. Roy. Soc. Lond., Ser.* A., 357, 767-804.

Louden, K. E., Osler, J. C., Srivastava, S. P. and Keen, C. E., 1996. Formation of oceanic crust at slow spreading rates: New constraints from an extinct spreading center in the Labrador Sea, *Geology,* 24, 771-774.

Ludwig, W. J., Nafe, J. E. and Drake, C. L., 1970. Seismic refraction, in *The Sea, New concepts of the sea floor evolution*, edited by Maxwell, A. E., 53-84, Wiley-intersci., New York.

Lutter, W. J. and Nowack, R. L., 1990. Inversion for crustal structure using reflections from the PASSCAL Ouachita experiment, *J. Geophys. Res.*, 95, 4633-4646.

MacLean, B. C., 1991. Structure and isopach 1: depth to pre-Mesozoic basement and oceanic layer 2; In *East Coast Basin Atlas Series: Scotian Shelf*, Atlantic Geoscience Centre, Geological Survey of Canada, 75.

Marillier, F., Keen, C. E., Stockmal, G. S., Quinlan, G., Williams, H., Colman-Sadd, S. P. and O'Brien, S. J., 1989. Crustal structure and surface zonation of the Canadian

Appalachians: implications of deep seismic reflection data, *Can. J. Earth Sci.,* 26, 305-321.

Marzoli, A., Renne, P. R., Piccirillo, E. M., Ernesto, M., Bellieni, G. and Min, A. De, 1999. Extensive 200-million-year-old continental flood basalts of the Central Atlantic Magmatic Province, *Science* 284: 616-618.

Miller, D. J. and Christensen, N. I., 1997. Seismic velocities of lower crustal and upper mantle rocks from the slow-spreading Mid-Atlantic Ridge, south of the Kane Transform zone (MARK), *Proc. Ocean Drill. Program Sci. Results,* 153, 437-454.

Minshull, T. A. and White, R. S., 1996. Thin crust on the flanks of the slow-spreading Southwest Indian Ridge, *Geo. J. Int.,* 125, 139–148.

Muller, M.R., Minshull, T.A. and White, R.S., 1999. Segmentation and melt supply at the Southwest Indian Ridge, *Geology*, 27, 867-870.

National Geophysical Data Center, 1988. ETOPO-5 Bathymetry/Topography data, Data announcement 88-MG-02, National Oceanic and Atmospheric Administration, U.S. Dept. of Commerce, Boulder, Colo.

Oakey, G.N. and Dehler, S.A., 2004. Atlantic Canada magnetic map series: Scotian shelf and surrounds, Open File Rep. 1814, Geological Survey of Canada, Calgary, Alb.

Osler, J. and Louden, K.E., 1995. Extinct spreading center in the Labrador Sea: crustal structure from a two-dimensional seismic refraction velocity model, *J. Geophys. Res.,* 100, 2261-2278.

Pérez-Gussinyé, M. and Reston, T. J., 2001. Rheological evolution during extension at nonvolcanic rifted margins: onset of serpentinization and development of detachments leading to continental breakup, *J. Geophys. Res.,* 106, 3961-3975.

Prosser, S., 1993. Rift-related linked depositional systems and their seismic expression, in: Williams, G. D. and Dobb, A. (eds), *Tectonics and Seismic Sequence Stratigraphy*, Geol. Soc. Spec. Publ. Lond., 71, 35-66.

Reid, I. D., 1994. Crustal structure of a nonvolcanic rifted margin east of Newfoundland, *J. Geophys. Res.,* 99, 15161-15180.

Royden, L. and Keen, C. E., 1980. Rifting process and thermal evolution of the continental margin of eastern Canada determined from subsidence curves, *Earth Planet. Sci. Lett.*, 51, 343-361.

Sahabi, M., Aslanian, D. and Olivet, J.-L., 2004. Un nouveau point de départ pour l'histoire de l'Atlantique central, Comptes Rendus Geosciences, 336, 12, 1041-1052.

Salisbury, M.H. and Keen, C.E., 1993. Listric faults imaged in oceanic crust, *Geology,* 21, 117-120.

Sandwell, D. T. and Smith, W. H. F., 1997. Marine gravity anomaly from Geosat and ERS 1 satellite altimetry, *J. Geophys. Res.,* 102, 10039-10054.

Sawyer, D.S., Whitmarsh, R.B., Klaus, A., *et al.* (including Milliken, K. L.), 1994. *Proceedings of the Ocean Drilling Program*, Initial Reports, 149, College Station, TX, 719.

Shimeld, J., 2004. A comparison of salt tectonic subprovinces beneath the Scotian Slope and Laurentian Fan, in *Salt Sediment Interactions and Hydrocarbon Prospectivity: Concepts, Applications, and Case Studies for the 21st Century*, 24th Annual Conference, Post, P., Olson, D., Lyons, K., Palmes, S., Harrison, P. and Rosen N., editors. Gulf Coast Section Society of Economic Paleontologists and Mineralogists Foundation (GCSSEPM), Houston, TX (CD format).

Sleep, N.H. and Barth, G.A., 1997. The nature of oceanic lower crust and shallow mantle emplaced at low spreading rates, *Tectonophysics*, 279, 181–191.

Srivastava, S. P. and Keen, C. E., 1995. A deep seismic reflection profile across the extinct Mid-Labrador Sea spreading center, *Tectonics,* 14, 372-389.

Talwani, M. and Abreu, V., 2000. Inferences regarding initiation of oceanic crust formation from the U.S. east coast margin and conjugate south Atlantic margins, in *Atlantic rifts and continental margins*, edited by Mohriak W. and Talwani, M., 211-233, American geophysical Union, Geophysical Monograph 155, Washington, DC.

Talwani, M., Ewing, J., Sheridan, R. E., Holbrook, W. S. and Glover, L. III., 1995. The EDGE experiment and the U.S. Coast Magnetic Anomaly, in NATO/ARW Series book *Rifted Ocean-Continent Boundaries*, (ed. Banda, E., Talwani, M. and Torne, M.), Amsterdam: Kluwer, 155-181.

Talwani, M., Worzel, J. L. and Landisman, M., 1959. Rapid gravity computations for two-dimensional bodies with application to the Mendocino submarine fracture zone, *J. Geophys. Res.,* 64, 49-59.

Wade, J.A., 1981. Geology of the Canadian Atlantic margin from Georges Bank to the Grand Banks, in: *Geology of the North Atlantic Borderlands*, Kerr, J. Wm. and Ferguson, A.J. (eds.), Canadian Society of Petroleum Geologists, Memoir 7, p. 447-460.

Wade, J. A. and MacLean, B. C., 1990. The geology of the southeastern margin: aspects of the geology of the Scotian Basin from recent seismic and well data, in *Geology of the Continental Margin Eastern Canada*, edited by Keen, M. J. and Williams, G. L., Geological Survey of Canada, Geology of Canada, No. 2, 167-238.

Welsink, H. J., Dwyer, J: D. and Knight, R. J., 1989. Tectono-stratigraphy of the passive margin off Nova Scotia, in *Extensional tectonics and stratigraphy of the North Atlantic margin*, edited by Tankard, A. J. and Balkwill, H.R., American Association of Petroleum Geologists, Memoir 46, 215-231.

White, R. S., McBride, J. H., Henstock, T. J. and Hobbs, R. W., 1994. Internal structure of Mesozoic oceanic crust, *Geology* 22, 597-600.

White, R. S. and McKenzie, D. P., 1989. Magmatism at rift zones: the generation of volcanic continental margins and flood basalts, *J. Geophys. Res.*, 94, 7685-7729.

White, R. S., McKenzie, D. and O'Nions, K., 1992. Oceanic crustal thickness from seismic measurements and rare earth element inversions, *J. Geophys. Res.*, 97, 19683-19715.

Williams, H., 1979. Appalachian Orogen in Canada, *Can. J. Earth Sci.*, 16, 792-807.

Zelt, C. A. and Forsyth, D. A., 1994. Modeling wide-angle seismic data for crustal structure: southeastern Grenville province, *J. Geophys. Res.*, 99, 11687-11704.

Zelt, C. A. and Smith, R. B., 1992. Seismic traveltime inversion for 2-D crustal structure, *Geophys. J. Int.*, 108, 16-34.

2.10 Appendix 2.A. Additional Record Sections with Phase Description

Additional record sections are included in this appendix. OBS locations are shown in Figure 2.2. Labels are defined in section 2.4.3. Other features refer to Figure 2.3. The phases for each OBS are described as follows:

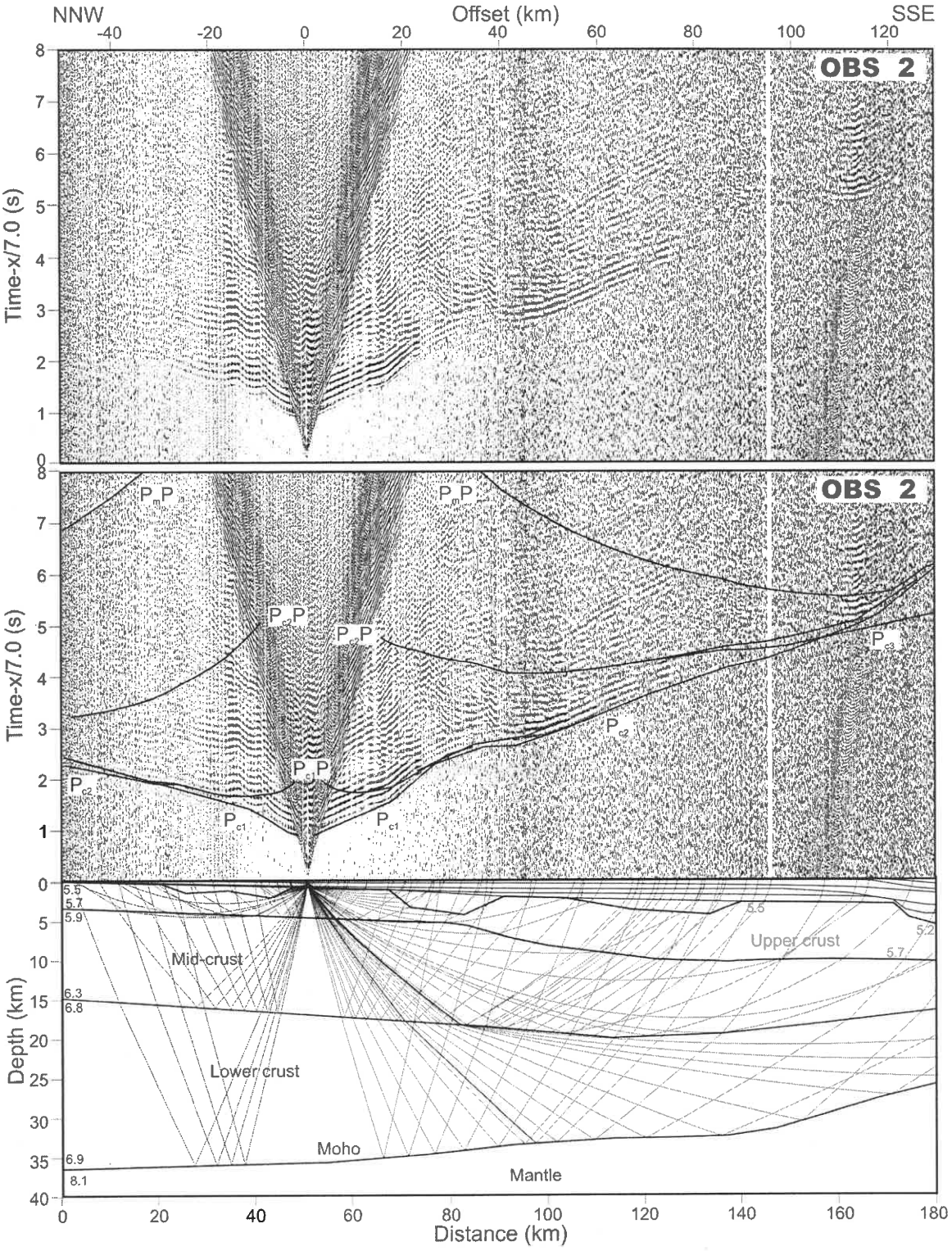

Figure 2.A1. Record section for OBS 2 (hydrophone component). On this station, phases P_{c1} and P_{c2} are imaged, but P_{c3} is weak and difficult to identify. Reflections from these layers ($P_{c1}P, P_{c2}P, P_mP$) are weak.

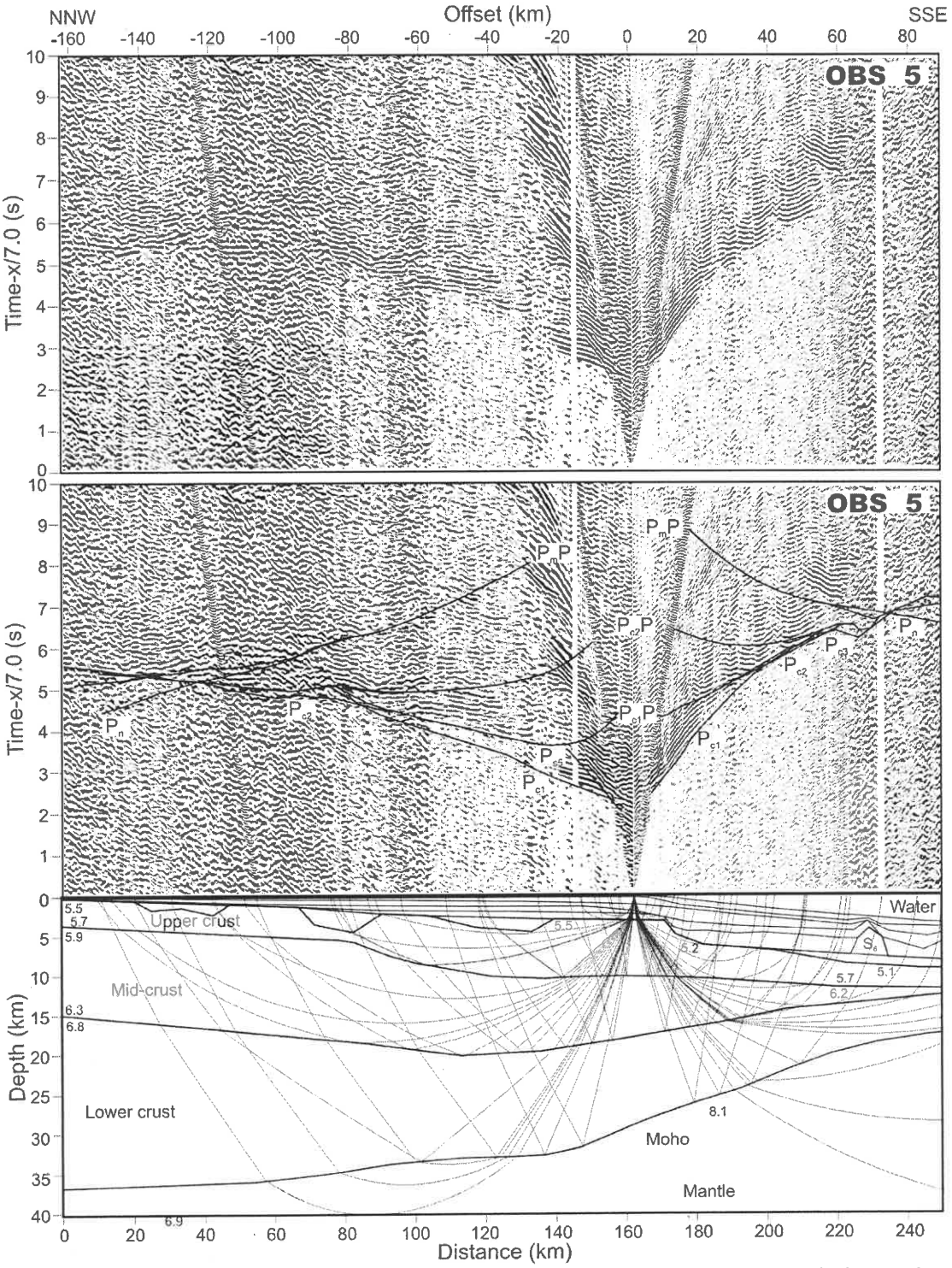

Figure 2.A2. Record section for OBS 5 (hydrophone component). OBS 5 is located at the shelf edge. On this record section, P_{c1} and P_{c2} and their corresponding reflection phases $P_{c1}P$ and $P_{c2}P$ are observed. P_mP is imaged at far offsets. P_n is less clear at offsets around -140 km.

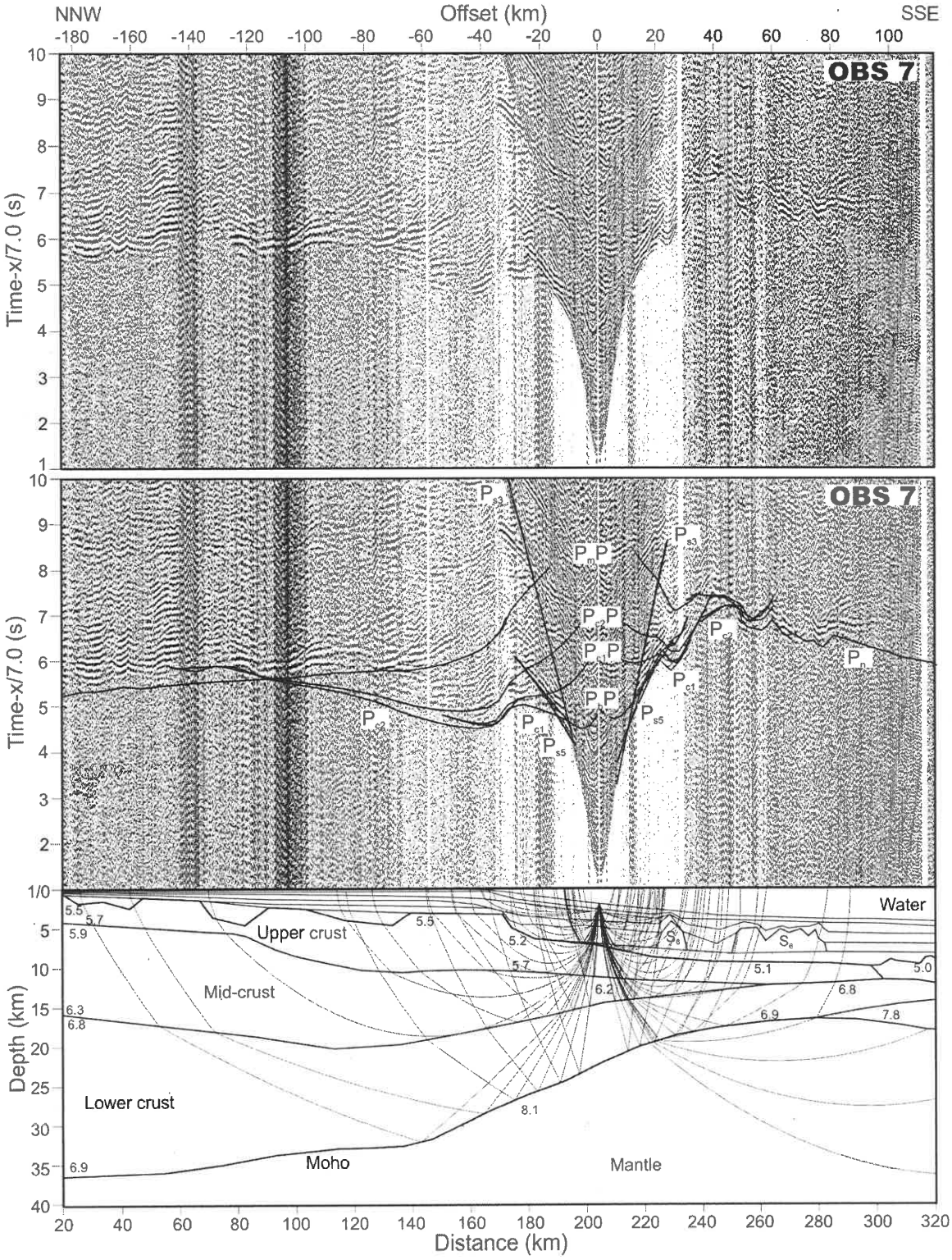

Figure 2.A3. Record section for OBS 7 (vertical geophone component). On this OBS, P_{c1} and P_{c2} and their corresponding reflections $P_{c1}P$ and $P_{c2}P$ are observed. P_mP is imaged at offsets from -40 km to -182 km. P_n is distorted by salt diapirs but is identifiable at offsets 50-100 km.

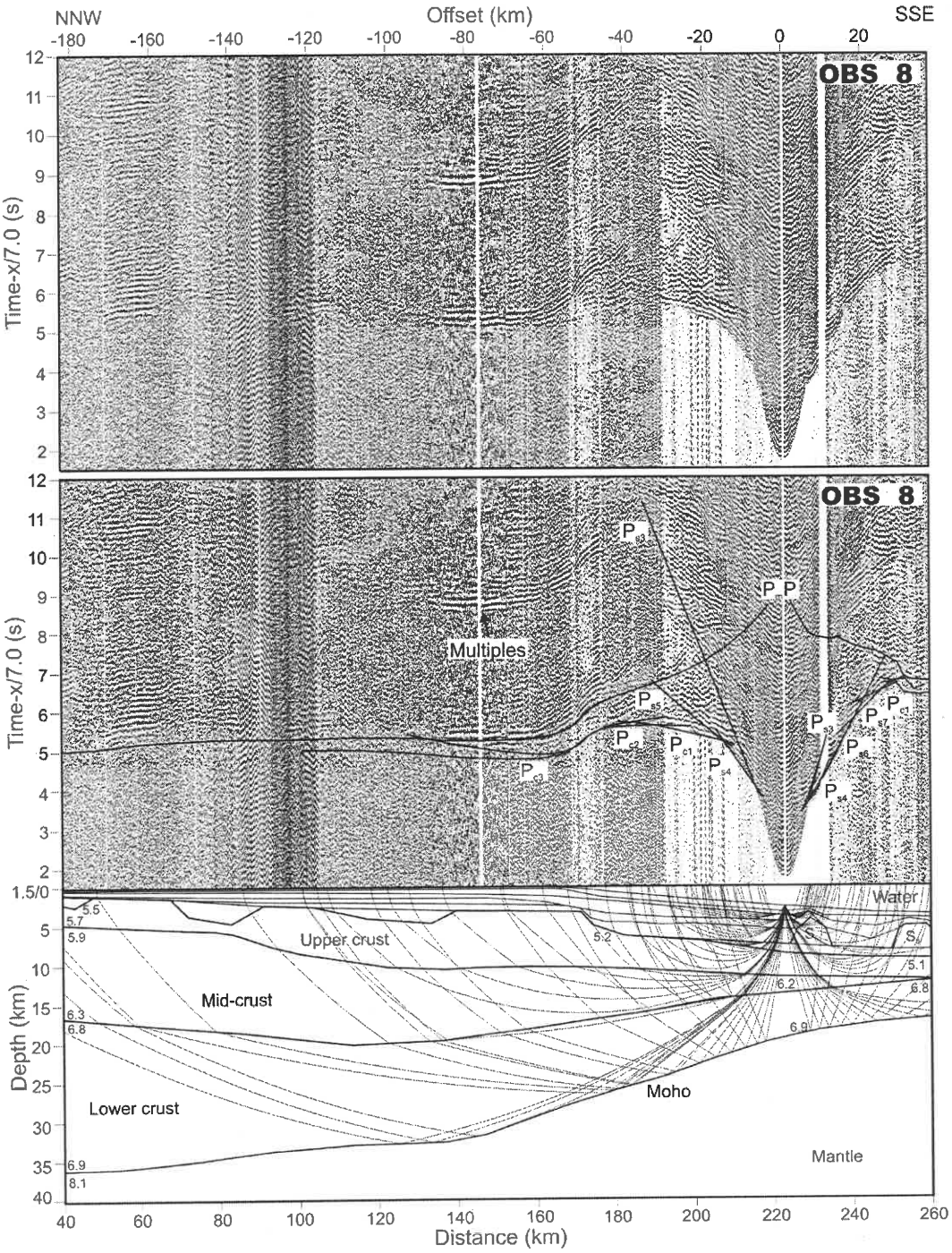

Figure 2.A4. Record section for OBS 8 (hydrophone component). The record section shows P_{c1} and weak P_{c2} and P_{c3} phases of the crustal layers beneath the slope area where most thinning of the continental crust occurs (distance 150-250 km). P_mP and its multiple from offsets -40 km to -180 km provide constraints for the Moho geometry beneath the slope area.

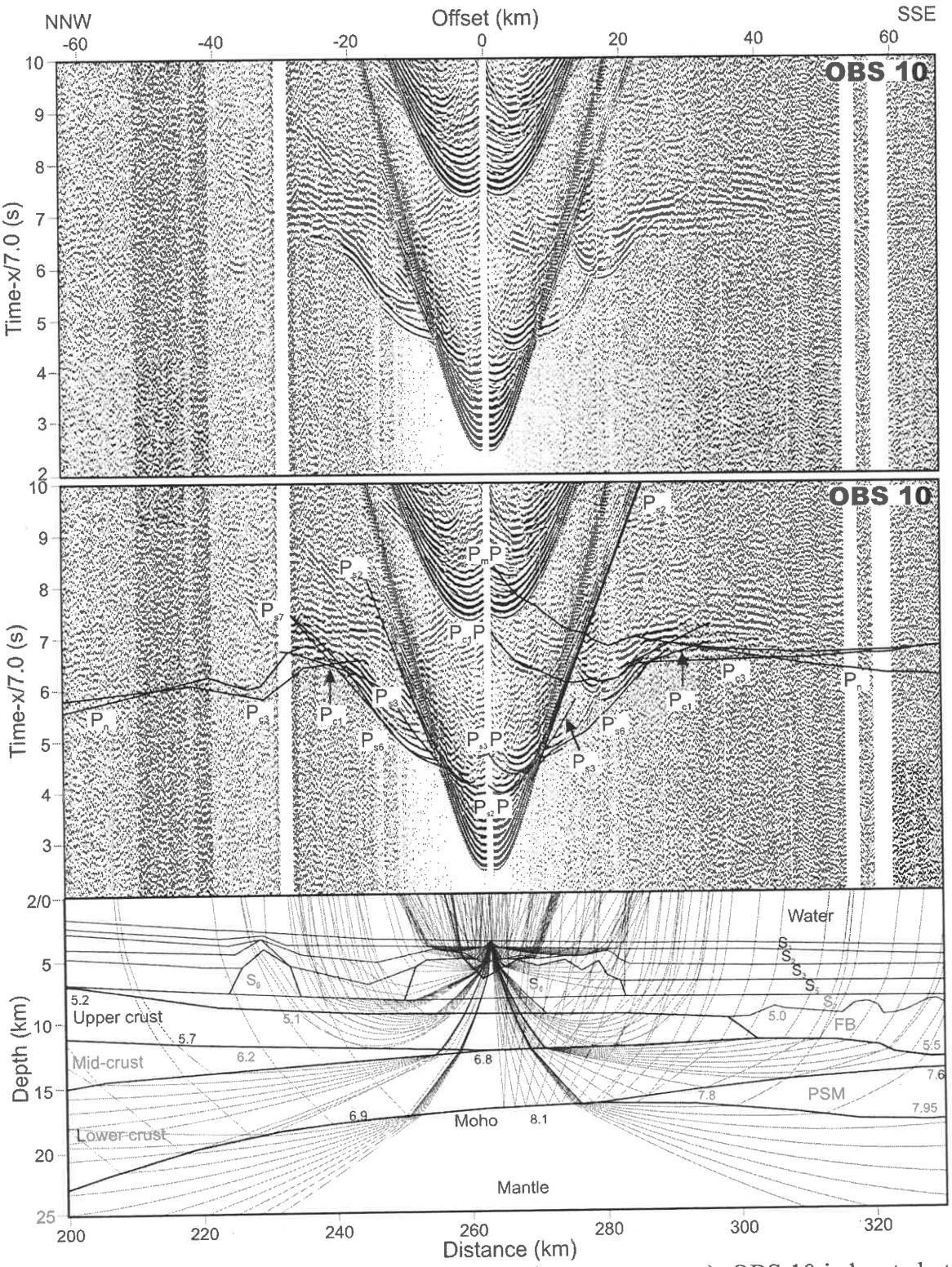

Figure 2.A5. Record section for OBS 10 (hydrophone component). OBS 10 is located at over the salt diapir structure. Refraction from the salt units (P_{s6}) is observed. Phase P_{c1} is disturbed by the irregular geometry of the salt diapirs. Phase P_{c3} is imaged on the SSE side at offsets 20-50 km and is weak but identifiable on the NNW side from -30 km to -40 km. P_mP is observed at offsets 20-60 km and P_n is observed at far offsets.

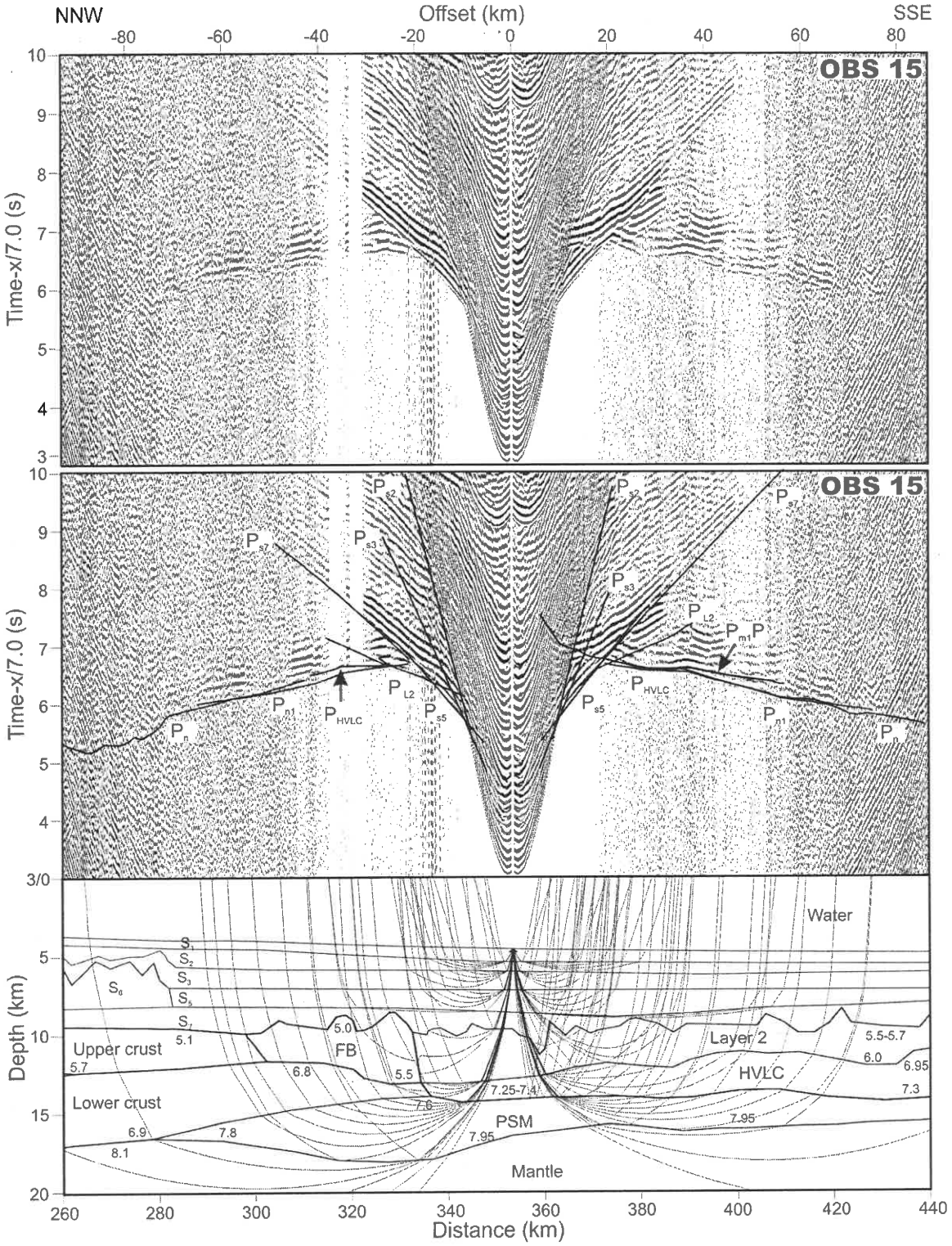

Figure 2.A6. Record section for OBS 15 (vertical geophone component). Phases P_{L2}, P_{HVLC}, P_{n1} and P_n are imaged on both sides as first or recognizable second arrivals. The reflection $P_{m1}P$ from the base of the HVLC layer appears at the SSE side at offsets 40-60 km.

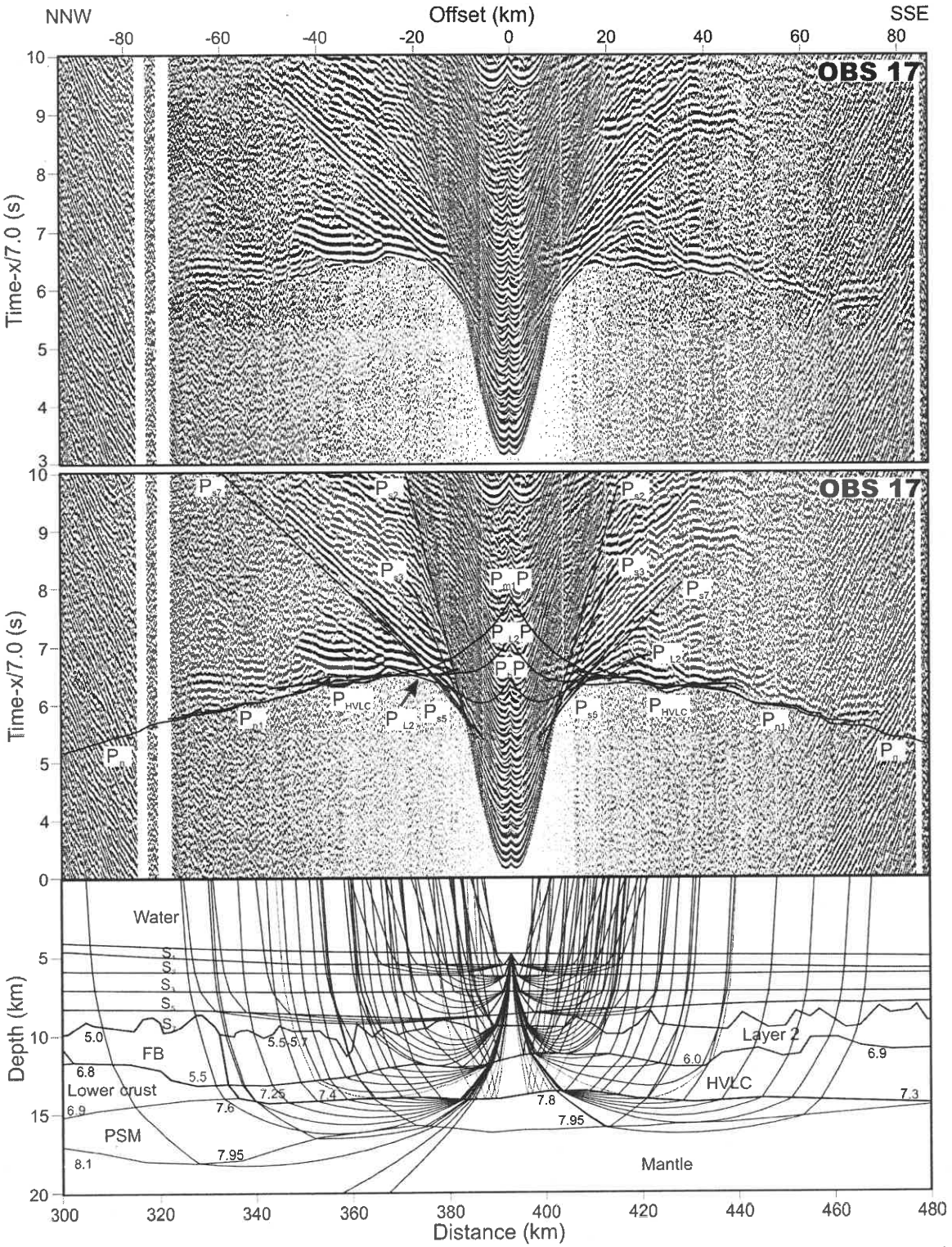

Figure 2.A7. Record section for OBS 17 (vertical geophone component). Phases P_{L2} and P_{HVLC} are imaged as first or recognizable second arrivals. Reflection $P_{m1}P$, and refraction Phase P_{n1} are observed on both sides. P_n is observed at far offsets.

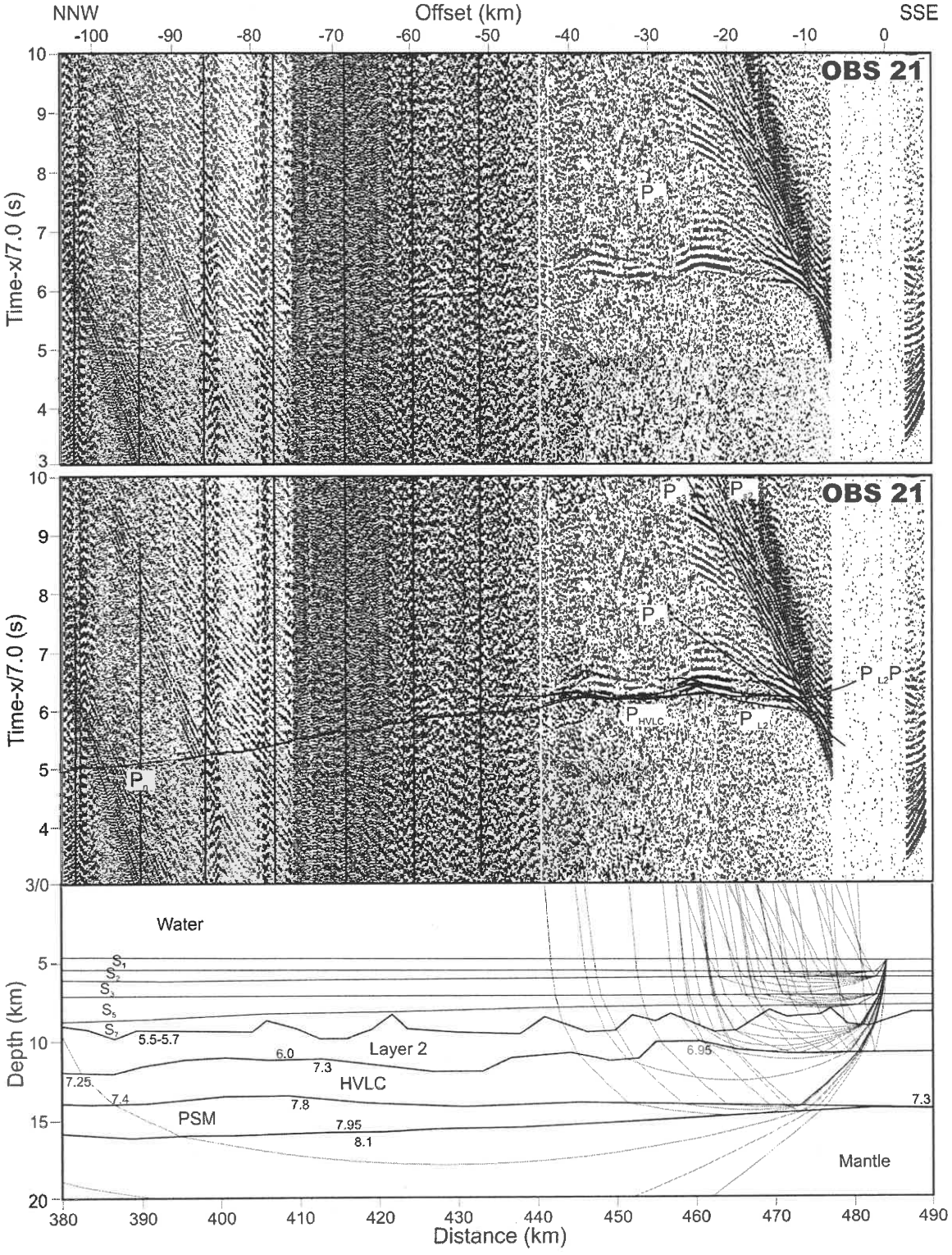

Figure 2.A8. Record section for OBS 21 (hydrophone component). OBS 21 is located at the seaward end of the profile. Phases P_{L2} and P_{HVLC} are weakly imaged. Mantle refraction (P_n) is observed at far offsets between -75 km and -100 km as recognizable arrivals.

CHAPTER 3

CRUSTAL STRUCTURE OF THE CENTRAL NOVA SCOTIA MARGIN OFF EASTERN CANADA (PART II)—RESULTS FROM PRE-STACK MIGRATION OF SEISMIC REFLECTION DATA

3.1 Introduction

In Chapter 2, the wide-angle seismic refraction data across the central Nova Scotia margin indicate that this margin segment is non-volcanic and therefore, the East Coast Magnetic Anomaly (ECMA) in this region is not caused by excessive volcanism during rifting. This implies that there should be no seaward dipping reflections (SDR), which would otherwise be indicative of volcanic extrusives (Keen and Potter 1995a), existing beneath the slope. Unfortunately, the image of basement structure across the slope was masked by overlying diapiric salt structures in the previous seismic reflection profile derived from post-stack migration. Re-imaging the basement structure beneath the slope salt province should provide further evidence for determining the volcanic or non-volcanic character of the central Nova Scotia margin.

In addition, the velocity model suggests that the continent-ocean boundary (COB) is located at the seaward edge of a series of basement fault blocks, ~50 km seaward of the previous interpretation (e.g. Salisbury and Keen 1993). The continent-ocean transition in the revised interpretation consists of a layer of serpentinized upper mantle beneath the faulted basement blocks with the presence of significant lateral velocity variation. The seismic image in the previous reflection profile, however, did not show reflectivity signatures corresponding to the structural variation. The seismic images across the faulted

basement blocks may also not be accurately imaged through post-stack migration. Post-stack migration can provide accurate images in regions with horizontal and gently dipping strata (e.g. < 10-15 degrees). For complex media with larger dip angles and irregular geometry, however, the subsurface structure can not be accurately imaged due to mid-point smearing (e.g. Yilmaz 2001). The midpoint smearing due to post-stack migration can be circumvented by migrating the unstacked seismic data, i.e. pre-stack migration.

Velocity information plays a key role in migration. The velocity field required for migration is conventionally converted from stacking velocity which is assumed to be an approximation of RMS velocity (Lillie 1999). However, the stacking velocity obtained from NMO correction may vary with dip even if the medium velocity is constant (Levin 1971). Pre-stack migration techniques delay velocity analysis until the seismic data have been fully migrated so that estimation of the velocity field can be improved. However, large velocity uncertainties still exist for deep structures due to small amount of NMO correction at large depths in offshore ultra-deep water regions. One obvious approach to reduce the velocity uncertainty at large depths is to extend the acquisition arrays to larger offsets so as to increase the amount of NMO correction. This has been adopted by modern 2D regional seismic surveys. For instance, recent 2D profiles offshore Nova Scotia acquired by GX Technology Corporation used a streamer up to 9 km long. For most previous seismic profiles with shorter streamer lengths, an alternative approach is to use the velocity field constrained by coincident wide-angle seismic refraction data. Over the past decade, a number of modern wide-angle seismic refraction lines have been

acquired coincident with older reflection profiles (e.g. Louden and Chian 1999; Funck et al. 2004; Wu et al. 2006). The velocities from ocean bottom seismometers (OBS) data are defined by the refracted rays of individual layers and therefore, are better estimations of interval velocities for deep crustal structures, compared to those derived from short streamer MCS data.

To improve the seismic images across the slope diapiric province and the faulted basement blocks, which were previously derived from post-stack migration, pre-stack time migration techniques are used to reprocess short sections of the LITHOPROBE profile 88-1A (Figure 3.1; Keen et al. 1991b) over the central Nova Scotia slope. Section S crosses the diapiric slope region, and section F is located at the seaward end of 88-1A, which is characterized by a series of basement fault blocks (Figure 3.2). Pre-stack time migration of common-offset migration and equivalent offset migration (EOM) were adopted for migration. The medium velocities constrained by the coincident OBS data and that converted from stacking velocity were utilized for migration and time-to-depth conversion. Finally, to illustrate the improved depth images and correlate them with regional observations, the results of pre-stack time migration are compared to the pre-stack depth migrated sections of NovaSpan Project profiles 1600 and 5100 (Figure 3.1) in the adjacent region.

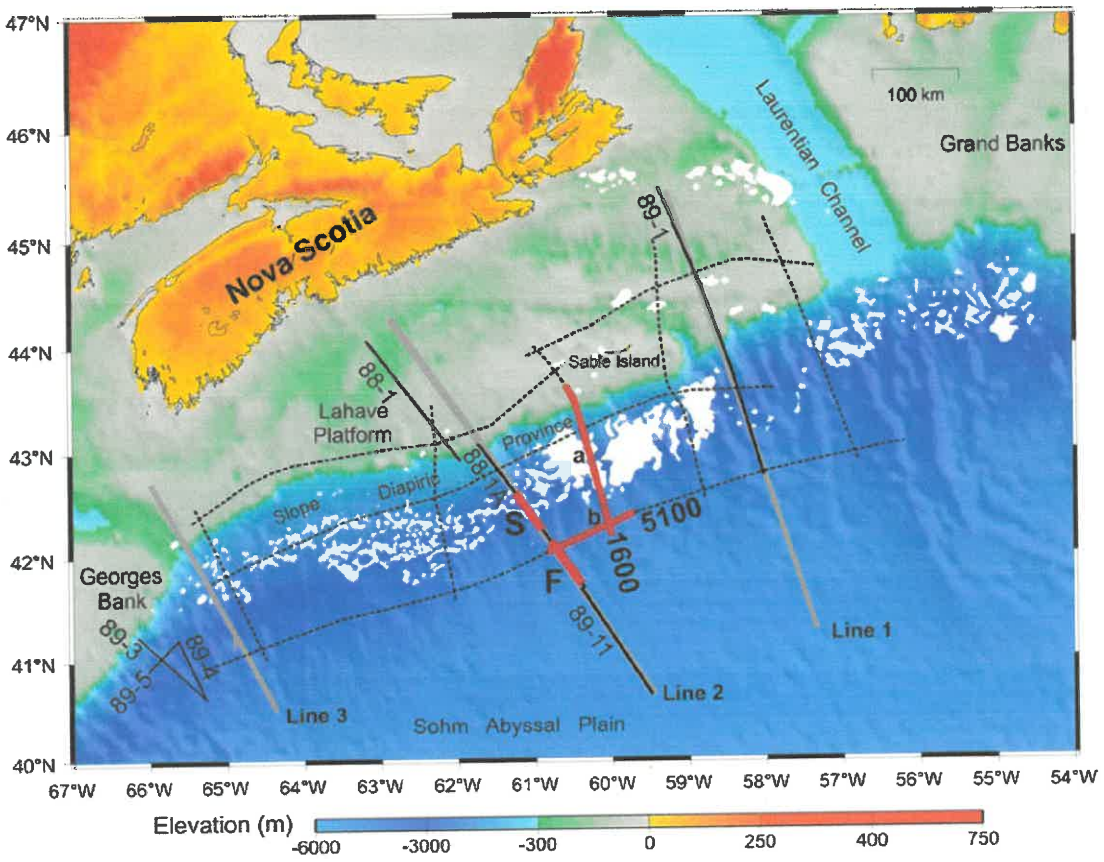

Figure 3.1. Location map of seismic lines. Relevant multi-channel seismic (MCS) reflection lines in the study area are shown as solid black lines: lines 88-1, 1A (Keen *et al.* 1991b), line 89-1 (Keen and Potter 1995b), lines 89-3, 4, 5 (Keen and Potter 1995a), BGR line 89-11 (unpublished data by the German Federal Agency of Natural Resources and Geosciences). The seismic refraction lines (Lines 1-3) are marked by grey lines (Funck et al. 2004; Wu et al. 2006). The red lines are sections presented in this paper: S crosses the slope diapric province; F crosses the fault basement blocks at the seaward end of 88-1A; and 5100 and 1600 are two profiles of the NovaSpan project (dashed lines; data courtesy GX Technology Corporation). The highlighted (red) sections, including a short section along 5100 and two short sections a and b along NovaSpan profile 1600, are shown in Figures 3.10 and 3.12, respectively. The white patches indicate the location of the Jurassic salt over the Slope Diapiric Province (Shimeld 2004).

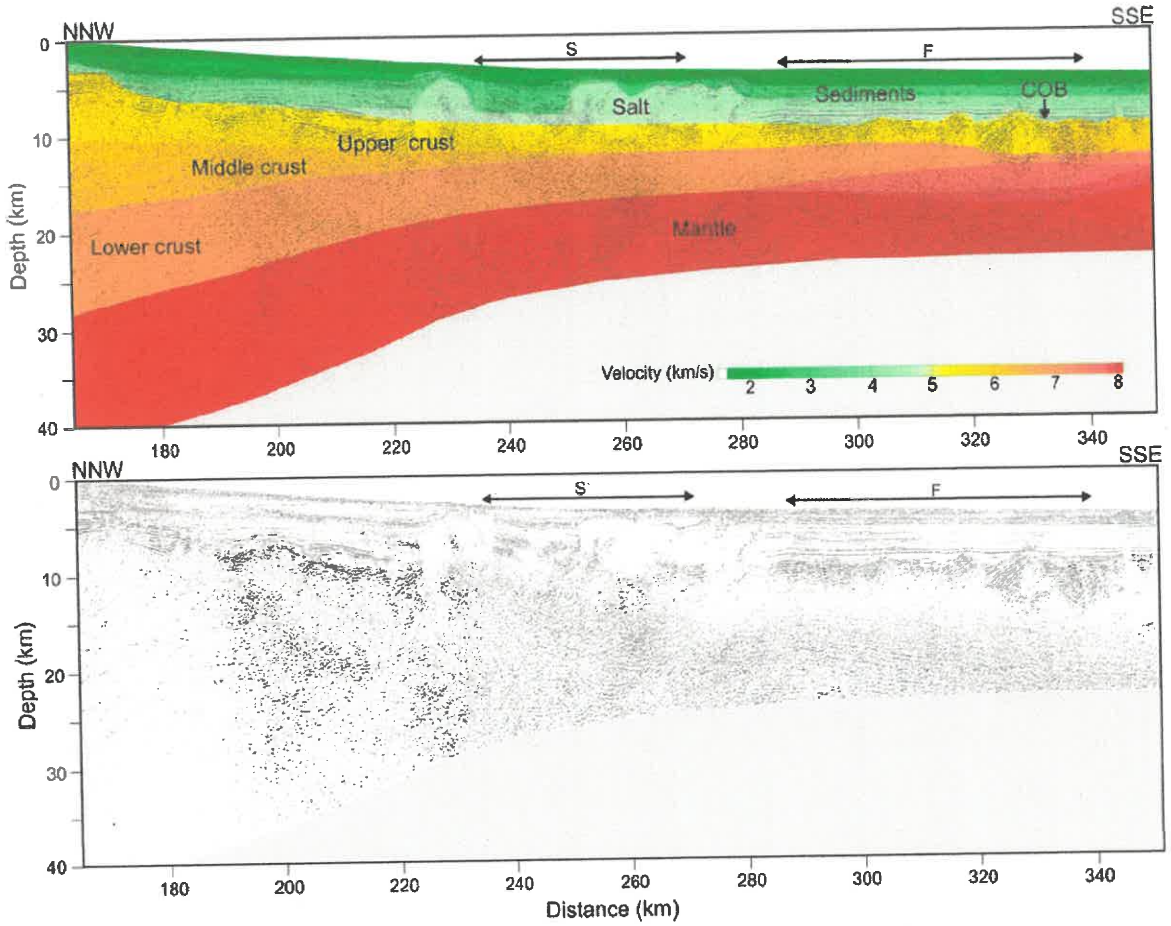

Figure 3.2. (Top) Depth section of LITHOPROBE line 88-1A converted from the time section (Keen *et al.* 1991b) using the velocity model (shown in colors) constrained by coincident OBS data (after Wu et al. 2006). (Bottom) the same depth section of line 88-1A without covered by velocity model. The horizontal scale is the distance along the velocity model. Sections S and F are reprocessed in this chapter. COB: continent-ocean boundary. The velocity scale is shown in the lower part of the seismic section.

3.2 Reflection Seismic Data

Two seismic reflection data sets are presented in this study. Sections S and F are short portions of LITHOPROBE profile 88-1A (Keen et al. 1991b). The seismic data were acquired by Western Geophysical Limited in 1988. A tuned airgun array was used for the source, with a total volume of 133 liters. The shot spacing is 80 m with a near offset of 250 m. A 4800-m-long streamer was used with 180 receiver groups, resulting in group interval of 26.67 m and 30-fold CMP gathers. The raw shot data seaward of the section S were missing and therefore there is a gap between sections S and F (Figure 3.1).

Two NovaSpan Project profiles, 5100 and 1600, are presented for comparison. The NovaSpan profiles were acquired by GX Technology Corporation in 2003. The source is a tuned airgun array with a volume of 70 liters. The shooting interval is 50 m with a 180 m near offset. The streamer is 9000 m long, which is much longer than that of line 88-1A. The number of receiver groups is 360 and the group interval is 25 m. The CMP fold is 90, compared to 30 for the LITHOPROBE data. NovaSpan project profile 1600 is a dip section northeast of section F, while NovaSpan project profile 5100 is a strike line that intersects sections F and NovaSpan project profile 1600.

3.3 Methodologies

3.3.1 Pre-Stack Time Migration

The velocity model constrained by OBS data (see Chapter 2) indicates significant lateral velocity variations across the continental slope and rise. In principle, the existence of strong lateral velocity variations requires pre-stack depth migration. However, pre-stack depth migration routines were not available in the processing software Claritas. In

addition, the coincident OBS data have provided additional velocity constraints that are determined independently by larger offset refraction phases within individual subsurface strata and are often constrained by multiple adjacent OBS instruments. The velocity field is more accurate (demonstrated in section 3.3.2) for the deep structures, compared to that converted from stacking velocities, and therefore is able to increase depth control even when time migration routines are used. The depth control of this technique is proven to approach to that of pre-stack depth migration (see section 3.3.3). Therefore, a practical alternative to a full pre-stack depth migration is to apply pre-stack time migrations followed by a depth conversion.

Two pre-stack time migration techniques—common-offset migration and EOM were applied to the reflection seismic data. Common-offset migration is a conventional migration technique that reformats pre-stack seismic data into common offset gathers and uses them to perform velocity analysis and stacking based on the hyperbolic moveout assumption. This technique can yield a good representation of the subsurface structure by transforming the non-zero-offset CMP data into zero-offset sections that can be migrated by conventional zero-offset migration algorithms, such as finite difference migration (Claerbout 1985). As a result, reflections will be moved spatially closer to the real reflectors, compared to their unmigrated positions.

EOM is an adaptation of the Kirchhoff pre-stack migration (Schneider, 1978), which focuses diffraction energy for all subsurface scatterpoints in an earth model and locates it to the scattering positions. This method rewrites the double-square root traveltime

equation to a single square root format (Bancroft et al. 1998). For a given subsurface scatterpoint, the EOM method computes the equivalent offsets for all samples within an arbitrary migration aperture and maps them onto an equivalent offset plane, called common scatter point (CSP) gather. A CSP gather collects all scattered energy for an output location into a 2D array, where migration can be completed by a conventional normal hyperbolic moveout correction (Bancroft and Geiger, 1994; Bancroft et al., 1995).

In principle, EOM is based on the migration of diffracted energy from individual scatterers rather than reflected energy from reflectors. Thus, steeply dipping events can be imaged since a reflector is treated as a group of individual scatterers (Bancroft et al. 1998). This is an advantage for EOM, compared to the conventional common-offset migration. However, EOM may lose part of the high frequency components when many traces or samples on the CMP plane are binned and averaged within each bin size of the CSP gather (see Appendix C) and therefore, may impair the overall resolution (see section 3.4.2). Common-offset migration and EOM were utilized to reprocess previous seismic reflection data that had limited acquisition spread and were originally processed by post-stack migration. Two methods were adopted so as to demonstrate the potentially different images due to using different migration techniques. Detailed processing is described in Appendices C and D.

3.3.2 Velocities in Migration and Depth Conversion

Both migration and time-to-depth conversion require accurate interval velocities of the medium. Figure 3.3 compares the velocities derived from stacking MCS data and coincident OBS data along section F (Figure 3.1). Although the stacking velocities

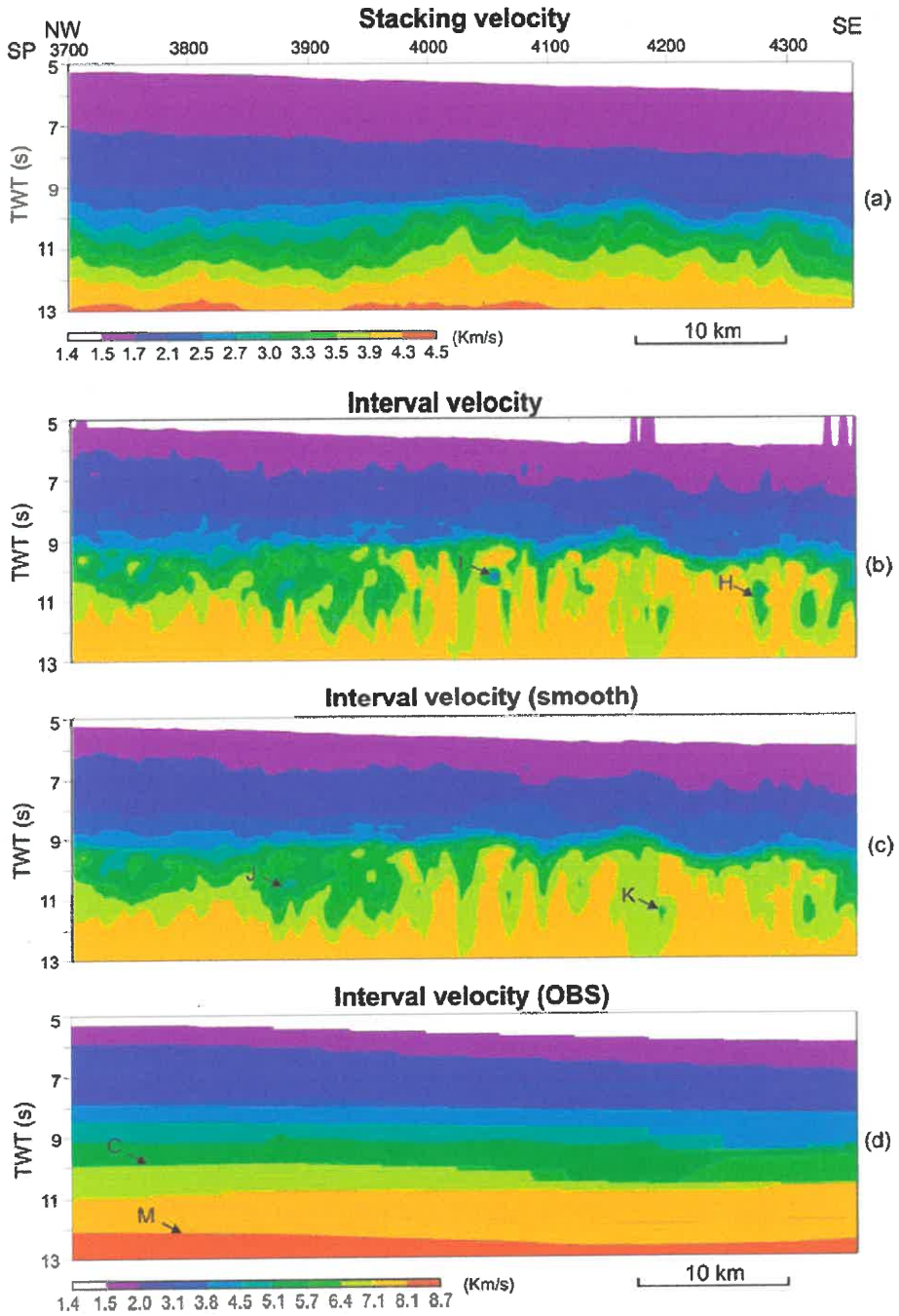

Figure 3.3. Various types of velocities determined from seismic data analyses. (a) Stacking velocities with the velocity scale beneath. (b) Interval velocities converted from stacking velocity (a) using the Dix equation (Sheriff and Geldart, 1995). (c) The smoothed interval velocity model of (b). Marked features in sections (b) and (c) indicate velocity inversions. (d) The velocity model constrained by the coincident OBS data (Wu et al. 2006). The velocity scale for interval velocities (b), (c) and (d) is shown at the bottom. Marked features I, H, J, K, C and M are discussed in text.

(Figure 3.3a) obtained from the conventional NMO correction can be converted to the interval velocities through the Dix equation (e.g. Sheriff and Geldart, 1995), the converted interval velocity field is often irregular (Figure 3.3b) and must be smoothed (Figure 3.3c). Unrealistic medium velocities, including inversions (e.g. H and I in Figure 3.3b, J and K in Figure 3.3c), may result from the conversion. The medium velocity based on modeling of coincident OBS data (Figure 3.3d) shows that the velocities at 5-8 seconds (TWT) are virtually the same as those in Figure 3.3c. However, the velocity at > 8 seconds (TWT) in Figure 3.3d (e.g. C and M) is higher and smoother than that in Figure 3.3c. The velocity uncertainties in Figure 3.3c are produced due to increasingly smaller moveouts or the lack of distinct reflections at large depths, which is particularly true for older seismic reflection data with short acquisition arrays. The velocities in Figure 3.3d are determined by larger offset refraction phases, which are equivalent to a much longer streamer array in MCS data acquisition; therefore, the velocity field constrained by OBS data is more accurate for the deep structures.

The impact of velocity on migration is demonstrated in Figure 3.4. The seismic data across the faulted basement blocks are migrated using the interval velocities in Figures 3.3c and 3.3d as migration velocity, and the time sections after migration are shown in Figures 3.4a and 3.4b, respectively. In Figure 3.4, the faulted blocks show noticeable differences in the dip angles of landward dipping reflectors (e.g. R1 and R2) and the overall shape of the fault blocks (e.g. around SP 4200). In addition, the basement velocities are high (e.g. 5.5-8.1 km/s) and, therefore, a small variation in time domain represents a large variation in depth. This is demonstrated in the depth sections in Figure

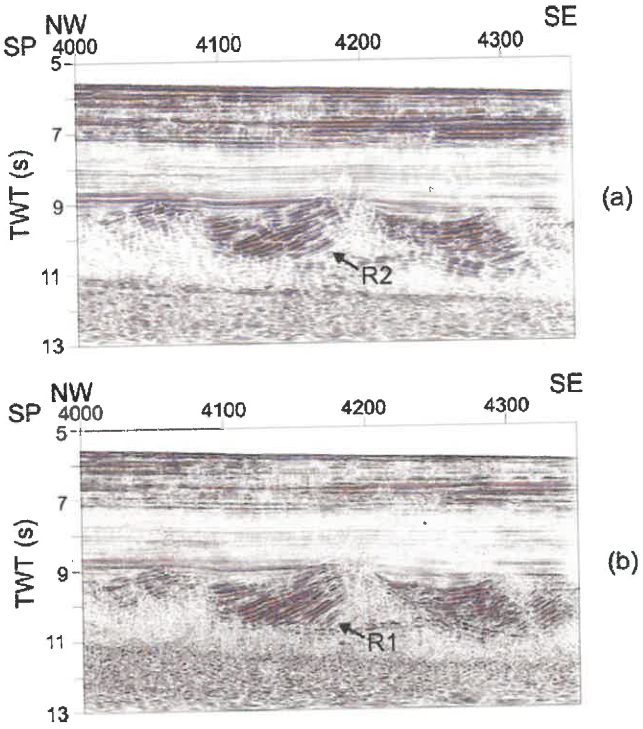

Figure 3.4. Comparison of time sections using the different sources of velocity for migration: (a) using the smoothed interval velocity (Figure 3.3c) converted from stacking velocity, (b) using the velocity model constrained by coincident OBS data (Figure 3.3d). Features marked by letters (R1 and R2) are discussed in text.

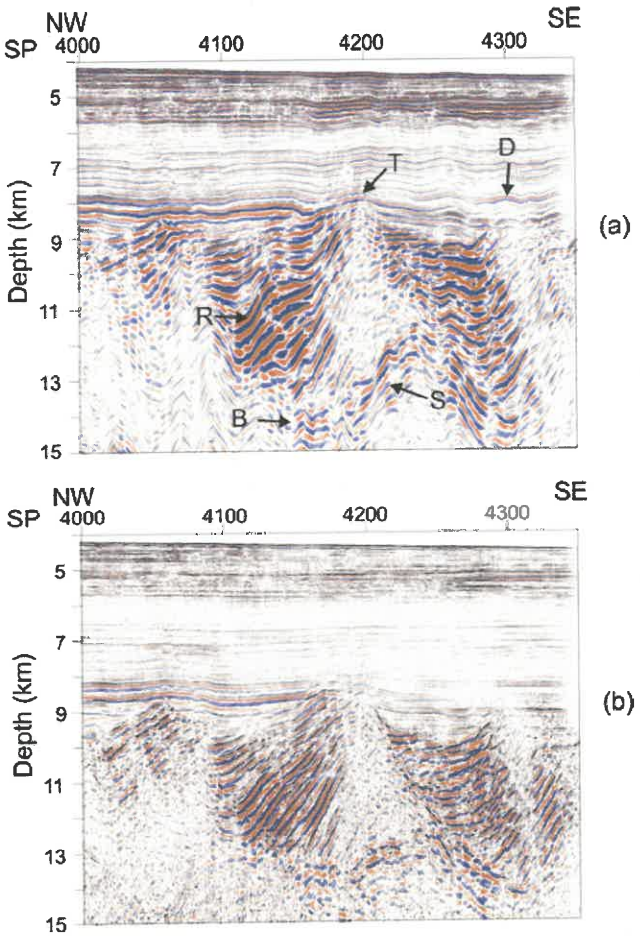

Figure 3.5. Comparison of depth sections using different sources of velocity for depth conversion: (a) using the smoothed interval velocity (Figure 3.3c) converted from stacking velocity, (b) using the velocity model constrained by coincident OBS data (Figure 3.3d). Features marked by letters are discussed in text.

3.5, which are converted from Figures 3.4a and 3.4b using the velocities in Figures 3.3c and 3.3d, respectively.

In Figure 3.5a, weak distortions are noticeable within the sediments (e.g. D), while major distortions are prominent in the basement (e.g. R) and subbasement image (e.g. S), which are not visible in Figure 3.5b. The depths of some major features, for instance, the top and bottom boundaries of the large basement fault block (T and B, Figure 3.5a), and its overall shape also have been distorted. The distortion is obviously caused by the irregular velocity contours shown in Figure 3.3c. The result indicates that the medium velocity constrained by coincident OBS data, if available, is appropriate for migration and depth conversion. The interval velocity field converted from stacking velocity might be suitable for pre-stack time migration in terms of the relatively less prominent distortion in time domain, but it needs to be highly smoothed before being used for depth conversion and the velocities may still be inaccurate for deep structures.

3.3.3 Depth Control of Pre-Stack Time Migration and Depth Conversion

To assess the capability of depth imaging of pre-stack time migration followed by depth conversion, Figure 3.6 compares the depths of sedimentary layers at the crosspoint of section F and NovaSpan profile 5100 (Figure 3.1). Figure 3.6a is derived from pre-stack time migration and converted to depth using the velocity field constrained by OBS data. Figure 3.6b is derived by pre-stack depth migration using the velocity constrained by modern seismic data with 9 km offset (data courtesy GX Technology Corporation). The shallow sedimentary layers A, B and C in Figure 3.6a are at the same depths as the

sedimentary layers A, B and C in Figure 3.6b (within 100 m). Slight difference occurs at depth D (*ca.* 100 m) and the depth discrepancy increases to ~200-300 m at layers E and F. The total thickness of sediments or the depth of basement agrees to within 200 m (G, Figure 3.6).

The depth discrepancy for lower sedimentary layers E and F may have multiple causes. Anisotropy due to compaction of clay material may have resulted in different horizontal and vertical velocities. Bartolome et al. (2005) showed that the velocity constrained by OBS data may differ up to ±10 % for the sediment and upper crust, compared to velocities derived from depth focusing. Figure 3.6c indicates, however, that the maximum difference in depth is within 5% and only occurs at the deeper sedimentary layers, while the depth difference for the total sedimentary layers is around 2% (or ~200 m). If the depth discrepancy is attributed to anisotropy, its effect in this case is less than 2%, which is smaller than the result of Bartolome et al. (2005). In addition, the depth discrepancy may result from the OBS velocities that poise large velocity contrasts across layer boundaries (dashed cyan marked by an arrow at depth ~7 km, Figure 3.6d), while the 1D velocity profile used for depth focusing (red curve, Figure 3.6d) is smooth without abrupt velocity boundaries. Furthermore, the depth differences in Figures 3.6a and 3.6b may also reflect the velocity uncertainties generated either by OBS data modeling (e.g. large OBS spacing) or velocity analysis of MCS data (e.g. short streamer length). Therefore, anisotropy may not necessarily be a major issue for the depth discrepancy and no corrections were applied to the velocities constrained by OBS data. To obtain more

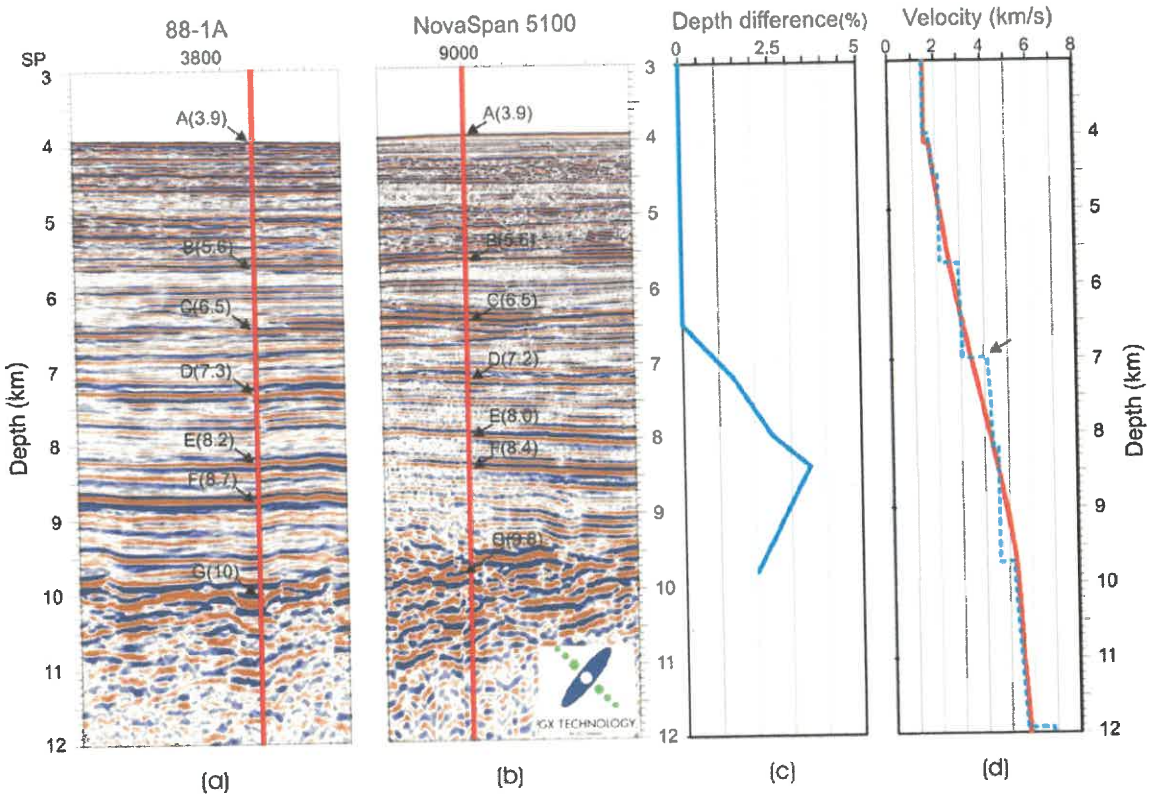

Figure 3.6. Depth comparison at the crosspoint of LITHOPROBE 88-1A (section F) and NovaSpan-5100. Section (a) is a close-up section of 88-1A, which is derived from pre-stack time migration followed by depth conversion, while section (b) is a close-up section of NovaSpan-5100, which is derived from pre-stack depth migration. The crossover locations are marked by vertical bars on each profile. Marked points in sections (a) and (b) are expected to occur at same depths; while the depths in the seismic sections (a) and (b) are denoted in parentheses, respectively. Section (c) shows the depth differences relative to the specific depths in percentage. Section (d) shows the 1D velocity profiles at the crosspoint of LITHOPROBE 88-1A (section F) and NovaSpan Project profile 5100, derived from modeling of OBS data (dashed cyan line, this thesis) and from pre-stack depth migration (red curve, data courtesy GX Technology Corporation), respectively.

accurate depth images, detailed well information and well ties, such as VSP (vertical seismic profiling) and synthetics, are required.

3.4 Reprocessed Images of the Complex Structures Across the Transition Zone

3.4.1 Image over the Slope Salt Structure (Section S)

Section S crosses the slope diapiric province (Figures 3.1 and 3.2). Various depth images of section S are compared in Figure 3.7. Figure 3.7a is the depth image derived from post-stack migration. Figure 3.7b was derived from pre-stack time migration using the velocity model in Figure 3.8a, which was obtained from modeling of OBS data. Compared to Figure 3.7a, the pre-stack time migration algorithm has improved the images of the salt and sub-salt structures and the basement surface beneath the salt.

First of all, the salt boundaries are more distinct and much easier to identify. In the post-stack migrated section, the abrupt termination of subparallel sedimentary sequences suggests that the salt flank is a vertical boundary (A, Figure 3.7a). In Figure 3.7b, however, the seismic image at the same location indicates a clear non-vertical salt flank (P, Figure 3.7b). The images of the top (e.g. T) and base salt (e.g. B) boundaries are also substantially improved, with much stronger reflectivity from surrounding sediments. The salt distribution on the cross section can be easily identified as one or two salt canopies, rather than diapiric structures in the post-stack migrated section. The improved salt images are consistent with the salt structure derived from recent industry seismic data, and demonstrate noticeable improvements compared to results of post-stack migration of recent industry seismic data (Shimeld 2004).

Figure 3.7. Depth images of section S across the slope diapiric province. Section (a) is derived from post-stack migration. Section (b) is derived from pre-stack time migration followed by depth conversion using the velocities constrained by coincident OBS data (shown in Figure 3.8a). Section (c) is derived from pre-stack time migration followed by depth conversion using the velocities converted from stacking velocity (shown in Figure 3.8b). Features marked by letters are discussed in the text. The dashed line indicates the basement surface in the OBS model (see Figure 2.8 in chapter 2). Vertical exaggeration: 1.25.

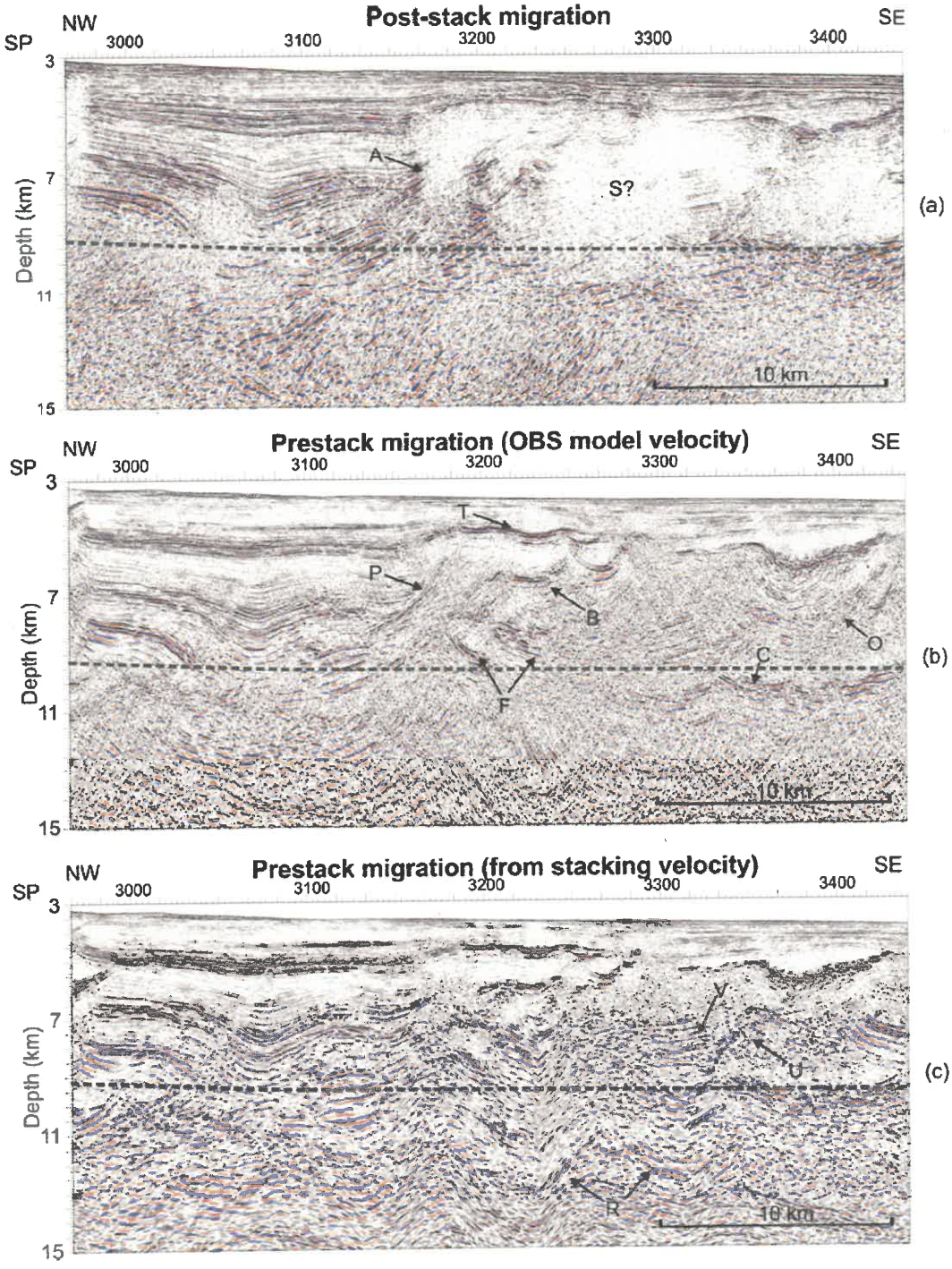
Post-stack migration
NW
SE
SP
3000
3100
3200
3300
3400
3
7
11
15
Depth (km)
A
S?
10 km
(a)
Prestack migration (OBS model velocity)
NW
SE
SP
3000
3100
3200
3300
3400
3
7
11
15
Depth (km)
T
P
B
O
C
F
10 km
(b)
Prestack migration (from stacking velocity)
NW
SE
SP
3000
3100
3200
3300
3400
3
7
11
15
Depth (km)
V
U
R
10 km
(c)

Figure 3.8. Velocity models used for migration and depth conversion in Figure 3.7. (a) Interval velocity derived from modeling of the coincident OBS data (Wu et al. 2006; see Chapter 2). (b) Interval velocity converted from stacking velocity. (c) Comparison of 1D velocity profiles between sections (a) and (b) at distances 245, 255 and 265 km, respectively. The blue curves are extracted from section (a) while red curves from section (b). The velocity scale is shown beneath section (b). Selected interval velocities (km/s) are also displayed in the models for comparison.

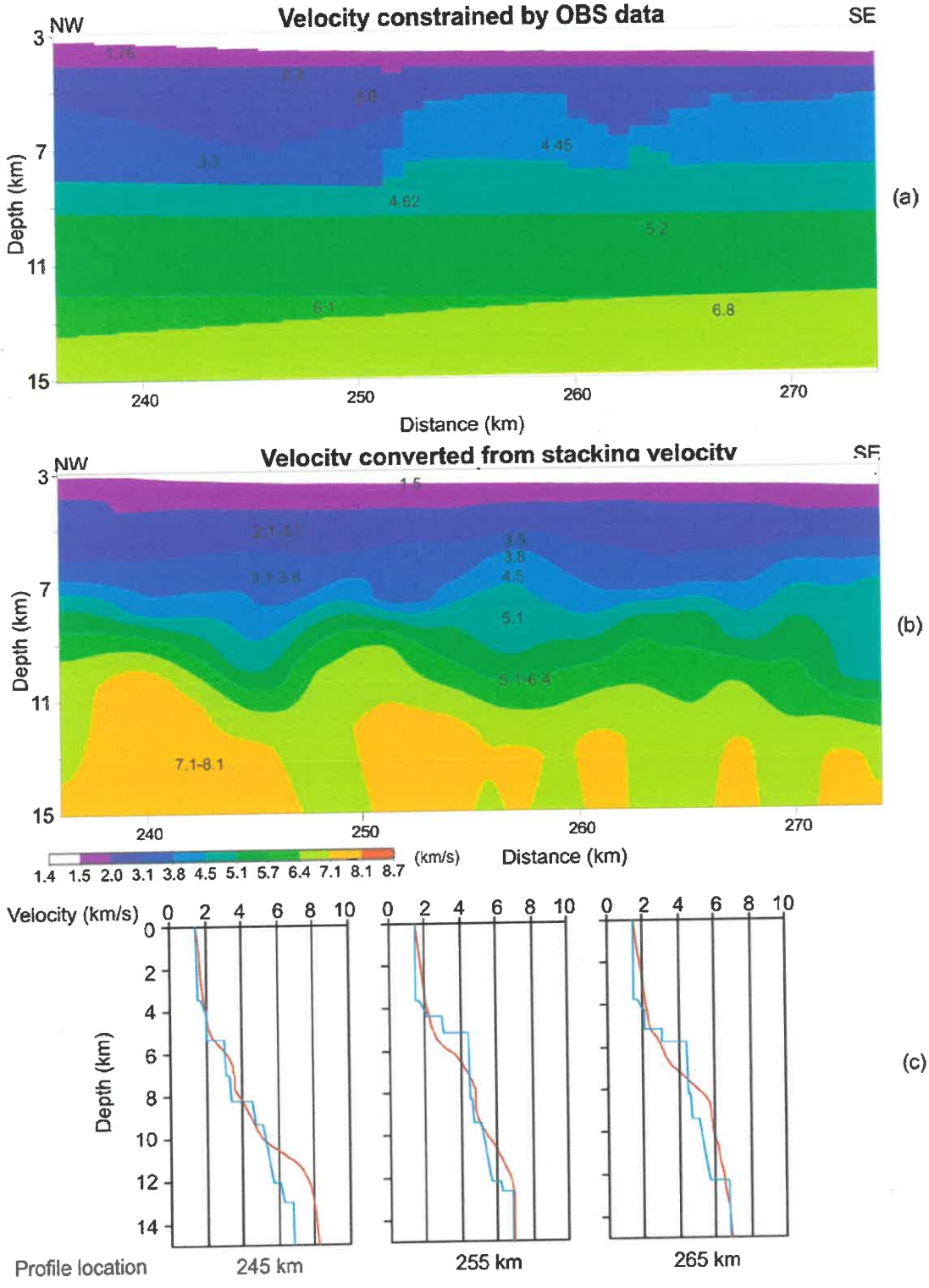
Velocity constrained by OBS data
NW
SE
Depth (km)
Distance (km)
1.76
4.46
4.62
5.2
6.1
6.8
(a)
Velocity converted from stacking velocity
NW
SE
Depth (km)
Distance (km)
1.5
3.5
3.8
4.5
5.1
7.1-8.1
(b)
1.4 1.5 2.0 3.1 3.8 4.5 5.1 5.7 6.4 7.1 8.1 8.7 (km/s)
Velocity (km/s)
Depth (km)
Profile location
245 km
255 km
265 km
(c)

The images of sub-salt structure are also improved. The rotated high-amplitude reflections beneath the salt canopies in the pre-stack migrated section (e.g. F, Figure 3.7b) may indicate autochthonous salt near basement, which might represent feeders of the allochthonous salt canopy. These features are absent in the post-stack migration section (Figure 3.7a). In addition, Figure 3.7a would suggest that most of the non-reflective area (marked by S?) might be identified as a massive salt diapiric body. Figure 3.7b, however, demonstrates that most of the strata beneath the salt structure are not salt or not dominated by salt, although the internal fine structure is still not clearly imaged. The improved image of the salt and sub-salt structure indicates that the velocity model (Figure 3.8b) might be further refined to fit the improved image of the salt canopy in Figure 3.7b. This, in return, may be able to further improve the image of the salt structure. To further improve the image of the salt, iterations of pre-stack migration and refining velocity model are required (see below), which is equivalent to the efforts of a full pre-stack depth migration.

Most importantly, the basement structure also stands out more distinctively, compared to the post-stack section. With the improved images of the salt and sub-salt structures, the basement surface beneath the salt canopy is much better focused (C, Figure 3.7b). The improved basement image shows no evidence for the existence of SDR sequences that may have been masked or blurred by salt units, which is consistent with the interpretation of a non-volcanic margin across the central Nova Scotia margin. However, the depth of basement surface does not exactly match with the basement boundary in the OBS model (dashed line, Figure 3.7b) as it does in Figure 3.7a. This might be caused by the relatively

higher velocity for the overlying sediment during migration, which is suggested by the slight over-migration smiles (e.g. O, Figure 3.7b). The time-to-depth conversion may also have an impact on this due to the abrupt velocity boundary from sediment to basement, similar to the depth discrepancy for the lower sediment (see section 3.3.3, Figure 3.6).

In order to further improve the image for this area, the interval velocity (Figure 3.8b) converted from the stacking velocity was utilized for migration. Figure 3.8b shows a similar 2D velocity model to that in Figure 3.8a, both of which show velocity-contour variations within the sediment due to the irregular geometry of diapiric structure (above 9 km for Figures 3.8a and 3.8b). However, differences between these two models are clear as indicated by their 1D velocity profiles. At distances 255 km and 265 km (depths 6-8 km, Figure 3.8c), the velocities derived from NMO correction (red lines) are ~2 km/s lower than those in the OBS velocity model (blues lines), although the difference may partly result from the discontinuous velocity boundaries derived from OBS data compared to the continuous velocity profiles converted from stacking velocities. The lower velocities are consistent with the pre-stack migrated images (Figure 3.7b), which suggests an absence of salt at this region. At distance 245 km, the 1D continuous velocity profile matches very well with the discontinuous velocity profile, except for the depths > 11 km (left panel, Figure 3.8c) where the stacking velocities are poorly resolved (see Figure 3.8a).

Figure 3.7c is a depth section derived from pre-stack time migration using the velocity model in Figure 3.8b. Figure 3.7c illustrates further improvements for the salt structure

and basement features compared to results described in Figure 3.7b. First, the over-migrated features in Figure 3.7b (e.g. O) are absent in Figure 3.7c and some weak features are better imaged (e.g. U). In addition, the reflections in Figure 3.7c (e.g. V) are almost horizontal while these reflectors in Figure 3.7b indicate larger dip angles. If these reflections represent horizontal sedimentary layers, then the velocity in the vicinity of these features should be less than the typical salt velocities of 4.45 km/s (Shimeld 2004). The improved seismic images also indicate that the sediment here is not salt, or at least not dominated by salt, which is consistent with the reduced velocity field shown Figure 3.8b. Furthermore, the basement surface in Figure 3.7c is consistent with the basement boundary in the OBS model (dashed line). On the other hand, some features are less clear, compared to Figure 3.7b. First, the distinguishable salt flank (e.g. P) in Figure 3.7b is not recognizable in Figure 3.7c. Secondly, the salt canopy in Figure 3.7b is ~0.4 km thicker than that in Figure 3.7c. This is due to the fact that the velocity (4.45km/s) derived from the OBS data is more than 1.0 km/s faster than that converted from stacking velocity at location 255 km (Figure 3.8c). Wells penetrating Argo formation on the shelf and slope (Shimeld 2004) indicate similar salt velocities to the OBS model, suggesting that the thickness of salt in Figure 3.7b is a reasonable estimation. The real thickness, however, may depend on drilling through the salt canopies in this area. In addition, prominent stretching occurs in the subbasement images in Figure 3.7c (e.g. R), which is due to the unconstrained high velocities below about 11 km in Figure 3.8b. This demonstrates again that the velocity for deep structures are better constrained in the OBS velocity model than that derived from NMO correction. Except for these different

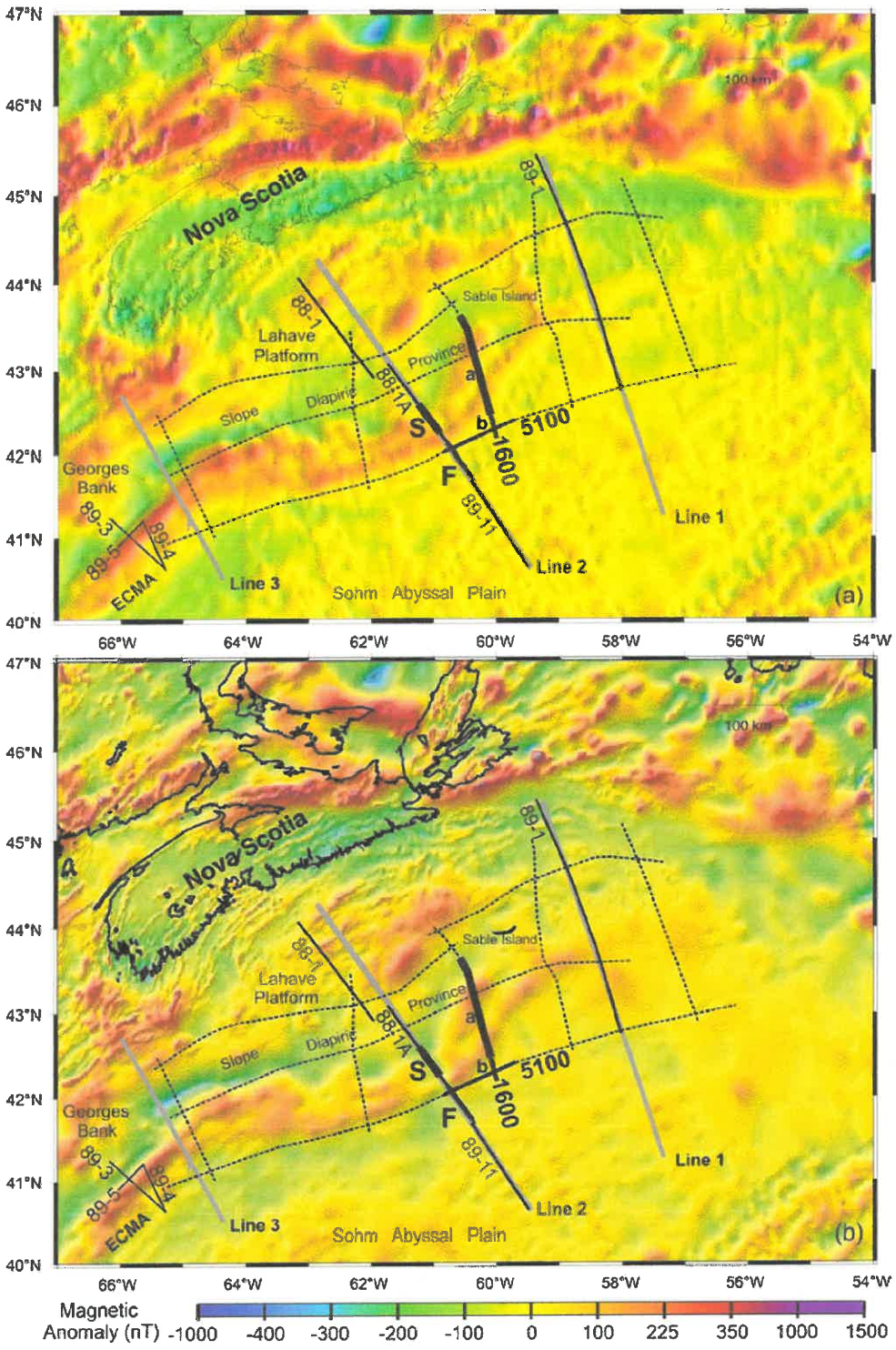

Figure 3.9. Two magnetic anomaly maps offshore Nova Scotia. Map (a) is taken from Verhoef *et al.* (1996) and (b) from Oakey and Dehler (2004). For other features refer to Figure 3.1.

features, the images of salt structure and basement features are similar in Figures 3.7b and 3.7c, both of which show flat basement without SDR sequences in the basement.

The flat basement beneath the diapiric structure is associated with a 50-km-wide major magnetic anomaly in an earlier version of magnetic data (Figure 3.9a; Verhoef et al., 1996). The absence of SDR sequences in reprocessed seismic images would demonstrate that the ECMA in this region is not related with extrusive magmatism in the basement. However, a more recent magnetic map with finer grid of data shows that the ECMA along section S is reduced (Figure 3.9b; Oakey and Dehler, 2004). The amplitude of magnetic anomaly in this later grid appears to be reduced by a constant, suggesting that a different base value might have been applied. However, a direct correlation of the basement features and the ECMA becomes less clear since the magnetic anomaly has been restricted to a narrow region further seaward of this profile (Figure 3.9b). Unfortunately, the raw seismic shot data at that location were missing.

To further verify whether or not there exist SDR sequences that are related to the ECMA in this region, a parallel profile in the adjacent region, NovaSpan 1600 (Figures 3.1 and 3.9), which crosses the salt structure and the ECMA (Figure 3.1), is presented in Figure 3.10. Note that the ECMA is well developed (~220 nT) in both versions of the magnetic anomaly along the NovaSpan profile 1600, with two high-amplitude anomaly peaks (I and II, Figure 3.10). Beneath the major anomaly I, the basement surface identification is problematic from the seismic image. The regional result offshore Nova Scotia indicates that the basement depths at this location are deep (e.g. ~16-19 km; Louden et al., 2004). The weak reflections may suggest the appearance of basement (marked by dashed line).

However, no evidence indicates the existence of SDR sequences in the vicinity of basement boundary. The basement structure beneath anomaly II is better imaged, with unequivocal basement surface seaward of SP 2000. This area is covered by extensive salt canopies, similar to the section S along 88-1A. Again, the basement image does not show any evidence of SDR sequences beneath the magnetic anomaly, although the basement surface landward of SP 2000 is still not well imaged due to the disturbance of overlying salt. These results are consistent with the observations along 88-1A and further confirm that the ECMA in this region is not caused by volcanic extrusives in the basement. Instead, recent magnetic models in this region indicate that these anomalies are produced through inclusion of magnetic (eroded volcanic) material as infill above salt structures and volcanic rock that rafted above salt (Dehler, personal communication).

In addition, Figure 3.10 shows images of the salt flank (e.g. P), the reflective top and base of the salt canopies (e.g. T and B, respectively), the images of subsalt structure (e.g. F), which are similar to those observed in Figure 3.7b. This indicates that pre-stack time migration has achieved results approaching to that of pre-stack depth migration when velocity constrained by coincident OBS data is used. Furthermore, the salt along profile NovaSpan 1600 mobilized ~40-50 km seaward (Figure 3.10), while the salt along 88-1A (Figure 3.7) demonstrates only a few kilometres mobilization. The variant mobilization along section S and NovaSpan 1600 is consistent with the transition of salt subprovince from autochthonous salt to allochthonous salt that takes place along the central margin segment (see Figure 3.13; Shimeld 2004).

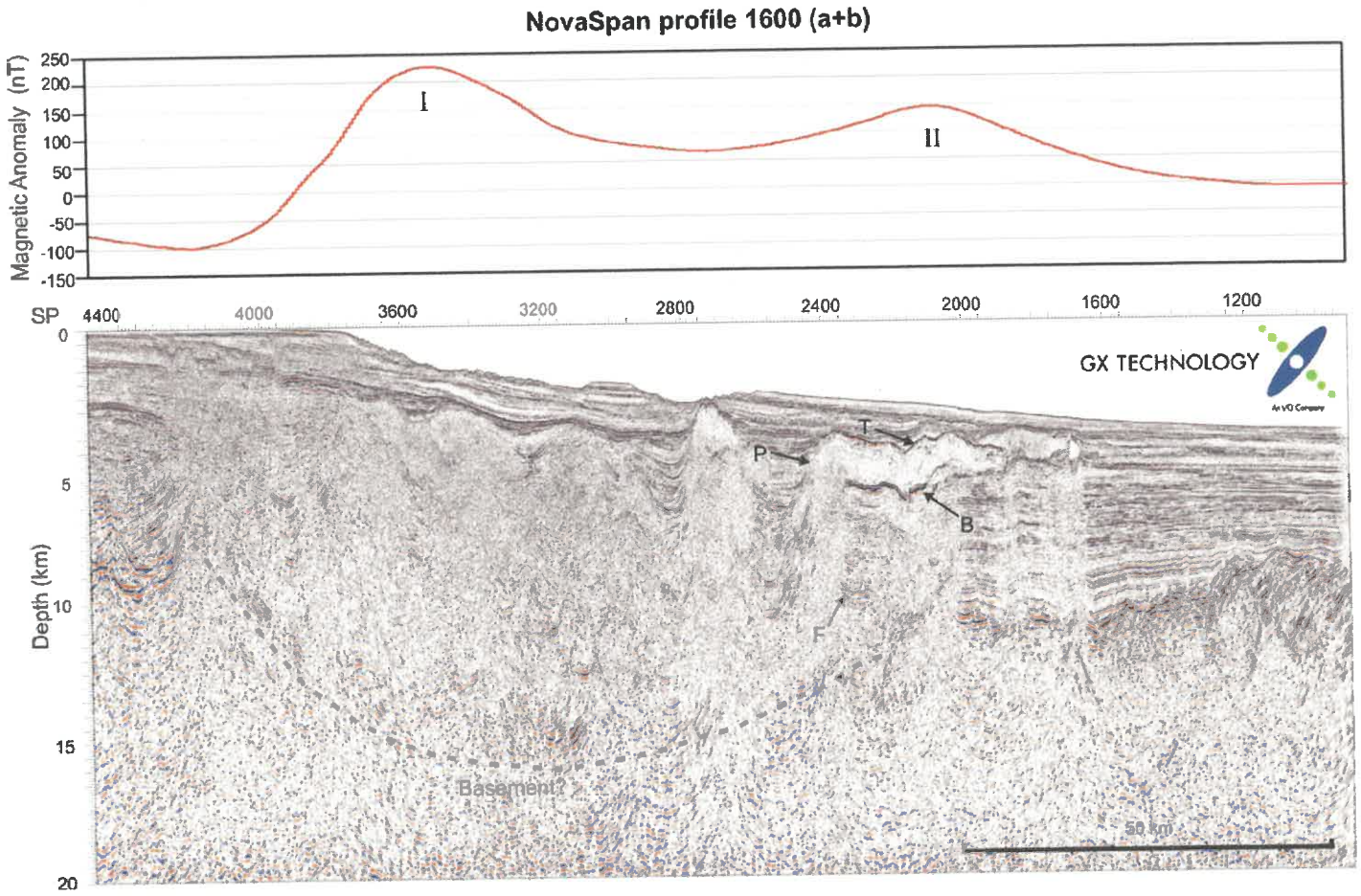

Figure 3.10. A depth section of the NovaSpan profile 1600 (section a at the landward portion of 1600, see Figure 3.1). The data are migrated using pre-stack depth migration. Magnetic anomalies I and II are two positive peaks of ECMA along this profile. Marked features are discussed in the text. Data courtesy of NovaSpan Project, GX Technology Corporation. Dashed line indicates the possible basement surface.

3.4.2 Images of the Highly Faulted Continental Basement (Section F)

Section F is the seaward part of 88-1A (Figure 3.1). Figure 3.11b shows a depth section migrated by EOM, which is converted from time to depth using the velocity model constrained by OBS data (Figure 3.3d). For comparison, the post-stack-migrated section is shown in Figure 3.11a. EOM has improved the images of basement and subbasement structure, compared to the post-stack migrated section, as follows.

Firstly, simplified reflectivity is imaged in the basement. In the pre-stack migrated section, the basement landward of SP 4200 is mostly transparent except for some discontinuous but almost horizontal reflections beneath the basement surface (R1, Figure 3.11b); while the basement seaward of SP 4200 demonstrates strong reflectivity. The difference in reflectivity may reflect the transition of basement character, with continental crust terminating at the major fault block and oceanic basement accreting further seaward. This is consistent with the interpretation based on the coincident OBS data described in the previous chapter. In contrast, the sub-basement in the post-stack migrated section is generally reflective for both continental and oceanic crust, with diffusive reflectivity throughout the basement layer. There are also short coherent landward dipping reflectors imaged within the crust by post-stack migration (R2, Figure 3.11b) that are removed by pre-stack migration. An additional difference between the sections is that the landward dipping reflectors in the post-stack migrated section between SP 4000-4100 (R3, Figure 3.11a) are narrower with reduced dipping angles in the pre-stack migrated section (R4, Figure 3.11b). The wider zone of the landward dipping

reflectors in Figure 3.11a appears to be the remnant energy of undermigrated hyperbolae in the unmigrated section.

In addition, the landward dipping reflectors within the major basement fault block present two different patterns. The dipping reflectors in the post-stack-migrated section (SP 4100-4200, R5 in Figure 3.11a) fans against the major fault plane, while this reflection package can be more clearly divided into two separate phases in the pre-stack migrated section (Figure 3.11b). The reflectors in the upper part still fans out against the fault plane (R6, Figure 3.11b), while the underlying unit is characterized by high-amplitude, sub-parallel reflectors (R7, Figure 3.11b). The different patterns of reflectivity help differentiate the strata in the major fault block. The upper low-amplitude fan-shape reflections gradually flatten upwards, possibly indicating syn-rift sediments deposited at a subsiding half-graben. The lower high-amplitude subparallel reflection package is probable pre-rift material, faulted and rotated during continental rifting. This is consistent with the results derived from OBS modeling in chapter 2 in contrast with previous interpretations that the dipping reflectors are generated by excessive volcanic overflows during drifting (Salisbury and Keen 1993).

Furthermore, the subbasement structure beneath the faulted basement blocks is also improved. The sub-basement beneath the fault blocks in the post-stack migrated section is imaged as a wide band of horizontally smeared reflections (S1, Figure 3.11a). In the pre-stack migrated section, these reflectors are almost horizontal (S2, Figure 3.11b).

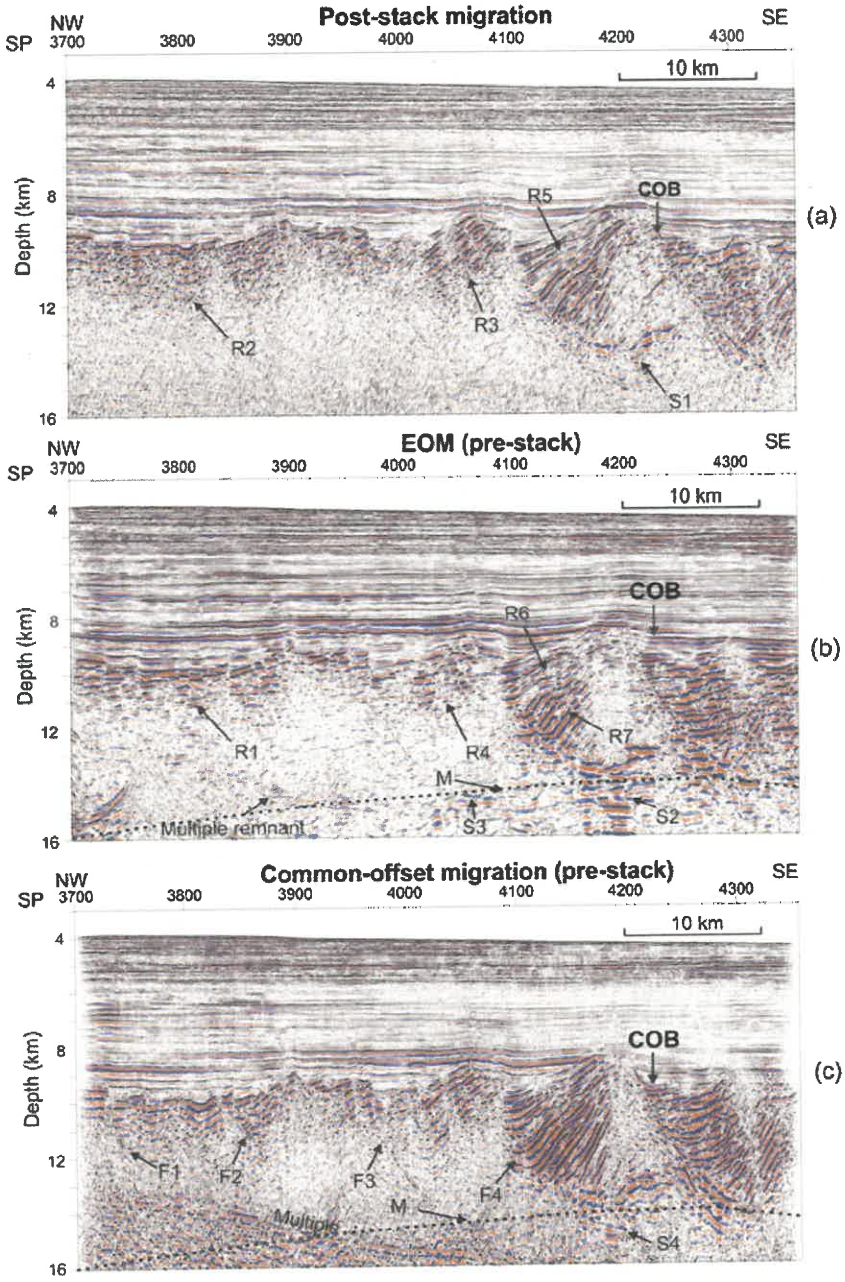

Figure 3.11. Depth sections of the section F at the seaward end of 88-1A. (a) Depth section derived from post-stack finite difference migration. (b) Depth section derived from EOM pre-stack time migration algorithm. (c) Depth section derived from pre-stack time migration on the common-offset plane. Velocity model constrained by wide-angle OBS data (Figure 3.3d) was used in the migration and depth conversion of sections (b) and (c). The continent-ocean boundary (COB) is based on the velocity model constrained by the coincident OBS data. Features marked by letters are discussed in the text. The Moho boundary in the OBS velocity model (see Chapter 2) is denoted as dotted lines in (b) and (c). Vertical exaggeration: 2.

Based on the velocity model constrained by coincident OBS data (Figure 2.8, see Chapter 2), the continent-ocean boundary (COB) is located at the seaward edge of the fault blocks, which is near the seaward termination of the horizontal reflectors. Therefore, they may be related to the last stage of continental rifting and breakup. Weak reflections (S3, Figure 3.11b) appear beneath the fault blocks, extending landward until they are lost within the remnant multiples. These reflections roughly coincide with the Moho boundary in the velocity model (M, Figure 3.11b) and merge into the horizontal reflectors (S2, Figure 3.11b) until they terminate beneath the major fault block. These weak reflections may, therefore, represent the rising Moho boundary before final continental breakup.

An alternative depth section using finite difference migration (Claerbout 1985) on the common-offset plane is shown in Figure 3.11c. The pre-stack time migrated depth section also demonstrates improved basement images but presents different features compared to those in Figure 3.11b. A series of smaller-scale basement faults are imaged landward of the major fault block (e.g. F1-F3 in Figure 3.11c), which are not well imaged by EOM in Figure 3.11b. All these faults, including the major fault (F4, Figure 3.11c), penetrate into the basement with increasing fault throws. This indicates that the last portion of continental crust has been progressively faulted and become increasingly brittle to the southeast, which is consistent with the rheological models within the brittle regime (Pérez-Gussinyé and Reston 2001). These faults are located over a low-velocity mantle layer which is interpreted as partially serpentinized mantle layer in Chapter 2. The faults may allow seawater to penetrate the entire crust and serpentinize the upper mantle,

therefore supporting a model of serpentinized upper mantle beneath the continent-ocean transition zone. In addition, Figure 3.11c demonstrates better horizontal resolution with a sharp basement surface, compared to Figure 3.11b. However, the major structural features, for instance, the fault plane of the major listric fault (F4, Figure 3.11c), are less clear compared to Figure 3.11b. The sub-surface structure beneath the major fault, for example, the wide horizontal band of smearing reflectors (S3, Figure 3.11b) and the possible Moho reflection (M, Figure 3.11c), are also less well focused compared to Figure 3.11b.

Similar basement features described above are also imaged in the adjacent regions. Figures 3.12a and 3.12c illustrate the depth images of two NovaSpan project profiles, 1600 and 5100, across similar faulted basement blocks about 80 km northeast of section F (Figure 3.1). For comparison, the depth image of section F shown in Figure 3.11b is also included (Figure 3.12b). The dip section of NovaSpan 1600 (Figure 3.12c), which is parallel to section F, demonstrates the similar reflectivity pattern of fault and dipping events as described in Figure 3.12b. The thicknesses and horizontal extent of the faulted basement blocks are comparable. The strike profile 5100 (Figure 3.12a) also shows similar images of basement fault blocks to those observed along section F (Figure 3.12b). The horizontal extent of faulted basement blocks along the strike line appears to be elongated, indicating that the basement blocks may be largely two dimensional. These depth images of the fault basement blocks indicate the highly faulted basement blocks are similar in character and may be spatially connected.

Figure 3.12. Depth images of pre-stack time migration and pre-stack depth migration. Section (a) is a depth section of NovaSpan 5100 along the Scotian margin using pre-stack depth migration (data courtesy NovaSpan Project, GX Technology Corporation). Section (b) is a depth section at the seaward end of 88-1A (section F), which is reprocessed by pre-stack time migration using EOM algorithm and converted to depth using velocity model constrained by coincident OBS data. Section (c) is a depth section of NovaSpan 1600 (section b at the seaward portion of 1600, see Figure 3.1). The crossover locations are marked by vertical bars on each profile. The detailed sedimentary depths at the crosspoint of 88-1A and NovaSpan 5100 are compared in Figure 3.6. Vertical exaggeration: 2.

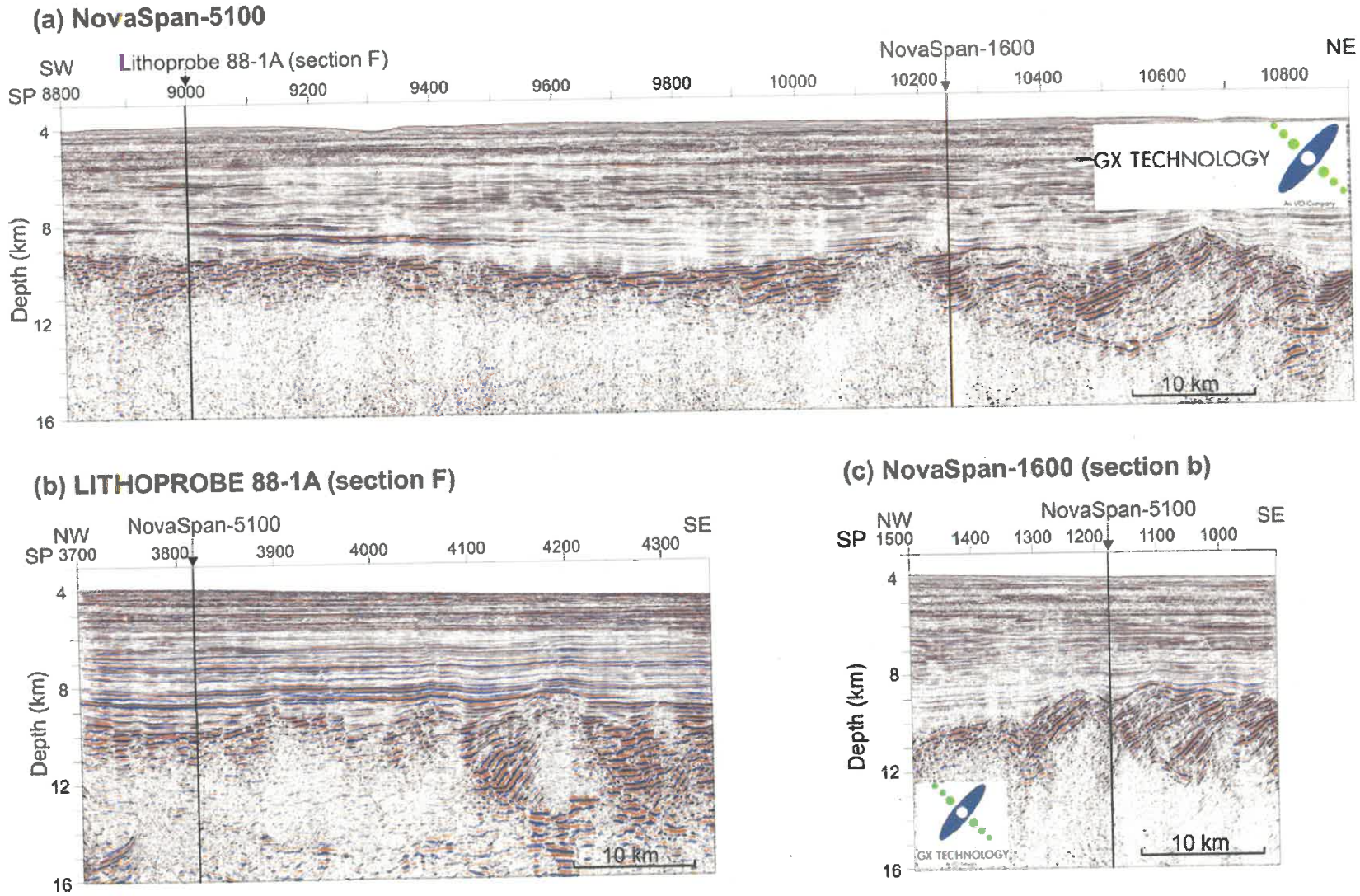
(a) NovaSpan-5100
SW
Lithoprobe 88-1A (section F)
NovaSpan-1600
NE
SP 8800
9000
9200
9400
9600
9800
10000
10200
10400
10600
10800
Depth (km)
4
8
12
16
GX TECHNOLOGY
10 km
(b) LITHOPROBE 88-1A (section F)
NW
NovaSpan-5100
SE
SP 3700
3800
3900
4000
4100
4200
4300
Depth (km)
4
8
12
16
10 km
(c) NovaSpan-1600 (section b)
NW
NovaSpan-5100
SE
SP 1500
1400
1300
1200
1100
1000
Depth (km)
4
8
12
16
GX TECHNOLOGY
10 km

Figure 3.13 shows the possible spatial relationship of the faulted basement bocks. Based on the velocity model in Chapter 2, the COB is located at the seaward edge of the faulted basement blocks (also shown in Figure 3.13 as medium black dashed line). If the faulted basement blocks are spatially connected, they are traced back to the salt structure sited beneath the continental slope. Whether or not these features extend further back to the slope area requires denser seismic lines. More importantly, the faulted basement blocks coincide with a transition of crustal structure along this margin. The velocity model across the central margin segment demonstrates a platformal outer shelf with a few kilometres of sediments (6-8 km) in the deep basin further seaward of the slope area. While across the northern margin segment, a deep basin is developed over the outer shelf with up to 16 km thick sediment fill (Funck et al. 2004). Furthermore, the location of the faulted basement blocks also coincides with the transition of salt subprovince from autochthonous salt to allochthonous salt (thick black dashed line). The slope area from line 88-1A to the south is dominated by autochthonous salt without prominent seaward mobilization. In contrast, the slope area from the NovaSpan 1600 to the north is characterized by allochthonous salt which has migrated seaward up to ~100 km (Figure 3.13; Shimeld 2004). The tilted basement fault blocks may represent a transfer zone in the vicinity of the central Nova Scotia margin, where the margin changes its rifting character from the south to the north. A thorough understanding of the coincidence of these features requires comparison with observations on the conjugate Morocco margin.

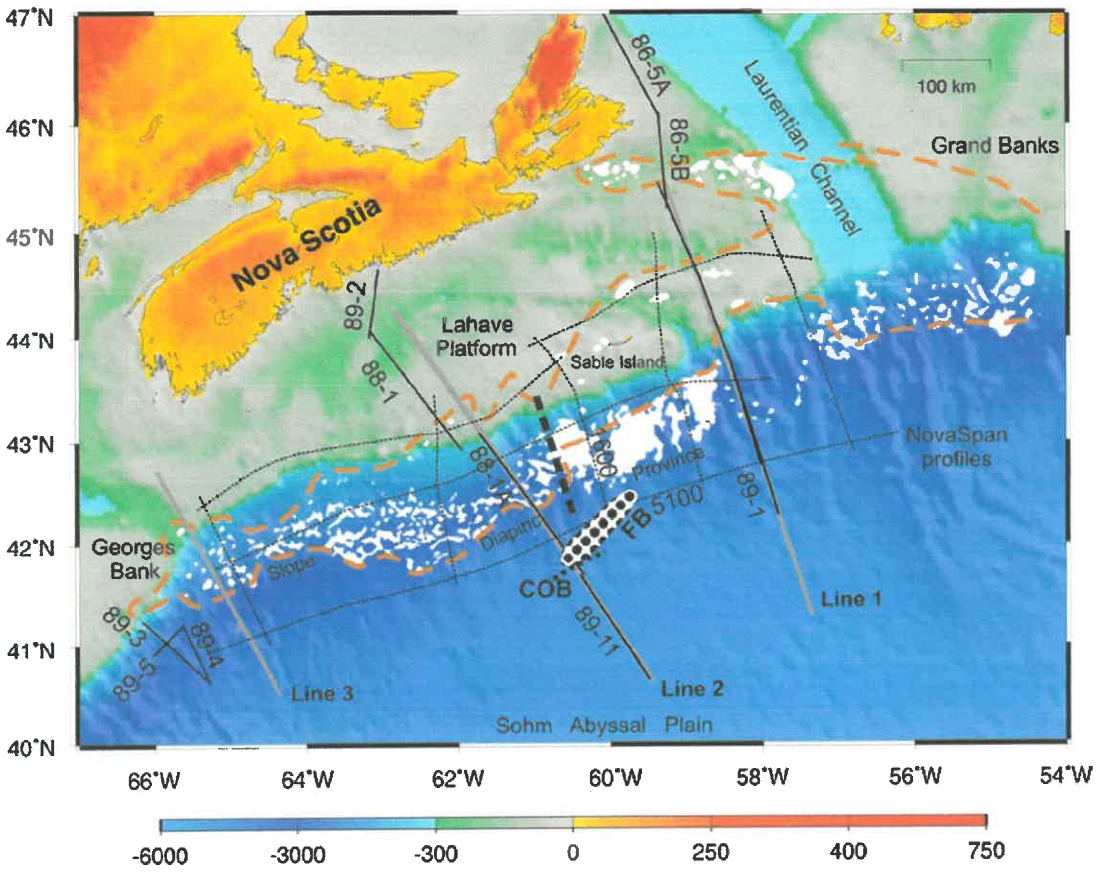

Figure 3.13. Location of the faulted basement blocks (FB) and correlation with other features across the central Nova Scotia margin. The distribution of the FB along 88-1A and NovaSpan lines are denoted as a doted area. The white patches indicate the current location of the Jurassic salt, while the orange-dashed line denotes the autochthonous salt boundary over the Slope Diapiric Province, with a transition (thick black dashed line) from autochthonous salt to allochthonous salt between 88-1A and NovaSpan 1600. COB: continent-ocean boundary. For other features refer to Figure 3.1.

3.5 Conclusions

To improve the structural images over the central Scotian slope, we applied pre-stack time migration to two sections of previous MCS profiles using common-offset migration and EOM techniques. Pre-stack time migration of the older seismic data enhanced the images of sediment and crust over the slope, compared to previous images derived from post-stack migration. Across the salt dirpiric province (section S), the images of salt structure demonstrate distinct boundaries from non-salt sediments. The improved sub-salt image indicates that the massive diapiric structure in the post-stack migrated section consists of salt canopies in the upper part and non-salt sediments beneath the salt canopies. The improved image of section S and the depth image of NovaSpan 1600 in the adjacent region do not indicate the presence of SDR sequences underneath the diapiric structure. Therefore, the ECMA in this region is not related with volcanic extrusives in the basement, supporting the interpretation of a non-volcanic margin based on coincident OBS data.

Across the faulted basement blocks (section F), the newly processed section shows different reflectivity across the continent-ocean boundary. The dipping reflectors within the major fault demonstrate two reflectivity patterns, suggesting syn-rift sediments in the upper part and pre-rift material underneath. NovaSpan profiles 5100 and 1600 also illustrate similar faulted basement in the adjacent regions. The appearance of the faulted basement blocks coincides with the transition from autochthonous salt to allochthonous salt and the transition of two types of crustal structures from the central Nova Scotia margin to the northern margin segment. These features may indicate a character change

of rifting of the North Atlantic margin system across the central margin segment. A better understanding of the character of the Nova Scotia margin may require further comparison of these features with observations on the Morocco margin conjugate.

CHAPTER 4

RECONSTRUCTION OF THE NOVA SCOTIA AND MOROCCO MARGINS

Early reconstructions of the relative positions of the Nova Scotia and Morocco margin conjugates were based on geometric fits of coastlines, isobaths, seafloor spreading magnetic lineations/fracture zones, or paleomagnetic data (e.g. Bullard et al. 1965; LePichon et al. 1977; Lefort and van der Voo 1981). More recently, the slope magnetic anomalies and the relative locations of salt basins on the opposite sides were also used to match the conjugates (e.g. Klitgord and Schouten 1986; Sahabi et al. 2004). In addition, Tari and Molnar (2005) proposed a reconstruction of this margin pair by correlating the syn-rift structure based on recent seismic reflection and gravity data. Relevant plate reconstruction poles of the conjugates are listed in Table 4.1.

With the recent seismic data from the margin conjugates, the crustal structure now is better defined by detailed velocity structures. In Chapter 2, the velocity model, as well as the characteristic reflection seismic images, indicates that the continent-ocean boundary (COB) is located at the seaward edge of a series of faulted basement blocks (FB), which is ~50 km seaward of its previous interpretation (Salisbury and Keen 1993). Prestack migration of the coincident MCS data (see Chapter 3) also shows that the basement changes its reflectivity pattern across the COB and therefore further supports the interpretation of the velocity model. These enhanced seismic images and the most recent industry profiles (e.g. NovaSpan Project lines) across the central Nova Scotia margin demonstrate that seaward dipping reflectors (SDR) are not imaged in the basement

beneath the low-amplitude East Coast Magnetic Anomaly (ECMA). The combined results of MCS data and OBS data indicate that the ECMA in this region is not caused by excessive volcanism at the COB and therefore cast doubt about the feasibility of using this anomaly to reconstruct the conjugates.

Table 4.1 Plate reconstruction poles of the NW African plate (Morocco) relative to the North American plate.

Closure	Age (Ma)**	Latitude	Longitude	Angle of rotation	Reference*
M25	156	66.7°	-15.85°	-64.9°	[1]
Minimum	175	66.97°	-12.34°	-74.57°	[2]
	195	64.31°	-15.19°	-77.09° (south)	[3]
		66.31°	-11.78°	-72.59° (north)	
	N/A	66.92°	-12.45°	-74.42°	[4]
	N/A	66.92°	-12.45°	-74.42°	[5]
	167	64.31°	-15.19°	-77.09°	This thesis
Maximum	175	66.95°	-12.02°	-75.55°	[2]
	N/A	67.6°	-14.0°	-74.8°	[6]
	N/A	66.95°	-13.35°	-76.74°	[7]
	176	64.31°	-15.19°	-80.58°	This thesis

* [1] Tucholke and Ludwig (1982), [2] Klitgord and Schouten (1986), [3] Sahabi et al. (2004), [4] Tari and Molnar (2005), [5] LePichon et al. (1977), [6] Bullard et al. (1965), [7] Lefort and van der Voo (1981).

** The ages for this thesis are calculated from chron M25 (155.7 Ma; Gradstein et al. 2004) using a spreading rate of 1.9 cm/y (Klitgord and Scouten 1986). The ages for the remaining minimum or maximum closures come from the original references [2] and [3].

The conjugate reconstructions are examined based on the new seismic processing results. This chapter begins with the reconstruction at chron M25. The conjugates are further reconstructed to pre-seafloor-spreading time based on the detailed velocity models derived from recent OBS data and the correlation with seismic reflection images, slope magnetic anomalies and salt distributions from both conjugates. The goal is to understand the development of the transitional margin from volcanic and non-volcanic character across Nova Scotia and Morocco.

4.1 Reconstruction to Chron M25

Figure 4.1 shows the reconstruction of the Nova Scotia and Morocco margin conjugates at chron M25 (Tucholke and Ludwig, 1982; Table 4.1). Magnetic anomaly M25 (155.7 Ma; Gradstein et al. 2004) is the earliest seafloor spreading magnetic anomaly that can be correlated on both sides of the conjugate margins (Klitgord and Schouten 1986; Verhoef et al. 1991). From anomaly M25 to the coasts of Nova Scotia and Morocco, until the appearance of the slope magnetic anomalies, the seafloor is characterized by weak magnetic anomalies created during the Jurassic magnetic quiet zone (JMQZ; Vogt, 1973). Within the JMQZ, some of these weak reversal sequences were later identified as seafloor spreading magnetic anomalies prior to chron M25 along both conjugate margins (e.g. Barrett and Keen 1976; Roeser et al. 2002). However, these magnetic lineations are not continuous along the margin and can not be correlated unambiguously with each other. Therefore, ages and seafloor spreading rates older than M25 can not be determined from seafloor spreading magnetic lineations.

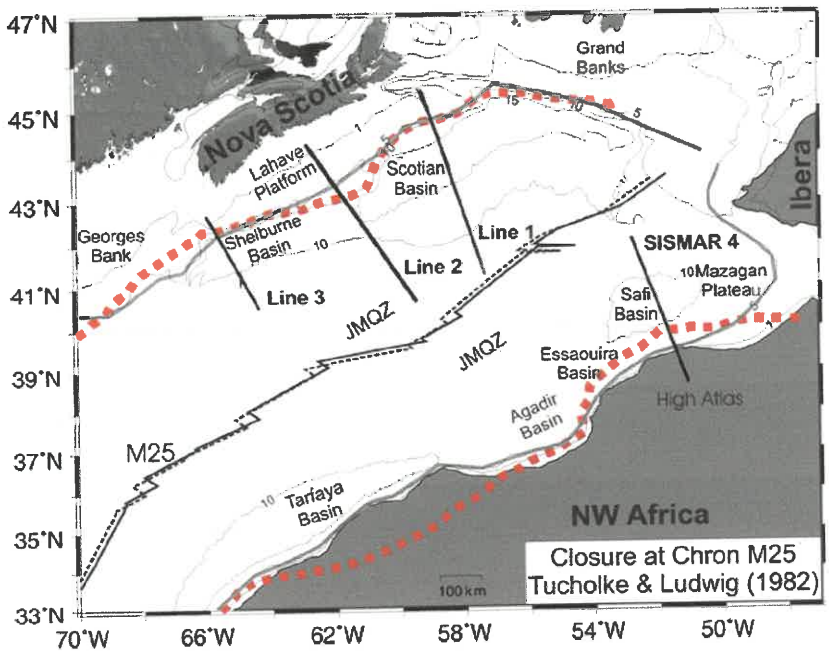

Figure 4.1. Plate reconstruction of the NW African continent relative to the North American plate at chron M25 (Tucholke and Ludwig, 1982). The matched magnetic anomaly M25 (155.7 Ma; Gradstein et al. 2004) is denoted as a pair of solid (Moroccan side) and broken (Scotian side) lines. The thick lines are the most recent OBS profiles, including SMART Lines 1, 2 and 3 from the Nova Scotia side (Dehler et al. 2003; Funck et al., 2004; Wu et al., 2006), and SISMAR 4 from Morocco side (Contrucci et al. 2004). The contours are the depths to basement in km. The basement depth off Nova Scotia is taken from Oakey and Start (1995). The basement depth off Morocco is calculated from the bathymetry data (National Geophysical Data Center, 1988) and the total sediment thickness data (Divins 2007). Positions of hinge zones shown in red are taken from Tari and Molnar (2005). The 5-km depth-to-basement contours (grey lines) are adopted to represent the relative location of the conjugates for further reconstruction. JMQZ: Jurassic magnetic quiet zone.

Figure 4.1 also shows the basement depths on both flanks of M25. The basement depth off Nova Scotia is taken from Oakey and Start (1995). The basement depth off Morocco is calculated from the bathymetry (National Geophysical Data Center, 1988) and the total sediment thickness (Divins 2007). According to this figure, the basement off Nova Scotia, particularly off Cape Breton Island, is ~5 km deeper than that around the Safi Basin off Morocco. The deep basement of the Scotian Basin may due to thick (~16 km) sediment loading, which is ~10 km thicker than the sediment fill off Morocco. The shallower basement off Morocco may have been affected by the Atlas compression in the northern region (Beauchamp et al., 1999). The wide-spread hotspot activity on the Morocco side may also have elevated the basement (Louden et al. 1989; Holik et al. 1991).

On the other hand, the basement off Nova Scotia demonstrates a gradual deepening in contrast to the basement off Morocco, which dramatically deepens offshore with dense depth-to-basement contours closely following the coastline. This indicates an asymmetry across the margin pair. The 5-km depth-to-basement contour along the Scotian margin (thick grey line) roughly follows the hinge zone based on the refraction velocity models (Dehler et al. 2003; Funck et al. 2004; Wu et al. 2006). Although this contour off Morocco is less consistent with the hinge zone (Tari and Molnar 2005), they are still close to each other from the Agadir Bain to the Safi Basin. This contour on both sides is adopted to represent the relative positions of the margin pair for further reconstructions.

To restore the positions of the conjugates prior to chron M25, additional geological and geophysical information is required. This thesis utilizes the slope magnetic anomalies, salt distribution, and more importantly, the results of the recent seismic profiles on the

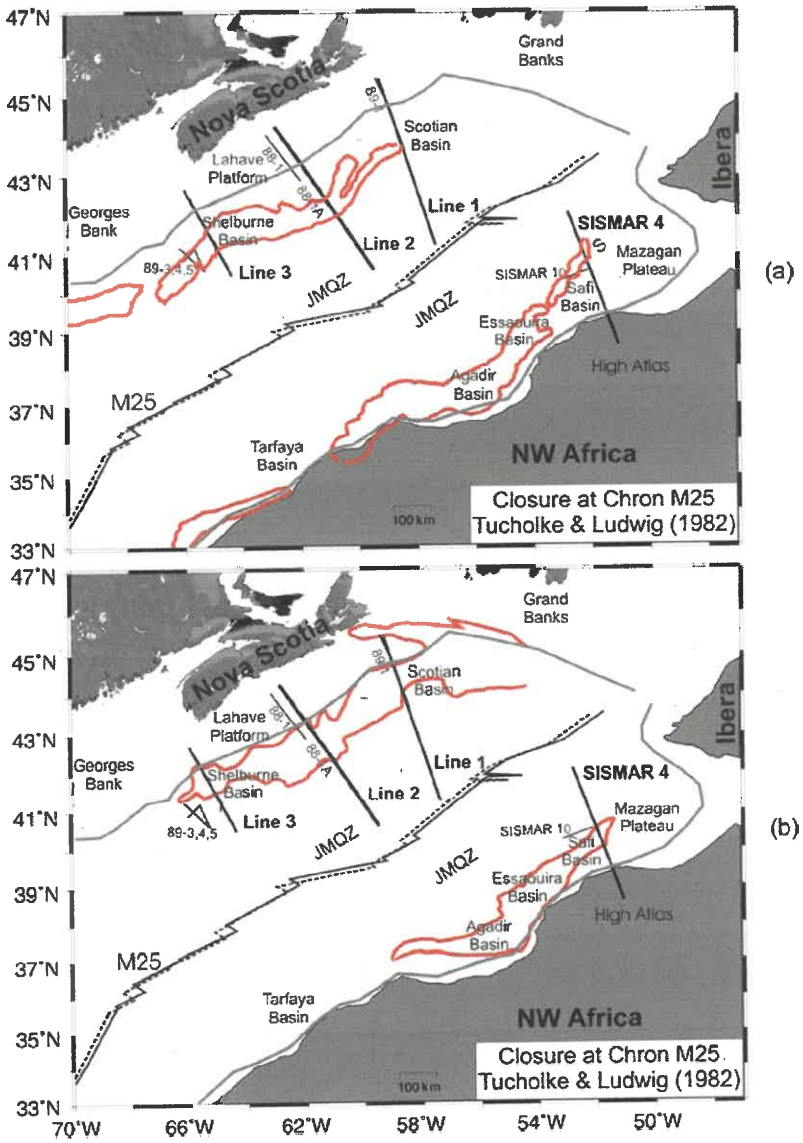

Figure 4.2. (a) The magnetic anomalies (red) from the opposite sides of the conjugates in the reconstruction of the NW Africa relative to the North America at chron M25. The East Coast Magnetic Anomaly (ECMA) off North America is taken from (Verhoef et al., 1996). The West African Coast Magnetic Anomaly (WACMA) is taken from Verhoef et al. (1996), Roeser et al. (2002) and Liger (1980). (b) The distributions of salt diapirs (red) off Nova Scotia and Morocco taken from Shimeld (2004) and Tari et al. (2003), respectively. The thin lines are MCS profiles shown for reference: lines 88-1, 1A (Keen *et al.* 1991b), line 89-1 (Keen and Potter 1995b), lines 89-3, 4, 5 (Keen and Potter 1995a), SISMAR 10 (Maillard et al. 2006). 88-1A is coincident with Line 2 and 89-1 with Line 1. The 5-km basement depth contours on both sides are adopted to represent the relative positions of the margin pair for Figures 4.3 to 4.8. For other features refer to Figure 4.1.

opposite sides to constrain closures at continental breakup and pre-rift positions. Figure 4.2a shows the slope magnetic anomalies (red lines) offshore Nova Scotia and Morocco. The ECMA off North America shows the distribution of positive values taken from Verhoef et al. (1996). The West African Coast Magnetic Anomaly (WACMA) consists of three components. The northeast portion, the S anomaly, is the positive anomaly taken from Roeser et al. (2002). The WACMA between 36°N and 40°N is taken from Verhoef et al. (1996). The anomaly south of 36°N (Tarfaya Basin) is digitized from the available magnetic profiles (Liger 1980), and is only shown for completeness but will not be used for further reconstruction for this margin pair. In past decades, the ECMA and WACMA were thought to mark the COB along either side of the conjugates (e.g. Roeser 1982; Klitgord and Schouten, 1986; Holik et al. 1991; Keen et al., 1991b; Keen and Potter, 1995a; Roeser et al. 2002). Based on this feature, the Nova Scotia and Morocco margins were reconstructed to continental breakup (e.g. Klitgord and Schouten, 1986; Sahabi et al., 2004), which will be presented in section 4.2.

Figure 4.2b shows the distribution of salt diapirs along the opposite sides of the conjugates (red lines). The salt limit off Nova Scotia is taken from Shimeld (2004), indicative of the distribution of autochthonous salt. The salt boundary along the Morocco margin denotes the distribution of present-day salt taken from Tari et al. (2003). Across the southern and northern portions of the margin, the seaward salt mobilization is limited based on existing MCS profiles (e.g. <10 km; Holik et al., 1991; Contrucci et al. 2004; Maillard et al. 2006). Across the central part of the Moroccan margin (near the Essaouira Basin), the salt may have mobilized ~40 km over the steepest slope area; however, the

maximum salt mobilization at the seaward edge of the salt basin is estimated to be 15-20 km (Tari and Molnar 2005). Therefore, the present-day salt off Morocco is considered be autochthonous at the scale of these reconstructions. The salt basins on the opposite sides were used to indicate the relative locations of the conjugates (e.g. Sahabi et al. 2004). This study compares the distribution of autochthonous salt as a proxy for the landward and seaward limits of rifted continental crust on both sides, assuming that the salt formed in a uniform rift basin (Klitgord and Schouten 1986).

More importantly, a few up-to-date wide-angle seismic refraction profiles have been shot across both sides of the conjugates (Figure 4.2). The SMART lines present a full coverage along the Scotian margin (Dehler et al. 2003; Funck et al. 2004; Wu et al. 2006), while only one refraction seismic transect, SISMAR 4, is available across the northern Moroccan margin (Contrucci et al. 2004). Thus, no refraction data are available at the conjugate locations of SMART Lines 2 and 3. These available transects extend from the continental crust with full thickness into the JMQZ, almost approaching M25 where unequivocal oceanic crust exists.

Based on the velocity models derived from the modern ocean bottom seismometer (OBS) data, the seaward limit of the continental crust (SLCC) is determined by removing the oceanic basement (e.g. Line 2) and exposed upper mantle (e.g. SMART Line 1; Funck et al. 2004). The SLCC along SMART Line 3 is interpreted half way from the landward appearance to the oceanward disappearance of the SDR sequences, assuming that the transition zone consists of half, highly-thinned continental crust and half initial oceanic

crust (Dehler, personal communication, 2007). The pre-rift positions are also calculated by balancing the cross-sectional area before and after rifting. The better constrained estimations of the crustal structure across the entire margin pair provide an opportunity to re-examine and consequently, to improve the previous reconstructions.

4.2 Reconstruction to the Onset of Seafloor Spreading (Minimum Closure)

4.2.1 Minimum Closure of Klitgord and Schouten (1986)

Minimum closure is a reconstruction of a margin pair after removal of oceanic crust from both sides. Figure 4.3 shows a reconstruction of Nova Scotia and Morocco by Klitgord and Schouten (1986). It represents a minimum closure of these conjugates by rotating the NW African plate to the North American continent (Table 4.1). In this reconstruction, the SLCC along the east coast of North American plate was considered to be marked by the ECMA, which was supposed to match its counterpart, WACMA, along the NW African plate. Due to data scarcity and the weak amplitude of WACMA, this minimum closure was accomplished by placing the ECMA against the seaward edge of the NW African salt diapiric province, which was also thought to mark the oceanward limit of continental crust (Jansa and Wiedmann, 1982; Roeser et al., 2002).

To examine the fit of this minimum closure, current delineations of the WACMA and salt distribution off Morocco (Figure 4.2) were rotated to the Nova Scotia side using the pole of rotation of Klitgord and Schouten (1986). Figure 4.3a indicates that the WACMA (red) does not match very well with its counterpart ECMA (green) with an obvious longitudinal misfit of ~150 km. The overall fit of magnetic anomalies from the opposite sides can be improved by an eastward movement of the Morocco margin, as indicated by

the arrow. Note that the northeast portion of the WACMA, the so-called S anomaly (Roeser et al. 2002), does not have its homologue on the Nova Scotia side and will be further discussed by correlating with results of the recent seismic data.

Figure 4.3b indicates that the distributions of salt units from the opposite sides largely overlap with each other. The autochthonous salt should indicate the original locations of the rifted basin, assuming that all autochthonous salt units from both sides formed within a uniform basin (Klitgord and Schouten, 1986). The overlap of salt distribution suggests an overlap of rifted continental crust for the closure at the SLCC. This is still true if seaward salt mobilization occurred before the continental breakup. If the salt structures on the conjugates were not deposited within a uniform basin, the exact location of the COB or SLCC will not be inferred by restoring the past positions of the salt units. However, the salt distributions from the conjugates should not overlap at the minimum closure because overlapped salt distribution suggests overlapped rifted continental crust, assuming that all autochthonous salt formed within restricted basins in the nascent Atlantic (Klitgord and Schouten, 1986; Holik et al. 1991). A better fit of the salt distributions from the conjugate margins would require less closure (indicated by an arrow).

The fit of the closure is further examined by comparing the results of recent seismic data. Figure 4.3c shows that the SLCC derived from recent OBS profiles. Across the northern part of the conjugates, SMART Line 1 and SISMAR 4 are conjugate to each other in this reconstruction. At this conjugate location, the continental crust derived from SMART Line 1 overlaps the African continental crust. Similarly, the SLCC interpreted along

Figure 4.3. The minimum closure of Klitgord and Schouten (K&S; 1986). (a) The magnetic anomalies from both sides of the conjugates. The green lines denote the distribution of ECMA off Nova Scotia. The red lines mark the WACMA off Morocco, which have been rotated to match the ECMA using the pole of rotation of Klitgord and Schouten (1986; Table 4.1). Anomaly S is the northern portion of the WACMA (Roeser et al. 2002). (b) The restored salt distributions from the opposing sides. The green line indicates autochthonous salt distribution off Nova Scotia (Shimeld 2004). The red line denotes the rotated salt distribution off Morocco (Tari and Molnar 2005). (c) Interpretations of modern OBS profiles are projected onto the closure. The color bars indicate the extent of the continental crust derived from OBS data. The SLCC: the seaward limits of continental crust. The grey area indicates the fixed North American plate. The Moroccan plate is filled with square pattern. The arrows indicate the potential movement of the Moroccan plate as discussed in the text. SISMAR 4 is shown as a grey line. For other features refer to Figures 4.1 and 4.2. The color bars indicate the extent of the continental crust derived from OBS data.

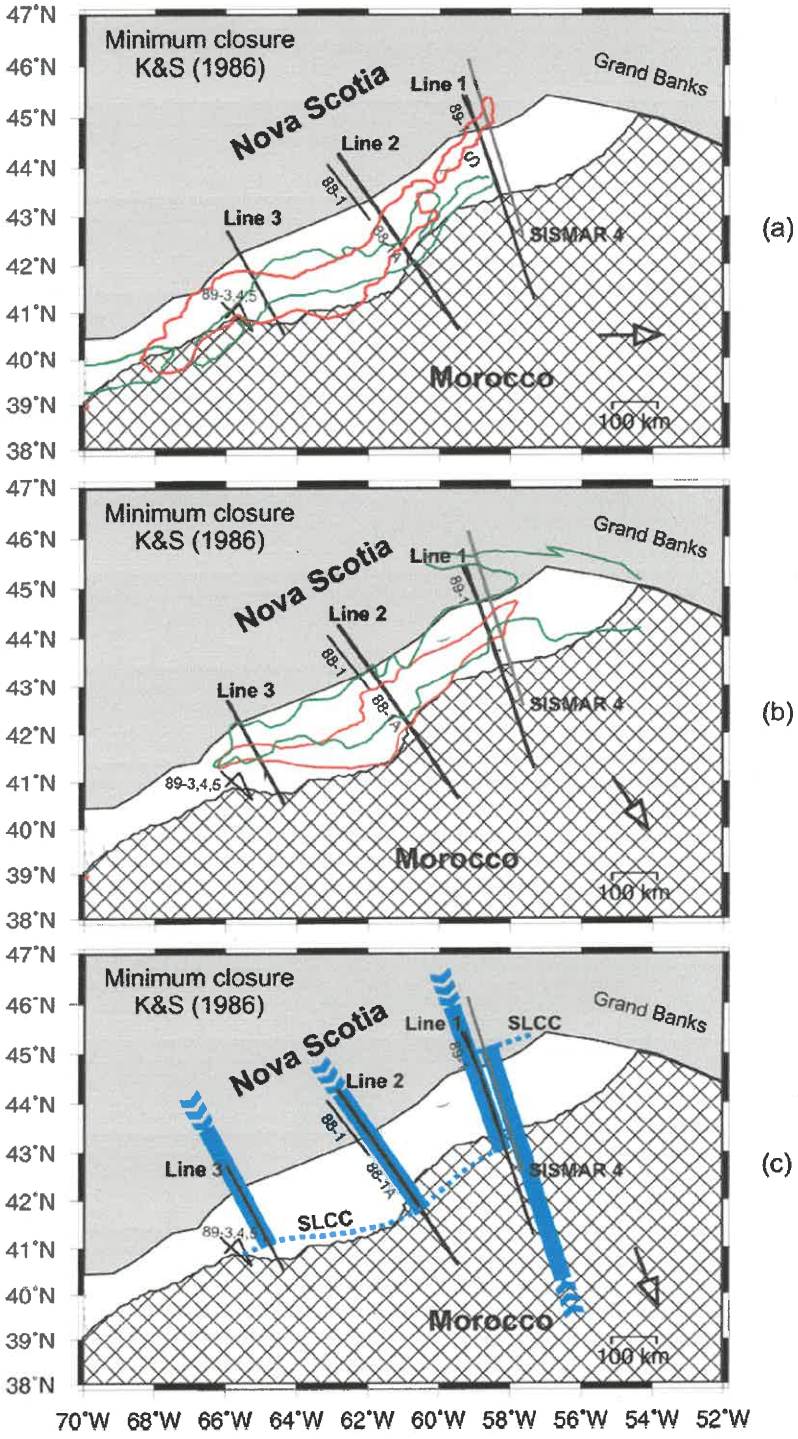
Minimum closure
K&S (1986)
Nova Scotia
Grand Banks
Line 1
Line 2
Line 3
SISMAR 4
89-3,4,5
Morocco
100 km
(a)
(b)
(c)
SLCC
47°N
46°N
45°N
44°N
43°N
42°N
41°N
40°N
39°N
38°N
70°W
68°W
66°W
64°W
62°W
60°W
58°W
56°W
54°W
52°W

SISMAR 4 (Contrucci et al. 2004) is located on the continental shelf interpreted on SMART Line 1, where autochthonous salt is imaged further seaward (Shimeld 2004). Across the central and southern portions of the conjugates, the continental crust derived from Line 2 and Line 3 also overlaps the Moroccan continental crust, with the landward limits located at the Morocco side of the restored positions of magnetic anomalies and salt units. The overlapped continental crust also indicates less closure for the opposing sides.

The minimum closure of Tari and Molnar (2005) is based on fitting the basement embayment of the Sable subbasin and the basement promontory offshore Essaouira. The pole of rotation is similar to that of Klitgord and Schouten (1986). The misfit of the slope magnetic anomalies and salt distributions and overlapping of continental crust in this reconstruction will be similar to that seen above. Therefore, less closure should also be suggested as a minimum closure for this conjugate.

4.2.2 Minimum Closure of Sahabi et al. (2004)

To improve the fit of the minimum closure above, Sahabi et al. (2004) proposed a reconstruction by fitting the magnetic anomalies and salt basins from the conjugate sides (Figure 4.4). In this case, both the ECMA and WACMA are still thought to mark the COBs (i.e. SLCC in this case) along both margins. One difference for this closure is that the conjugate margins are less closed compared to the closure of Klitgord and Schouten (1986). The other difference is that the WACMA is divided at a position near the Agadir Basin into a southern portion and a northern portion, which are rotated to fit the ECMA using separate poles of rotation (Table 4.1). The main purpose of a separate rotation for

the northern part is to account for the younger Atlas compression (Beauchamp et al. 1999) and to improve the overall fit with ECMA.

Figure 4.4a demonstrates an improved fit of the WACMA and ECMA. The WACMA presents an almost identical shape to the ECMA, with a slight overlap across the SW Nova Scotia margin. A problem for this fit is that the S anomaly does not have a homologue on the Nova Scotia side, which casts doubt about the feasibility of using this anomaly to constrain the minimum closure of the margin pairs. If the S anomaly is generated by the SLCC, similar magnetic anomalies should be observed on the Scotian side. Lack of a magnetic homologue for the S anomaly indicates that this anomaly may not mark the SLCC. The recent refraction velocity models also show that the high-amplitude ECMA across the SW Scotian margin along Line 3 roughly coincides with the SLCC. However, the low-amplitude ECMA from SMART Line 2 (this thesis) to Line 1 (Funck et al. 2004) does not represent the location of the SLCC. Therefore, the magnetic anomalies from the central part of the conjugates to the north should not be used to match the seaward termination of the continental crust.

Figure 4.4b shows the restored salt distributions from the conjugate sides. Across the southwest conjugate locations, the salt limits fit very well. Across the northeastern-most conjugate locations, the salt limits still overlap with each other (e.g. along SISMAR 4), suggesting less closure at the time of continental breakup. Hence, a separate rotation, which is intended to improve the fit of magnetic anomalies, is not required for this part of the conjugates. Across the central margin conjugates (from Line 2 to Line 1), a gap exists between the seaward limits of the salt. Since the autochthonous salt across the southwest

Figure 4.4. The minimum closure of Sahabi et al. (2004). (a) The magnetic anomalies from the opposite sides of the conjugates. The WACMA (red) is divided into two parts at a position near the Agadir Basin (Figure 4.1). The southern and northern portions of the WACMA are rotated separately to match with ECMA (green). The poles of rotation are shown in Table 4.1. (b) The restored distributions of salt diapirs from both sides of the conjugates. (c) Interpretations of modern OBS profiles from both sides are projected onto the closure. The ECMA and WACMA are also shown as grey solid and grey dashed lines for direct correlation with seismic results. SLCC indicates the seaward limits of rifted continental crust derived from recent OBS data. For other features refer to Figures 4.1 and 4.2.

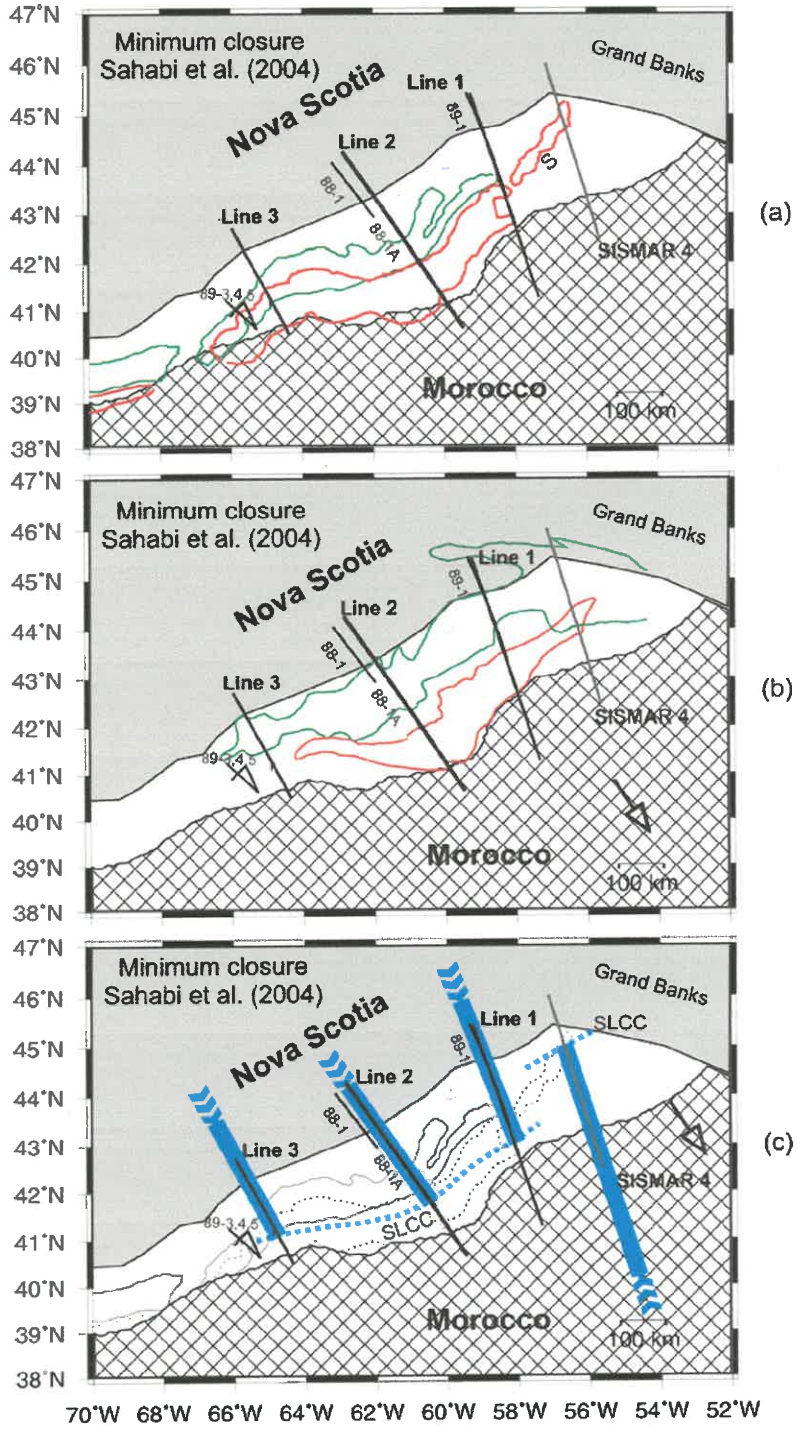
Minimum closure
Sahabi et al. (2004)
Nova Scotia
Grand Banks
Line 1
Line 2
Line 3
89-1
88-1
88-1A
89-3,4,5
SISMAR 4
Morocco
100 km
(a)
(b)
(c)
SLCC
47°N
46°N
45°N
44°N
43°N
42°N
41°N
40°N
39°N
38°N
70°W 68°W 66°W 64°W 62°W 60°W 58°W 56°W 54°W 52°W

and northeast conjugate locations is well defined by MCS profiles (Holik et al., 1991; Contrucci et al. 2004; Maillard et al. 2006), the misfit for the central conjugates suggests that the salt structures from the opposing sides may not form within a uniform basin. Alternatively, salt may form in one rifted basin but it may be truncated over basement highs during syn-rift times, such as some area of the Tafelney Plateau off Morocco that is conjugate to the central Nova Scotia margin (Molnar et al. 2002).

The SLCCs derived from recent OBS profiles are projected onto this closure (Figure 4.4c). Although the fit of continental crust for the central and southern conjugate locations are not constrained by OBS data on the Morocco side, the SLCCs interpreted along Line 2 (Wu et al., 2006) and Line 3 (Dehler, personal communication, 2007) are close to the matched magnetic anomalies (grey lines). Across the northern part of the conjugates, the seismically derived continental crust overlaps with each other for more than 100 km, unless this part of the margin separated along a transform zone. However, this seems to be unlikely because the SLCC (short dashed line) derived from SISMAR 4 is situated on the Nova Scotia shelf, where extensive autochthonous salt is observed (Figure 4.4b; Shimeld, 2004). The overlapped continental crust from the opposite sides also suggests less closure, which is consistent with the implications derived from the overlap of oceanward salt limits. Therefore, a separate rotation for the northern part of the conjugates is not required.

4.2.3 A Modified Minimum Closure

A modified minimum closure is suggested below based on the combined correlation of magnetic anomalies, salt limits, and seismic results. For this modified closure, the

southern and northern conjugate locations are fit by different types of constraints. Across the southern conjugate locations, no OBS data are available on the Morocco side. However, this part of the conjugates is volcanic and the slope magnetic anomaly is directly related with rifting volcanism (Keen and Potter 1995a). The ECMA on the Nova Scotia side has been modeled as a result of extrusives evidenced by SDR sequences that occupy the seaward end of the rifted continental crust (Alsop and Talwani 1984; Dehler, et al. 2003). Therefore, the slope magnetic anomalies from the opposite sides are still utilized to fit the southern part of the conjugates.

For the northern conjugate locations, the minimum closure is constrained by seismic results derived from modern OBS profiles. However, the COB or SLCC along SISMAR 4 is previously based on the location of the S anomaly. This relationship of the SLCC and the S anomaly is re-examined in the velocity model and adjacent MCS data. Figure 4.5a is the velocity model along SISMAR 4, where no velocity boundary or significant velocity variation is observed across the S anomaly (Contrucci et al., 2004). In fact, along both SMART Line 1 and Line 2 off Nova Scotia, the thinned continental crust extends ~50 km seaward of the ECMA (Funck et al. 2004; Wu et al. 2006). This suggests that the S anomaly, or even most of the WACMA in this region, does not mark the COB or SLCC on the Morocco margin.

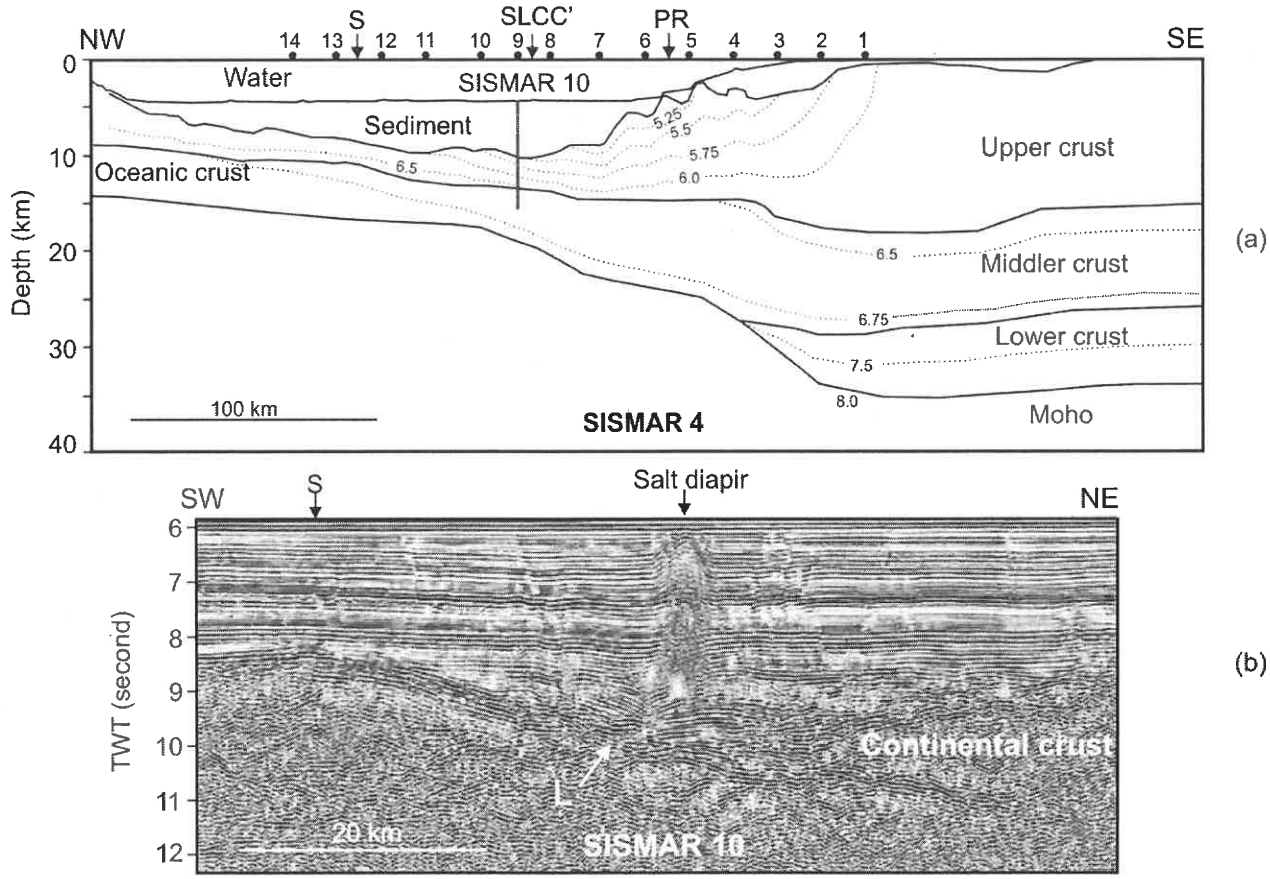

Figure 4.5. (a) The velocity model along SISMAR 4 after Contrucci et al. (2004). The filled circles above the velocity model mark the locations of OBS instruments, labelled by numbers. The dotted lines in the velocity model indicate the velocity contours (km/s). S denotes the location of S anomaly, which was thought to represent the COB in this region. SLCC′ is the seaward limit of continental crust re-interpreted from the combined results of velocity structure and seismic image. PR: pre-rift position. (b) The seismic image of MCS profile SISMAR 10 (Maillard et al. 2006). Its location is shown in Figure 4.2, and also indicated by a vertical bar below OBS 9 in (a). L: landward dipping reflector.

Figure 4.5b shows the seismic image for a perpendicular MCS profile SISMAR 10 (see Figure 4.2 for location). According to this profile, the continental crust pinches out against a northeast dipping reflector L (Maillard et al. 2006), and its seaward limit, based on this profile, has been delimited by the last occurrence of salt. This seismic image shows that the S anomaly is about 30-40 km further seaward of the SLCC and obviously related with a basement high underneath and therefore, it does not mark the COB or SLCC. Similar seismic images with salt diapiric structure are observed along SISMAR 4 (Contrucci et al., 2004; Maillard et al. 2006), suggesting that the SLCC should also be delimited by the last salt diapir (SLCC' between OBS 8 and 9, Figure 4.5b). This re-interpretation is supported by the velocity model where strong lateral gradients are present landward of the salt unit but vanish seaward of the salt structure, consistent with a transition from continental crust to oceanic crust.

With the above constraints, the modified reconstruction is represented in Figure 4.6. The pole of rotation of this reconstruction is same as that of Sahabi et al. (2004) for the southern part of the conjugates (Table 4.1), but only one rotation is required to reconstruct the entire Morocco margin with its conjugate Nova Scotia margin. This produces a reduced closure for the northern conjugate locations, but the same fit as that of Sahabi et al (2004) for the central and southwestern conjugate segments.

Figure 4.6. Modified minimum closure of Sahabi et al. (2004) based on the correlation of magnetic anomalies, salt distribution, and seismic results from both sides. (a) The magnetic anomalies from the opposite sides. (b) The restored positions of salt limits. (c) Interpretations of modern OBS profiles from both sides are projected onto the closure. SLCC is the seaward limit of continental crust based on the location of the S anomaly (Contrucci et al. 2004). SLCC' is the re-interpreted SLCC based on the combined results of velocity model and seismic image (re-interpretation see text 4.2.3). The reconstruction pole is listed in Table 4.1. For other features refer to Figures 4.1 and 4.2. The colour bars indicate the extent of the continental crust derived from OBS data.

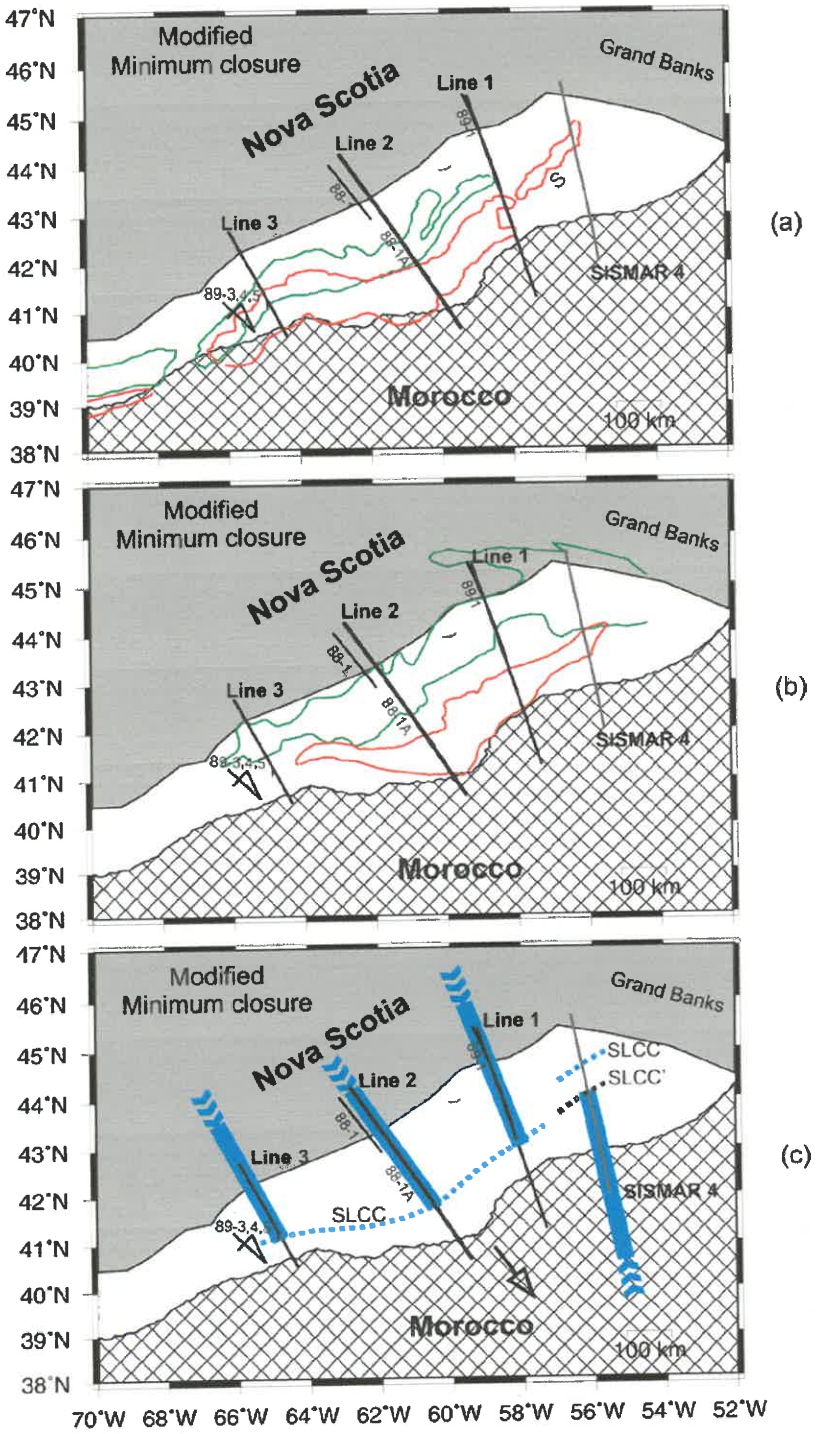
Modified
Minimum closure
Nova Scotia
Grand Banks
Line 1
Line 2
Line 3
SISMAR 4
Morocco
100 km
(a)
(b)
(c)
SLCC
SLCC'
47°N
46°N
45°N
44°N
43°N
42°N
41°N
40°N
39°N
38°N
70°W
68°W
66°W
64°W
62°W
60°W
58°W
56°W
54°W
52°W

In this reconstruction, the ECMA and WACMA fit very well across the southern conjugates, but they start to separate from the central part of the conjugate to the north (Figure 4.6a), indicating a change in character across the central margin segment. The salt limits from the opposite sides fit very well across the southern and northern parts of the conjugates respectively (Figure 4.6b). A gap still exists between the restored salt distributions across the middle part of the conjugates. This gap may be due to the basement highs that lack salt deposition during syn-rift time, such as the faulted basement blocks off Nova Scotia and the Tafelney plateau off Morocco. With the re-interpretation of SLCC (SLCC', Figure 4.6c) along SISMAR 4, the continental crust across the northern margin conjugates are matched with each other.

4.3 Reconstruction to Pre-Rift Position (Maximum Closure)

4.3.1 Maximum Closure of Klitgord and Schouten (1986)

Maximum closure is a reconstruction of a margin pair to the pre-rift position after removal of extended continental crust from both sides. Reconstruction to the pre-rift position requires the estimation of the landward limit of crustal extension. Klitgord and Schouten (1986) used the landward edge of the rifted basins to represent the pre-rift positions, from which the pole of rotation was calculated (Table 4.1). Their maximum closure of the Nova Scotia and Morocco margin conjugates is presented in Figure 4.7.

With the recent wide-angle seismic refraction data carried out on both sides of the conjugates, the landward limits of crustal extension can be better estimated from the well-defined velocity models by balancing the cross sectional area before and after rifting,

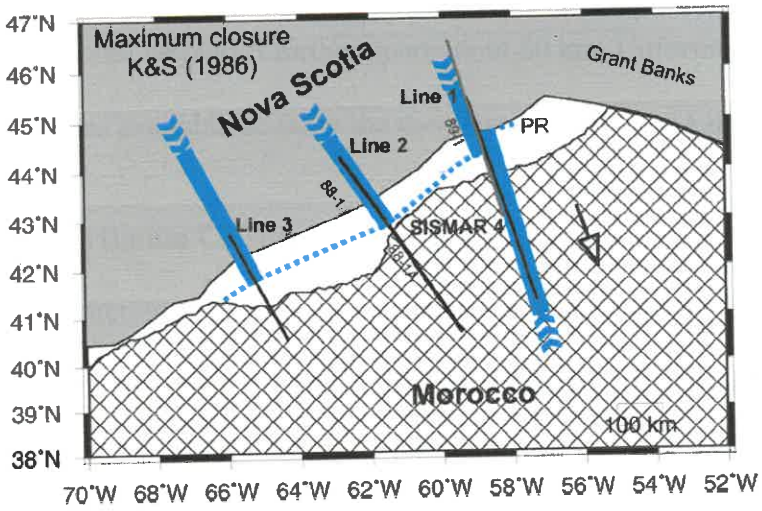

Figure 4.7. The maximum closure of Klitgord and Schouten (1986). The pole of rotation is shown in Table 4.1. The colour bars indicate the extent of full thickness continental crust derived from the up-to-date wide-angle seismic refraction data, with dotted lines indicating the front of pre-rift position from both sides. PR: pre-rift position. For other features refer to Figures 4.1 and 4.2.

assuming that the continental material is volumetrically conserved. The pre-rift position is obtained from the total cross sectional area of continental crust, including the rifted portion, divided by the thickness of unstretched continental crust. The calculated pre-rift positions are projected onto the maximum closure. Across the northern part of the conjugates, the SMART Line 1 and SISMAR 4 were exactly conjugate to each other at the pre-rift position. According to this projection, the interpreted continental crust with full thickness from the opposite sides still overlaps more than 50 km, indicating the maximum closure should be placed further apart about 50 km. Unfortunately, there are no refraction seismic lines available so far at the conjugate locations of Line 2 and Line 3.

4.3.2 A Modified Maximum Closure

An alternate reconstruction to the pre-rift positions is determined so as to eliminate the overlapping of continental crust. Section 4.2.3 demonstrated that the modified minimum closure of Sahabi et al. (2004) improved the correlation of the seismically derived results as well as the slope magnetic anomalies and salt distributions from both sides of the conjugates. Using this modified minimum closure as starting point (Figure 4.8a), the conjugates are further reconstructed to match the full thickness continental crust on both sides (Figure 4.8b), assuming a constant pole of rotation from the initial rift to final continental breakup. In the modified maximum closure, the transect SISMAR 4 is not exactly at the conjugate location of SMART Line 1, but they are ~40-50 km apart from each other and therefore still close enough to be considered as conjugate lines. The overlapped continental crust in the closure of Klitgord and Schouten (1986; Figure 4.7) is eliminated by a reduced closure. The reconstruction pole for this maximum closure is

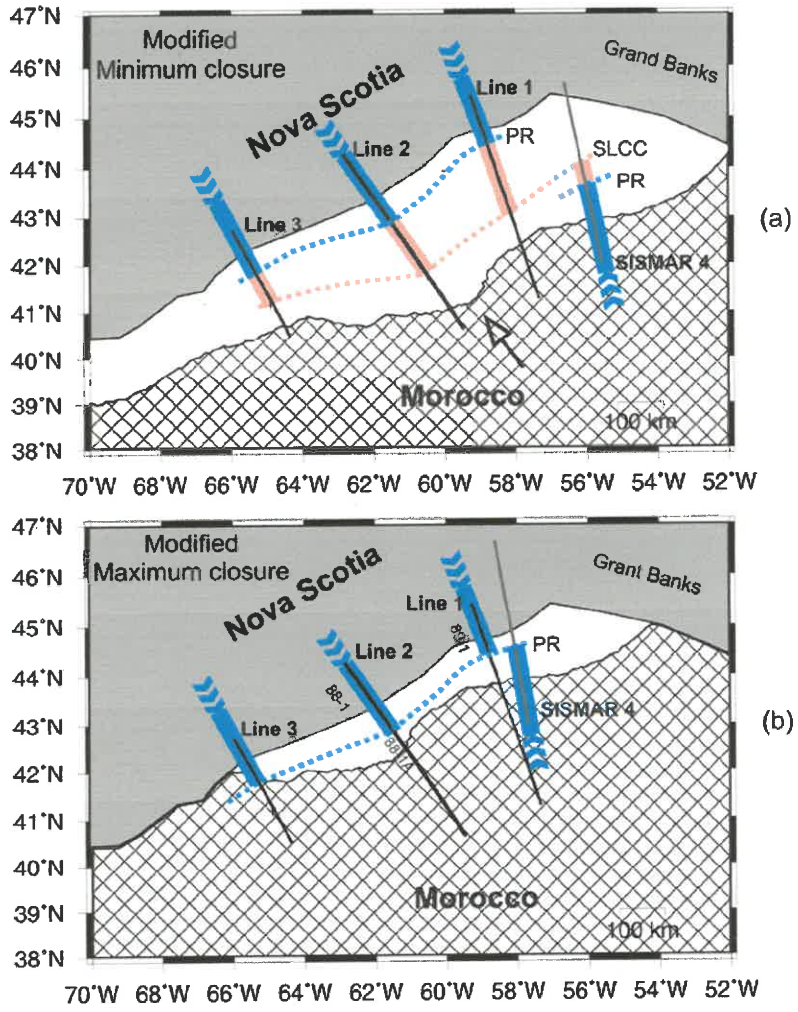

Figure 4.8. (a) The modified minimum closure of the Nova Scotia and Morocco margin conjugates at the seaward limit of rifted continental crust. (b) A maximum closure of the margin conjugates at pre-rift time after removal the rifted continental crust, assuming a fixed pole of rotation from pre-rift position to continental breakup. The extended continental crust is denoted as pink bars; while the pre-rift continental crust with full thickness is shown as blue bars. The pole of rotation is shown in Table 4.1. For other features refer to Figures 4.1 and 4.2.

shown in Table 4.1. This maximum closure may be further constrained if additional OBS transects become available across the central and southern Morocco margin.

4.4 Conclusions

A number of reconstructions of the Scotian/Moroccan margin conjugates have been re-examined based on the latest results derived from the recent seismic refraction and reflection data, as well as magnetic and salt distribution from both sides of the conjugates. The seismic data show that the pre-rift full thickness continental crust overlaps in the maximum closure determined by Klitgord and Schouten (1986). A new maximum closure of this margin pair is suggested by eliminating the overlapped pre-rift full thickness continental crust between the northern margin conjugates.

The minimum closure of Sahabi et al. (2004) improved the fit of the two sides of the margin pair compared to that of Klitgord and Schouten (1986); however, the S magnetic anomaly off NW Morocco does not have a homologue offshore Nova Scotia. In addition, velocity models of refraction data show that the rifted continental crust still overlaps in the minimum closure after two separate rotations of the southern and northern Morocco margin. A modified minimum closure is suggested so as to eliminate the overlapped rift crust across the northern margin conjugates. This proposed minimum reconstruction is similar to the rotation of Sahabi et al. (2004) for the southern portion of the conjugates, but no additional rotation is required for the northern part of conjugates. This minimum reconstruction also improved the correlation of magnetic anomalies and salt distribution from the opposing sides of the conjugates.

CHAPTER 5

DEVELOPMENT OF THE NOVA SCOTIA AND MOROCCO MARGIN CONJUGATES

5.1 Seismic Data Across the Nova Scotia/Morocco Margin Conjugates

The development of the Nova Scotia and Morocco margin conjugates is investigated based on a series of seismic profiles across the continental breakup front (CBF) from both sides. Figure 5.1 shows the seismic lines in the minimum closure of the conjugate margins proposed in chapter 4 (see Figure 4.6). Wide-angle-seismic refraction transects, as previously discussed, include the SMART Lines 1-3 (Dehler et al. 2003; Funck et al. 2004; Wu et al. 2006) across the Scotian margin and SISMAR 4 (Contrucci et al. 2004) across the northern Moroccan margin.

The MCS profiles off Nova Scotia include LITHOPROBE line 88-1A and a number of NovaSpan Project lines (data courtesy GX Technology Corporation). Line 88-1A (Keen et al. 1991b) is a composite profile of post-stack and pre-stack migrations as presented in chapter 3. The section form SP 3010 to SP 3489 was migrated using pre-stack time migration on the common-offset plane (see Appendix D). The portion between SP 3700-4356 was migrated using pre-stack time migration on the equivalent-offset plane (see Appendix C). The remainder of 88-1A was migrated by post-stack migration technique in the time domain. The NovaSpan Project profiles presented below include five dip lines 1100-2000 and an 800-km-long strike line 5100. Acquisition parameters for these lines are described in section 3.2.

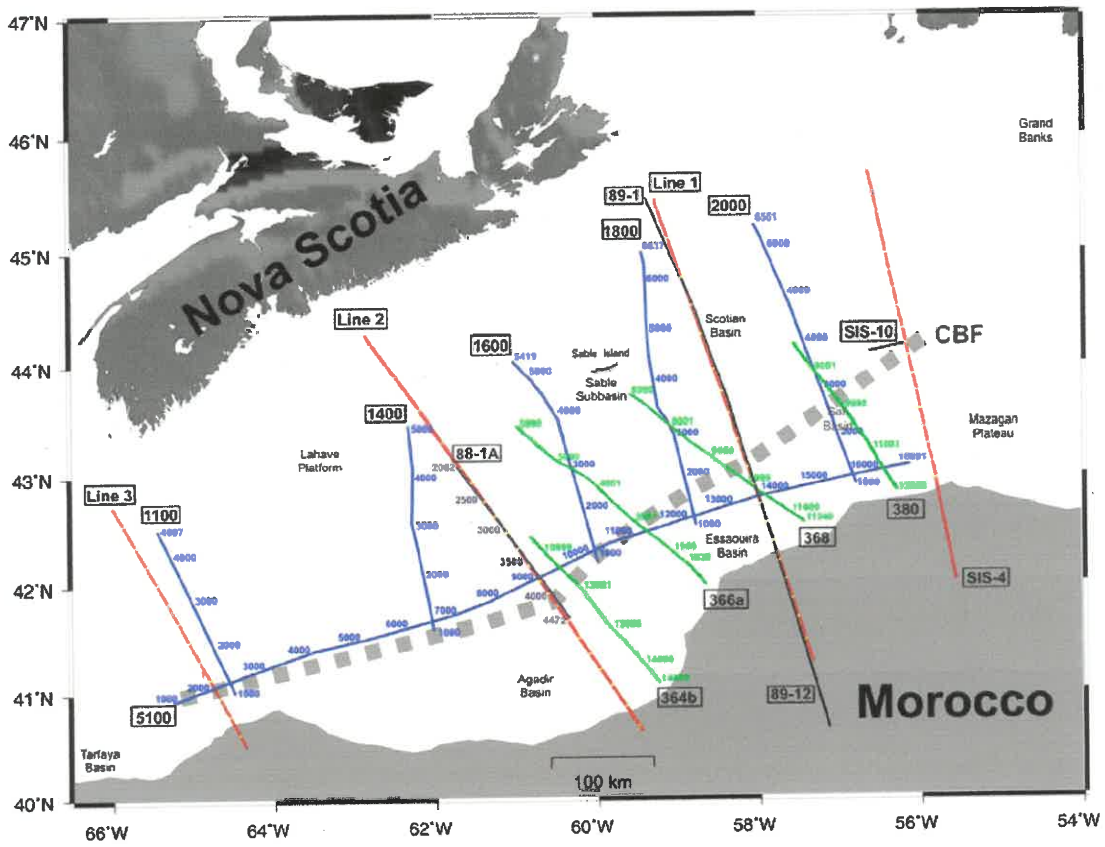

Figure 5.1. Seismic lines in the minimum closure of the conjugate margins of Nova Scotia and Morocco. The red lines are the most recent OBS profiles, including SMART Lines 1, 2 and 3 from the Nova Scotia side (Dehler et al. 2003; Funck et al., 2004; Wu et al., 2006), and SISMAR 4 from Morocco side (SIS-4, Figure 5.1; Contrucci et al. 2004). The yellow dots along the refraction lines indicate the OBS location. The MCS profiles from the Nova Scotia side include 88-1A (Keen et al. 1991b), 89-1 (Keen and Potter 1995b), BGR line 89-12 (unpublished), denoted as black lines, and NovaSpan Project profiles 1100, 1400, 1600, 1800, 2000, and 5100 (marked as blue lines; data courtesy GX Technology Corporation). The MCS profiles from the Morocco side include SISMAR 10 (SIS-10, short black line, Figure 5.1) and Conrad lines 364b, 366a, 368 and 380 (marked as green lines; Holik et al. 1991). Numbers in boxes are profiles numbers. Shot points (SP) for all MCS lines are labelled for location reference. CBF: the continental breakup front, which is derived from the seaward limits of continental crust (SLCC; see Figure 4.6) along the conjugates according to the minimum reconstruction in chapter 4.

The MCS profiles across the Morocco margin, including 364b, 366a, 368, and 380, were acquired during cruise Conrad 2405-06 in 1983 (Holik et al. 1991). A streamer with 48 channels at 50 m spacing was used for data acquisition. Airgun source volume was 1864 cubic inches. The stacked data were retrieved from Marine Seismic Data Center at the University of Texas (http://www.ig.utexas.edu) and migrated in this study using a finite difference migration algorithm (Claerbout 1985). The sediment velocities for migration were adopted from Bartolome et al. (2005), where velocities were derived from depth focusing of MCS data in this region. The basement velocities come from the coincident sonobuoy data along the Conrad profiles (Holik et al. 1991). The combined velocities were also utilized for time to depth conversion.

According to Figure 5.1, MCS lines 88-1A and 364b, NovaSpan 1600 and 366a, NovaSpan 1800 and 368, and NovaSpan 2000 and 380, are conjugate to each other across the CBF. Seismic features on both sides of the CBF are compared across these conjugate locations in the following sections. The dip lines NovaSpan 1100, 1400 and the strike profile 5100 are also shown to elucidate the along-strike structural variation.

5.2 Seismic Images Across the Continental Breakup

5.2.1 Seismic Images along the Conjugate Transects

5.2.1.1 88-1A versus Conrad 364b

The lines 88-1A and Conrad 364b are conjugate profiles across the central segment of the Scotian and Moroccan Conjugates (Figure 5.2). At the seaward end of 88-1A, a series of FBs are observed seaward of the diapiric salt. As discussed in chapters 2 and 3, these FBs

are interpreted as the last portion of highly thinned and rotated continental crust. The CBF is situated at the seaward termination of the FBs, with oceanic crust accreted further seaward. At the conjugate location off Morocco (lower panel, Conrad line 364b), FBs are also observed seaward of the diapiric salt structure. No refraction seismic data are available in this region to determine the detailed velocities and the nature of the FBs. However, these FBs occur landward of the CBF according the proposed minimum reconstruction (see chapter 4), in a symmetrical pattern to observations from the conjugate position. This indicates a continental character for the FBs seaward of the salt along Conrad 364b as well.

The basement at the seaward end of Conrad 364b is characterized by remnant energy of hyperbolic diffraction due to incomplete migration. This feature suggests the appearance of oceanic crust, which is also observed at the conjugate side. The matching features from the opposing sides demonstrate symmetrical breakup geometry across the central segment of the conjugate margins.

The symmetry is also illustrated by similar widths of the rifted continental crust and similar sediment loading at the CBF. The seaward limit of the rifted continental crust for the central Scotian margin is about 150 km from the hinge zone (upper panel, Figure 5.2). On Conrad line 364b, with the hinge zone located at the landward end of this profile (Tari and Molnar 2005), the width of the stretched continental crust is ~140 km, similar to that on the conjugate side. The sediment fill at the CBF is also limited (~6-8 km) on either side, although the sediment on the Morocco side is ~1-2 km thicker than that of the

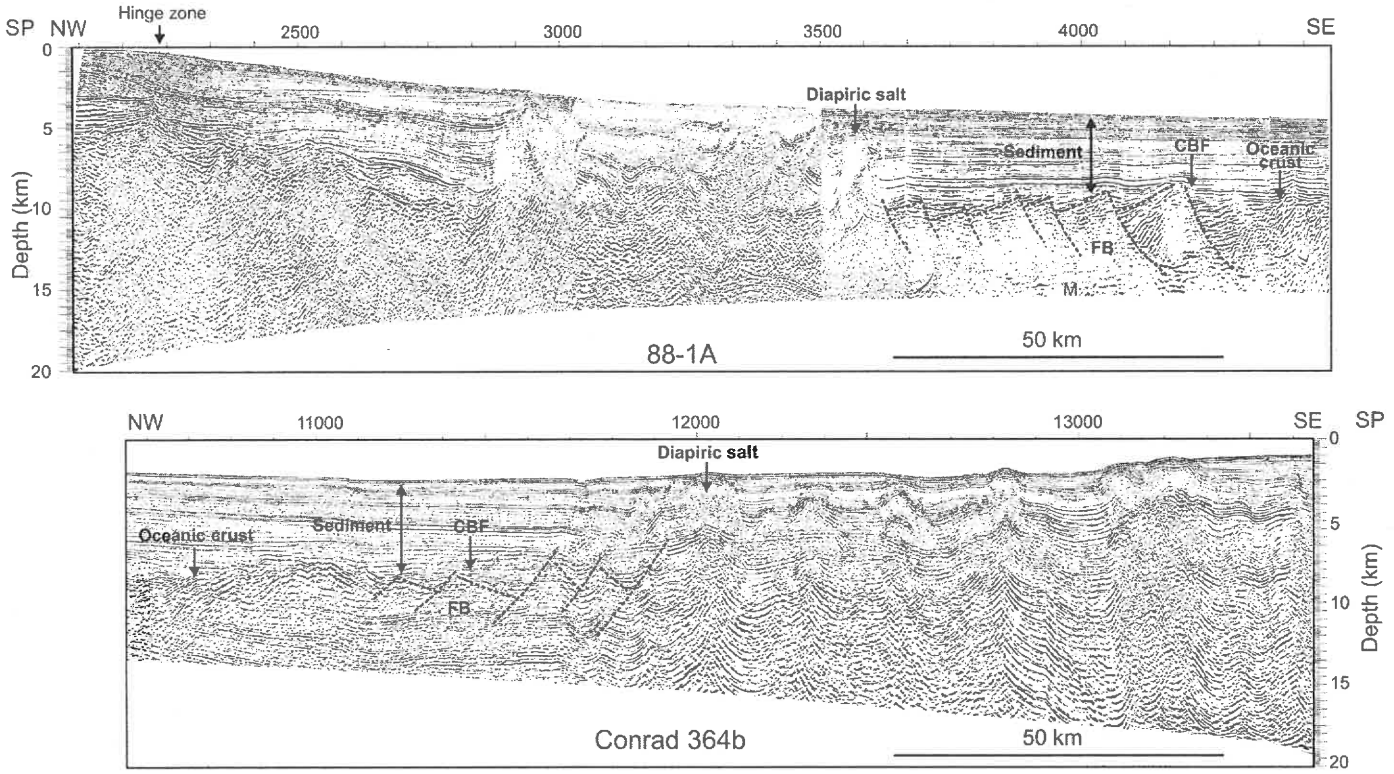

Figure 5.2. Depth sections of conjugate profiles of 88-1A and Conrad 364b. The MCS line 88-1A (Keen et al. 1991b) is a composite profile of post-stack and pre-stack migrations. The section between SP 3010-3489 was migrated using pre-stack time migration on the common-offset plane (see Appendix D). The portion between 3700-4356 was migrated using pre-stack time migration on the equivalent-offset plane (see Appendix C). The remainder of 88-1A was migrated by post-stack migration technique in time domain. The Conrad line 364b and other Conrad lines are taken from Marine Seismic Data Center of the Lamont-Doherty Earth Observatory and migrated in this study using the finite difference migration algorithm. The sediment velocities for migration were adopted from Bartolome et al. (2005), where velocities were derived from depth focusing of MCS data in this region. The basement velocities come from the coincident sonobuoy data along the Conrad profiles (Holik et al. 1991). The velocities were also utilized for converting the above time sections to depth. COB: continent-ocean boundary; FB: faulted basement block.

Scotian side. The relatively thicker sediment off Morocco may include the late sediment fill due to the erosion of the High Atlas Mountains (Beauchamp et al. 1999), or later addition of volcaniclastics of the Cenozoic volcanism, which occurred on the Morocco side (e.g. Funck et al. 1996) but is not observed on the Scotian side. The relatively thicker sediment off Morocco will be further discussed in section 5.4.2.

5.2.1.2 NovaSpan 1600 versus Conrad 366a

Figure 5.3 shows the conjugate profiles of NovaSpan 1600 and Conrad 366a. Similar to Figure 5.2, FBs are imaged seaward of the salt structure on both sides of the conjugate profiles. However, the FBs along Conrad 366a appear to be more elevated blocks bounded by major faults of opposing polarities, in contrast to the relatively small and subdued FBs formed by uniformly seaward dipping faults on NovaSpan 1600. Based on the minimum closure in chapter 4, the CBF is consistent with the termination of the FBs off Nova Scotia, although it is not clear if more FBs exist further seaward.

Along Conrad 366a, however, additional FBs are observed oceanward of the CBF, suggesting that the breakup of this specific conjugate segment may follow an irregular boundary (CBF-2), illustrated by the Tafelney Plateau (see Figure 5.7) off Essaouira that is oblique to the general strike of the conjugates (Tari et al. 2003). Further seaward, a crustal reflection is locally imaged (R1, lower panel, Figure 5.3), above which the basement is featured by remnant energy of hyperbolic diffraction. The nature of this reflection is not definitive; however, the basement (O, lower panel, Figure 5.3) seaward of this reflection, as well as the seafloor above (SF, lower panel, Figure 5.3), is shallower.

This reflection may be related to the wide-spread hotspot activity that elevated the basement off Morocco (Louden et al. 1989; Holik et al. 1991), illustrated by the prominent occurrence of seamounts further seaward (Ye et al. 1999).

Not only do the FBs imaged on both sides of the conjugates present different geometries, the width of rifted continental crust and sedimentation are also imaged in asymmetrical patterns. The seaward limit of the FBs along NovaSpan 1600 is ~180 km from the hinge zone (upper panel, Figure 5.3); while on the Conrad line 366a, with the hinge zone located at the landward end of this profile (shown in Figure 5.7), the width of the stretched continental crust (to CBF-2) is ~120 km. In addition, the sediment fill along NovaSpan 1600 is more than 10 km thick with prominent salt canopies; while the sediment thickness along Conrad 366a is generally less than ~6 km with limited diapiric salt, except for some thick sediment fill within the major fault basins. The formation of the thick sediment fill within the major fault basins off Morocco will be discussed in section 5.4.2. These features indicate asymmetrical crustal structure across the margin pair.

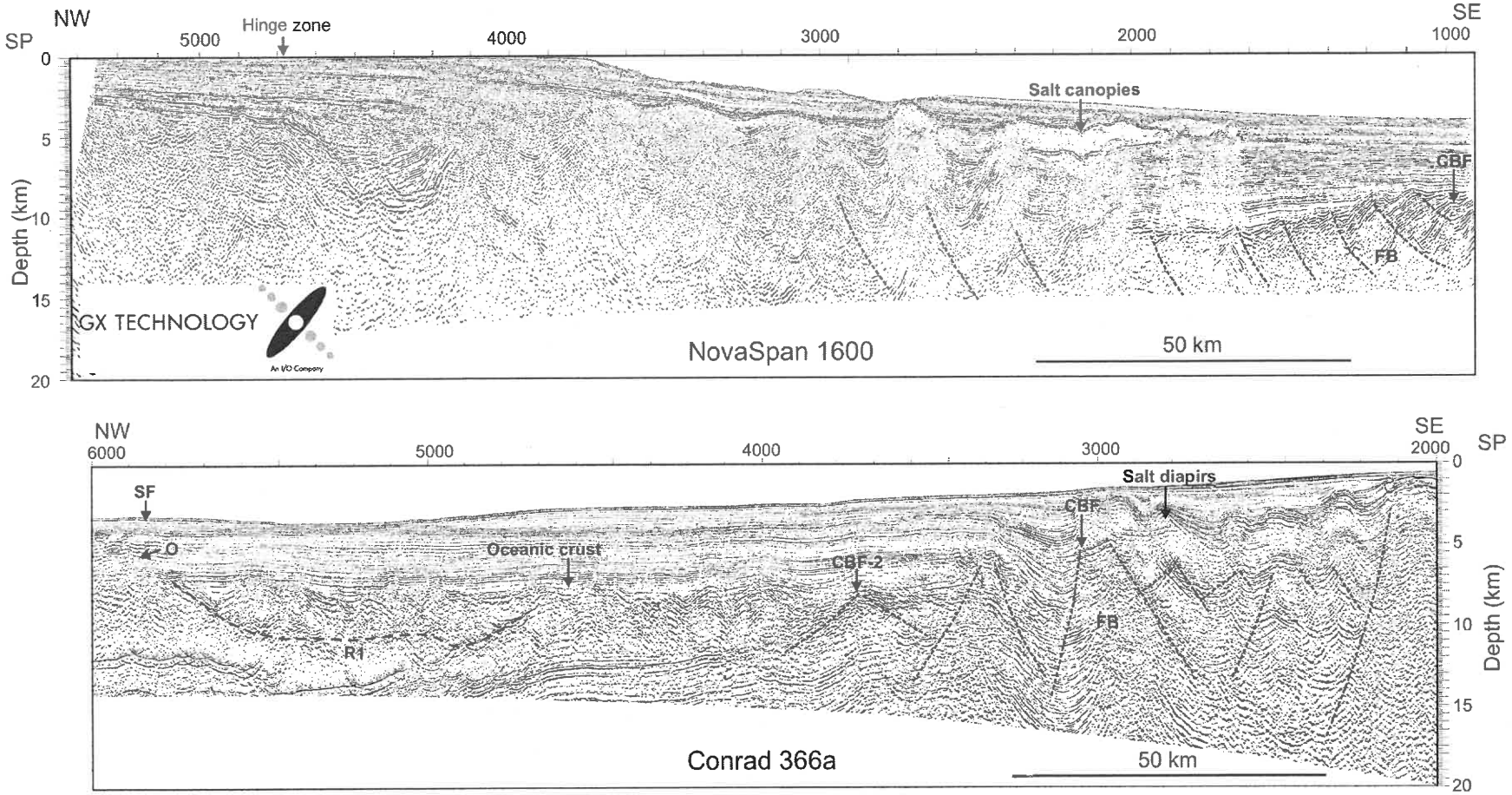

Figure 5.3. Depth sections of conjugate profiles of NovaSpan 1600 and Conrad 366a. CBF-2 is the specific continental breakup front (CBF) that is interpreted from the seismic profile. Marked features are discussed in text. Features refer to Figures 5.1 and 5.2.

5.2.1.3 NovaSpan 1800 versus Conrad 368

Figure 5.4 shows the conjugate profiles of the NovaSpan 1800 and Conrad 368. On the Scotian side, the CBF is located beneath the seaward edge of the salt canopy at the southeast end of NovaSpan 1800, no FBs are imaged similar to those along 88-1A and NovaSpan 1600. Instead, the basement here is quite smooth (S, upper panel). No velocity information is available for this region, but this line is very close to SMART Line 1 (Funck et al. 2004), and the smooth basement topography is also similar to that at the seaward end of 89-1 (see Figure 5.9a; Keen and Potter 1995b), which was interpreted as exposed mantle based on the velocities derived along coincident refraction profile Line 1. This indicates that the smooth basement along NovaSpan 1800 may also be exposed mantle. However, this is less certain due to the fact that the crustal structure varies greatly along the margin according to the velocity models of SMART Lines. Note that a strong reflector is imaged in the basement, starting at the CBF and extending further seaward (M, upper panel, Figure 5.4). The character of this reflector and the basement above this reflector will be further discussed in section 5.3.2 by correlating with reflectivity along the neighbouring profiles.

On the conjugate side (Conrad 368, lower panel), the CBF based on proposed minimum reconstruction is roughly situated at the seawardmost dirpiric salt, where a deep fault basin is imaged seaward. Further seaward of the fault basin, small scale FBs are imaged bounded by seaward dipping faults, similar to the FB shown in Figures 5.2, and 5.3, indicating that some highly thinned continental remnant still exists seaward of the fault basin. This re-located seaward limit of the rifted continental crust (CBF-2, lower panel,

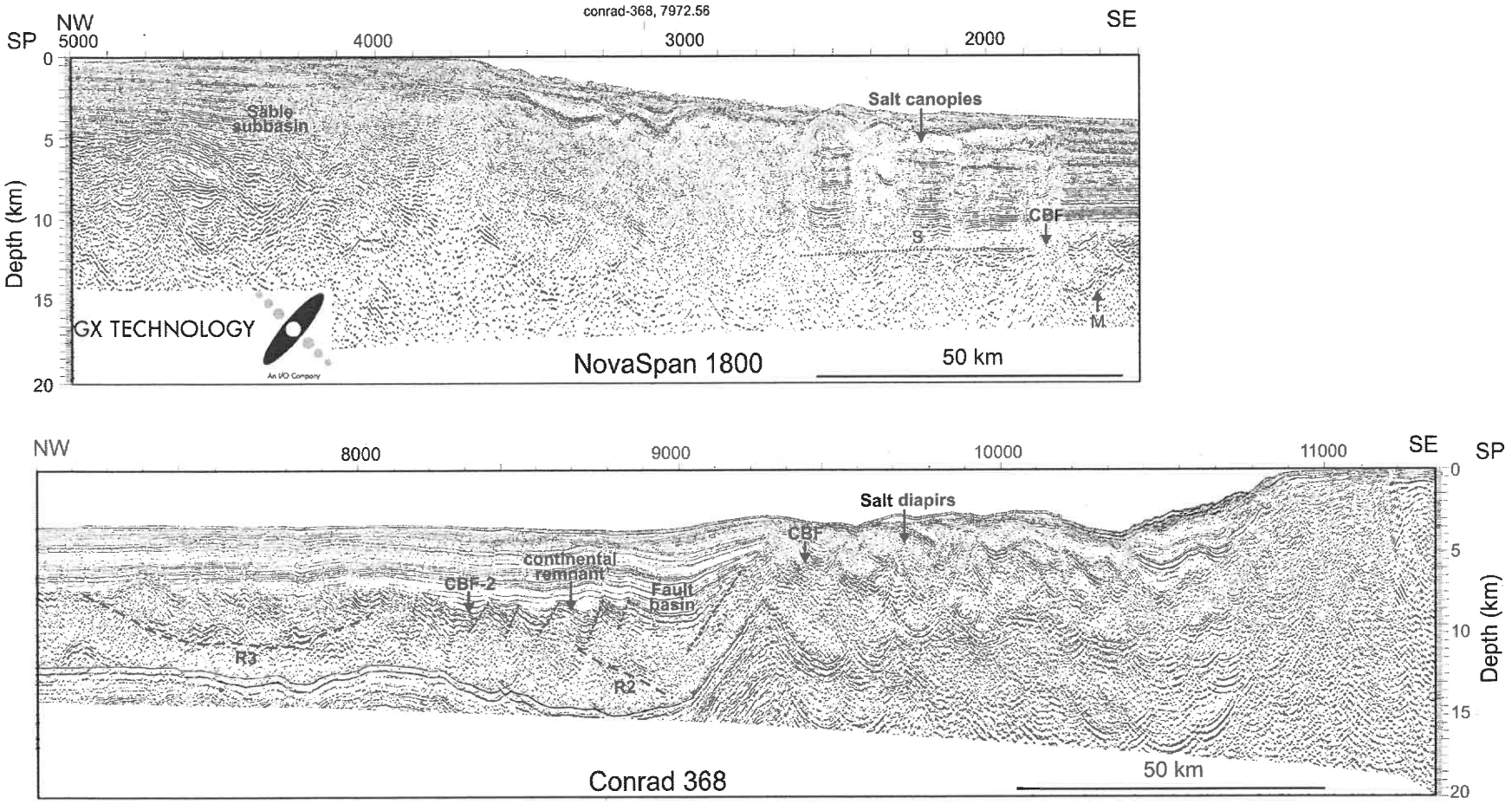

Figure 5.4. Depth sections of conjugate profiles of NovaSpan 1800 and Conrad 368. Features refer to Figures 5.1 and 5.2.

Figure 5.3) is shifted seaward of the CBF based on the proposed minimum reconstruction. Therefore the continental breakup across this specific conjugate segment may also be irregular (CBF-2, Figure 5.4, lower panel), similar to that imaged along Conrad 366a.

A reflection is present beneath the last portion of continental basement along Conrad 368 (R2, lower panel, Figure 5.4). This reflection rises from underneath the fault basin and reaches the base of the FBs (roughly at SP 8500). The character of the basement and underlying reflector will be further discussed in the following section. Further seaward, a second crustal reflection is locally imaged (R3, lower panel, Figure 5.4), which is similar to the reflection R1 imaged in Figure 5.3.

The sediment loading on both sides is imaged in an asymmetrical pattern, similar to observation along the conjugate profiles of NovaSpan 1600 and Conrad 366a (Figure 5.3). The sediment fill along NovaSpan 1800 is up to ~12 km thick and also characterised by prominent salt canopies, in contrast to the thinner sediment loading (~5-6 km) with diapiric salt along Conrad 368.

5.2.1.4 NovaSpan 2000 versus Conrad 380

Figure 5.5 shows the northeastmost pair of conjugate MCS profiles NovaSpan 2000 and Conrad 380. At the seaward end of NovaSpan 2000, the basement image is similar to that of NovaSpan 1800 (Figure 5.4) and that observed along 89-1 (Figure 5.9a), indicating that the smooth basement along NovaSpan 2000 may also be exposed mantle. Along profile Conrad 380, the basement topography seaward of the diapiric salt (at SP 9800) is

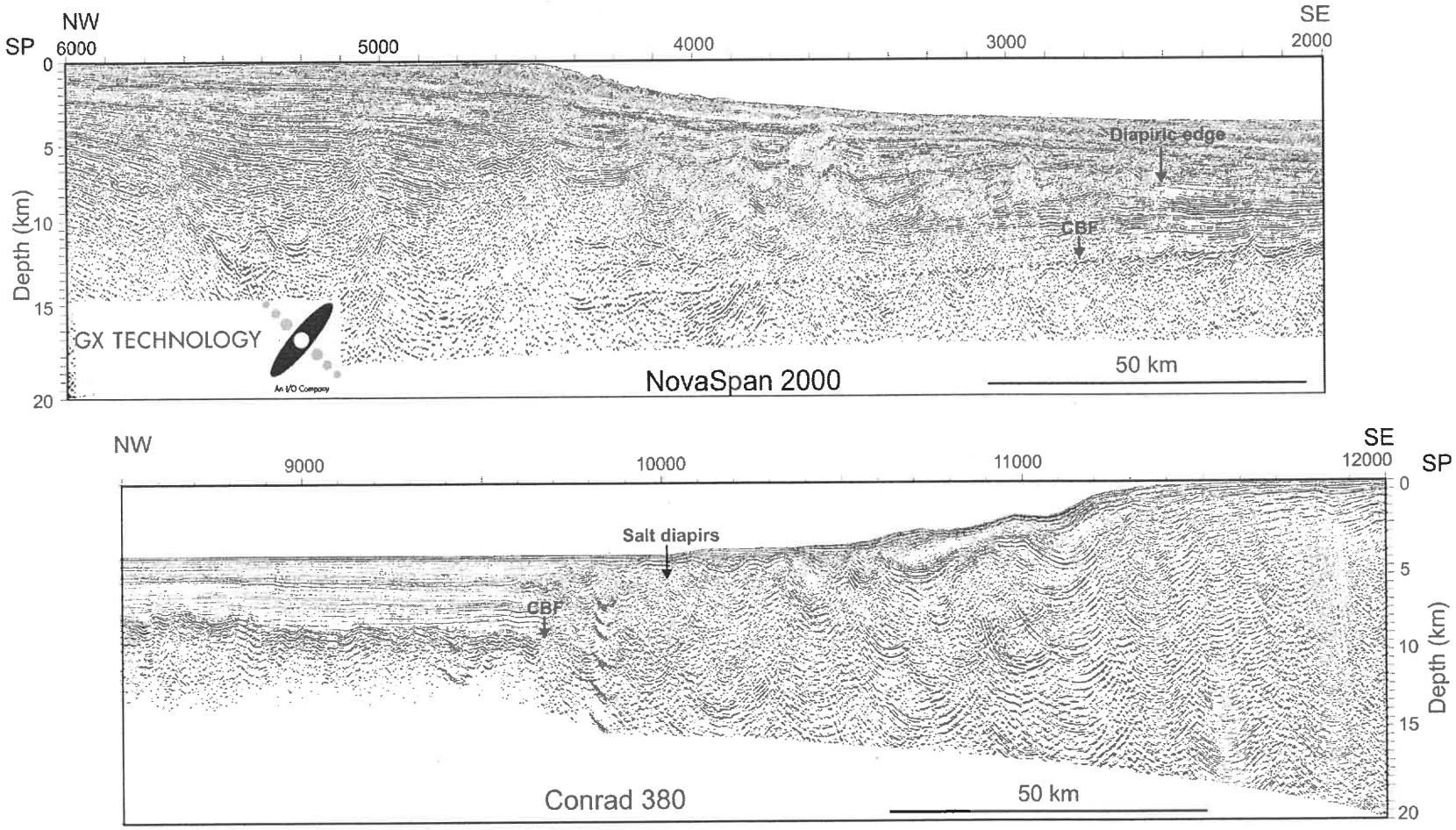

Figure 5.5. Depth sections of conjugate profiles of NovaSpan 2000 and Conrad 380. Features refer to Figures 5.1 and 5.2.

fairly smooth, which is untypical of slow spreading oceanic crust, or rifted continental crust. However, the CBF based on the proposed reconstruction (in chapter 4) is located at the oceanward edge of the salt diapirs, indicating that the basement seaward is more likely oceanic character. Unfortunately, the basement structure is not fully imaged along this profile because no seismic data exists beneath the depth of 12 km.

5.2.2 Seismic Images along Strike Profile NovaSpan 5100

The structural variation along the strike of the Scotian margin is shown in Figure 5.6. At the southwestern end of the strike line NovaSpan 5100 (Figure 5.6c), dipping reflections are imaged in the basement. The seismic expression of these reflections is characterized on dip sections as seaward dipping reflectors (SDR; Keen and Potter 1995a), which are also observed along the dip profile NovaSpan 1100 (SDR, Figure 5.6a). These SDR are thought to be seismic expressions of extrusive rocks of rift volcanism across the SW Scotian margin (Keen and Potter 1995a; Dehler 2007, personal communication). Northeast of profile NovaSpan 1100, SDR sequences are no longer observed (e.g. NovaSpan 1400 in Figure 5.6b, 88-1A).

A ~100-km-wide zone (VNT, Figure 5.6c), featured by rugged basement topography with greater depths than the basement on either side, appears at the disappearance of the SDR sequences and ends at a major basement high (BH, Figure 5.6c). This zone seems to be highly faulted or compressed, illustrated by the V-shape basement topography, and marks a transition where the SDR sequences occur to the southwest but no longer appear to the northeast.

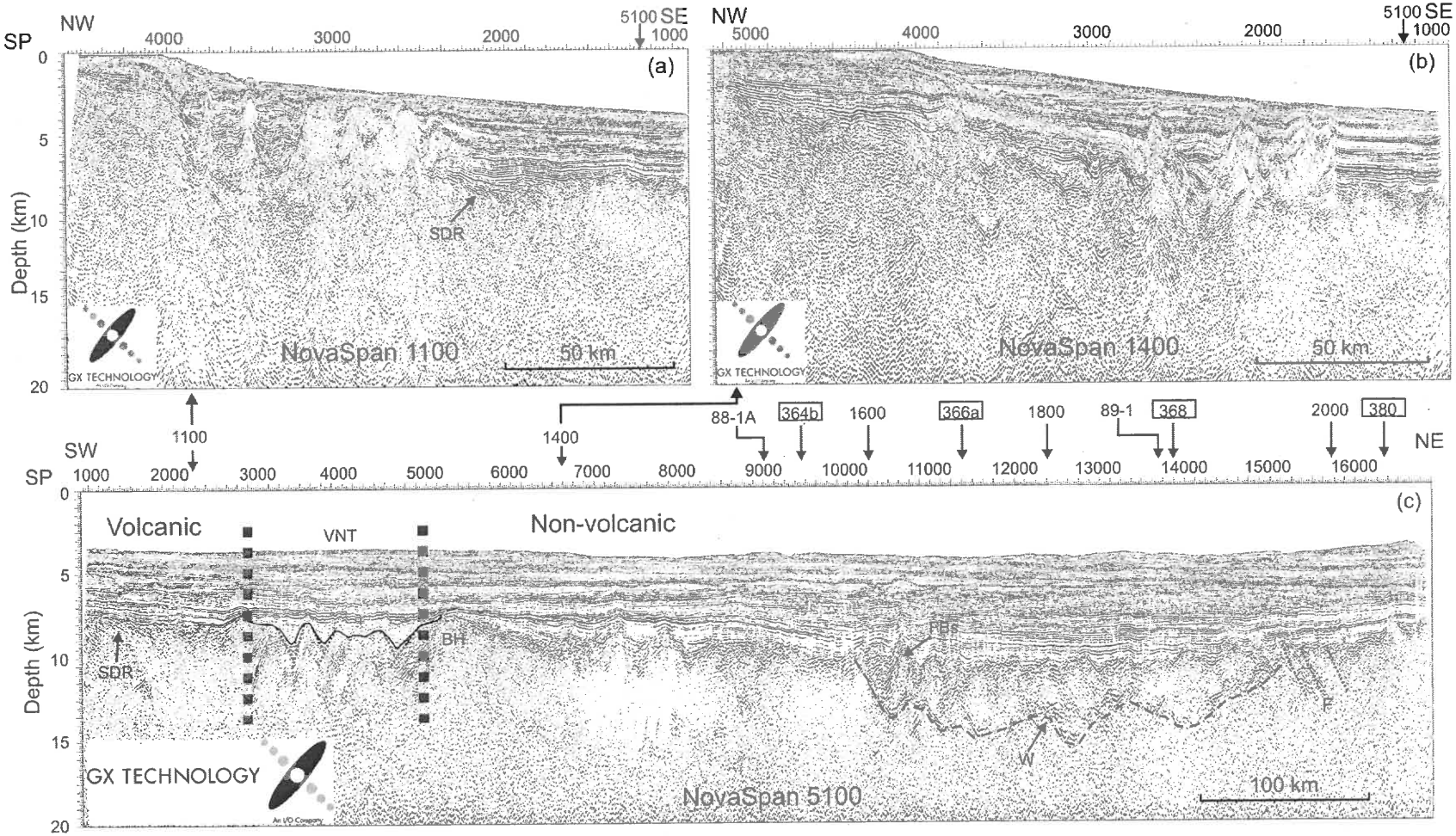

Figure 5.6. Depth sections of the strike profile NovaSpan 5100 and two dip profiles NovaSpan 1100 and 1400. The crosspoints for all dip profiles are marked along the strike line NovaSpan 5100, with the line numbers off Nova Scotia open and the lines off Morocco in boxes. The volcanic to non-volcanic transition (VNT) is indicated by a vertical dashed line. SDR: seaward dipping reflectors. For other features refer to Figures 5.1 and 5.2.

Further northeast, faulted basement blocks (FBs) are imaged between SP 10000-11500. According the proposed minimum reconstruction, these FBs are spatially coincident with those which appear on lines 88-1A, NovaSpan 1600, and Conrad line 364b, 366a and 368, forming a zone of FBs at the continental breakup front between the central and northern segments of the margin conjugates (green region, Figure 5.7).

From this FB zone to almost the northeast end of this profile, the basement is characterized by an irregular reflector (W, Figure 5.6), which starts from the base of the FBs and extends ~250 km towards northeast until it reach the top of the basement around SP 16000, where a 30-km-wide band of NE dipping events appear in the basement (F). As shown in Figure 5.4, this reflector is also imaged at the seaward end of the dip profile NovaSpan 1800 and LITHOPROBE 89-1 (Keen and Potter 1995b) and BGR 89-12 (unpublished). The plan view of these major reflections is outlined in Figure 5.7 (yellow region). The nature of the basement above it will be discussed in the section 5.3.1.2.

5.2.3. Structural Variation along the Scotian and Moroccan Conjugates

The general structures derived from foregoing seismic profiles are summarized in the map of minimum reconstruction (Figure 5.7). The southwestern part of the Scotian margin is volcanic, illustrated by the SDR sequences in the basement along a number of MCS profiles (e.g. 89-3 and 4, NovaSpan lines 1100 and 5100) and thickened high-velocity lower crust layer along SMART Line 3, indicative of underplated rocks (Dehler 2007, personal communication).

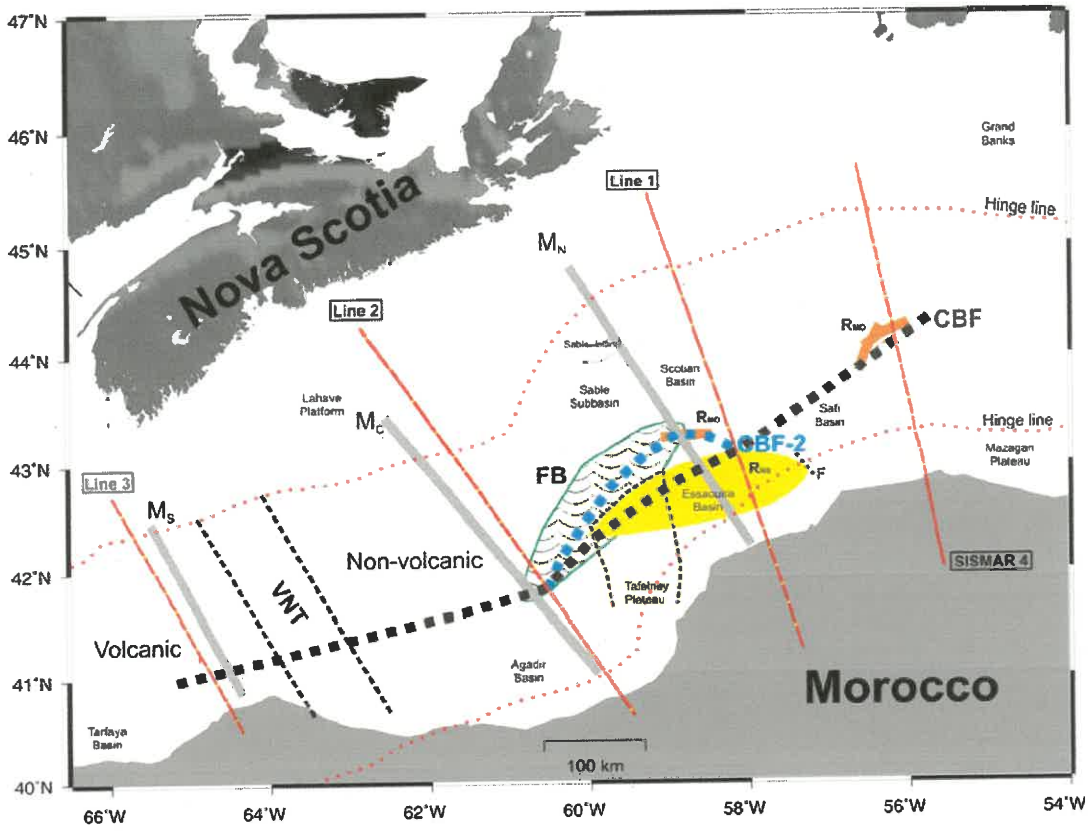

Figure 5.7. Major structural features along the Scotian/Moroccan conjugates. The black dotted line represents the continental breakup front (CBF) based on the minimum reconstruction proposed in chapter 4. The blue dotted line represents the continental breakup front (CBF-2) based on the seismic profiles presented in this chapter. The red dotted lines indicate the hinge lines taken from Tari and Monlar (2005). The yellow area indicates the distribution of crustal reflections off Nova Scotia (R_{NS}) derived from MCS profiles LITHOPROBE 89-1, BGR 89-12, NovaSpan lines 5100 and 1800. The orange bars denote the locations of crustal reflection observed off Morocco (R_{MO}). M_S, M_C and M_N (grey lines) indicate the locations of conceptual models across the southern, central and northern margin segments in Figures 5.13-5.15. The two black dashed lines indicate the volcanic to non-volcanic transition (VNT) along the conjugate margins. The Tafelney Plateau is marked by a blue dashed line. FB: faulted basement blocks. For other features refer to Figure 5.1.

Northeast of Line 3, however, the characteristic features for excessive volcanism are no longer observed. A 100-km-wide zone featured by rugged basement topography and relatively deeper basement depths represents a transition (VNT, Figures 5.6 and 5.7) that separated the volcanic SW Scotian margin from the non-volcanic margin to the northeast. This transition is not yet defined on the Morocco margin due to the overprinting of more recent Cenozoic volcanism, but the same transitional character should apply to the Morocco side based on the proposed minimum reconstruction in chapter 4. Therefore, the majority of the Scotian/Moroccan conjugate margins, except for the southwestmost part, were rifted by non-volcanic extension.

Between the central (Line 2) and northern conjugate segments (Line 1, a zone of fault blocks (FB, green zone, Figure 5.7) appears near the CBF derived from reconstruction (see chapter 4). Across the central segment, these FBs are symmetric, with their seaward limits consistent with the CBF on both sides. Northeast of Line 2, FBs still appear on both sides of the conjugate profiles until they disappear north of the Tafelney Plateau or south of the Sable basin in the proposed minimum closure. The elongated FB zone extends obliquely against the general strike of the conjugates such that the continental breakup front also deviates from the CBF to the Scotian side, leaving an irregular breakup boundary in this region (dotted blue line CBF-2, Figure 5.7). The irregular breakup boundary in this region will be related to different rifting styles along this margin pair in the following sections.

The northeast margin pair is characterized by intra-basement reflections on both sides. For the Nova Scotia margin, the strong reflections are consistently imaged on the dip

profiles of LITHOPROBE 89-1 and NovaSpan 1800 and the strike profile NovaSpan 5100 at depths of 11-15 km, indicating one major crustal reflector (yellow patch, R_{NS}, Figure 5.7). The southwest limit of the reflector is delimited by the FBs and the east boundary delimited by a band of NE dipping events F (also see Figure 5.6c at SP 15000-16000). However, it is not clear whether these reflections extend further landward or seaward. The landward limit may have been obscured by overlying salt or salt related structures. More seismic data are also required further seaward in order to delineate the seaward limit of this major reflector. The nature of this major reflector will be discussed further in section 5.3. On the Morocco side, a crustal reflection R_{MO} is locally imaged (Figure 5.7) beneath a faulted basement (Figure 5.4). To northeastmost of the Morocco margin, an intra-basement reflection is imaged along MCS profile SISMAR 10 (Figure 5.7) near SISMAR 4 (Contrucci et al. 2004). However, such a reflection is not clearly imaged in between, along Conrad 380. The nature of this major reflector will also be discussed in the following section 5.3.1.

5.3 Discussion

Figure 5.7 shows that the northern part of the Scotian/Moroccan margin conjugates are characterized by intra-basement reflections on both sides (R_{MO} and R_{NS}). These reflections appear landward or seaward of the CBF (or CBF-2) and therefore, may be related to the breakup of the northern portion of the conjugate pair. The nature of these reflections and their relationship to the separation of the northern margin segment are discussed below.

5.3.1 Reflections of the Northeast Moroccan Margin (R_{MO})

The reflections imaged along SISMAR line 10 (Figure 5.8b) have been interpreted as a lithospheric detachment within the African plate, from which Maillard et al. (2006) proposed a conceptual model for breaking up the northern margin segment. According to this model, the northern portion of the margin pair was separated along a low-angle (6°-7°) lithospheric detachment (see Figure 5.12), leaving the upper plate of rifted crust on the Moroccan side and the lower plate of exposed mantle on the Scotian margin. This model is based on the seismic results from refraction profiles SMART Line 1 (Funck et al. 2004) and SISMAR 4 (Contrucci et al. 2004), which were considered at conjugate locations according to reconstruction of Sahabi et al. (2004). However, the minimum reconstruction proposed in chapter 4 shows that SMART Line 1 and SISMAR lines are offset ~200 km along the margin (Figures 5.1 and 5.7). Therefore, the breakup geometry based on the model of Maillard et al. (2006) may not be applicable for the entire northern portion of the conjugate margin.

This is illustrated by the absence of a clear crustal/lithospheric detachment further southwestward off Morocco. Along line Conrad 380, which is ~100 km west of SISMAR 4, no reflection is imaged in the basement (Figure 5.5). Along Conrad 368, which is further southwest of Conrad 380 (Figure 5.1), although a weak local reflection is imaged in the basement (R2, Figure 5.4), this reflection (R2) is not a comparable feature to the "L" reflector imaged along SISMAR 10 (Maillard et al. 2006). The time sections of these two profiles are presented in the same scale in Figure 5.8. The "L" reflector consists of a 0.5 s thick (TWT) band of high-amplitude parallel reflections that dip landward to ~12 s

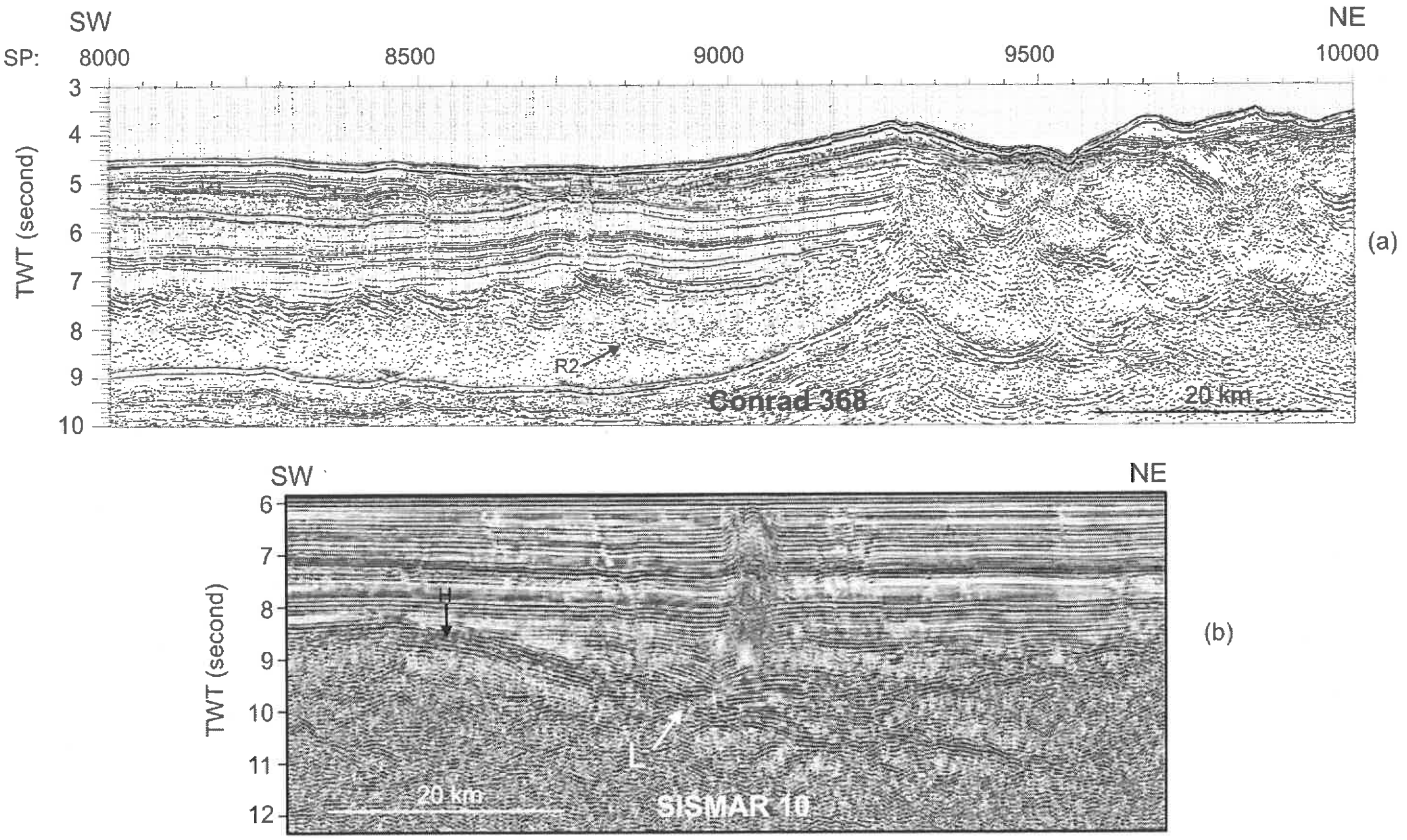

Figure 5.8. (a) Time section of Conrad 368 shown Figure 5.4b (Holik et al. 1991). (b) The seismic image of MCS profile SISMAR 10 after Maillard et al. (2006). This profile perpendicularly crosses SISMAR 4 at the CBF, which is shown in Figure 4.2. Sections (a) and (b) are plotted in same scale. R2 and L are intra-basement reflections.

(see Figure 6 of Maillard et al. 2006). This reflector also outcrops to the basement surface at a basement high with internal layering (H, Figure 5.8b). The reflection R2 along Conrad 368 is a narrow (~ 5 km wide) and disjointed feature (Figure 5.8a). Its amplitude is much weaker and without internal layering, compared to "L" in Figure 5.8b. Reflection R2 also does not reach the basement surface and it is not clear how deep it extends due to the appearance of multiples. Furthermore, SISMAR 10 is one profile perpendicular to SISMAR 4 (see Figure 5.1), the "L" reflection imaged along SISMAR 4 and other SISMAR lines dips to northeast, rather than southeast. These features suggest that the crustal or lithospheric detachment observed along SISMAR lines does not extend to profile Conrad 380 and further to the southwest.

5.3.2 Reflections of the Northeast Scotian Margin (R_{NS})

Figure 5.7 shows that crustal reflections are also imaged seaward of the rifted continental crust off Nova Scotia (yellow patch). Based on the velocity model along SMART Line 1 (Funck et al. 2004), the crustal reflection imaged at the seaward end of coincident MCS profile 89-1 (Figure 5.9a) is interpreted as a velocity boundary within the upper mantle. The layer above this reflector was interpreted as highly serpentinzed exposed mantle, which is characterized by smooth basement topography and constant thickness (~2 km). The layer underneath was interpreted to be partially serpentinized mantle. According to this view, the intra-basement reflection is ascribed to an abrupt vertical change in the degree of serpentinization of the upper mantle (Funck et al. 2004).

Figure 5.9. (a) Part of migrated time section of MCS line 89-1 (Keen and Potter, 1995b). (b) Part of migrated time section of BGR line 89-12 (unpublished, data courtesy German Federal Agency of Geosciences and Natural Resources). (c) Part of the migrated depth section of NovaSpan 5100 (unpublished, data courtesy GX Technology Corporation). The horizontal scale for (a) and (b) is distance along the velocity model (Funck et al. 2004). Horizontal scales are same for all sections. Crossover points are marked. Circles mark the location of OBS. Features marked by letters are M, intra-basement reflector; SHSM, seaward limit of highly serpentinized mantle; S, relatively smooth basement at the crossover point on NovaSpan 5100; R, relatively rough basement on NovaSpan 5100.

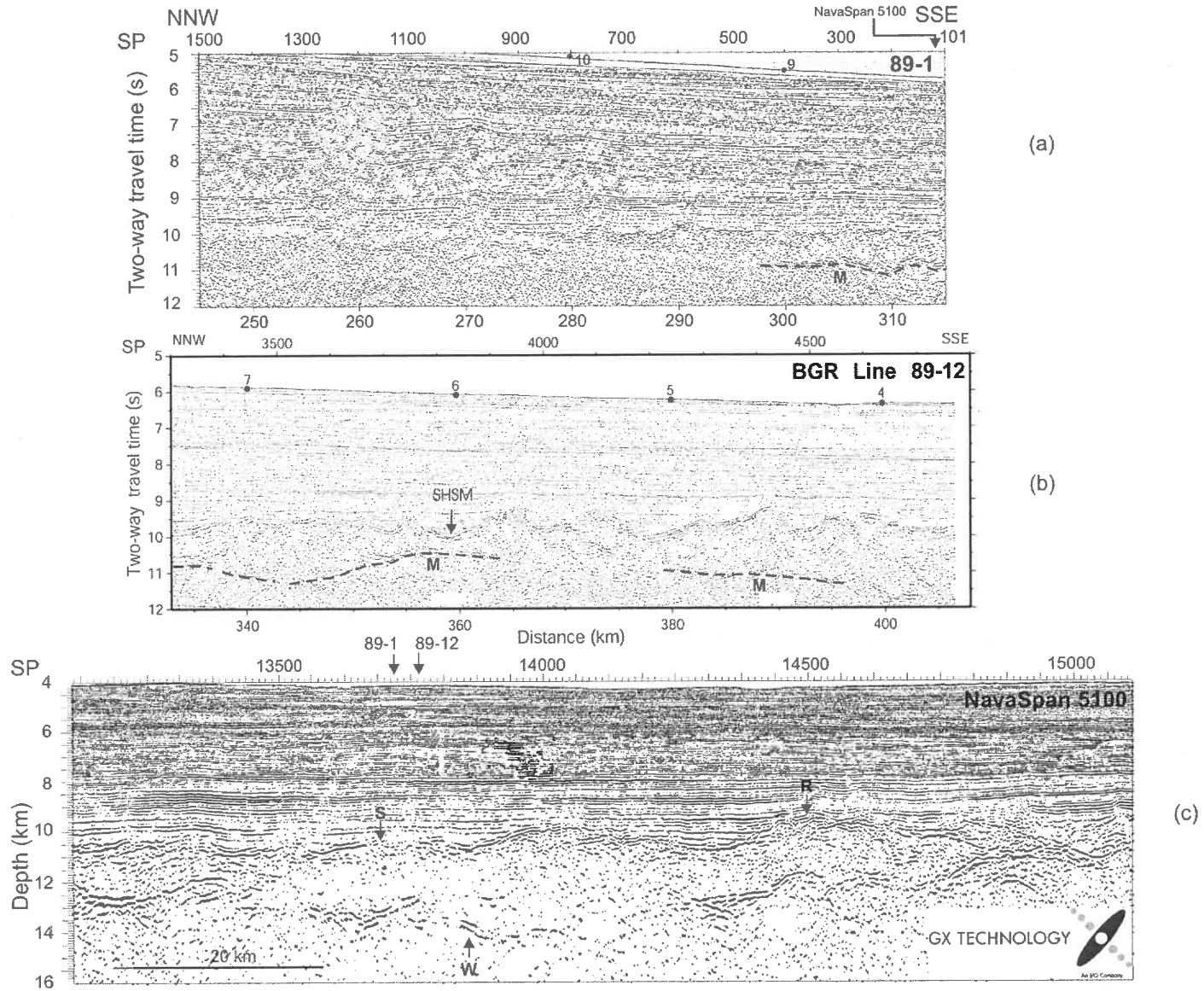
NNW
SSE
NavaSpan 5100
SP
1500
1300
1100
900
700
500
300
101
89-1
Two-way travel time (s)
M
250
260
270
280
290
300
310
(a)
NNW
3500
4000
4500
SSE
BGR Line 89-12
SHSM
340
360
380
400
Distance (km)
(b)
89-1
89-12
13500
14000
14500
15000
NavaSpan 5100
Depth (km)
S
R
W
20 km
GX TECHNOLOGY
(c)

However, the seismic images further seaward of 89-1 are not consistent with this interpretation. Figure 5.9b is a migrated time section of BGR 89-12 seaward of 89-1. Along BGR 89-12, intra-basement reflections are continuously imaged (M, Figure 5.9b), which are unequivocal Moho reflections based on the seismic velocities derived from refraction data (Funck et al. 2004). These intra-basement reflections are consistent in depth with that imaged at the seaward end of 89-1 (M, Figure 5.9a), suggesting that the upper basement layer at the seaward end of 89-1 may also have an oceanic character. In addition, although the upper basement layer has a constant thickness (~1 s TWT or ~2 km) for ~15 km distance at the seaward end of 89-1, its thickness varies greatly further seaward, from less than 0.5 s TWT (SP 3800, Figure 5.9b) to 1.5 s TWT (SP 4500, Figure 5.9b). The variable thickness from the seaward end of 89-1 to the upper layer along 89-12 is also imaged along the strike profile NovaSpan 5100 (Figure 5.9c). Such variations are consistent with the observed oceanic crust for slow seafloor spreading rates (e.g. Jokat et al. 2003; Hopper et al. 2004).

More importantly, the velocity contrast across the intra-basement reflector in the velocity model of Line 1 is rather unusual for mantle serpentinization. Serpentinization results from hydration when mantle material is exposed to seawater or seawater penetrates into mantle. As water penetrates down into mantle, this process usually decreases gradually because of the reduction of seawater influx. Thus we expect to observe a gradual decrease of mantle serpentinization with depth, which is expressed in seismic survey by steep velocity gradients rather than an abrupt velocity discontinuity.

This velocity gradient has been found on most of the non-volcanic passive continental margins. Figure 5.10 shows a number of velocity profiles where the thin upper basement layers were interpreted to be exposed mantle or oceanic crust. For the southeast Newfoundland Basin margin (Lau et al. 2006a; Lau et al. 2006b), the P-wave velocities for the highly serpentinized exposed mantle layer and the partially serpentinized mantle underneath are 4.4-6.4 km/s and 6.4-7.8 km/s (N, Figure 5.10), respectively. No abrupt velocity jump occurs from the basement surface down to the normal mantle. For the case of Iberia Abyssal Plain margin (Dean et al. 2000), the highly serpentinized exposed mantle across IAM-9 presents velocities varying from 4.5-7.3 km/s, with a small velocity contrast (~0.3 km/s) from this layer to the partially serpentinized layer underneath (I, Figure 5.10). The velocity contrast across the Labrador Sea margin (Chian et al. 1995a; Chian et al. 1995b) is relatively large (L, Figure 5.10) compared to the above examples; however, the nature of the upper basement layer is also less definitive. It could alternately consist of continental crust, oceanic crust or exhumed mantle (Chian et al. 1995a). In contrast, the velocity profile for SMART Line 1 presents a sharp velocity contrast (from 5.2 km/s to 7.2 km/s; S1, Figure 5.10), which is consistent with those of the northern Flemish Cap margin (F1, Figure 5.10) and the Arctic Gakkel mid-ocean ridge (G, Figure 5.10), where the upper basement is interpreted to be oceanic crust overlying a partially serpentinized mantle (Jokat et al. 2003; Hopper et al. 2004; Funck et al. 2004). These three margins (red lines, Figure 5.10) can be distinguished from remaining margins along the North Atlantic shown in Figure 5.10 by the strong velocity contrasts and low gradients across the boundary from the thin upper basement layer to the partially serpentinized mantle underneath. Furthermore, the velocity gradient within the upper

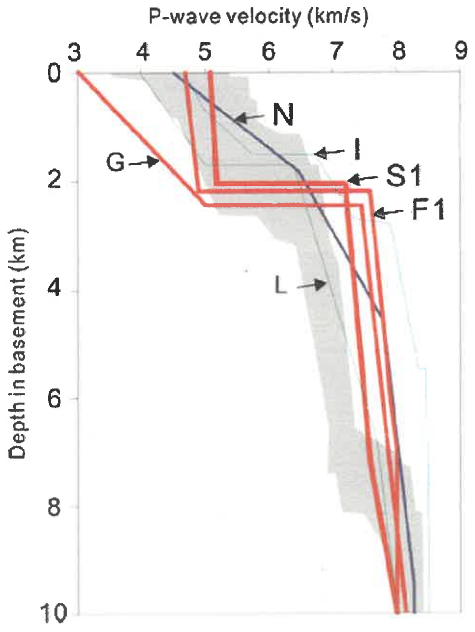

Figure 5.10. One-dimensional velocity profiles for a number of passive margins along the North Atlantic. S1: SMART Line 1 (Funck et al. 2004); N: Southeast Newfoundland Basin margin (Lau et al. 2006a); F1: Flemish Cap margin line 1 (Funck et al. 2003; Hopper et al. 2004); I: Iberia Abyssal Plain IAM-9 (Dean et al. 2000); L: Labrador margin (Chian et al. 1995a); G: Gakkel mid-ocean ridge (Jokat et al. 2003). The red lines show sharp velocity contrasts across the boundary from the upper basement layer to the layer underneath, while the remaining velocity profiles present varying velocity gradients across that boundary. Shaded area bounds the velocities for typical Atlantic oceanic crust (59-170Ma; White *et al.* 1992).

basement layer for SMART Line 1 is also very low (0.1^{-s}), which is quite unusual for highly serpentinized mantle compared to velocity profiles of similar kind margins (e.g. I, L, N in Figure 5.10). The above features would also favour an oceanic character for the upper basement layer, rather than a highly serpentinized exposed mantle off the northern Nova Scotia margin.

An alternative seismic characteristic that would argue against this interpretation comes from the "smooth" basement at the seaward end of the 89-1 (Figure 5.9a), which is inconsistent with oceanic crust of extremely slow spreading rates. The roughness of the relatively "smooth" basement topography for this region is quantified using the approach of Malinverno (1991), who measured the roughness as the root-mean-square (RMS) deviation of the top of the oceanic crust from a best-fitting straight line for a series of profiles across ridge axes. The seismic data used for roughness calculation is the section between distances 290-360 km shown in Figures 5.9a and 5.9b. These time sections are converted to depth using velocity model of Funck et al. (2004). The residual depths and statistical RMS roughness for this zone is shown in Figure 5.11a.

Figure 5.11a demonstrates that the residual depths from distance 290-340 km are within ±300 m with one exception at distance ~305 km. From distances 340 km to 370 km, the residual depths gradually increase to ± 600 m. The RMS roughness for this entire zone is 215 m (Figure 5.11b), which is within the normal range of the mean basement roughness values of Malinverno (1991) and Goff (1991, 1992) for oceanic basement at half spreading rate of 19 mm/yr (filled "◊" marked by A, Figure 5.11c). This indicates that the

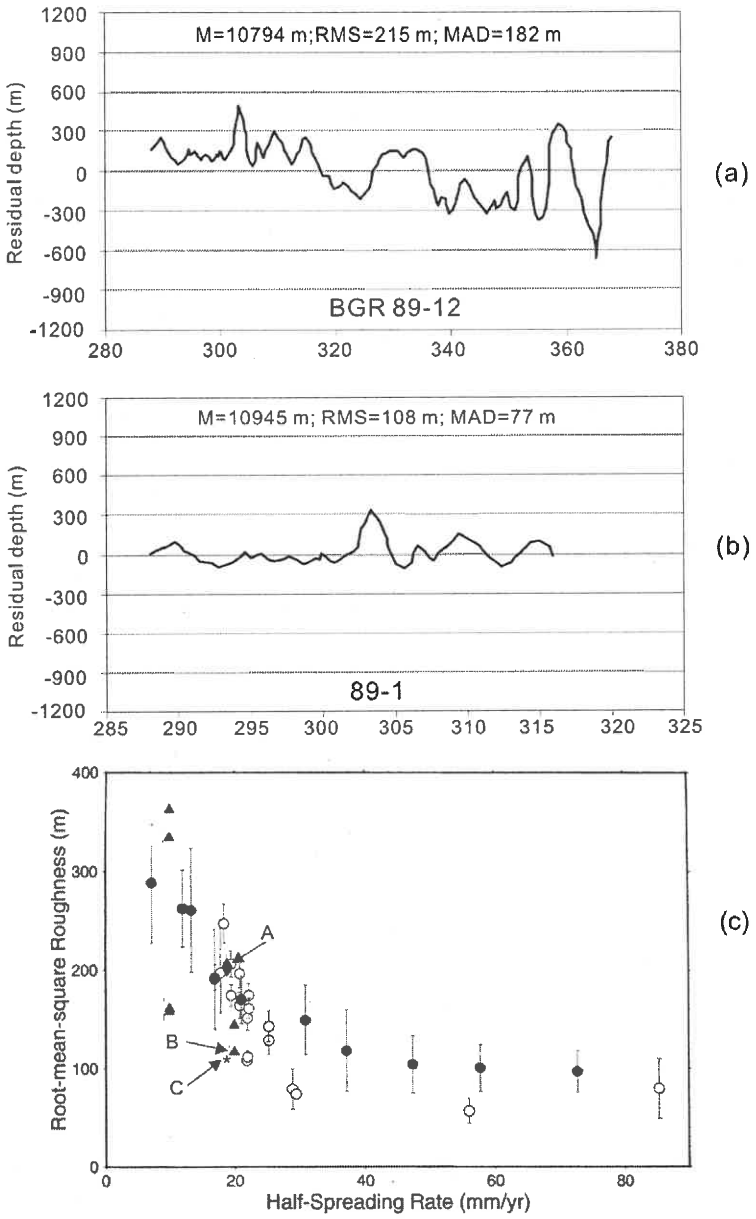

Figure 5.11. (a) Residual basement relief after removal of the mean value of the basement topography (10794 m) for the relatively smooth basement from distances 290 km to 370 km along BGR 89-12 (unpublished), which is ~2.34 km north of 89-1. (b) Residual basement relief after removal of mean value of basement topography (10945 m) along 89-1, which is the landward portion of relatively smooth basement in (a). (c) The oceanic basement roughness versus half-spreading rate after Minshull (1999). Filled and open circles with error bars mark mean roughness values from Malinverno (1991) and Goff (1991, 1992), respectively. Triangles mark roughness of Mesozoic oceanic crust based on seismic data of Blake Spur lines, Canaries line and mid-Atlantic Ridge line at the equator. Markers "◆" (labeled by A) and "*" (labeled by C) are roughness values calculated in this study. "*" is derived in panel (a), "◆" is based on calculation in (b). M: mean depth; MAD: mean absolute deviation; RMS: root-mean-square.

"smooth" basement topography from the seaward end of 89-1 (Figure 5.9a) to the landward portion of 89-12 (Figure 5.9b) can still be classified as oceanic crust according to the statistical RMS roughness for the specific spreading rate.

However, the basement at seaward end of 89-1 (290-315 km, Figure 5.9a) does seem to be much "smoother" than the basement further seaward. The RMS roughness for this narrow zone is quantified separately without including the relatively rougher seaward portion. Figure 5.11b shows the residual depths and corresponding RMS roughness, which is also compared with the statistical oceanic basement roughness in Figure 5.11c. Figure 5.11c shows that the RMS roughness for the "extremely smooth" basement ("*" marked by C, Figure 5.11c) is less than the mean roughness of Malinverno (1991), Goff (1991; 1992) and Minshull (1999) for spreading rate of 19 mm/yr. The low roughness number (108 m) indicates the basement at the seaward end of 89-1 is "smoother" than typical oceanic crust for this particular spreading rate, and may therefore support the interpretation of exhumed and highly serpentinized mantle (Funck et al. 2004). Note that the oceanic crust along the Blake Spur lines 711/714 (Morris et al. 1993), based on the result of Minshull (1999), also bears anomalously smooth basement relief (roughness: 117 m; triangle marked by "B") for a similar seafloor spreading rate (~19 mm/yr) to this case. Minshull (1999) ascribed that anomalously smooth basement to the influence of the Cape Verde hotspot and an isolated melt anomaly in the mantle at the time of crustal formation. For the non-volcanic eastern Canadian margins and their European conjugates, the basement across the OCT zone is most likely comprised of serpentinized upper

mantle (Louden and Chian 1999). The extremely smooth basement relief in this case may due to no melt supply at the onset of seafloor spreading.

According to the forgoing discussion, neither of the alternate interpretations is fully supported by observations, with seismic velocities largely supporting the oceanic interpretation while the basement relief more likely supporting an exposed mantle layer. The *P*-wave velocities of the highly serpentinized mantle layer are also within the normal range of oceanic layer 2 (White et al. 1992; shaded area in Figure 5.10), indicating that these two scenarios may not be discriminated from each other simply by seismic surveys. Or, these two scenarios may be concurrent at the initial stage of ocean opening. This could happen at slow rates when melt production was so limited that volcanic lava flows could not fully fill the gap between the separated plates. Lau et al. (2006a) reported a similar case across the transitional basement of the Newfoundland margin, where refraction data of one instrument support the existence of exhumed serpentinized mantle, while the refraction data of adjacent instrument prefer oceanic layer in the upper basement. If this is true, mantle exhumation persisted for a period of time while a small amount of magma was generated intermittently to form the upper thin layer of mixed nature.

5.4 Formation of the Scotian and Moroccan Conjugate Margins

Figure 5.12a shows the conceptual model for a minimum of reconstruction of the Scotian and Moroccan Conjugates proposed by Tari and Molnar (2005). According to this model, the southwest and northeast segments of the Scotian/Moroccan conjugates were

suggested to break up in opposite asymmetries, leaving the upper plate on the Morocco side and a lower plate to the Scotian side for the northeastern segment and the opposite configuration for breakup of the southwestern segment. A more detailed model was proposed by Maillard et al. (2006) across the northestern conjugate margin pair (Figure 5.12b), based on the seismic results of SMART Line 1 (Funck et al. 2004) and SISMAR lines (Contrucci et al. 2004; Maillard et al. 2006). This model is characterized by asymmetrical rifting along a low-angle detachment within the Moroccan plate, which is generally consistent with the conceptual model of Tari and Molnar (2005).

However, no similar detachment is observed along the Conrad profiles (see Figures 5.2-5.5). The reconstruction proposed in chapter 4 also shows that SMART Line 1 and SISMAR lines are not at conjugate positions (grey line SMART1-SISMAR4, Figure 5.12). Furthermore, the seismic images across the central conjugate segments indicate symmetrical breakup geometry instead of entirely asymmetrical rifting. These results suggest that the previous conceptual models need to be revised using recent observations. Two types of conceptual models are constructed across the central and northeastern margin segments, respectively, based in addition on the results presented in this thesis, as well as available publication.

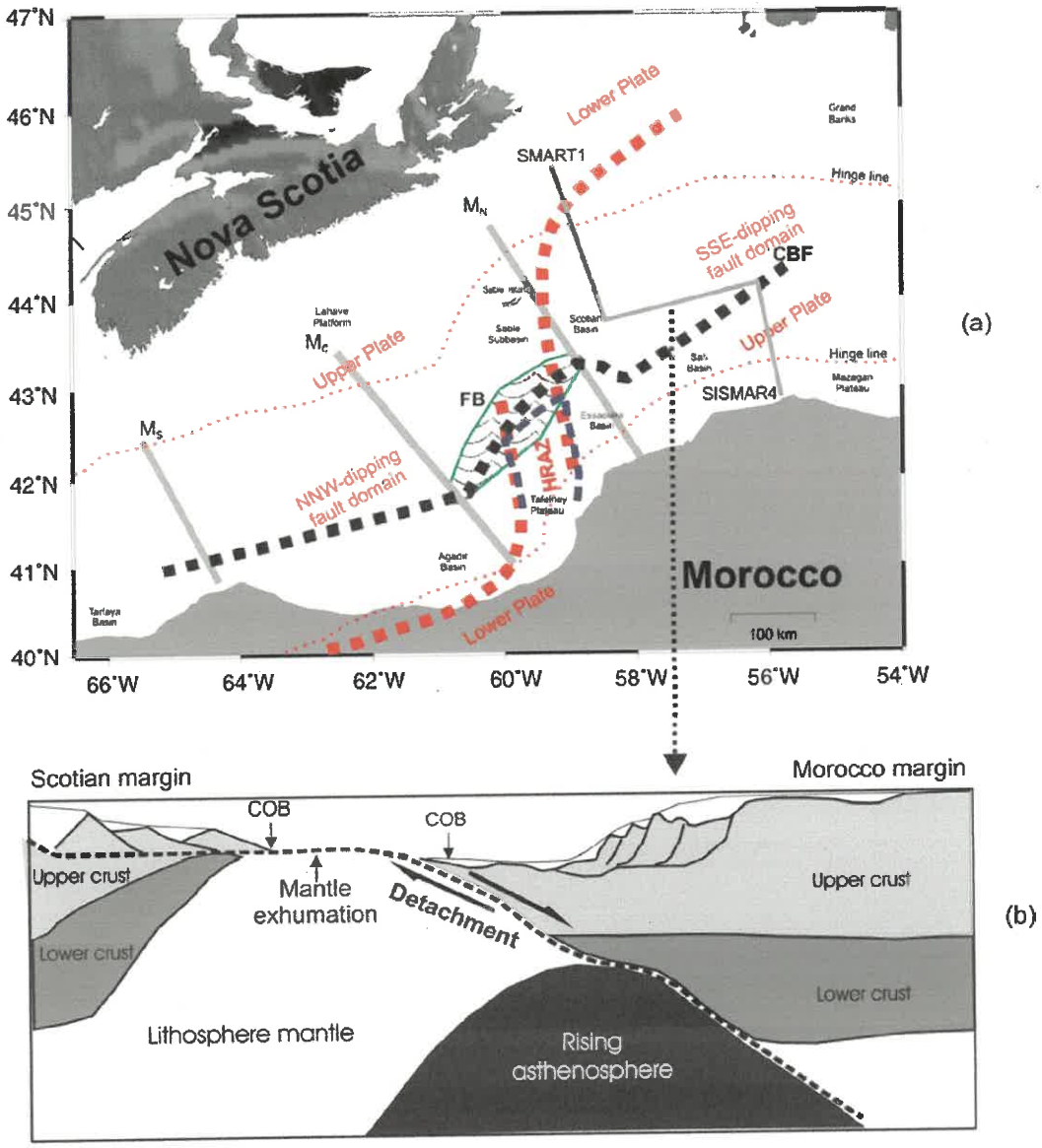

Figure 5.12. (a) Conceptual model of Tari and Molnar (2005) for reconstruction of the Scotian/Moroccan margin conjugates. The red dotted lines indicate the separation geometries based on the conceptual model of Tari and Molnar (2005) and marked features in red indicate the details of this model. M_S, M_C and M_N (thick grey lines) indicate the locations of conceptual models across the southern, central and northern margin segments in Figures 5.13-5.15. For other features refer to Figure 5.7. (b) The conceptual model of Maillard et al. (2006) across the northeastern segment of the Scotian/Moroccan conjugate margin, which is based on the seismic result of SMART Line 1 (Funck et al. 2004) and SISMAR 4 (Contrucci et al. 2004). The approximate location of (b) is indicated by a thin grey line in (a). CBF: continental breakup front; COB: continent-ocean boundary; FB: faulted blocks; HRAZ: high relief accommodation zone.

5.4.1 Conceptual Models Across the Central Margin Segment

The formation of the central Nova Scotia/Morocco conjugate segment (location see Figure 5.7, M_C) is shown at Triassic, Jurassic and Cretaceous ages (Figure 5.13). As rifting began during middle Triassic (Barrett and Keen 1976; Wade and MacLean 1990), the central Nova Scotia margin experienced thermal uplift and erosion (Figure 5.13a). This is constrained by a depth-dependent geodynamic model across the Lahave Platform, which indicated that lithospheric thinning extended about 100 km further landward of the crustal thinning (Keen and Beaumont 1990). There was no such evidence indicative of uplift and erosion off Morocco at syn-rift age (Broughton and Trepaniér 1993). Therefore, the central segment of the conjugate margins may have started to form by asymmetrical rifting across the conjugate segment, with a non-uniform pattern of crustal and lithopsheric thinning on the Scotian side and more likely a uniform pattern on the Morocco side (Figure 5.13a).

From middle Triassic to early Jurassic, limited subsidence due to a small amount of crustal thinning created a platformal cross section on the Scotian side (Figure 5.13b), which is illustrated by modelling of seismic refraction data along SMART Line 2 (see chapter 2 of this thesis). This is not known to exist on the Morocco side due to lack of wide-angle seismic data. The crustal structure across the central margin segments before final breakup, however, is quite symmetrical, illustrated by the FBs symmetrically imaged on the opposing sides of the CBF. The symmetry is also reflected by similar widths of extended continental crust (Figure 5.2). Mantle serpentinization occurred at the final stage of continental rifting beneath the FB blocks due to seawater penetration

through the highly brittle and rifted thin crust, illustrated by the velocity structure along SMART Line 2 on the Scotian side (see chapter 2), although it is not well known on the conjugate side. The Scotian/Moroccan conjugate margins separated during early to middle Jurassic (Barrett and Keen 1976; Klitgord and Schouten 1988; Wade and MacLean 1990).

Seafloor spreading started after the continental breakup with creation of oceanic crust (Figure 5.13c). According the velocity model along SMART Line 2 (Wu et al. 2006), the oceanic crust immediately seaward of the highly thinned continental crust is only 1-2 km thick, but it gradually thickens to 5-7 km, which is within the global range of normal oceanic crust (White et al. 1992). Oceanic crust appears to have accreted symmetrically on both sides, based on seismic image along Conrad profile 364b (Figure 5.2). Mantle serpentinization ceased soon after the onset of seafloor spreading.

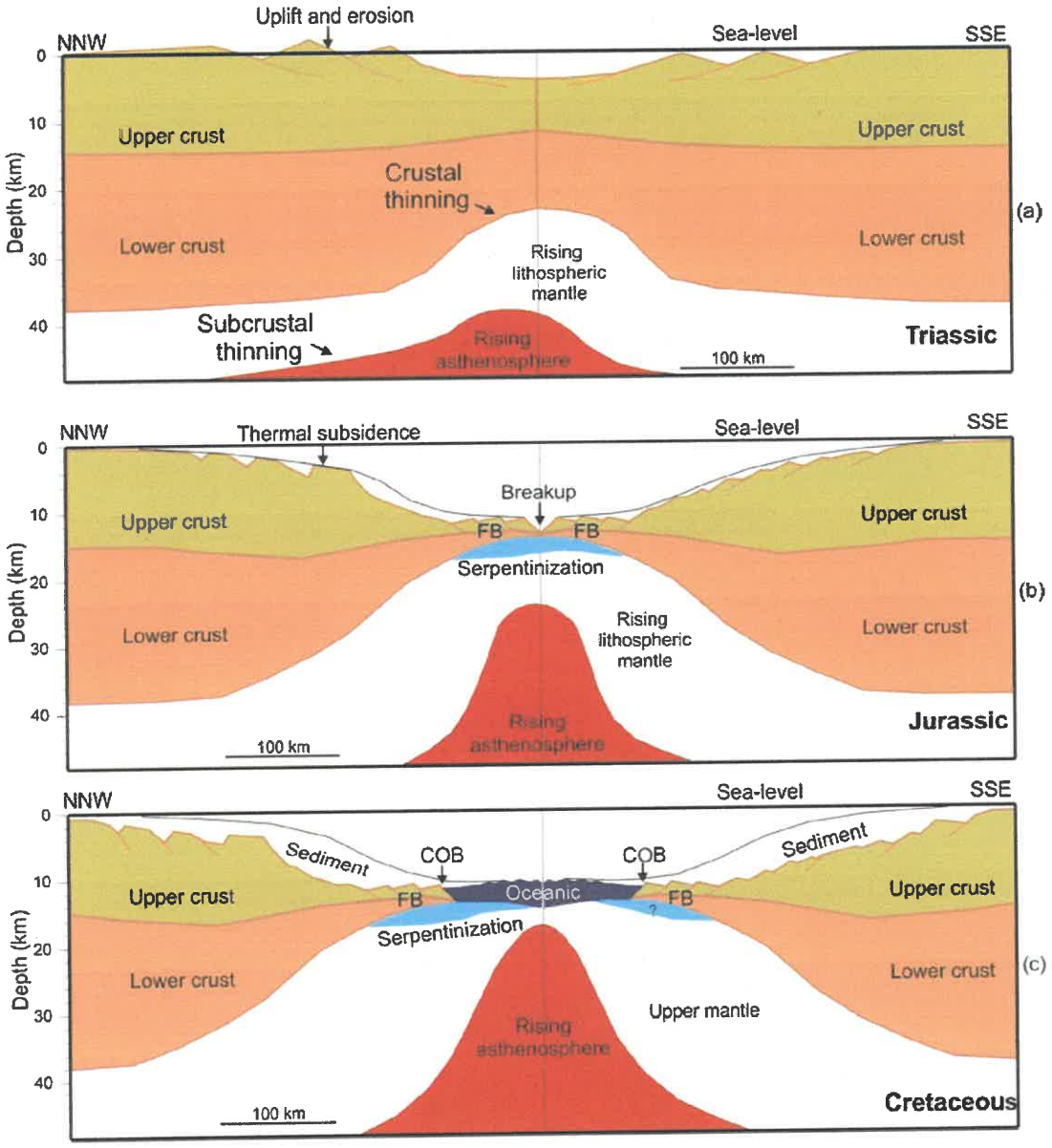

Figure 5.13. Formation of the central segment (M_C) of the Nova Scotia/Morocco conjugates (location see Figures 5.7 and 5.12). Major features at Triassic (early stage of rifting), Jurassic (syn-rift till continental breakup) and Cretaceous (seafloor spreading) ages are shown in sections (a), (b) and (c), respectively. Marked features are discussed in the text. COB: continent-ocean boundary; FB: faulted blocks.

5.4.2 Conceptual Models Across the Northeastern Margin Segment

Figure 5.14 is a schematic depiction of the rifting and early seafloor spreading across the northeastern segment of the conjugate margin (location see Figures 5.7 and 5.12, M_N). At the early stage of rifting (Figure 5.14a), extension was dominated by relatively uniform thinning of the crust and lithosphere, which is constrained by the geodynamic models across the Scotian Basin (Keen and Beaumont 1990) and later further verified by velocity model derived from refraction seismic data (Funck et al. 2004). In contrast to the Lahave platform across the central Scotian margin, the uniform thinning for the northern margin segment produced an initial subsidence in the rifted region, instead of uplift and erosion. It is unknown whether a uniform crustal and lithospheric thinning occurred or not on the Morocco side; however, there is no evidence that uplift and erosion occurred during the middle Triassic or early Jurassic ages (Broughton and Trepaniér, 1993). According to the only available refraction profile SISMAR 4 across Morocco margin (Contrucci et al. 2004), the depths and thicknesses of stretched continental crust beneath the outer shelf are similar to observation along SMART Line 1 (Funck et al. 2004). Therefore, the crustal rifting across the northeastern margin segment M_N is more likely symmetrical during the Triassic stage.

Figure 5.14. Formation of the northestern segment of the Nova Scotia/Morocco conjugates (location see Figure 5.7, M_N). Major features at Triassic (early stage of rifting), Jurassic (syn-rift till continental breakup), late Jurassic to early Cretaceous (seafloor spreading) and Cretaceous (Atlasic compression) ages are shown in sections (a), (b), (c) and (d), respectively. Marked features are discussed in the text.

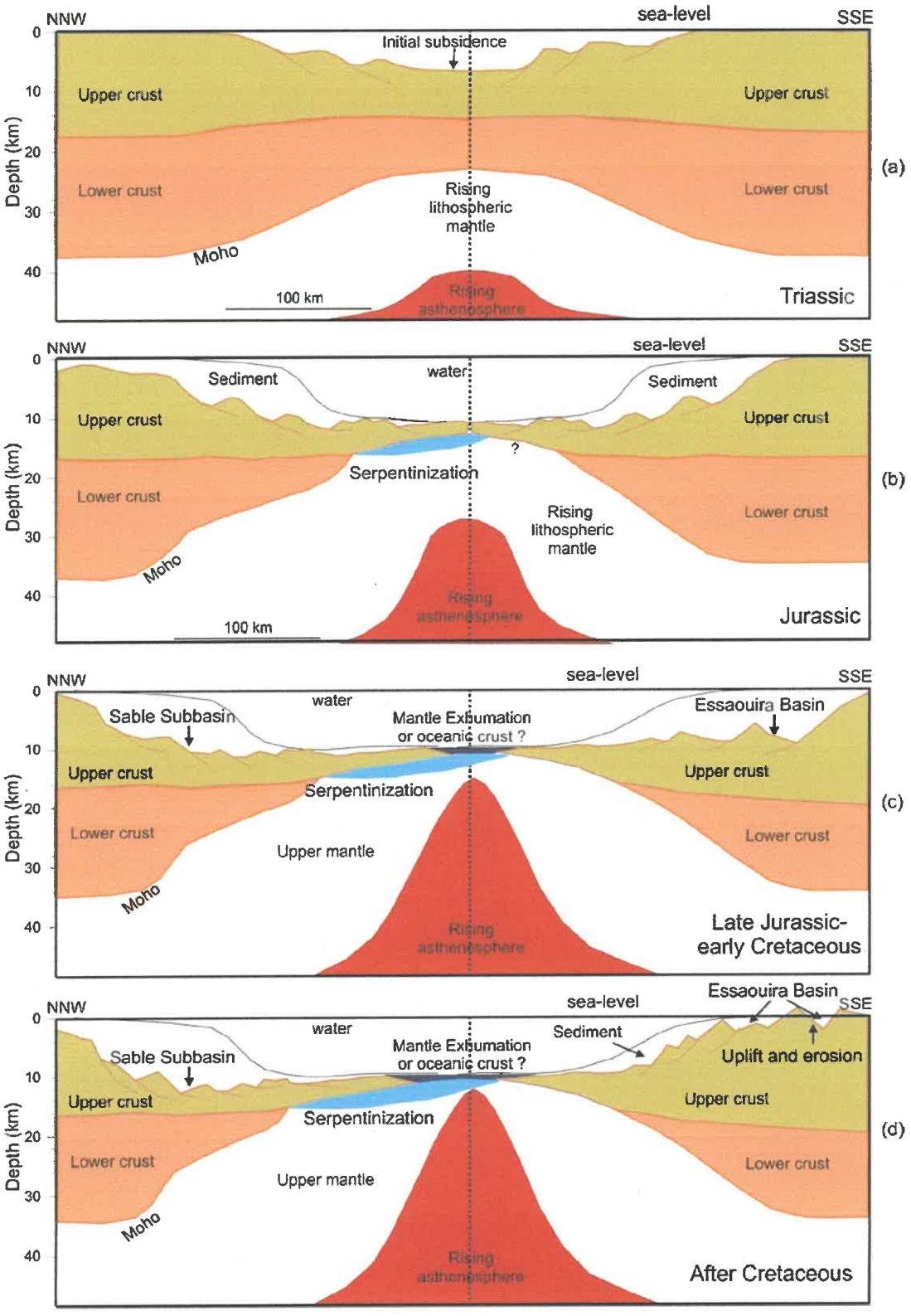
NNW
sea-level
SSE
Initial subsidence
Upper crust
Upper crust
Lower crust
Lower crust
Rising lithospheric mantle
Moho
100 km
Rising asthenosphere
Triassic
(a)
Depth (km)
0
10
20
30
40
Sediment
water
Sediment
Serpentinization
?
Rising lithospheric mantle
Jurassic
(b)
Sable Subbasin
Mantle Exhumation or oceanic crust ?
Essaouira Basin
Upper mantle
Late Jurassic-early Cretaceous
(c)
Sediment
Uplift and erosion
After Cretaceous
(d)

The crustal structure during the Jurassic is only definable offshore Nova Scotia (Figure 5.14b). The velocity structure along SMART Line 1 shows that the lower crust broke up before the upper crust, which is highly thinned to ~3 km and extends ~70 km further oceanward (Funck et al. 2004). A low percentage of mantle serpentinization occurred beneath the thinned upper crust, which may also be due to water penetration through the highly thinned crust. The absence of a steep velocity gradient along SISMAR 4 (Contrucci et al 2004) suggests that mantle serpentinization may not have occurred on the conjugate side. However, no detachment was imaged in the Moroccan margin along the Conrad lines. This suggests that an asymmetrical rift pattern or upper/lower plate separation is not fully supported by current observations.

At the first stage of seafloor spreading from middle Jurassic to early Cretaceous (Figure 5.14c), either extremely thin oceanic crust (~2 km thick) or exposed upper mantle was present above a major intra-basement reflection. The small velocity gradient for this thin upper layer and the sharp velocity contrast to that of the layer underneath more likely supports an oceanic character; however, the quantitative basement roughness for this region may support either interpretation. The crustal structure at this stage is more likely symmetrical, illustrated by the deep rift basins evolved on both sides of the conjugate profiles. The deep basin off Nova Scotia still exists at present day, as the Sable Subbasin. Off Morocco, seismic surveys and hydrocarbon drilling show that the present-day Essaouira Basin has more than 5 km thick of Oxfordian shale (late Jurassic) in the vicinity of Toukimt field, which is onshore at present (Broughton and Trepaniér 1993). Including the sediment accumulated in the early-middle Jurassic and late Triassic, the

total sediment fill before the Atlasic compression in the Essaouira Basin was up to 10 km thick (see Figure 3 of Broughton and Trepaniér 1993), which should be comparable to the sediment loading in Sable Subbasin at this stage.

From Cretaceous and Tertiary to present day (Figure 5.14d), a major feature for the recent post-rift structure is a deep basin with ~16 km sediment fill off Nova Scotia in contrast to the much thinner (~6 km thick) sediment accumulation off Morocco (see Figure 5.4). The deep basin off Nova Scotia results from initial subsidence due to uniform crustal and lithospheric thinning, and subsequent subsidence due to thermal cooling with seafloor spreading, which persists to present day. Off Morocco, however, subsidence and sediment accumulation ceased at Cretaceous and Tertiary due to the emergence of compressive Atlasic tectonics that extends from what is now the Atlantic margin of Morocco to the Mediterranean coast (Broughton and Trepaniér 1993; Beauchamp et al. 1999). The Essaouira Basin was uplifted and tilted seaward, with up to 3 km of Jurassic and Cretaceous sediment eroded (Broughton and Trepaniér 1993). The eroded material spread to the vast current offshore area, which is illustrated by the thick (~10 km) sediment accumulation within the faulted blocks (lower panel, Figure 5.3, at SP 3100), and the relatively thicker and shallower sediment off Morocco than off Nova Scotia along conjugate profiles 88-1A and Conrad 364b (see Figure 5.2 and section 5.2.1). The major uplift and erosion occurred between Oligocene and Miocene (30-20 Ma), although uplift and erosion may have started in late Jurassic and early Cretaceous (Beauchamp et al. 1999).

5.5 Varying Volcanism along the Scotian and Moroccan Conjugate Margins

Figure 5.15 shows the varying volcanism along the margin conjugates. The southern margin segment M_S (Figure 5.15c) is characterized by a larger amount of syn-rift melt, illustrated by SDR sequences in the MCS seismic image (see Figures 5.6a and 5.6c), indicative of extrusive rock. The melt intrusion also occurred, which cooled and solidified as the rifted crust drifted away, resulting in underplating and thickening the rifted crust according to the OBS data (Dehler 2007, personal communication).

The evidence for melt generation is not observed across the central margin segment M_C (Figure 5.15b). First of all, no SDR sequences are imaged in the depth seismic profiles of line 88-1A and NovaSpan profiles (see Figures 3.7 and 3.10). In addition, evidence of underplating is absent beneath the rifted continental crust. Instead, serpentinization of the upper mantle is interpreted beneath highly thinned brittle crust (FBs, Figure 5.15b), based on the velocity model of SMART Line 2 (see chapter 2). These observations differ from the results across the southern conjugate segment and therefore allow the central segment to be classified as a non-volcanic margin. The limited melt generation is also observed along the northeastern margin segment M_N (Figure 5.15a).

The varying volcanism is further illustrated by varying thickness of oceanic crust after the onset of seafloor spreading. Across the SW margin segment, normal oceanic thickness (~5-7 km) is generated (Figure 5.15c). Across the central margin conjugate, only ~1-2 km thick oceanic crust is interpreted seaward of the highly thinned continental remnant, although the oceanic crust gradually thickened to 5-7 km as melt generation became normal afterwards (Figure 5.15b). For the northeastern margin segment, however,

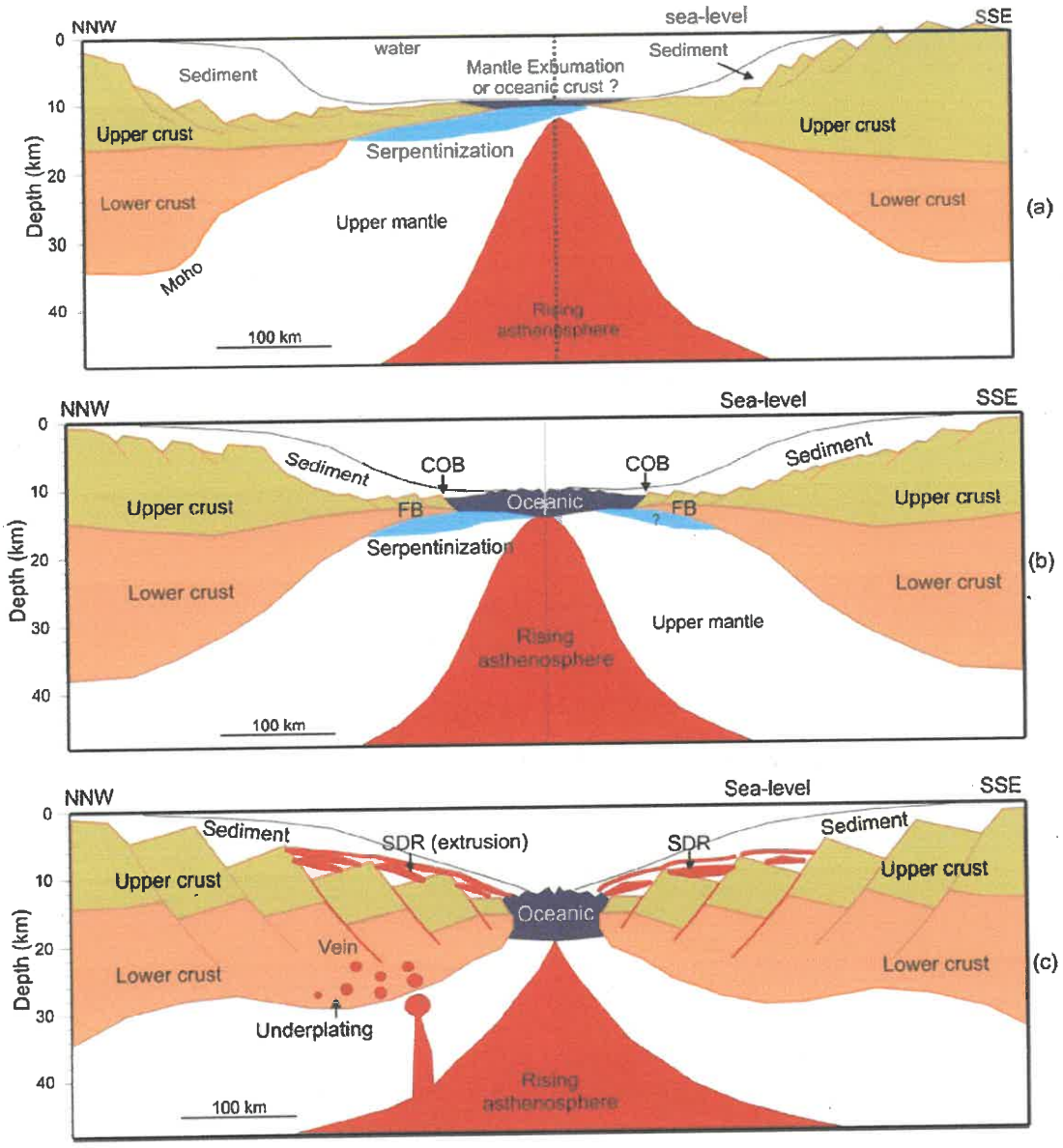

Figure 5.15. Variation of volcanism along the Nova Scotia/Morocco conjugates: (a) the conceptualized crustal structure across the northeastern segment (Figure 5.14b), (b) crustal structure across the central segment (Figure 5.13c), and (c) crustal structure across the SW segment, respectively. Marked features are discussed in the text.

virtually no or very thin (~2 km thick) oceanic crust was generated. Even after the normal seafloor spreading started, the oceanic crust is only ~4 km (Funck et al. 2004). The increasingly thinner oceanic crust from the southwestern segment to the central segment or lack of oceanic crust (e.g. the northeastern segment) after continental breakup indicates a decreasing of post-rift volcanism, which is consistent with the varying syn-rift volcanism along this margin pair.

5.6 Conclusions

Two types of conceptual models are presented for the formation of the Scotian/Moroccan margin conjugates. The rifting of the northern conjugate segment started with a symmetrical extension (middle to late Triassic) and breakup (early to middle Jurassic); but post-rift shortening of the High Atlas rift system (Cretaceous to Tertiary) caused uplift and erosion on the Morocco side, resulting in asymmetrical patterns of crustal structure and sedimentation. Across the central segment of the conjugates, uplift and erosion occurred on the Scotian margin at the early stage of rifting (middle to late Triassic). The absence of syn-rift uplift and erosion off Morocco suggests an asymmetrical initial rift pattern for the central segment. However, the Jurassic breakup geometry and subsequent seafloor spreading became more symmetric for the central segment.

The two types of conceptual models demonstrate reversed asymmetry for the crustal structure across the central (M_C) and northestern (M_N) segments of the Scotian/Moroccan margin conjugates, which is consistent with the structural features described by Tari and

Monlar (2005). However, the seismic profiles and well data from both sides of the conjugate margins show that the reversed asymmetry can not entirely be attributed to asymmetrical rifting. The asymmetrical crustal structure across the northern margin segment (M_N) is caused by the Atlasic tectonic compression after the breakup of the conjugate plates, rather than by crustal rifting. In addition, a major detachment is absent for the major portion of the Scotian/Moroccan margin conjugates, except for the northeastmost part along SISMAR 4. Therefore, the asymmetrical rifting along a lithospheric detachment suggested by Maillard et al. (2006) would only be valid for the northeastmost portion of the Scotian/Moroccan margin pair.

The recent MCS data show that excessive Mesozoic volcanism only occurred at the southwestmost part of the conjugates, illustrated by the SDR sequences that disappear ~100 km north of the SW Scotian margin. The basement north of the disappearance of SDRs is characterized by a ~100 km zone of rugged basement topography and relatively deeper basement depths, suggesting that the volcanic to non-volcanic transition takes place within this narrow zone. No SDR sequences are observed further northeast, indicating that the major part of the Scotian/Moroccan margin conjugates, except for the southwesternmost part, is non-volcanic in character. The conceptual models of syn-rift and post-rift volcanism, based on observed seismic data, show decreasing volcanism from the southern to the northern margin conjugates.

CHAPTER 6

CONCLUSION

The focus of this thesis has been to investigate the crustal structure of the transition from volcanic rifting to non-volcanic rifting along the Nova Scotia margin. This thesis has presented new results of a WAR/R profile across the central Nova Scotia margin and pre-stack time migration of the coincident MCS data. In addition, the results of the WAR/R and MCS data off Nova Scotia have been combined with existing results off Morocco in the context of minimum reconstruction so as to understand the rifting style and formation of this margin pair.

6.1 Conclusion

1) The central Nova Scotia margin is non-volcanic in character, without evidence of excessive volcanism found in the WAR/R and MCS data. The velocity model derived from the WAR/R data along Line 2 does not shows a thickened layer with characteristic high velocities beneath the rifted continental crust, suggesting that magmatic underplating did not occur in this region of the margin. Results of pre-stack migration of MCS data do not show SDR sequences in the basement underneath the ECMA across the central Scotian margin. Therefore, the ECMA with reduced amplitude along the major part of Scotian margin is not related to a wedge of igneous rocks in the basement.
2) Extensive syn-rift volcanism only occurred across the southwesternmost Scotian margin. Extensive surface volcanism, indicated by the characteristic SDRs along NovaSpan profile 5100, disappears ~100 km north of SMART Line 3. No SDRs are

observed further to the northeast, suggesting that the major part of the Scotian margin is non-volcanic, except for the southwesternmost part near Georges Bank. The volcanic to non-volcanic transition takes place within a ~100-km-wide zone characterized by rugged basement topography and relatively deeper basement. This transition zone is consistent with an abrupt amplitude reduction of the ECMA.

3) Although excessive syn-rift volcanism is lacking from the central to the northern Scotian segments, the crustal structure indicates a continuing decrease in post-rift volcanism. The OCT zone of Line 2 consists of a Partially Serpentinized Mantle layer, overlain by highly faulted continental crust in the northwest and oceanic crust immediately seaward of COB in the southeast. In contrast, the OCT zone of Line 1 comprises a PSM layer overlain by a 70-km-wide layer of either exposed and highly serpentinized mantle or extremely thin oceanic crust (~2 km). This suggests that at the time of breakup, a small amount of magma was generated across the central margin segment while the northern Nova Scotia margin was extremely magma-starved. The oceanic crust for Line 1 is ~4 km thick, whereas a more normal thickness (5-7 km) of oceanic crust is imaged at the seaward of Line 2. The thickness variation also implies a decreasing magma supply from the central to the northern margin segment.

4) The transition of the contrasting crustal structures from the central to the northern Scotian margin segments is coincident with a transition from autochthonous salt diapirs along Line 2 to allochthonous salt canopies along Line 1 and the presence of FBs between the two segments. The northern segment presents an abrupt crustal thinning with a deep basin beneath the outer shelf. While the continental crust along

the central segment consists of a platformal crustal structure across the outer shelf. The contrasting crustal structures are characterized by contrasting styles of salt mobilization, with autochthonous salt diapirs overlying the gentle slope of Line 2 and allochthonous salt canopies extending into the deep basin along Line 1. The transition of these two types of crustal structure also coincides with the appearance of FBs between the central and the northern margin segments. The consistency of transitions for crustal structure, salt mobilization, and the appearance of FBs indicate a change in character from the central and northern Scotian margin segments.

5) A minimum closure and a maximum closure of the Scotian/Moroccan margin pair have been proposed based on the recent seismic data, as well as magnetic anomalies and salt distribution from both sides. The proposed minimum reconstruction is similar to the rotation of Sahabi et al. (2004) for the southern portion of the conjugates, but no additional rotation is required for the northern part of conjugates. This modified reconstruction suggests that the S magnetic anomaly off NW Morocco, which does not have a homologue offshore Nova Scotia, should not be used to constrain the fit of conjugate parts. By further eliminating the rifted continental crust between the northern conjugate margin segments, a maximum closure has also been constructed, which requires less rotation than that of Klitgord and Schouten (1986).

6) According to the proposed minimum reconstruction, two types of asymmetrical crustal structures are presented across the Scotian/Moroccan margin conjugates. Across the northern conjugate segment, rifting (middle to late Triassic) and breakup (early to middle Jurassic) takes place in a more symmetrical pattern. However, post-rift compression of the High Atlas rift system (Cretaceous to Tertiary) caused uplift

and erosion on the Morocco side, resulting in a shallow Essaouira Basin (<10 km deep) with thin (~5-6 km) sediment offshore Morocco, in contrast to a deeper Sable Subbasin (up to 19 km deep) with much thicker (~16 km) sediment formed off Nova Scotia. Across the central segment of the conjugates, uplift and erosion occurred off Nova Scotia at the early stage of rifting (middle to late Triassic), resulting in a platformal continental shelf. Such a platformal outer shelf is lacking at the conjugate position due to absence of syn-rift uplift and erosion off Morocco, suggesting an asymmetrical initial rift pattern. However, the Jurassic breakup geometry and subsequent seafloor spreading became more symmetric. Therefore, the asymmetrical crustal structure across the central segment was produced by non-uniform crustal and lithopsheric thinning during syn-rift extension, whereas the asymmetry for the northern segment is due to post-rift compression of the High Atlas. This interpretation argues against previous conceptual models, where the separation of this margin pair was ascribed to a transfer zone or a major detachment, resulting in an upper plate of rifted crust on the Moroccan side and a lower plate of exposed mantle on the Scotian margin across the northern segments, with the opposite asymmetry across the central segment. A major detachment is absent for the major portion of the margin pair, indicating that the reversed asymmetry in crustal structures should not be attributed to lithospheric detachments or a transfer zone.

6.2 Future Work

1) The results of this thesis indicate that the volcanic to non-volcanic margin transition occurs in a narrow region, with clear evidence of extensive surface volcanism

disappearing ~100 km northeast of SMART Line 3. The volcanic to non-volcanic margin transition seems to occur within a ~100 km zone of rugged basement topography with relatively deeper basement depths. A detailed velocity model across this zone would be very useful to elucidate the transition in crustal structures of volcanic and non-volcanic segments and the nature of this transition zone. For instance, is it an unrecognized transform fault zone or a major crustal boundary? The answer to such questions will reveal what has controlled the volcanic to non-volcanic margin transition. This goal can be accomplished by a strike profile of WAR/R survey coincident with the existing NovaSpan profile 5100. A couple of dip WAR/R profiles between Line 2 and Line 3 are also recommended so as to obtain a full description of the velocity structure at the volcanic-nonvolcanic transition.

2) Results in chapters 2 and 3 suggest that the ECMA with reduced amplitude along the central to the northern margin are not associated with syn-rift volcanism. The cause of the diminishing magnetic anomaly would be an interesting topic for future studies.

3) The nature of the smooth basement across the OCT zone is still ambiguous, with seismic velocities indicating the oceanic crust while the basement relief is more consistent with an exposed mantle layer. In order to determine whether it is serpentinized mantle or oceanic crust, a strike WAR/R profile across the smooth basement at the seaward end of MCS line 89-1 is required such that we will be able to see if anisotropy, which is a common feature for serpentinizied mantle, exists within the smooth basement. This is important because a relatively smooth topography is often observed cross the OCT zone for other northern North Atlantic margins, where the nature of the upper basement layer is less definitive.

4) Pre-stack time migration techniques have significantly improved the images of the diapiric structure and the basement underneath, compared to the result of post-stack migration. However, diapiric structures are 3D features with extremely irregular geometry. The existing 2D WAR/R or MCS data and 2D migration techniques may still not have accurately imaged the complex structures. 3D data set and 3D migration are required to further improve the images of the diapiric structure for purposes of petroleum exploration, and more importantly, to improve the basement image for the purpose of crustal structural studies.

5) The results of chapter 2 suggest that the FBs at the seaward end of 88-1A are highly stretched continental crust, which extends the seaward limit of continental crust ~50 km oceanward compared to some previous interpretations. The oceanward extension of continental crust suggests that these FBs may be of importance for petroleum exploration. Based on the minimum reconstruction in chapter 4 and 5, the FBs also appear at the seaward end of the rifted continental crust at the conjugate positions off Morocco, where similar structures are being considered for exploration. However, the distribution of the FBs off Nova Scotia is yet not well defined except for a recent 2D survey that imaged the FBs in the adjacent region. A detailed delineation of the distribution and the internal structure of these FBs would require a number of additional MCS profiles or a 3D survey across the deep water area of the central Scotian margin.

6) With the recent WAR/R survey (SMART lines) and 2D regional MCS survey (NovaSppan Project data), our understanding of the crustal structure and the volcanic to non-volcanic transition off Nova Scotia has been much improved. Based on the

minimum reconstruction proposed in chapter 4, the volcanic to non-volcanic transition derived off Nova Scotia may apply to Morocco margin. However, a full understanding of the formation of the Scotian/Moroccan margin pair requires results of equivalent studies on the Morocco side. Two WAR/R profiles, one across the entire central and one across the southern Morocco margin, are crucial to this topic. This will, in return, provide direct constraints for reconstruction of the Scotian/Moroccan margin pair.

BIBLIOGRAPHY

Alsop L. E., and Talwani, M., 1984. The East Coast Magnetic Anomaly, Science, New Series, 226, No. 4679, 1189-1191.

Anderson, D.L., 1994. The sublithospheric mantle as the source of continental flood basalts: the case against the continental lithosphere and plume head reservoirs. *EPSL*, 123, 269-280.

Anderson, D. L., Y.-S. Zhang, and T. Tanimoto, 1992. Plume heads, continental lithosphere, flood basalts and tomography, in Magmatism and the Causes of Continental Break-up, vol. 68, edited by B. C. Storey, T. Alabaster, and R. J. Pankhurst, 99-124, Geol. Soc. Lond., London.

Armstrong, R. L., Besancon, J., 1970. A Triassic time scale dilemma: K-Ar dating of Upper Triassic mafic igneous rocks, Eastern U.S.A. and Canada and post-Upper Triassic plutons, Western Idaho, U.S.A. Eclogae Geol. Helv. 63, 15–28.

Arthur, J. D., 1988. Petrogenesis of early Mesozoic tholeiite in the Florida basement, and an overview of Florida basement geology: Florida Geological Survey, Tallahassee, Report of Investigation no. 97, 39 p.

Austin, J. A., Jr., Stoffa, P. L., Phollips, J., D., Oh, J., Sawer, D. S., Purdy, G. M., Reiter, E.,Makris, J., 1990. Crustal structures of the southeast Georgia embayment-Carolina trough: Preliminary results of a composite seismic image of a continental suture (?) and a volcanic passive margin, Geology, 18, 1023-1027.

Baksi, A.K., 1997. The timing of Late Cretaceous alkalic igneous activity in the northern Gulf of Mexico basin, southeastern USA: Journal of Geology, 105, 629-643.

Baksi, A. K., and Archibald, D. A., 1997. Mesozoic igneous activity in the Maranhao province, northern Brazil: $^{40}Ar/^{39}Ar$ evidence for separate episodes of basaltic magmatism: Earth and Planetary Science Letters, 151, 139-153.

Bancroft, J. C. and Geiger, H. D., 1994. Equivalent offset CRP gathers: 64th Annual Internat. Mtg., Soc. Expl. Geophys.,Expanded Abstracts, 672-675.

Bancroft, J. C., Geiger, H. D., Foltinek, D., and Wang, S., 1995. Pre-stack migration by equivalent offsets and commonscatter point (CSP) gathers: 57th Mtg. Eur. Assoc. Expl Geophys., Extended Abstracts, Session: P124.

Bancroft, J. C., Geiger, H. D., and Margrave, G. F., 1998. The equivalent offset method of pre-stack time migration: Geophysics, 63, No. 6, 2042-2053.

Barr, S. M. and Raeside R. P., 1989. Tectono-stratigraphic terranes in Cape Breton Island, Nova Scotia: Implications for the configuration of the northern Appalachian orogen, Geology, 17, 822-825.

Barrett, D. L., M. J. Berry, J. E. Blanchard, M. J. Keen, and R. E., McAllister, 1964. Seismic studies on the eastern seaboard of Canada: the Atlantic coast of Nova Scotia, Can. J. Earth Sci., 1, 10-22.

Barrett, D. L. and Keen, C. E., 1976. Mesozoic magnetic lineations, the magnetic quiet zone, and sea floor spreading in the northwest Atlantic, J. Geophys. Res., 81, 4875-4884.

Bartolome, R.; Contrucci, I.; Nouze, H.; Thiebot, E.; Klingelhoefer, F., 2005. Using the OBS wide-angle reflection/refraction velocities to perform a pre-stack depth migration image of the "single bubble" multichannel seismic: example of the Moroccan margin, Journal of Applied Geophysics, 57, 107-118.

Beauchamp, W., R. W. Allmendinger, M. Barazangi, A. Demnati, M. El Alji, and M. Dahmani, 1999. Inversion tectonics and the evolution of the High Atlas Mountains, Morocco, based on a geological-geophysical transect, Tectonics, 18(2), 163–184.

Benn, K., Horne, R. J., Kontak, D. J., Pignotta, G. S. and Evans, N. G., 1997. Syn-Acadian emplacement model for the South Mountain batholith, Meguma Terrane, Nova Scotia: Magnetic fabric and structural analyses, Geological Society of America Bulletin, 109, 1279-1293.

Bertrand, H. 1991. The Mesozoic tholeiitic province of northwest Africa: A volcano-tectonic record of the early opening of the central Atlantic.In Kampunzo, A. B. and R. T. Lubala, eds., The Phanerozoic African plate, pp. 147-191. New York: Springer-Verlag.

Bown, J. W. and White, R. S., 1995. Effect of finite extension rate on melt generation at rifted continental margins, J. Geophys. Res., 100, 18011-18029.

Broughton, Paul, and André Trepaniér, 1993. Hydrocarbon Generation in the Essaouira Basin of Western Morocco. A.A.P.G. Bull., 77, N° 6, 999 -1015.

Bullard, E. C., Everett, J. E. and Smith, A. G., 1965. The fit of the continents around the Atlantic, Royal Society of London Philosophical Transactions Series A, 258, 41–51.

Burke, K.B.S., Hamilton, J.B., and Gupta, V.K., 1973. The Caraquet dike: Its tectonic significance, Can. J. Earth Sci., 10, 1760-1768.

Cannat, M., 1993. Emplacement of mantle rocks in the seafloor at mid-ocean ridges, J. Geophys. Res., 98, 4163-4172.

Carmichael, C.M., and Palmer, H.C. 1968. Paleomagnetism of the Late Triassic North Mountain Basalt of Nova Scotia, J. Geophys. Res., 73, 2811– 2822.

Caroff, M., Bellon, H., Chauris, L., Carron, J.-P., Chevrier, S., Gardinier, A., Cotten, J., Le Moan, Y., Neidhart, Y., 1995. Magmatisme fissural Triasico-Liasique dans l'ouest du Massif Armoricain (France): Petrologie, age, et modalities des la mise en place. Can. J. Earth Sci. 32, 1921-1936.

Chian, D., and K. E. Louden, 1994. The continent-ocean crustal transition across the southwest Greenland margin, J. Geophys. Res., 99(B5), 9117–9136.

Chian, D., Louden, K. E. and Reid, I., 1995a. Crustal structure of the Labrador Sea conjugate margin and implications for the formation of nonvolcanic continental margins, J. Geophys. Res., 100, 24239-24253.

Chian, D., Keen, C., Reid, I. and Louden, K. E., 1995b. Evolution of non-volcanic rifted margins: new results from the conjugate margins of the Labrador Sea, Geology, 23, 589-592.

Chian, D., Louden, K.E., Minshull, T.A. and Whitmarsh, R.B., 1999. Deep structure of the ocean-continent transition in the southern Iberia Abyssal Plain from seismic refraction profiles: Ocean Drilling Program (Legs 149 and 173) transect, J. Geophys. Res., 104, 7443-7462.

Christensen, N. I. and Mooney, W. D., 1995. Seismic velocity structure and composition of the continental crust: A global view, J. Geophys. Res., 100(B6), 9761–9788.

Claerbout, J. F., 1985. Imaging the earth's interior: Blackwell Scientific Publications, Inc.

Clarke, D.B., and Chatterjee, A.K. 1992. Origin of peraluminous granites in the Meguma Zone of southern Nova Scotia: a synthesis. Joint Annual Meeting of GAC/AGC, Wolfville, abstract, 17, A18.

Coffin, M. F., Gahagan, L.M., Lawver, L.A., Lee, T.-Y., and Rosencrantz, E., 1992. Atlas of Mesozoic/Cenozoic reconstructions (200 Ma to Present Day), Plates Progress Report No. 1-0192, University of Texas Institute for Geophysics Technical Report 122, 49 pp.

Cole, P. B., Minshull, T. A. and Whitmarsh, R. B., 2002. Azimuthal seismic anisotropy in a zone of exhumed continental mantle, West Iberia margin, Geophys. J. Int., 151, 517-533

Colman-Sadd, S.P., 1982. Two stage continental collision and plate driving forces, Tectonophysics, 90, 263-282.

Contrucci I., F. Klingelhofer, J. Perrot, R. Bartolome, M. A. Gutscher, M. Sahabi, J. Malod and J. P. Rehault, 2004 - The crustal structure of the NW Moroccan continental margin from wide-angle and reflection seismic data, Geophys. J. Int., 159, 1, 117-128.

Dean, S. M., Minshull, T.A., Whitmarsh, R. B. and Louden, K. E., 2000. Deep structure of the ocean-continent transition in the southern Iberia Abyssal Plain from seismic refraction profiles: The IAM-9 transect at 40°20'N, J. Geophys. Res., 105, 5859-5885.

de Boer, J.Z., McHone, J.G., Puffer, J.H., Ragland, P.C. and Whittington, D. 1988. Mesozoic and Cenozoic magmatism, In The Geology of North America, Volume I-2: The Atlantic Continental Margin, U.S. Sheridan R.E. and Grow J.A. (eds.), Geological Society of America, Boulder, Colorado, 217-241.

Deckart, K., G. Féraud, and H. Bertrand. 1997. Age of Jurassic continental tholeiites of French Guyana/Surinam and Guinea: Implications to the initial opening of the central Atlantic Ocean. Earth Plan. Sci. Let., 150, 205-220.

Dehler, S.A., Keen, C.E., Funck, T., Jackson, H.R., and Louden, K., 2003. Structure of a volcanic to non-volcanic transitional margin segment off Nova Scotia, Atlantic Canada, EGS/AGU/EUG Joint Annual Meeting, April 2003, Nice, France.

Dehler, S. A., Keen, C. E., Funck, T., Jackson, H. R. and Louden, K. E., 2004. The limit of volcanic rifting: A structural model across the volcanic to non-volcanic transition off Nova Scotia. Eos Trans. AGU, 85(17), Jt. Assem. Suppl., Abstract T31D-04.

Divins, D.L., 2007. NGDC, Total Sediment Thickness of the World's Oceans and Marginal Seas, Retrieved date from http://www.ngdc.noaa.gov/mgg/sedthick/sedthick.html.

Eldholm, O. and Thiede, J. and ODP Leg 104 Shipboard Scientific Party 1986. Ocean drilling at the Vøring Plateau in the Norwegian Sea. Nature, 319, 360–361.

Ernst, R.E. and Buchan, K.L., 2001. Large mafic magmatic events through time and links to mantle plume heads, in Ernst, R.E. and Buchan, K.L. (eds.), Mantle Plumes: Their Identification Through Time: Geological Society of America, Special Paper 352, 483-575.

Fitton J.G., Saunders A.D., Larsen L.M., Fram M.S., Demant A., Sinton C., 1995. Leg 152 Shipboard Scientific Party Magma sources and plumbing systems during break-up of the SE Greenland margin: preliminary results from ODP Leg 152. Journal of the Geological Society, London, 152, p.985-990.

Fodor, R.V., Sial, A.N., Mukasa, S.B., McKee, E.H., 1990. Petrology, isotope characteristics, and K-Ar ages of the Maranhao, northern Brazil, Mesozoic basalt province. Contr. Min. Pet. 104, 555-567.

Foulger, G.R. and D.L. Anderson, 2005. A cool model for the Iceland hotspot, *J. Volc. Geotherm. Res.*, 141, 1-22.

Funck, T., Dickmann, T., Rihm, R., Krastel, S., Lykke-Andersen, H., Schmincke, H.-U., 1996. Reflection seismic investigations in the volcaniclastic apron of Gran Canaria and implications for its volcanic evolution, Geophys. J. Int. 125, 519–536.

Funck, T., Hopper, J. R., Larsen, H. C., Louden, K. E., Tucholke, B. E. and Holbrook, W. S., 2003. Crustal structure of the ocean-continent transition at Flemish Cap: Seismic refraction results, J. Geophys. Res., 108(B11), 2531, doi: 10.1029/2003JB002434.

Funck, T., Jackson, H. R., Louden, K. E., Dehler, S. A. and Wu, Y., 2004. Crustal structure of the northern Nova Scotia rifted continental margin (Eastern Canada), J. Geophys. Res., 109, B09102, doi: 10.1029/2004JB003008.

Given, M. M., 1977. Mesozoic and early Cenozoic geology of offshore Nova Scotia, Bulletin of Canadian Petroleum Geology, 25 (1), 63-91.

Goff, J.A., 1991. A Global and regional analysis of near-ridge abyssal hill morphology. J. Geophys. Res. 96: 21713–21737.

Goff, J.A., 1992. Quantitative characterization of abyssal hill morphology along flow lines in the Atlantic Ocean, J. Geophys., Res. 97: 9183–9202.

Gohn, G. S., Gottfried, D., Lanphere, M. A., and Higgins, B. B., 1978. Regional implications of Triassic or Jurassic age for basalt and sedimentary red beds in the South Carolina Coastal Plain: Science, 202, 887-890.

González, A., Córdoba, D. and Vales, D., 1999. Seismic crustal structure of Galicia continental margin, NW Iberian Peninsula, Geophys. Res. Lett., 26, 1061-1064.

Gradstein, F.M., Ogg, J.G. and Smith, A.G., 2004. A Geologic Time Scale 2004. Cambridge University Press.

Greenough, J. D., Jones, L. M., and Mossman, D. J., 1989. Petrochemical and stratigraphic aspects of North Mountain basalt from the north shore of the Bay of Fundy, Nova Scotia, Canada, Can. J. Earth Sci., 26, 2710-2717.

Greenough, J.D., and Papezik, V.S., 1986. Petrology and geochemistry of the early Mesozoic Caraquet dyke, New Brunswick, Canada, Can. J. Earth Sci., 23, 193–201.

Greenough, J.D., and Papezik, V.S. 1987. The petrology of North Mountain Basalt from the wildcat oil well Mobil Gulf Chinampas N-37, Bay of Fundy, Can. J. Earth Sci., 24: 1255–1260.

Hames, W.E., McHone, J.G., Ruppel, C., and Renne, P. (editors), 2002. *The Central Atlantic Magmatic Province: Insights from Fragments of Pangea:* Am. Geophys. Union Monograph, 136, 267 p.

Hames, W.E., Renne, P.R., and Ruppel, C., 2000. New evidence for geologically instantaneous emplacement of earliest Jurassic Central Atlantic magmatic province basalts on the North American margin, *Geology,* 28, 9, 859-862.

Hayatsu, A., 1979. K-r isochron age of the North Mountain basalt, Nova Scotia, Can. J. Earth Sci. 16, 973–975.

Herzberg, C., 2004. Partial crystallization of mid-ocean ridge basalts in the crust and mantle, J. Petrol., 45, 2389-2405.

Hiscott, R.N., Wilson, R.C.L., Gradstein, F.M., Pujalte, V., García-Mondéjar, J., Boudreau, R.R. and Wishart, H.A., 1990. Comparative stratigraphy and subsidence history of Mesozoic rift basins of North American, Am. Ass. Petrol. Geol. Bull., 74, 60-76.

Holbrook, W. S. and Kelemen, P. B., 1993. Large igneous province on the US Atlantic margin and implications for magmatism during continental breakup, Nature, 364, 433-436.

Holbrook, W.S., Mooney, W.D. and Christensen, N.I., 1992. The seismic velocity structure of the deep continental crust, in Continental lower crust. Edited by Fountain, D.M., Arculus, R. and Kay, R., Elsevier, Amsterdam, pp. 1-43.

Holik, J.S., Rabinowitz, P. D. and Austin, J. A., 1991. Effects of Canary hotspot volcanism on structure of oceanic crust off Morocco, J. Geophys. Res., 96, 12039-12067.

Hopper, J. R., Funck, T., Tucholke, B. E., Larsen, H. C., Holbrook, W. S., Louden, K. E., Shillington, D. and Lau, H., 2004. Continental breakup and the onset of ultraslow seafloor spreading off Flemish Cap on the Newfoundland rifted margin, Geology, 32(1), 93-96, doi:10.1130/G19694.1.

Ings, S.J. and Shimeld, J.W., 2006. A new conceptual model for the structural evolution of a regional salt detachment on the northeast Scotian margin, offshore eastern Canada. American Association of Petroleum Geologists Bulletin, 90: 1407-1423.

Jackson, H.R., Chian, D., Louden, K. and M. Salisbury, M., submitted. Crustal Structure of the Meguma Terrane Offshore of Nova Scotia and its Tectonic Implications, Can. J. Earth Sci..

Jackson, H.R., Chian, D., Salisbury, M. and Shimeld, J., 2000. Preliminary crustal structure from the Scotian margin to the Maritimes Basin from wide-angle reflection/refraction profiles, Geocanada 2000, The Millennium Geoscience Conference Cdrom, May 29-June 2, Calgary, Alberta.

Jackson, H. R., Keen, C. E. and Keen, M. J., 1975. Seismic structure of the continental margins and ocean basins of southeastern Canada, Geol. Surv. Can. Pap. 74–51, p. 13.

Jansa, L.F., and Pe-Piper, G., 1985, Early Cretaceous volcanism on the northeastern American margin and implications for plate tectonics: Geological Society of America Bulletin, 96, 83–91.

Jansa, L.F., and Wiedmann, J., 1982. Mesozoic-Cenozoic development of the eastern North American and northwest African continental margins: a comparison, 215–269. In: Geology of the northwest African Margin. Ed.U. von Rad, K. Hinz, M. Sarnthein and E. Seibold. Springer-Verlag, Berlin/Heidelberg/New York.

Jokat, W., Ritzmann, O., Schmidt-Aursch, M. C., Drachev, S., Gauger, S. and Snow, J., 2003. Geophysical evidence for reduced melt production on the Arctic ultraslow Gakkel mid-ocean ridge, Nature, 423, 962-965.

Keen, C. E. and Beaumont, C., 1990. Geodynamics of rifted continental margins, in Geology of the Continental Margin of Eastern Canada, Edited by Keen, M. J. and Williams, G. L., Geological Survey of Canada, Geology of Canada, No. 2, 393-472.

Keen, C. E. and Cordsen, A., 1981. Crustal structure, seismic stratigraphy, and rift processes of the continental margin off eastern Canada: ocean bottom seismic refraction results off Nova Scotia, Can. J. Earth Sci., 18, 1523-1538.

Keen, C. E., Kay, W. A., Keppie, D., Marillier, R., Pe-Piper, G. and Waldron, J. W. F., 1991a. Deep seismic reflection data from the Bay of Fundy and marine: tectonic implication for the northern Appalachian, Can. J. Earth Sci., 28, 1096-1111.

Keen, C. E., Keen, M. J., Barrett, D. L., and Heffler, D. E., 1975. Some aspects of the ocean-continent transition at the continental margin off eastern North America. In Off-shore Geology of Eastern Canada, Vol. 2, Regional geology, edited by W. J. M. van der Linden and J. A. Wade, Geological Survey of Canada, 189-197.

Keen, C. E., and B. D., Loncarevic, I. Reid, J. Woodside, R. T. Howorth, and H. Williams, 1990. Tectonic and geophysical overview, In Geology of Canada, No. 2, Geology of the continental margins of eastern Canada, Edited by M. J., Keen, G. L. Williams. Geological Survey of Canada, Ottawa, Ont., 31-85.

Keen, C. E., MacLean, B. C. and Kay, W. A., 1991b. A deep seismic reflection profile across the Nova Scotia continental margin, offshore eastern Canada, Can. J. Earth Sci., 28, 1112-1120.

Keen, C. E. and Potter, P., 1995a. The transition from a volcanic to nonvolcanic rifted margin off eastern Canada, Tectonics, 14, 359-371.

Keen, C. E. and Potter, P., 1995b. Formation and evolution of the Nova Scotian rifted margin: Evidence from deep seismic reflection data, Tectonics, 14, 918-932.

Kelemen, P. B. and Holbrook, W. S., 1995. Origin of thick, high-velocity igneous crust along the U.S. East Coast Margin, J. Geophys. Res., 100, B7, 10,077-10,094.

Keppie, J. D., 1989. Northern Appalachian terranes and their accretionary history, in Terranes in the circum-Atlantic Paleozoic Orogens, edited by Dallmeyer, R. D., Geological Society of America, Special Paper, 230,159-192.

Keppie, J.D., and Dallmeyer, R.D. 1995. Late Paleozoic collision, delamination , short-lived magmatism, and rapid denudation in the Meguma Terrane, (Nova Scotia, Canada): constraints from 40Ar/39Ar isotopic data, Can. J. Earth Sci., 32: 644-659.

King, S.D., and Anderson, D.L., 1995. An alternative mechanism of flood basalt formation, *EPSL*, 136, 269-279.

King, S.D., and Ritsema J., 2000. African Hot Spot Volcanism: Small-Scale Convection in the Upper Mantle Beneath Cratons, Science, 290, 1137 – 1140.

Klitgord, K. D. and Schouten, H., 1986. Plate kinematics of the central Atlantic, in The Geology of North America, Volume M, The Western North Atlantic Region, edited by Vogt P. R. and Tucholke, B. E., 351-378, Geological Society of America, Boulder, Colo.

Korenaga, J., Holbrook, W.S., Kent, G.M., Kelemen, P.B., Detrick, R.S., Larsen, H. C., Hopper, J.R. and Dahl-Jensen, T., 2000. Crustal structure of the Southeast Greenland margin from joint refraction and reflection seismic tomography, J. Geophys. Res., 105, 21, 591–21, 614.

Lau, K. W. H., Louden, K. E., Funck, T., Tucholke, B.E., Holbrook, W.S., Hopper, J.R., and Larsen, H.C., 2006a. Crustal structure across the Grand Banks - Newfoundland Basin continental margin (Part I) - Results from a seismic refraction profile, Geophys. J. Int. 167, 127-156.

Lau, K. W. H., Louden, K.E., Deemer, S., Hall, J., Hopper, J.R., Tucholke, B.E., Holbrook, W.S., and Larsen, H.C., 2006b. Crustal structure across the Grand Banks - Newfoundland Basin continental margin (Part II) - Results from a seismic reflection profile, Geophys. J. Int. 167, 157-170.

Levin F.K., 1971. Apparent velocities from dipping interface reflections: Geophysics, 36, 510-516.

Lefort, J. -P. and Van der Voo, R., 1981. A kinematic model for the collision and complete suturing between Gondwanaland and Laurasia in the Carboniferous, J. Geol., 89, 537-550.

LePichon, X., Sibuet, J. C. and Francheteau, J., 1977. The fit of the continents around the North Atlantic Ocean. Tectonophysics, 38, 169–209.

Liger, J.-L.,1980. Structure profonde du bassin sénégalo-mauritanien– Interprétation des données gravimétriques et magnétiques, Trav. Lab. Sci. Terre, Saint-Jérôme, Marseille, 16.

Lillie, R. J., 1999. Whole Earth Geophysics, An Introductory Textbook for Geologists and Geophysicists. Prentice-Hal, Inc.

Loncarevic, B. D., Courtney, R. C., Fader, G. B. J., Giles, P. S., Piper, D. J. W., Costello, G., Clarke, J. E., Hughes and Stea, R. R., 1994. Sonography of a glaciated continental shelf, Geology, 22, 747-750.

Louden, K. E. and Chian, D., 1999. The deep structure of non-volcanic rifted continental margins, Phil Trans. Roy. Soc. Lond., Ser. A., 357, 767-804.

Louden, K.E., Dadey, J.A., and Srivastava, S.P., 1989. Heat flow measurements at ODP Site 646, In Srivastava, S.P., Arthur, M., Clement, B., et al. (eds.), Proc. ODP, Sci. Results, 105, Ocean Drilling Program, College Station, TX, pp. 923-931.

Louden, K. E., Osler, J. C., Srivastava, S. P. and Keen, C. E., 1996. Formation of oceanic crust at slow spreading rates: New constraints from an extinct spreading center in the Labrador Sea, Geology, 24, 771-774.

Louden, K. E., Tucholke, B. E. and Oakey, G. N. 2004: Regional anomalies of sediment thickness, basement depth and isostatic crustal thickness in the North Atlantic Ocean. Earth and Planetary Science Letters, 193-211.

Ludwig, W. J., Nafe, J. E. and Drake, C. L., 1970. Seismic refraction, in The Sea, New concepts of the sea floor evolution, edited by Maxwell, A. E., 53-84, Wiley-intersci., New York.

Lutter, W. J. and Nowack, R. L., 1990. Inversion for crustal structure using reflections from the PASSCAL Ouachita experiment, J. Geophys. Res., 95, 4633-4646.

MacLean, B. C., 1991. Structure and isopach 1: depth to pre-Mesozoic basement and oceanic layer 2; In East Coast Basin Atlas Series: Scotian Shelf, Atlantic Geoscience Centre, Geological Survey of Canada, 75.

Maillard A., J. Malod, E. Thiébot, F. Klingelhoefer and J.-P. Réhault, 2006 - Imaging a lithospheric detachment at the continent–ocean crustal transition off Morocco, Earth Planet. Sci. Lett., 241, 686-698.

Malinverno, A., 1991. Inverse square-root dependence of mid-ocean ridge flank roughness on spreading rate. Nature 352: 58–60.

Marillier, F., Keen, C. E., Stockmal, G. S., Quinlan, G., Williams, H., Colman-Sadd, S. P. and O'Brien, S. J., 1989. Crustal structure and surface zonation of the Canadian Appalachians: implications of deep seismic reflection data, Can. J. Earth Sci., 26, 305-321.

Marzoli, A., Renne, P. R., Piccirillo, E. M., Ernesto, M., Bellieni, G. and Min, A. De, 1999. Extensive 200-million-year-old continental flood basalts of the Central Atlantic Magmatic Province, Science 284: 616-618.

Mauffret A. and Montadert L., 1987. Rift tectonics on the passive continental margin off Galicia (Spain). Mar. Petrol. Geol., 4, 49-70.

McBride, J.H., 1991. Constraints on the structure and tectonic development of the Early Mesozoic South Georgia rift, southeastern United States; seismic reflection data processing and interpretation. Tectonics 10, 1065-1083.

McHone, J. G., D. P. West, Jr., A. M. Hussey II., and N. W. McHone.1995. The Christmas Cove dike, coastal Maine: Petrology and regional significance. Geol. Soc. Am. Abs. with Prog., 27, 67-68.

McHone, J.G., 2000. Volatile emissions of Central Atlantic Magmatic Province basalts: Mass assumptions and environmental consequences, in Hames, W.E., McHone, J.G., Renne, P.R., and Ruppel, C., editors, *The Central Atlantic Magmatic Province*: American Geophysical Union, Geophysical Monograph, 136, 241-254.

Miller, D. J. and Christensen, N. I., 1997. Seismic velocities of lower crustal and upper mantle rocks from the slow-spreading Mid-Atlantic Ridge, south of the Kane Transform zone (MARK), Proc. Ocean Drill. Program Sci. Results, 153, 437-454.

Minshull, T. A, 1999. On the roughness of Mesozoic oceanic crust in the western North Atlantic, Geophys. J. Int. 136 (1), 286–290.

Minshull, T.A., Dean, S.M., White, R.S., and Whitmarsh, R.B., 2001. Anomalous melt production after continental break-up in the southern Iberia Abyssal Plain. In Wilson, R.C.L., Whitmarsh, R.B., Taylor, B., and Froitzheim, N. (Eds.), Non-volcanic Rifting of Continental Margins: Evidence From Land and Sea. Geol. Soc. Spec. Publ. London.

Minshull, T. A. and White, R. S., 1996. Thin crust on the flanks of the slow-spreading Southwest Indian Ridge, Geo. J. Int., 125, 139–148.

Molnar, J, Tari, G., Ashton P. and Thompson P., 2002. Correlation of syn-rift structural elements across the central Atlantic between Morocco and Nova Scotia, AAPG distinguished lecture 2002.

Montes-Lauar, C. R., Pacca, I. G., Melfi, A. J., Piccirillo, E. M., Bellieni, G., Petrini, R., and Rizzieri, R., 1994, The Anari and Tapirapua Jurassic formations, western Brazil: paleomagnetism, geochemistry, and geochronology: Earth and Planetary Science Letters, v. 128, p. 357-371.

Morris, E., Detrick, R. S., Minshull, T. A., Mutter, J. C., White, R. S., Su, W. and Buhl, P. 1993. Seismic structure of oceanic crust in the western North Atlantic. J. Geophys. Res., 98, 13,879-13,903.

Moullade, M., Brunet, M.-F. and Boillot, G., 1988. Subsidence and deepening of the 160 Galicia margins: the paleoenvironmental control. In Proceedings of the Ocean Drilling Program, Scientific Results, Vol. 103, pp. 733-740, ed. Mazullo, E.K., Ocean Drilling Program, College Station, TX.

Muller, M.R., Minshull, T.A. and White, R.S., 1999. Segmentation and melt supply at the Southwest Indian Ridge, Geology, 27, 867-870.

Murphy, J.B., van Staal, C.R. and Keppie, J.D.1999. Middle to Late Paleozoic Acadian orogeny in the northern Appalachians: a Larmide-style plume-modified orogeny? Geology, 27: 653- 656.

Mutter, J.C., W.R. Buck and C.M. Zehnder, 1988. Convective Partial Melting 1. A model for the formation of thick basaltic sequences during the initiation of spreading, J. Geophys. Res., 93, 1031-1048.

National Geophysical Data Center, 1988. ETOPO-5 Bathymetry/Topography data, Data announcement 88-MG-02, National Oceanic and Atmospheric Administration, U.S. Dept. of Commerce, Boulder, Colo.

Oakey, G.N. and Dehler, S.A., 2004. Atlantic Canada magnetic map series: Scotian shelf and surrounds, Open File Rep. 1814, Geological Survey of Canada, Calgary, Alb.

Oakey, G.N. and Start, A., 1995. ADigital Compilation of Depth to Basement and Sediment Thickness for the North Atlantic and Adjacent Coastal Land Areas: Geological Survey of Canada Open File Report No. 3039.

Officer, C. B. and Ewing, M., 1954. Geophysical investigations in the emerged and submerged Atlantic coastal plain. Part VII. Continental shelf, continental slope, and continental rise south of Nova Scotia, Geol. SOC. Am. Bull., 65, 653-670.

Oliveira, E.P., Tarney, J., Joao, X.J., 1990. Geochemistry of the Mesozoic Amapa and Jari dyke swarms, northern Brazil: Plume-related magmatism during the opening of the central Atlantic. In: Parker, A.J., Rickwood, P.C., Tucker, D.H. (Editors), Mafic dikes and emplacement mechanisms. Balkemia, Rotterdam, Netherlands, 173-183.

Olsen, P.E., 1997. Stratigraphic record of the early Mesozoic breakup of Pangea in the Laurasia-Gondwana rift system: Annual Reviews of Earth and Planetary Science, 25, 337-401.

Olsen, P. E., Hubert, J. F. and Mertz, K. A., 1981. Eolian dune field of Late Triassic age, Fundy Basin, Nova Scotia, Geology, 9: 557-559

Osler, J. and Louden, K.E., 1995. Extinct spreading center in the Labrador Sea: crustal structure from a two-dimensional seismic refraction velocity model, J. Geophys. Res., 100, 2261-2278.

Papezik, V.S., and Barr, S.M. 1981. The Shelburne dike, an early Mesozoic diabase dike in Nova Scotia: mineralogy, petrology, and regional significance, Can. J. Earth Sci., 18: 1346–1355.

Papezik, V. S. and Hodych, J. P., 1980. Early Mesozoic diabase dikes of the Avalon Peninsula, Newfoundland: Petrochemistry, mineralogy, and origin: Canadian Journal of Earth Sciences, 17, 1417-1430.

Pe-Piper, G. and Jansa, L.F., 1986: Triassic olivine- normative diabase from Northumberland Strait, Eastern Canada: implications for continental rifting. Can. J. Earth Sci., 23, 1013-1021.

Pe-Piper, G., Jansa, L.F., and Lambert, R., St.J., 1992, Early Mesozoic magmatism on the eastern Canadian margin: Petrogenetic and tectonic signifi cance, in Puffer, J.H., and Ragland, P.C., eds., Eastern North American Mesozoic Magmatism: Geological Society of America Special Paper 268, 13–36.

Pe-Piper G., Piper, D.J.W., Keen, M.J., and McMillan, N.J., 1990. Igneous rocks of the Eastern Canadian continental margin. Chapter 2 in: Geology of the continental margin off Eastern Canada, M.J.Keen and G.L. Williams (ed.); Geological Survey of Canada, Geology of Canada, no.2, 75-85.

Pérez-Gussinyé, M. and Reston, T. J., 2001. Rheological evolution during extension at nonvolcanic rifted margins: onset of serpentinization and development of detachments leading to continental breakup, J. Geophys. Res., 106, 3961-3975.

Philpotts, A. R. and A. Martello. 1986. Diabase feeder dikes for the Mesozoic basalts in southern New England. Am. Jour. Sci. 286,105-126.

Pringle, G.J., Trembath, L.T., Pajari, G.J., Jr., 1974. Crystallization history of a zoned plagioclase. Mineral. Mag. 39, 867–877.

Prosser, S., 1993. Rift-related linked depositional systems and their seismic expression, in: Williams, G. D. and Dobb, A. (eds), Tectonics and Seismic Sequence Stratigraphy, Geol. Soc. Spec. Publ. Lond., 71, 35-66.

Reid, I. D., 1994. Crustal structure of a nonvolcanic rifted margin east of Newfoundland, J. Geophys. Res., 99, 15161-15180.

Reston, T. J.; Perez-Gussinye, M.; Phipps Morgan, J., 2003. Numerical Modelling of the Transition from Continental Rifting to Mantle Exhumation at the West Iberia Margin, American Geophysical Union, Fall Meeting 2003, abstract #T12A-0433.

Reynolds, P. H., Elias, P., Muecke, G. K. and Grist, A. M., 1987. Thermal history of the southwestern Meguma Group, Nova Scotia, from 40Ar/39Ar and fission track dating study of intrusive rocks;, Can. J. Earth Sci., 24, 1952-1965.

Roeser, H. A., 1982, Magnetic Anomalies in the Magnetic Quiet Zone off Morocco, in von, Rad, U., Hinz, K., Sarnthein, M., and Seibold, E. (eds.), Geology of the Northwest African Continental Margin, Springer Verlag, Berlin, pp. 60–68.

Roeser, H.A., Steiner, C., Schreckenberger, B., Block, M., 2002. Structural development of the Jurassic Magnetic Quiet Zone off Morocco and identification of Middle Jurassic Magnetic Lineations, J. Geophys. Res., (B10), 107.

Roest, W., R., Danobeitia, J., Verhoef, J., and Collette, B. J., 1992. Magnetic anomalies in the Canary Basin and the Mesozoic evolution of the Central North Atlantic. Marine Geophysical Research, 14, 1-24.

Rogers, H. D. 1985. Geology of the Igneous-Metamorphic Complex of Shelburne and eastern Yarmouth counties, Nova Scotia; in Current Research, Part A, Geological Survey of Canada, Paper 85-1A, 773-777.

Royden, L. and Keen, C. E., 1980. Rifting process and thermal evolution of the continental margin of eastern Canada determined from subsidence curves, Earth Planet. Sci. Lett., 51, 343-361.

Sahabi, M., Aslanian, D. and Olivet, J.-L., 2004. Un nouveau point de départ pour l'histoire de l'Atlantique central, Comptes Rendus Geosciences, 336, 12,1041-1052.

Salisbury, M.H. and Keen, C.E., 1993. Listric faults imaged in oceanic crust, Geology, 21, 117-120.

Sandwell, D. T. and Smith, W. H. F., 1997. Marine gravity anomaly from Geosat and ERS 1 satellite altimetry, J. Geophys. Res., 102, 10039-10054.

Sawyer, D.S., Whitmarsh, R.B., Klaus, A., et al. (including Milliken, K. L.), 1994. Proceedings of the Ocean Drilling Program, Initial Reports, 149, College Station, TX, 719.

Schermerhorn, L. J. G., Priem, H. N. A., Boelrijk, N. A., Hebeda, E.H., Verdumen, E. A. Th., and Verschure, R. H., 1978. Age and origin of the Messejana dolerite fault-dike system (Portugal and Spain) in the light of the opening of the North Atlantic Ocean: Journal of Geology, 86, 299-309.

Schenk, P. E., 1970. Regional variation of the flysch-like Meguma Group (Lower Paleozoic) of Nova Scotia compared to recent sedimentation off the Scotia Shelf; Geological Association of Canada, Special Paper 7, 127-153.

Schneider, W., 1978. Integral formulation for migration, Geophysics, 43, 49-76.

Sheridan, R. E., D. L., Musser, L., Glover III, J, I., Ewing, W. S., Holbook, G. M., Purdy, R., Hawman, and S. Smithson, 1993. Deep seismic reflection data of EDGE U.S. mid-Atlantic continental-margin experiment: Implications for Appalachian sutures and Mesozoic rifting and magmatic underplating, Geology, 21, 563-567.

Sherif, R. E., and Geldart, L. P., 1995. Exploration Seismology. Cambridge University Press.

Shimeld, J., 2004. A comparison of salt tectonic subprovinces beneath the Scotian Slope and Laurentian Fan, in Salt Sediment Interactions and Hydrocarbon Prospectivity: Concepts, Applications, and Case Studies for the 21st Century, 24th Annual Conference, Post, P., Olson, D., Lyons, K., Palmes, S., Harrison, P. and Rosen N., editors. Gulf Coast Section Society of Economic Paleontologists and Mineralogists Foundation (GCSSEPM), Houston, TX (CD format).

Shipboard Scientific Party, 1987. Site 637. *In* Boillot, G., Winterer, E.L., Meyer, A.W., et al., *Proc. ODP, Init. Repts.,* 103: College Station, TX (Ocean Drilling Program), 123–219.

Sleep, N. H., 1996. Lateral flow of hot plume material ponded at sublithospheric depths, J. Geophys. Res., 101(B12), 28,065–28,084.

Sleep, N.H. and Barth, G.A., 1997. The nature of oceanic lower crust and shallow mantle emplaced at low spreading rates, Tectonophysics, 279, 181–191.

Srivastava, S. P. and Keen, C. E., 1995. A deep seismic reflection profile across the extinct Mid-Labrador Sea spreading center, Tectonics, 14, 372-389.

Sundeen, D.A., 1989. Note concerning the petrography and K-Ar age of Cr-spinel-bearing olivine tholeiite in the subsurface of Choctaw County, north-central Mississippi: Southeastern Geology, 30, 137-146.

Sutter, J. F. and Smith, T. E., 1979. $^{40}Ar/^{39}Ar$ ages of diabase intrusions from Newark Trend Basins in Connecticut and Maryland: Initiation of Central Atlantic Rifting, *Am. J. Sci.* 279, 808–831.

Sutter, J. F., 1985. Progress on geochronology of Mesozoic diabase and basalts, US Geological Survey Circular 946, chapter 21, Page 110-114.

Talwani, M. and Abreu, V., 2000. Inferences regarding initiation of oceanic crust formation from the U.S. east coast margin and conjugate south Atlantic margins, in Atlantic rifts and continental margins, edited by Mohriak W. and Talwani, M., 211-233, American geophysical Union, Geophysical Monograph 155, Washington, DC.

Talwani, M., Ewing, J., Sheridan, R. E., Holbrook, W. S. and Glover, L. III., 1995. The EDGE experiment and the U.S. Coast Magnetic Anomaly, in NATO/ARW Series book Rifted Ocean-Continent Boundaries, (ed. Banda, E., Talwani, M. and Torne, M.), Amsterdam: Kluwer, 155-181.

Talwani, M., Worzel, J. L. and Landisman, M., 1959. Rapid gravity computations for two-dimensional bodies with application to the Mendocino submarine fracture zone, J. Geophys. Res., 64, 49-59.

Tari, G., Molnar, J. and Ashton, P., 2003. Examples of salt tectonics from West Africa: a comparative approach. In: T.J. Arthur, D.S. Macgregor and N.R. Cameron (Editors), Petroleum geology of Africa: New themes and developing technologies. The Geological Society, London, pp. 85-104.

Tari, G., and Molnar, J., 2005. Correlation of syn-rift structural between Morocco and Nova Scotia, Canada, 25th Annual GCSSEPM Foundation Bob F. Perkins Research Conference, Petroleum Systems of Divergent Continental Margin Basins, Houston, Texas.

Tucholke, B. E. and Ludwig, W. J., 1982, Structure and Origin of the J Anomaly Ridge, Western North Atlantic, J. Geophys. Res. 87, 9389–9407.

Vauchez, A., Tommasi, A., Barruol, G. and Maumus, J. 2000. Upper mantle deformation and seismic anisotropy in continental rifts. Phys. Chem. Earth (A), 25 (2): 111-117.

Verhoef, J., Collette, B. J., Danobeitia, J. J., Roeser, H. A., and Roest, W. R., 1991, Magnetic Anomalies off West-Africa (20°–38° N), Marine Geophys. Res. 13, 81–103.

Verhoef, J., W.R. Roest, R. Macnab, J. Arkani-Hamed, and Project Team, 1996. Magnetic anomalies of the Arctic and North Atlantic Oceans and adjacent land areas, Geol. Surv. Can. Open File Rep., 3125a.

Vogt, P.R., 1973. Early events in the opening of the North Atlantic. In implications of continental drift to the Earth Sciences (D.H. Tarling and S.K. Runcorn, ed.), Vol. 2, pp. 693–712.

Vogt, P.R., 1991. Bermuda and Appalachian-Labrador rises: Common non-hotspot processes? Geology, 19, 41-44.

Wade, J.A., 1981. Geology of the Canadian Atlantic margin from Georges Bank to the Grand Banks, in: Geology of the North Atlantic Borderlands, Kerr, J. Wm. and Ferguson, A.J. (eds.), Canadian Society of Petroleum Geologists, Memoir 7, 447-460.

Wade, J. A. and MacLean, B. C., 1990. The geology of the southeastern margin: aspects of the geology of the Scotian Basin from recent seismic and well data, in Geology of the Continental Margin Eastern Canada, edited by Keen, M. J. and Williams, G. L., Geological Survey of Canada, Geology of Canada, No. 2, 167-238.

Watt, W.S., 1969. The coast-parallel dike swarm of southern Greenland in relation to the opening of the Ladrador Sea, Can. J. Earth Sci., 6, 1320-1321.

Webster, T.L., Murphy, J.B. and Barr, S.M. 1998. Anatomy of a terrane boundary, an integrated structural, geographic information system and remote sensing study of the Late Paleozoic Avalon-Meguma terrane boundary drift. Can. J. Earth Sci., 35: 787-801.

Welsink, H. J., Dwyer, J. D. and Knight, R. J., 1989. Tectono-stratigraphy of the passive margin off Nova Scotia, in Extensional tectonics and stratigraphy of the North Atlantic margin, edited by Tankard, A. J. and Balkwill, H.R., American Association of Petroleum Geologists, Memoir 46, 215-231.

Wheeler, J.O., Hoffman, P.F., Card, K.D., et al., 1997. Geological Map of Canada, Geological Survey of Canada, Map D1860A, Ottawa Geological Survey of Canada.

White, R. S., McBride, J. H., Henstock, T. J. and Hobbs, R. W., 1994. Internal structure of Mesozoic oceanic crust, Geology, 22, 597-600.

White, R. S. and McKenzie, D. P., 1989. Magmatism at rift zones: the generation of volcanic continental margins and flood basalts, J. Geophys. Res., 94, 7685-7729.

White, R. S., McKenzie, D. and O'Nions, K., 1992. Oceanic crustal thickness from seismic measurements and rare earth element inversions, J. Geophys. Res., 97, 19683-19715.

Whitmarsh, R.B. and Miles, P.R. 1995. Models of the development of the West Iberia rifted continental margin at 40°30'N deducted from surface and deep-tow magnetic anomalies, J. Geophys. Res., 100, 3789-3806.

Whitmarsh R. B., White R. S., Horsefield S. J., et al, 1996. The ocean-continent boundary off the western continental margin of Iberia: Crustal structure west of Galicia Bank, J. Geophys. Res. Sol 101 (B12): 28291-28314.

Williams, H., 1979. Appalachian Orogen in Canada, Can. J. Earth Sci., 16, 792-807.

Williams, H., and Hatcher, R. D. 1982. Suspect terranes and accretionary history of the Appalachian Orogen. Geology, 10: 530-536.

Withjack, M.O., Schlische, R.W., and Olsen, P.E., 1998, Diachronous rifting, drifting, and inversion on the passive margin of central eastern North America: An analog for other passive margins: AAPG Bulletin, 82, 817-835.

Wu, Y., Louden, K.E., Funck, T., Jackson, H.R., and Dehler, S.A., 2006. Crustal structure of the central Nova Scotia margin off Eastern Canada, Geophys. J. Int. 166 (2), 878-906.

Ye, S., J.P. Canales, R. Rihm, J.J. Dañobeitia and J. Gallart, 1999. A crustal transect through the northern and northeastern part of the volcanic edifice of Gran Canaria, Canary Islands, J. Geodynamics., 28 (1), 3-26.

Yilmaz, Ö.Z., 2001. Seismic data analysis: processing, inversion, and interpretation of seismic data, second edition, SEG publication.

Zelt, C. A. and Forsyth, D. A., 1994. Modeling wide-angle seismic data for crustal structure: southeastern Grenville province, J. Geophys. Res., 99, 11687-11704.

Zelt, C. A. and Smith, R. B., 1992. Seismic traveltime inversion for 2-D crustal structure, Geophys. J. Int., 108, 16-34.

APPENDIX A

OBS DATA MODELING DOCUMENTS

Input and output files and tables for OBS data modeling are included in this appendix for reference. These include a table of OBS locations and depths (Table A.1), the shot-point locations (Table A.2), and the velocity-depth profiles (Figure A.1) used to convert seafloor travel times to seafloor depths, mainly used for OBS repositioning in Appendix B. The velocities obtained from sonic well log data for Nascapi, Glooscap, Acadia and Shubenacdie (BASIN database, Geological Survey of Canada, Dartmouth, Nova Scotia, Canada), which were used to constrain the velocity model, is shown in Figure A.2. An example of input file (r.in) for velocity modeling using RAYINVR and the final velocity model (v.in) are given in ASCII format of Zelt and Smith (1992).

Table A.1. OBS positions and depths along SMART Line 2

OBS #	Deployment [1]		Reposition [2]		Distance (km) [3]	Depth (m)
	Latitude (degree)	Longitude (degree)	Latitude (degree)	Longitude (degree)		
1	44.186295	-62.780191	44.185937	-62.781381	10.3051	240
2	43.891325	-62.485631	43.891501	-62.484758	50.7319	149
3	43.595477	-62.194519	43.595743	-62.193958	91.0646	98
4	43.307676	-61.914466	43.307672	-61.914035	130.2772	90
5	43.068345	-61.684533	43.069232	-61.683347	162.7222	131
6	42.936681	-61.558802	42.938567	-61.554836	180.6097	860
7	42.760178	-61.3913	42.762145	-61.387094	204.526	1977
8	42.624359	-61.263013	42.625973	-61.259615	222.9	2660
9	42.469692	-61.119012	42.470091	-61.118635	243.7286	3447
10	42.326812	-60.986284	42.324437	-60.992063	262.9629	3727
11	42.17586	-60.846161	42.17793	-60.843669	283.3154	3978
12	42.02786	-60.709662	42.02646	-60.718469	303.0414	4052
13	41.915191	-60.606182	41.920171	-60.603162	318.1819	4251
14	41.799626	-60.500629	41.798401	-60.506393	333.8908	4432
15	41.655018	-60.36914	41.653437	-60.370692	353.5534	4588
16	41.506835	-60.235464	41.508198	-60.229777	373.499	4698
17	41.360182	-60.103637	41.359741	-60.10323	393.0942	4778
18	41.212324	-59.9718	41.212504	-59.970941	412.8509	4838
19	41.059144	-59.835981	41.059057	-59.838242	433.2243	4881
20	40.861689	-59.66248	40.858426	-59.671336	459.5718	4935
21	40.676986	-59.49997	40.680954	-59.495622	484.208	5005

Note: [1] "Deployment" is the position where the OBS instrument is launched at surface.
[2] "Reposition" refers the OBS location on the seafloor which is calculated using the program specified in Appendix B.
[3] "Distance" refers to that to the last shot 3643 at 44.26334° N 62.85265° W.

Table A.2. Navigation of shooting along SMART Line 2 (every 100 shots)

Shot #	Longitude (degree)	Latitude (degree)
1	-59.4531	40.62861
100	-59.5267	40.70924
200	-59.6253	40.81996
300	-59.7146	40.92054
400	-59.8112	41.02974
500	-59.8976	41.12841
600	-59.99	41.23293
700	-60.0828	41.33696
800	-60.1696	41.43365
900	-60.2656	41.54005
1000	-60.3596	41.64652
1100	-60.4554	41.74891
1200	-60.5474	41.85071
1300	-60.6795	41.995
1400	-60.7814	42.10604
1500	-60.8816	42.21418
1600	-60.9732	42.31282
1700	-61.0554	42.4007
1800	-61.1504	42.50351
1900	-61.25	42.61052
2000	-61.3434	42.70938
2100	-61.4459	42.81828
2200	-61.5499	42.92828
2300	-61.6376	43.01915
2400	-61.7279	43.11283
2500	-61.8235	43.21278
2600	-61.9141	43.30691
2700	-62.018	43.4136
2800	-62.114	43.51291
2900	-62.1705	43.57066
3000	-62.2593	43.66151
3100	-62.3534	43.75695
3200	-62.4368	43.84162
3300	-62.5304	43.93634
3400	-62.6225	44.02821
3500	-62.7203	44.12649
3600	-62.813	44.22124
3643	-62.8527	44.26334

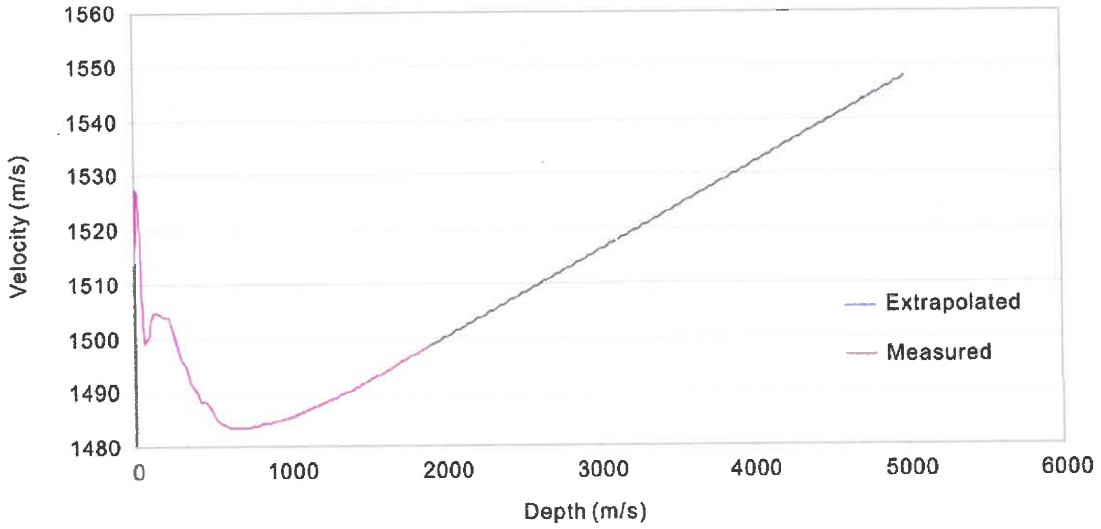

Figure A.1. Water-velocity profile for SMART Line2. The velocity-depth profile is derived from a conductivity, temperature and depth (CTD) measurement at 40° 30.86' N, 59° 41.42' W, near the southeastern end of Line 2. The CTD measurement was only conducted down to a depth of ~2 km; linear downward extrapolation of the velocity-depth function is applied for greater depths.

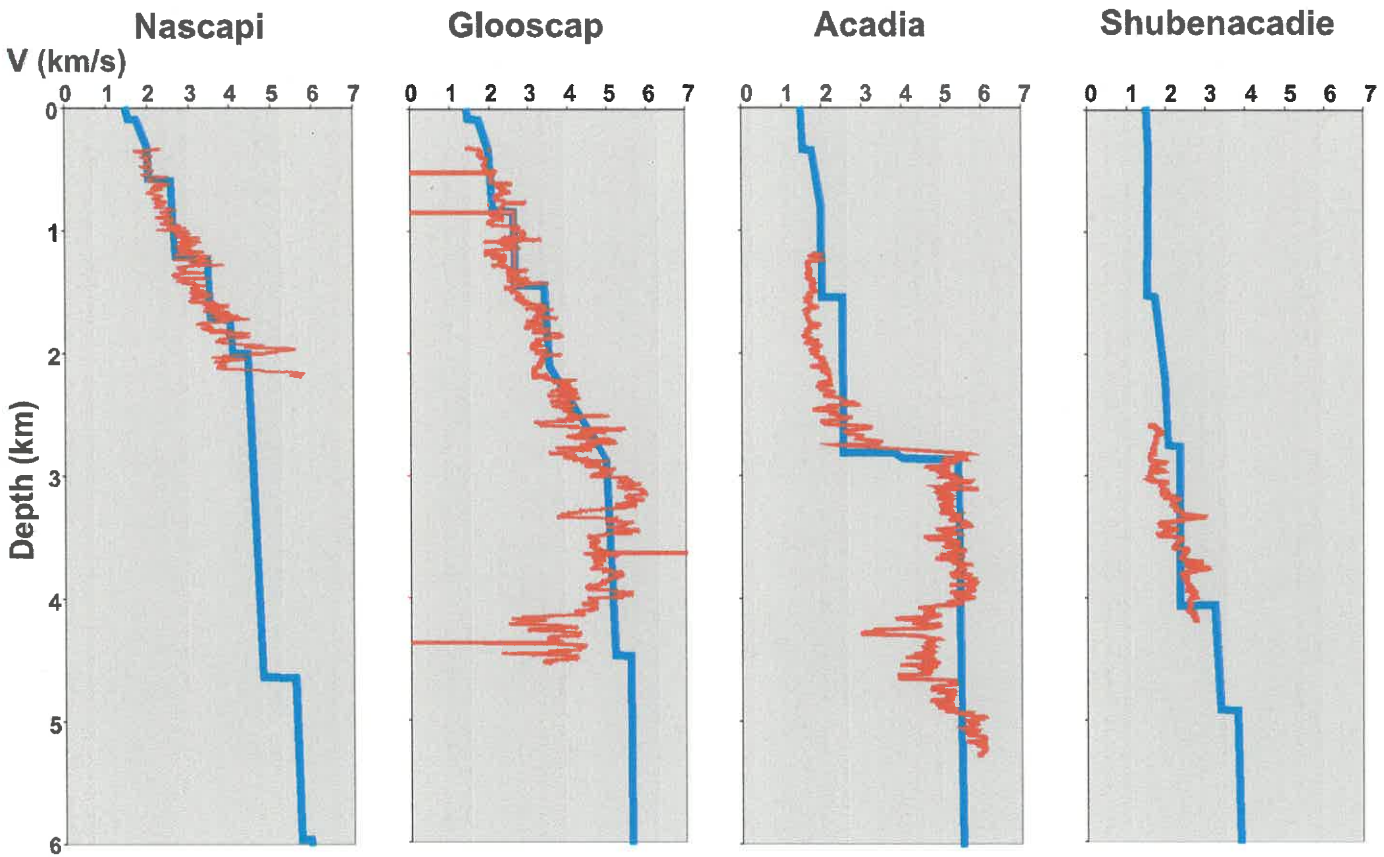

Figure A.2. Velocities obtained from sonic well log data for Nascapi, Glooscap, Acadia and Shubenacdie (BASIN database, Geological Survey of Canada, Dartmouth, Nova Scotia, Canada). The velocities (red curves) were used to constrain the velocity model, which is given in this appendix. For comparison, the velocities in the velocity model are shown as blue lines. For locations of the wells refer to Figure 2.9.

The following is an example of r.in for velocity modeling using RAYINVR in ASCII format of Zelt and Smith (1992):

```
&pltpar iroute=1,iseg=0,iray=2,ibnd=0,irays=0,ivel=0,
                              itx=1,itxout=1,idump=0,iszero=0,idash=0,isum=1,iplot=0,
                              idata=0,vred=7.0,nrskip=3,nskip=0,velht=0.05,
       symht=0.1,itxbox=1,isep=0,istep=0,ircol=3,irayps=0,
       itcol=3,ifcol=6,ibcol=0,
       mcol=8,14,1,4,14,
 colour=12, 3, 2, 2, 2, 6, 2, 9, 2, 4, 2, 4, 7, 14, 10, 13,
/
&axepar  xmin=0.,xmax=70.,xtmin=0.,xtmax=500.,xmm=70,
                                 ntickx=0, ndecix=-1,
        zmin=4., zmax=16., ztmin=0.,ztmax=18.,zmm=85, ntickz=0, ndeciz=-1,
        tmin=3.0,tmax=10.0,ttmin=3.0,ttmax=10.0, tmm=85, ntickt=0, ndecit=-1,
        xmint=0.,xmaxt=70.,xtmint=0.,xtmaxt=70.,xmmt=200, ntckxt=0,ndecxt=-1,
        iaxlab=1,itrev=0, sep=15, orig=15,
/
&trapar imodf=1, ibsmth=0, nbsmth=0, istop=0, crit=0., hws=1.0,
iraysl=1,ifast=1,
ishot=  0, 0, 0, 0, 0, 0, 0, 0, 0, 2, 0, 0, 0, 0, 0, 0, 0, 0, 0, 0,
xshot=  10.3051, 50.7319, 91.0646, 130.2772, 162.7222, 180.6097, 204.526, 222.9,
         243.7286, 262.9629, 283.3154, 303.0414, 318.1819, 333.8908, 353.5534,
         373.499, 393.0942, 412.8509, 433.2243, 459.5718, 484.208,
zshot=  0.24, 0.156, 0.098, 0.09, 0.131, 0.838, 1.929, 2.65, 3.428, 3.727, 3.960, 4.052,
         4.255, 4.430, 4.570, 4.680, 4.769, 4.831, 4.876, 4.935, 5.005,
irayt= 1,  1,  1,  1,  1,  1,  1,  1,  1,  1,  1,  1,  1,  1,  1,  1,
       1,  1,  1,  1,  1,  1,  1,  1,  1,  1,  1,  1,  1,  1,  1,  1,
ray = 1.2, 2.2, 3.1, 3.2, 4.1, 4.2, 6.1, 6.2, 7.1, 8.1, 9.1, 9.2,10.1,11.1,12.1,14.1,15.1,16.1
nray = 35, 35, 35, 35, 35, 35, 35, 30, 15, 35, 30, 30, 35, 35, 35, 40, 45, 80,
xsmax=0.,nsmax=45,
space=1.0, 2.0, 1.0, 1.0, 1.0, 2.0, 2.0, 2.0, 2.0, 2.0, 2.0, 2.0, 2.0, 2.0, 2.0, 1.0, 2.0,1.0,
aamin=0.50, aamax=85., step=0.05,
pois=0.5,0.25,0.25,0.25,0.25,0.25,0.25, 0.25,0.25,
nhray=30,
/
&invpar  invr=0,
ivray= 2,  0,  0,  0,  0,  0,  0,  0,  0,  0,  0,  0,  0,  0,  8,  0,
        bndunc=0.08, velunc=0.05,  ximax=2.0,
 /
```

The following is the velocity model (v.in) in an ASCII format of Zelt and Smith (1992):

1	0	499								
0	0	0								
	0	0								
1	0	499								
0	1.47	1.49								
	0	0								
1	0	499								
0	1.49	1.53								
	0	0								
2	0	3.68	4.99	7.59	11.43	15.27	23.26	30.07	35.04	38.79
1	0.19	0.19	0.22	0.23	0.25	0.24	0.2	0.17	0.17	0.15
	0	0	0	0	0	0	0	0	0	0
2	42.6	45.21	49.25	54.36	58.09	65.04	77.52	82.71	92.15	95.67
1	0.15	0.12	0.15	0.17	0.15	0.13	0.11	0.09	0.1	0.1
	0	0	0	0	0	0	0	0	0	0
2	99.34	100.19	149.14	150.38	159.41	164.55	171.73	174	178.9	181.32
1	0.1	0.1	0.1	0.09	0.11	0.16	0.37	0.47	0.76	0.87
	0	0	0	0	0	0	0	0	0	0
2	186.21	199.52	222.09	224.76	245.71	248.57	256.29	260.9	280.51	286.4
1	1.09	1.73	2.64	2.68	3.51	3.53	3.65	3.71	3.94	3.98
	0	0	0	0	0	0	0	0	0	0
2	293.83	299.64	310.33	319.77	328.96	338.45	357.78	400.6	428.51	450.88
1	3.97	4.01	4.15	4.28	4.39	4.47	4.62	4.8	4.87	4.91
	0	0	0	0	0	0	0	0	0	0
2	468.71	483.98	499							
0	4.96	5.02	5.02							
	0	0	0							
2	0	351.45	499							
0	1.75	1.7	1.7							
	0	0	0							
2	0	351.45	499							
0	2	1.95	1.95							
	0	0	0							
3	0	10.33	163.72	166.63	176.19	202.65	222.8	229.3	232.67	250.7
1	0.29	0.31	0.34	0.41	1.36	2.57	3.37	3.14	3.91	4.1
	0	0	0	0	0	0	0	0	0	0
3	283.19	301.63	317.97	348.85	393.24	421.5	445.65	471.3	499	
0	4.48	4.57	4.9	5.4	5.52	5.58	5.61	5.76	5.78	
	0	0	0	0	0	0	0	0	0	
3	0	130.46	179.15	203.29	223.05	262.94	283.14	302.7	326.45	359.9
1	2.05	2	2	2	2.01	2.03	2.05	2.11	2.1	2.05
	0	0	0	0	0	0	0	0	0	0
3	393.96	413.59	433.57	499						
0	2.04	2.04	2.06	2.06						
	0	0	0	0						

3	0	179.15	202.86	222.08	262.99	280.41	283.87	301.2	324.19	359.09
1	2.1	2.03	2.08	2.08	2.06	2.05	2.1	2.14	2.15	2.06
	0	0	0	0	0	0	0	0	0	0
3	394.88	433.93	499							
0	2.05	2.07	2.07							
	0	0	0							
4	0	10.33	30.81	50.04	91.06	131.02	152.52	164.1	180.93	192.86
1	0.29	0.31	0.32	0.51	0.62	0.86	1.07	1.26	2	2.6
	0	0	0	0	0	0	0	0	0	0
4	210.14	224.08	228.94	235.02	246.11	254.35	259.07	261.7	267.39	269.74
1	3.32	3.93	3.43	4.7	5.34	4.37	4.69	5.48	4.9	5.18
	0	0	0	0	0	0	0	0	0	0
4	273.67	276.65	280.1	281.12	281.7	283.39	302.6	334.5	351.71	393.04
1	4.98	4.96	4.58	4.86	5.21	5.65	5.84	5.92	6	6.25
	0	0	0	0	0	0	0	0	0	0
4	411.59	455.31	499							
0	6.18	6.08	6.1							
	0	0	0							
4	0	93.31	125.08	145.93	166.77	183.36	203.5	223.6	225.44	250.83
1	2.5	2.57	2.7	2.72	2.55	2.33	2.35	2.35	3	2.99
	0	0	0	0	0	0	0	0	0	0
4	261.74	282.06	282.77	303.1	333.97	367.39	393	431.2	468.6	499
0	2.99	3	2.9	3	3	2.8	2.79	2.65	2.44	2.45
	0	0	0	0	0	0	0	0	0	0
4	0	92.98	124.75	145.76	167.44	183.92	202.8	223.8	224.48	258.13
1	2.51	2.58	2.71	2.75	2.6	2.34	2.36	2.4	3.15	3
	0	0	0	0	0	0	0	0	0	0
4	281.47	302.81	333.79	367.01	401.76	432.14	469.09	499		
0	3.05	3.1	3.05	2.95	2.85	2.68	2.5	2.49		
	0	0	0	0	0	0	0	0		
5	0	10.33	30.53	49.97	90.8	115.59	148.06	153.4	162.07	167.87
1	0.29	0.31	0.54	0.71	1.3	1.43	1.48	1.65	1.99	2.55
	0	0	0	0	0	0	0	0	0	0
5	177.66	192.96	207.91	225.1	228.94	233.25	244.82	251.9	253.48	258.83
1	3.48	4.02	4.27	4.61	3.43	5.57	7.07	5.72	5.19	5.1
	0	0	0	0	0	0	0	0	0	0
5	261.78	266.75	269.83	273.87	276.38	278.82	280.05	282	302.93	349.6
1	6.72	5.25	5.72	5.26	6.13	5.38	6.48	6.96	7.02	7.19
	0	0	0	0	0	0	0	0	0	0
5	499									
0	7.22									
	0									
5	0	24.82	41.78	67.83	105.23	152.65	179.37	193.6	213.4	221.68
1	3.12	3.2	3.3	3.35	3.48	3.3	3	3.25	3.2	3.28
	0	0	0	0	0	0	0	0	0	0
5	499									
0	3.3									

	0									
5	0	12	24.73	41.78	67.67	129.71	184.76	214.4	499	
0	3.12	3.16	3.2	3.31	3.36	3.52	3.36	3.35	3.5	
	0	0	0	0	0	0	0	0	0	
6	0	20.57	47.73	67.32	91.18	130.19	152.88	161.3	164.91	167.87
1	0.32	0.67	1.1	1.42	1.87	2.11	2.31	2.4	2.45	2.55
	0	0	0	0	0	0	0	0	0	0
6	169.88	171.15	173.71	177.61	183.36	191.75	199.51	214.7	220.49	226.13
1	2.75	2.87	4.1	4.62	4.61	4.97	4.84	5.35	5.61	5.66
	0	0	0	0	0	0	0	0	0	0
6	229.37	233.25	234.83	250.11	251.86	253.48	258.83	261.8	266.75	269.83
1	4.24	5.57	7.95	8.33	5.72	5.19	5.1	6.72	5.25	5.72
	0	0	0	0	0	0	0	0	0	0
6	273.87	276.38	278.82	280.05	282.02	302.93	349.6	499		
0	5.26	6.13	5.38	6.48	6.96	7.02	7.19	7.22		
	0	0	0	0	0	0	0	0		
6	0	68.11	91.19	130.19	176.4	200.53	224.9	281.2	324.95	396.42
1	4.05	4.05	4.05	3.98	3.85	3.78	3.75	4.12	4.09	3.96
	0	0	0	0	0	0	0	0	0	0
6	431.18	499								
0	4.1	4.1								
	0	0								
6	0	68.11	90.19	173.54	194.94	222.93	237.22	249.8	283.15	325.28
1	4.2	4.06	4.06	4.07	3.95	4	4	4.3	4.4	4.25
	0	0	0	0	0	0	0	0	0	0
6	345.85	364.11	395.84	431.59	499					
0	4.22	4.21	4.11	4.15	4.15					
	0	0	0	0	0					
7	0	20.57	47.73	67.32	91.01	103.52	139.87	158.4	171.27	174.41
1	0.32	0.67	1.1	1.42	2.32	2.54	3.07	3.18	3.3	5.03
	0	0	0	0	0	0	0	0	0	0
7	182.26	224.19	226.13	229.37	233.25	234.83	250.11	251.9	253.48	258.83
1	6.37	7.65	5.66	4.24	5.57	7.95	8.33	5.72	5.19	5.1
	0	0	0	0	0	0	0	0	0	0
7	261.78	266.75	269.83	273.87	276.38	278.82	280.05	282	282.76	328.64
1	6.72	5.25	5.72	5.26	6.13	5.38	6.48	6.96	8.15	8.3
	0	0	0	0	0	0	0	0	0	0
7	374.6	390.77	405.81	422.3	441.69	456.99	466.19	477.2	499	
0	8.9	8.69	8.34	8.24	8	7.91	7.97	7.91	7.85	
	0	0	0	0	0	0	0	0	0	
7	0	223.97	233.12	250	252.45	279.15	499			
0	4.25	4.4	4.45	4.42	4.45	4.38	4.07			
	0	0	0	0	0	0	0			
7	0	224.02	243.54	285.13	499					
0	4.25	4.51	4.5	4.5	4.22					
	0	0	0	0	0					
8	0	20.57	47.73	67.32	91.01	103.52	139.87	158.4	171.27	174.41

1	0.32	0.67	1.1	1.42	2.32	2.54	3.07	3.18	3.3	5.03
	0	0	0	0	0	0	0	0	0	0
8	182.26	224.19	234.83	250.11	282.76	328.64	374.6	390.8	405.81	422.3
1	6.37	7.65	7.95	8.33	8.15	8.3	8.9	8.69	8.34	8.24
	0	0	0	0	0	0	0	0	0	0
8	441.69	456.99	466.19	477.18	499					
0	8	7.91	7.97	7.91	7.85					
	0	0	0	0	0					
8	0	90.72	106.1	138.93	182.27	213.63	252.39	283.2	294.45	310.12
1	4.4	4.4	4.9	4.9	4.55	4.6	4.6	4.55	4.58	4.7
	0	0	0	0	0	0	0	0	0	0
8	326.74	336.34	353.28	365.64	376.07	392.78	415.03	436.4	459.35	499
0	4.51	4.41	4.4	4.4	4.41	4.43	4.42	4.35	4.3	4.3
	0	0	0	0	0	0	0	0	0	0
8	0	82.16	106.1	140.09	182.1	213.96	253.04	282.6	294.77	310.12
1	4.5	4.45	5.13	5.16	4.65	4.75	4.75	4.6	4.6	4.72
	0	0	0	0	0	0	0	0	0	0
8	316.19	326.56	336.85	345.73	364.88	376.24	386.82	399.1	436.39	451.53
1	4.63	4.51	4.42	4.41	4.41	4.41	4.43	4.44	4.44	4.35
	0	0	0	0	0	0	0	0	0	0
8	455.77	467	470.18	499						
0	4.4	4.4	4.32	4.4						
	0	0	0	0						
9	0	20.57	25.51	34.19	43.09	47.73	67.32	71.82	82.8	91.01
1	0.32	0.67	1.81	1.53	2.45	1.1	1.42	3.67	4.64	2.32
	0	0	0	0	0	0	0	0	0	0
9	103.52	117.18	133.44	139.87	158.43	171.27	174.41	182.3	201.94	222.73
1	2.54	4.04	4.67	3.07	3.18	3.3	5.03	6.37	7.1	8.76
	0	0	0	0	0	0	0	0	0	0
9	243.73	283.42	297.84	301.08	304.83	306.42	314.8	316.7	318.29	318.82
1	9.35	9.54	9.9	9.84	9.05	9.27	9.64	8.85	8.75	8.77
	0	0	0	0	0	0	0	0	0	0
9	320.17	320.91	322.5	324.25	326.44	327.78	328.89	331.7	332.54	335.51
1	9.08	9.76	9.7	9.47	8.92	8.6	8.59	9.39	9.85	10.01
	0	0	0	0	0	0	0	0	0	0
9	335.84	336.89	338.41	341.67	343.72	344.88	347.65	353.3	354.77	356.76
1	9.76	9.63	9.59	10.1	9.84	9.32	9.68	9.66	10.08	10.21
	0	0	0	0	0	0	0	0	0	0
9	358.91	360	361.08	364.25	366.45	369.46	371.17	375.5	377.39	378.92
1	11.29	10.93	9.2	10.09	9.49	9.95	9.76	9.52	9.12	9.01
	0	0	0	0	0	0	0	0	0	0
9	383.31	386.73	389.45	392.75	404.07	405.94	409.77	412.6	416.12	417.34
1	9.33	9.92	9.38	9.4	9.49	8.78	9.3	9.95	9.95	9.68
	0	0	0	0	0	0	0	0	0	0
9	419.13	421.73	423.69	430.04	437.85	440.95	446.32	449.8	452.02	454.95
1	9.36	8.42	9.32	9.55	9.67	8.59	9.55	9.47	8.49	8.88
	0	0	0	0	0	0	0	0	0	0

9	456.91	462.38	465.2	469.34	471.53	475.79	477.1	479.3	481.98	487.35
1	8.41	9.56	9.47	8.18	8.62	8.48	8.1	9.09	9.2	8.32
	0	0	0	0	0	0	0	0	0	0
9	499									
0	8.3									
	0									
9	0	297.9	332.46	347.94	356.6	358.96	369.22	372.9	379.15	386.73
1	5.2	5.2	5.6	5.6	5.6	5.8	5.8	5.7	5.5	5.6
	0	0	0	0	0	0	0	0	0	0
9	392.45	400.16	405.94	416.56	421.57	428	450.23	462.4	499	
0	5.5	5.5	5.4	5.5	5.5	5.7	5.6	5.7	5.7	
	0	0	0	0	0	0	0	0	0	
9	0	332.47	334.54	499						
0	6.1	5.6	6.03	6.03						
	0	0	0	0						
10	0	20.57	25.51	34.19	43.09	47.73	67.32	71.82	82.8	91.01
1	0.32	0.67	1.81	1.53	2.45	1.1	1.42	3.67	4.64	2.32
	0	0	0	0	0	0	0	0	0	0
10	103.52	117.18	133.44	139.87	158.43	171.27	174.41	182.3	201.94	222.73
1	2.54	4.04	4.67	3.07	3.18	3.3	5.03	6.37	7.1	8.76
	0	0	0	0	0	0	0	0	0	0
10	243.73	283.42	297.84	301.08	304.83	306.42	314.8	316.7	318.29	318.82
1	9.35	9.54	9.9	9.84	9.05	9.27	9.64	8.85	8.75	8.77
	0	0	0	0	0	0	0	0	0	0
10	320.17	320.91	322.5	324.25	326.44	327.78	328.89	331.7	332.54	334.29
1	9.08	9.76	9.7	9.47	8.92	8.6	8.59	9.39	9.85	13.04
	0	0	0	0	0	0	0	0	0	0
10	342.27	359.21	366.14	372.93	380.46	386.48	390.13	395.6	400.72	406.35
1	13.11	12.6	12.1	11.81	12.03	12.14	11.66	11.25	11.12	11.28
	0	0	0	0	0	0	0	0	0	0
10	412.97	417.99	426.94	433.13	436.71	444.2	449.2	452.8	454.99	460.62
1	11.21	11.5	12.03	12.02	11.18	10.87	11.37	11.25	10.21	10.17
	0	0	0	0	0	0	0	0	0	0
10	465.54	472.05	478.98	499						
0	10.71	10.96	10.9	10.83						
	0	0	0	0						
10	0	302.01	332.18	334.74	348.11	359.36	370.61	385.2	404.86	416.44
1	5.1	5.1	5	7.15	7.25	7.28	7.32	7.25	7.25	7.3
	0	0	0	0	0	0	0	0	0	0
10	421.24	499								
0	6.95	6.85								
	0	0								
10	0	297.66	303.52	325.41	336.74	359.69	370.78	386.3	405.35	429.68
1	5	5.25	5.7	5.7	7.4	7.42	7.4	7.4	7.45	7.3
	0	0	0	0	0	0	0	0	0	0
10	461.28	499								
0	7.3	7.3								

	0	0								
11	0	20.57	25.51	34.19	43.09	47.73	67.32	71.82	82.8	91.01
1	0.32	0.67	1.81	1.53	2.45	1.1	1.42	3.67	4.64	2.32
	0	0	0	0	0	0	0	0	0	0
11	103.52	117.18	133.44	139.87	158.43	171.27	174.41	182.3	201.94	222.73
1	2.54	4.04	4.67	3.07	3.18	3.3	5.03	6.37	7.1	8.76
	0	0	0	0	0	0	0	0	0	0
11	243.73	283.42	297.84	301.08	304.83	306.42	314.8	316.7	318.29	318.82
1	9.35	9.54	9.9	9.84	9.05	9.27	9.64	8.85	8.75	8.77
	0	0	0	0	0	0	0	0	0	0
11	320.17	320.91	322.5	324.25	326.44	327.78	328.89	331.7	332.54	334.29
1	9.08	9.76	9.7	9.47	8.92	8.6	8.59	9.39	9.85	13.04
	0	0	0	0	0	0	0	0	0	0
11	336.41	342.64	361.51	374.91	383.85	390.63	400.56	408.7	418.76	430.83
1	13.91	14.28	13.99	13.93	14.09	14.02	13.58	13.55	14.02	14.27
	0	0	0	0	0	0	0	0	0	0
11	445.39	499								
0	14.02	14.54								
	0	0								
11	0	302.01	332.18	336.41	499					
0	5.1	5.1	5	5.5	5.79					
	0	0	0	0	0					
11	0	297.66	302.38	322.73	334.29	499				
0	5	5.25	5.5	5.5	5.6	5.79				
	0	0	0	0	0	0				
12	0	20.57	25.51	34.19	43.09	47.73	67.32	71.82	82.8	91.01
1	0.32	0.67	1.81	1.53	2.45	1.1	1.42	3.67	4.64	2.32
	0	0	0	0	0	0	0	0	0	0
12	103.52	117.18	133.44	139.87	158.43	171.27	174.41	182.3	201.94	222.73
1	2.54	4.04	4.67	3.07	3.18	3.3	5.03	6.37	7.1	8.76
	0	0	0	0	0	0	0	0	0	0
12	243.73	283.42	297.84	302.22	313.94	320.28	322.41	327.8	334.29	336.41
1	9.35	9.54	9.9	11.64	11.75	12.16	12.73	13.11	13.04	13.91
	0	0	0	0	0	0	0	0	0	0
12	342.64	361.51	374.91	383.85	390.63	400.56	408.66	418.8	430.83	445.39
1	14.28	13.99	13.93	14.09	14.02	13.58	13.55	14.02	14.27	14.02
	0	0	0	0	0	0	0	0	0	0
12	499									
0	14.54									
	0									
12	0	20.19	43.71	48.09	86.91	132.47	170.91	175.1	183.32	499
0	5.5	5.48	5.5	5.52	5.58	5.58	5.55	5.2	5.1	5.1
	0	0	0	0	0	0	0	0	0	0
12	0	224.02	499							
0	5.7	5.7	5.7							
	0	0	0							
13	0	70.09	78.64	83.31	93.1	100.25	122.4	137.1	144.74	158.42

1	3.73	5.46	5.62	5.98	7.67	8.57	10.33	10.63	10.43	10.33
	0	0	0	0	0	0	0	0	0	0
13	171.61	183.94	220.21	262.81	284.51	302.22	313.94	320.3	322.41	327.78
1	10.43	10.67	11.73	12.33	12.05	11.64	11.75	12.16	12.73	13.11
	0	0	0	0	0	0	0	0	0	0
13	334.29	336.41	342.64	361.51	374.91	383.85	390.63	400.6	408.66	418.76
1	13.04	13.91	14.28	13.99	13.93	14.09	14.02	13.58	13.55	14.02
	0	0	0	0	0	0	0	0	0	0
13	430.83	445.39	499							
0	14.27	14.02	14.54							
	0	0	0							
13	0	83.22	140.05	218.73	261.25	416.85	499			
0	5.9	5.95	6	6.03	6.2	6.85	6.85			
	0	0	0	0	0	0	0			
13	0	261.25	438.83	499						
0	6.3	6.3	7.05	7.05						
	0	0	0	0						
14	0	86.87	113.32	136.11	157.62	186.77	205.98	262.8	284.51	302.22
1	15.03	18.68	20.19	19.68	18.3	16.2	14.5	12.33	12.05	11.64
	0	0	0	0	0	0	0	0	0	0
14	313.94	320.28	322.41	327.78	334.29	336.41	342.64	361.5	374.91	383.85
1	11.75	12.16	12.73	13.11	13.04	13.91	14.28	13.99	13.93	14.09
	0	0	0	0	0	0	0	0	0	0
14	390.63	400.56	408.66	418.76	430.83	445.39	499			
0	14.02	13.58	13.55	14.02	14.27	14.02	14.54			
	0	0	0	0	0	0	0			
14	0	220.05	284.2	334.46	336.41	499				
0	6.78	6.82	6.81	6.87	6.9	6.71				
	0	0	0	0	0	0				
14	0	273.56	336.41	499						
0	6.9	6.9	7	6.9						
	0	0	0	0						
15	0	54.71	74.48	93.26	113.99	127.43	137.22	147.2	157.95	167.72
1	36.59	35.84	34.9	33.65	32.88	32.75	32.56	31.64	29.68	27.92
	0	0	0	0	0	0	0	0	0	0
15	180.33	192.6	205.78	218.78	231.66	245.8	262.11	278.4	292.77	307.1
1	25.99	24.33	21.98	19.94	18.54	17.62	16.93	16.55	15.55	14.73
	0	0	0	0	0	0	0	0	0	0
15	326.31	336.41	342.64	361.51	374.91	383.85	390.63	400.6	408.66	418.76
1	14.04	13.91	14.28	13.99	13.93	14.09	14.02	13.58	13.55	14.02
	0	0	0	0	0	0	0	0	0	0
15	430.83	445.39	499							
0	14.27	14.02	14.54							
	0	0	0							
15	0	337.19	351.75	363.83	385.17	405.52	423.89	499		
0	7.7	7.6	7.8	7.85	7.85	7.85	7.82	7.85		
	0	0	0	0	0	0	0	0		

15	0	278.95	351.75	385.99	402.11	424.55	499			
0	7.8	7.8	7.94	7.95	7.95	7.9	7.9			
	0	0	0	0	0	0	0			
16	0	54.71	74.48	93.26	113.99	127.43	137.22	147.2	157.95	167.72
1	36.59	35.84	34.9	33.65	32.88	32.75	32.56	31.64	29.68	27.92
	0	0	0	0	0	0	0	0	0	0
16	180.33	192.6	205.78	218.78	231.66	245.8	262.11	278.4	293.1	307.87
1	25.99	24.33	21.98	19.94	18.54	17.62	16.93	16.55	16.69	17.37
	0	0	0	0	0	0	0	0	0	0
16	317.2	327.62	337.06	345.53	353.34	362.79	373.37	380.5	388.75	396.06
1	17.95	18.08	17.89	17.07	16.44	16.12	15.73	15.91	16.2	16.04
	0	0	0	0	0	0	0	0	0	0
16	401.58	413.13	420.74	427.03	437.95	482.45	499			
0	16.04	15.88	15.85	15.69	15.6	14.43	14.54			
	0	0	0	0	0	0	0			
16	0	499								
0	8.1	8.1								
	0	0								
16	0	499								
0	8.5	8.79								
	0	0								
17	499									
0	40									

APPENDIX B

OBS REPOSITIONING PROGRAM "OBSLOC.M"

"OBSloc.m" is a Matlab program for repositioning the OBS instruments on seafloor. The earlier version of this program is a FORTRAN program running in DOS, written by Keith Louden in 1995. The Matlab version is a Windows-based executable file. Due to the frequent requests for additional instruction of how to use this program (for example, from graduate students from the University of Victoria), a basic instruction and sample input and output files are given in this appendix. The Matlab code of this program is printed out at end of this appendix. A CD is attached to the back cover of this thesis.

To locate the OBS position on seabed, the ship's echosounder data, the navigation of the shooting line (see Appendix A) and water velocity-depth profile (see Figure A.1 in Appendix A), and the direct travel time (DTT) from the OBS instrument to every shot are required. The ship's echosounder data provide water depth along the shooting line. The detailed water velocity-depth profile can be used to convert the seafloor depths into seafloor travel times. The actual travel times from the OBS instrument to all shots are recorded in the OBS data as direct travel times (DTT). The mechanism of this repositioning program is to seek for one point on the seabed, where the travel times from this point to all shots and the DTT have the least root mean square (RMS) residual travel times (distance). For a 2D survey, two points that have the least RMS error may be located on the seafloor. Only one of the two represents the OBS position on the seafloor. However, these two points should be conjugate points on either side of the shooting line; therefore, either point can provide correct distance for all seismic traces along the 2D

survey. For a 3D survey, the repositioned OBS instrument on seafloor should be definitive (one point).

Note that at least two assumptions are made for repositioning OBS instruments. One is that the OBS clock is correct, i.e. the OBS clock does not start earlier and later than scheduled recording. If OBS clock starts earlier than setup timing, the repositioned OBS instrument seems to have drifted to an unreasonable distance. On the other hand, if OBS clock starts later, the repositioned OBS instrument may look like floating above the seafloor. These are signs to check the OBS clock timing. The other assumption is that the water depth is constant in a certain range around the deployment position. Errors may result in area where bathymetry changes dramatically, for instance, over the slope or in the vicinity of a trench. However, the error caused by dramatic variation of water depths between the actual OBS location and the OBS deployment position can be reduced if the detailed bathymetry is known and well resolved. In this case, retrieve the water depth at the repositioned OBS instrument and use it as water depth at deployment, and run the "OBSloc.m" program again. This can be repeated until the repositioned OBS locations become stable.

The following is a simple manual for using this program. Some hints will be prompted in the heading area of the dialog window while running the program.

I. Start MatLab.

II. Execute "obsloc.m".

III. A dialog window is prompted. Locate and enter the water velocity-depth function file using the widows file browser (Figure B.1). A sample file is given as in Figure B.2.

IV. A second dialog window similar to Figure B.1 is prompted to input a file for DTT. The format of this file is given in Figure B.3.

V. A third dialog window is prompted to input the file of shot table. A sample shot table file is given in Figure B.4.

VI. A fourth dialog box is prompted to enter a file for saving the final result. The file contains the positions of re-located OBS instrument and the least RMS residual distance (in km). A sample file is shown in Figure B.5.

VII. Finally, through a dialog box, choose the maximal range for searching for the OBS instrument and the spacing of searching in meters. Default values are 250 m for maximum range and 5 m for searching grid.

VIII. When the program finishes running, a diagram (Figure B.6) will be automatically created with the detailed OBS location.

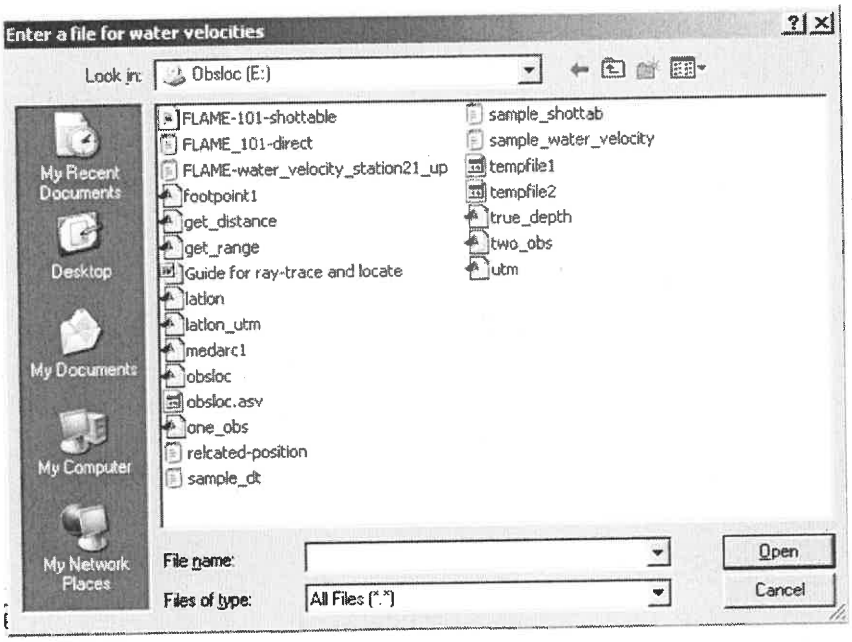

Figure B.1. A sample of dialog window for entering files. The file required to enter is indicated in the heading area on top of the window.

0	1496.28
17.29	1496.48
32.34	1494.12
43.74	1487.33
58.4	1484.22
…	…
1395.07	1485.64
1438.42	1486.16

Figure B.2. A sample of the water velocity-depth function file. The two columns represent "water depths" and "water velocities", respectively, delimited by a blank or a tab.

1292.0	3.0
7975	2186
7976	2177
7977	2173
7978	2166
7979	2162
7980	2153
7981	2144
7982	2140
7983	2131
7984	2124
7985	2120
7986	2111
7987	2103
7988	2100
7989	2090
…	…
7997	2038
7998	2029
7999	2021
8000	2017
8001	2011
8002	2007
8003	1999
8004	1991
8005	1985

Figure B.3. A sample of the DTT file. The first row contains measured water depth, and depth of detonation, delimited by a blank or tab. From the second row to the end of the file, the first column represents "shot number", while the second column, "direct travel time" (unit: ms).

```
Hudson 2002 Line 1 OBS16
  44.597500  -46.541500  OBS Ref. latitude and longitude
125 22 21  0.        Time of clock reset
   .0000          Clock drift rate (ms/hr)
   0              Delay in firing gun (interger msec)
   0              Offset(interger msec):obs&ship clocks
SHOT DAY HR MM    SEC   LATITUDE   LONGITUDE   RANGE
47043 217 15 46 14.1250  43.744538  -45.100616  149.200
47044 217 15 47 19.4270  43.745582  -45.102635  149.001
47045 217 15 48 23.4090  43.746562  -45.104469  148.818
47046 217 15 49 34.4950  43.747696  -45.106420  148.617
47047 217 15 50 43.8220  43.748930  -45.108336  148.410
```

Figure B.4. A sample of the shot table file. The first row contains comments of this data. The second row contains the latitude and longitude of the OBS instrument at deployment position, delimited by a blank or a Tab. The third to the seventh rows are also some comments. From the eighth row to the end of the file, each column contains the following information in sequence, delimited by blanks: "SHOT NUMBER" "DAY" "HOUR" "MINUTE" "SECOND" "LATITUDE (degree)" "LONGITUDE (degree)" "RANGE (km)"

```
48.68250 -126.88050 250.0  5.0  554
the best  fit OBS location:     48.68324 -126.88183  0.00906
the conjugate OBS location:  48.68420 -126.87982  0.01007
```

Figure B.5. A sample of the output file. The first row contains the "Latitude" and "Longitude" (in degree) of OBS position at deployment, "Maximum range" and "Spacing" of searching for OBS, and "Number of shots" that contribute to calculation, delimited by blanks. The second row contains the best-fit OBS position in "Latitude", "Longitude", and the "Least RMS of residual distance between the total range of "Assumed location of OBS from all shots" and the total range of "the actual OBS location from all shots" based on measurement (unit: km). The last row represents the conjugate OBS position, or indicates no conjugate OBS position after repositioning.

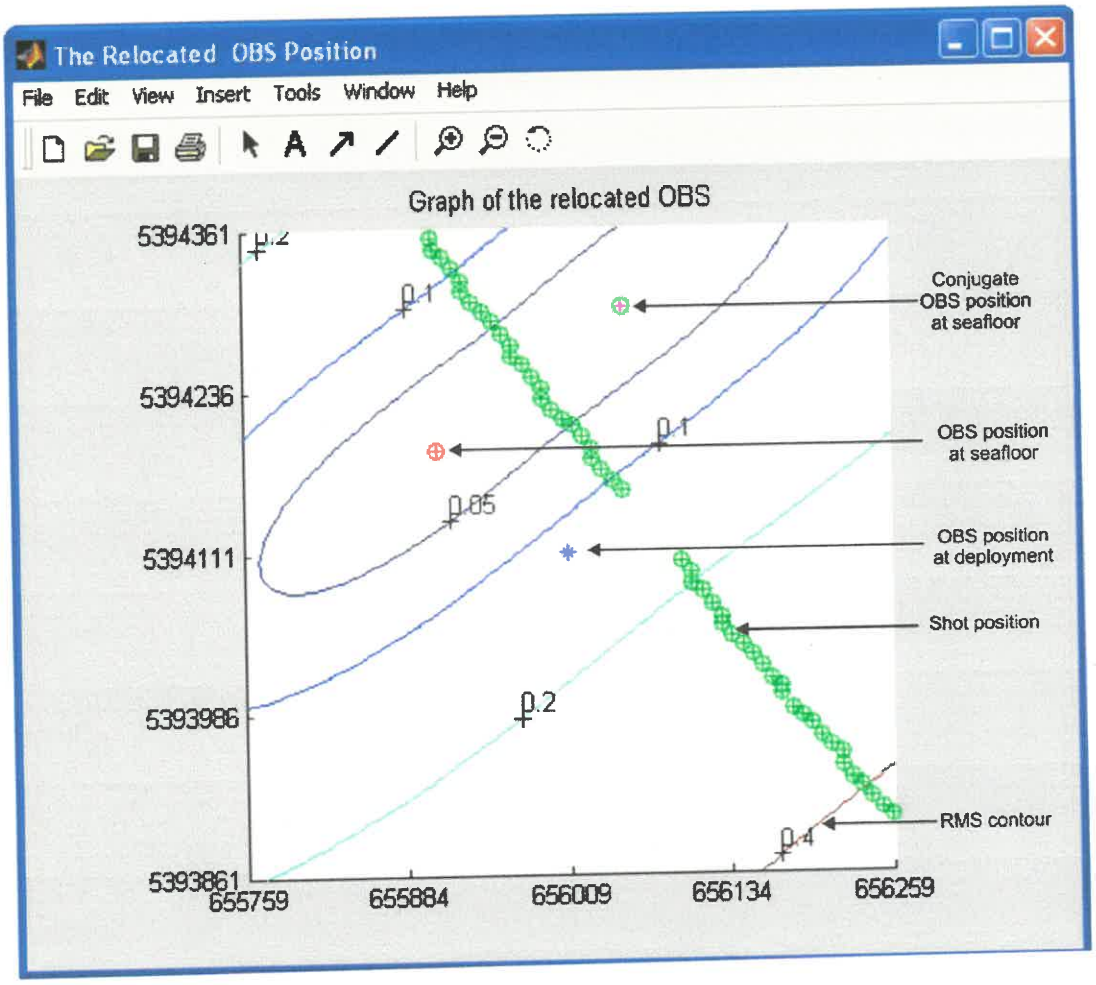

Figure B.6. A diagram showing the position of the OBS instrument on seafloor after repositioning. Contours are RMS of residual distance between the total range of "Assumed location of OBS from all shots" and the total range of "the actual OBS location from all shots" based on measurement (unit: km). The horizontal and vertical ticks are the UTM (Universal Transverse Mercator) coordinates (in meter).

The following is the Matlab cod of "obsloc.m" and its subroutines.

Main routine "Obsloc.m":

```
%This program aims at ray tracing and OBS repositioning.
%This Matlab program is translated from a FORTRAN program written by
% Keith Louden in 1995.

clear;
global water
% open files for input data:water velocity,direct time and shottable
% open a file for water depths and velocities
[filename, pathname] = uigetfile('*.*', 'Enter a file for water velocities');
   [fid1,message]=fopen(filename,'r');
% open file for direct time
[filename, pathname] = uigetfile('*.*', 'Enter a file for direct time');
   [fid2,message]=fopen(filename,'r');

% open file for shottable
[filename, pathname] = uigetfile('*.*','Enter the shot_table');
   [fid3,message]=fopen(filename,'r');

% open file for output
[filename, pathname] = uiputfile('*.*', 'Save the relocted OBS position in');
   [fid5,message]=fopen(filename,'w');
   [fid4,message]=fopen('tempfile1','w');

prompt={'Enter specified maximal range:','Enter specified least increment:'};
  def={'250','5'};
  dlgTitle='Specify the range and least increment:';
  lineNo=1;
  answer=inputdlg(prompt,dlgTitle,lineNo,def);
ymax=str2num(char(answer(1)));
xmax=ymax;
ydely=str2num(char(answer(2)));
xdely=ydely;

%read data from water.vel file
status=fseek(fid1,0,-1);
water=fscanf(fid1,'%f %f',[2 inf]);
water=water';
number_water_layer=size(water,1);

%Extend velocity distribution to greater depths
vel_inc=water(number_water_layer-1,2)-...
   water(number_water_layer-2,2);
```

```
dis_inc=water(number_water_layer-1,1)-...
   water(number_water_layer-2,1);
lay_inc=50-number_water_layer;

for j= 1 : lay_inc
   water(number_water_layer+j-1,1)= ...
      water(number_water_layer+j-2,1)+dis_inc;
   water(number_water_layer+j-1,2)=...
      water(number_water_layer+j-2,2)+vel_inc;
end

%read location (Lat&Lon) at which OBS is launched
%status=fseek(fid3,50, -1);
status=fseek(fid3,0,-1);
inputline=fgetl(fid3);
Latitude=fscanf(fid3,'%f',[1 1]);
Longitude=fscanf(fid3,'%f',[1 1]);
for n=0:5
 inputline=fgetl(fid3);
end

pre_position3=ftell(fid3);
fprintf(fid4,'%12.7f %12.7f\n',Latitude,Longitude);

%read head from DirectTime.inp
headDT(1:2)=0;
status=fseek(fid2,0,-1);
headDT(1)=fscanf(fid2,'%f',[1 1]);
headDT(2)=fscanf(fid2,' %f\n',[1 1]);

DEPTH=true_depth(headDT(1));  %corrected depth,i.e.,true depth
pre_position2=ftell(fid2);

%find the layer_number just below seabed
i=1;
while water(i,1)<DEPTH
   i=i+1;
   if i>50
      break
   end
end
water_layer_below_seabed=i;

%calculate the interface number at shot
     for i=1:35
        if water(i,1) >= headDT(2)
```

```
      interface_at_detonation=i;
      break
    end
  end

%calculate the interface number at seabed
for j=1:50
   if water(j,1) >= DEPTH
      interface_at_seabed=j;
      break
   end
 end

 %calculate which layer(at shot/seabed)is the shallower one
 if headDT(2) < DEPTH
    upper_layer=interface_at_detonation;
    lower_layer=water_layer_below_seabed;
    upper_depth=headDT(2);
    lower_depth=DEPTH;
 else
    upper_layer=water_layer_below_seabed;
    lower_layer=interface_at_detonation;
    upper_depth=DEPTH;
    lower_depth=headDT(2);
 end

 %find the maximum, minimum and mean velocity of water
 Vmax=water(upper_layer,2);
 Vmin=water(upper_layer,2);

 if (lower_layer-1) >= upper_layer
    for k=upper_layer:(lower_layer-1)
       if water(k,2) > Vmax
          Vmax=water(k,2);
       elseif water(k,2) < Vmin
          Vmin=water(k,2);
       else
    end
 end

 %problem could occur at the following part
 if lower_layer == upper_layer
    Vmean=water(upper_layer,2);%in fact,this part has no use
 else
    Dint=lower_depth-upper_depth;
    Vmean=(water(upper_layer,1)-upper_depth)/Dint...
```

```
            *water(upper_layer,2);
          if lower_layer ~= (upper_layer+1)
            n=lower_layer-2;
            for i=upper_layer : n
              Vmean=(water(i+1,1)-water(i,1))/...
                Dint*water(i,2)+Vmean;
            end
          end
            Vmean=Vmean+(lower_depth-water(lower_layer-1,1))/...
              Dint*water(lower_layer-1,2);
        end

        velocity_check=Vmax*Vmax-Vmin*Vmin;
        Depth_difference=DEPTH-headDT(2);

%read shot_number and direct_time from DirectTime.inp file
status=fseek(fid3,0, 1);
P_fid3=ftell(fid3);
status=fseek(fid2,0, 1);
P_fid2=ftell(fid2);

Direct_time(1:2)=0;
status=fseek(fid3,pre_position3, -1);
status=fseek(fid2,pre_position2, -1);
position_fid2=ftell(fid2);
position_fid3=ftell(fid3);

h = waitbar(0,'It is ray tracing,Please wait...');
while feof(fid2) ==0      %read data if not end of file
    Direct_time=fscanf(fid2,'%d %f',[2,1]);
    position_fid2=ftell(fid2);
    waitbar(position_fid2/P_fid2,h)
    if Direct_time(1)> 0
      Direct_time=Direct_time';
    else
      break
    end
    time_difference=Direct_time(2)/1000.0;

    shot_table(1:8)=0;
    while feof(fid3) ==0
      shot_table=fscanf(fid3,'%d %d %d %d %f %f %f %f',[8,1]);
      position_fid3=ftell(fid3);
      if (Direct_time(1)) == (shot_table(1))
        break
      end
```

```
    end
    shot_table(8)=abs(shot_table(8));

    Depth_check=Depth_difference*Depth_difference/...
       (time_difference*time_difference);

    if (velocity_check >= Depth_check)
       Velocity_del=Vmax*Vmax-Depth_check;
       if Velocity_del <= 0
         Velocity_del=0.0001;
       end
       Vmin=sqrt(Velocity_del)+0.1;
    end

    % Calculate maximal and minimal P value for direct water
    QC(1:3)=0;
    COS=Depth_difference/(time_difference*Vmax);
    if COS >= 1.0
       COS=1.0-0.1e-09;
    end
    QC(2)=sqrt(1.0 -COS*COS)/Vmin;

    COS=Depth_difference/(time_difference*Vmin);
    if COS >= 1.0
       COS=1.0-0.1e-09;
    end
    QC(1)=sqrt(1.0 - COS*COS)/Vmax;

    %Calculate the horizontal distance between shot and OBS
    Distance= get_distance(QC,Vmean,DEPTH,...
       upper_layer,headDT(2),...
       time_difference,lower_depth,upper_depth);
    Distance=Distance/1000.0;
    Distance_diferrence=Distance-shot_table(8);
    fprintf(fid4,'%d %10.5f %11.5f %7.3f %7.3f %7.3f\n',...
       Direct_time(1),shot_table(6),shot_table(7),...
       Distance,shot_table(8),Distance_diferrence);
 end
end
close(h);
fclose(fid1); fclose(fid2);
fclose(fid3); fclose(fid4);
global A A0 A2 A4 A6 A8 B E1 E2 F RECIPF k0 degrad

%Ellipsoidal parameters from Clark 1866 ellipsoid
%format long A
```

```
%format long B

A=6378206.4;
RECIPF=294.97898;
K0=0.9996;
RADDEG=57.29577951;
FE=500000.0;
F=1.0/RECIPF;
B=A-A*F;
E1=(A*A-B*B)/(A*A);
E2=(A*A-B*B)/(B*B);
degrad=1.7453292519945e-2;
DELM=100.0;

%Arc length constants:
A0=1.-0.25*E1-0.046875*E1*E1-0.01953125*E1^3.0-175.0/16384.*E1^4.0;
A2=0.375*(E1+0.25*E1*E1+0.1171875*E1^3.0-455.0/4096.0*E1^4.0);
A4=0.05859375*(E1*E1+0.75*E1^3.0-77.0/128.0*E1^4.0);
A6=35.0/3072.0*(E1^3.0-1.28125*E1^4.0);
A8=-315.0/131072.0*E1^4.0;

[fid4,message]=fopen('tempfile1','r');
[fid6,message]=fopen('tempfile2','w');
%read location (Lat&Lon) at which OBS is launched
status=fseek(fid4, 0, -1);
North1=fscanf(fid4,'%f' ,[1 1]);
East1=fscanf(fid4,'%f' ,[1 1]);

%calculate the central meridian in each zone
 CM=round(East1);
 cm=-177:6:177;
 n=size(cm');
 for i=1:n
    if CM < cm(i)+3 & CM > cm(i)-3
       CM=cm(i);
       break
    end
 end

%transfer Lat&lon of OBS position into UTM
UTM=latlon(North1,East1,CM);
North=UTM(1);
East=UTM(2);

%input data from fid1:input file
obs_loc=fscanf(fid4,'%d %f %f %f %f %f',[6,inf]);
```

```
obs_loc=obs_loc';
[number_of_record,n]=size(obs_loc);
 N=number_of_record;

 %fprintf(fid5,'%s %s %s\n',c1,c2,c3);
 fprintf(fid5,'%9.5f %9.5f %4.1f %4.1f %5d\n',...
   North1,East1,ymax,ydely,number_of_record);

 fprintf(fid6,'%9.5f %9.5f %4.1f %4.1f %5d\n',...
   North1,East1,ymax,ydely,number_of_record);

 L=2.0*ymax/ydely+1;
 M=2.0*xmax/xdely+1;

east=(East-xdely*((M+1.0)/2.0-1.0)):...
   xdely*(-1.0+M)/(M-1):...
   (East-xdely*((M+1.0)/2.0-M));

north=(North-ydely*((L+1.0)/2.0-1.0)):...
   ydely*(-1.0+L)/(L-1):...
   (North-ydely*((L+1.0)/2.0-L));

DELR(1:L,1:M)=0;
north_east(1:N,1:2)=0;

%a,b,c are the coeficients of a linear equation aX+bY+c=0%
a=0;
b=0;
c=0;
%r,s,t,w are tempery variables for calculating a,b,c%
r=0;
t=0;
s=0;
w=0;
for i=1:N
   north_east(i,:)=latlon_utm(obs_loc(i,2),obs_loc(i,3),CM);
   s=s+north_east(i,2)*north_east(i,2);
   t=t+north_east(i,2);
   w=w+north_east(i,2)*north_east(i,1);
   r=r+north_east(i,1);
end
a=N*w-t*r;
b=t*t-N*s;
c=-(b*r+a*t)/N;

h = waitbar(0,'It is re-locating, Please wait...');
```

```
for K=1:L
  for J=1:M
    for I=1:N
      DELN=(north(K)-north_east(I,1))*1.0e-3;
      DELE=(east(J)-north_east(I,2))*1.0e-3;
      RR2=sqrt(DELN*DELN+DELE*DELE);
      DDL(I)=RR2-obs_loc(I,4);
      DELR(J,K)=DELR(J,K)+DDL(I)*DDL(I);
    end
    DELR(J,K)=sqrt(DELR(J,K)/N);
    if DELR(J,K) < DELM
      DELM=DELR(J,K);
      for i=1:N
        DDLM(i)=DDL(i);
      end
      KMIN=K;
      JMIN=J;
    end
    waitbar(K*J/(L*M),h)
  end
end
close(h)

%Compute the position of OBS based on the computed minimum
YOBSM=North-ydely*((L+1.0)/2.0-KMIN);
XOBSM=East-xdely*((M+1.0)/2.0-JMIN);

for i=1:N   %re-consider this N
  fprintf(fid6,'%d %10.5f %10.5f %10.5f %10.5f\n',...
  obs_loc(i,1),obs_loc(i,2),obs_loc(i,3),obs_loc(i,4),DDLM(i));
end

LON_LAT=utm(YOBSM,XOBSM,CM);
YOBSM1=LON_LAT(1);
XOBSM1=LON_LAT(2);

fprintf(fid5,'the best  fit OBS location is :%10.5f %10.5f %8.5f\n',...
  YOBSM1,XOBSM1,DELM);

second_XOBSM=(b*b*XOBSM-a*b*YOBSM-a*c)/(a*a+b*b);
second_YOBSM=(a*a*YOBSM-a*b*XOBSM-b*c)/(a*a+b*b);
second_XOBSM=second_XOBSM+second_XOBSM-XOBSM;
second_YOBSM=second_YOBSM+second_YOBSM-YOBSM;

DY=(YOBSM-second_YOBSM)*1.0e-3;
DX=(XOBSM-second_XOBSM)*1.0e-3;
```

```
DXY=0.5*sqrt(DX*DX+DY*DY);

second_min=100;
second_KMIN=0;
second_JMIN=0;
for K=1:L
  for J=1:M
    DY=(north(K)-second_YOBSM)*1.0e-3;
    DX=(east(J)-second_XOBSM)*1.0e-3;
    Dxy=sqrt(DX*DX+DY*DY);
    if Dxy < DXY  &  DELR(J,K) < second_min
      second_min=DELR(J,K);
      second_KMIN=K;
      second_JMIN=J;
    end
  end
end
second_YOBSM=North-ydely*((L+1.0)/2.0-second_KMIN);
second_XOBSM=East-xdely*((M+1.0)/2.0-second_JMIN);
second_LON_LAT=utm(second_YOBSM,second_XOBSM,CM);
second_YOBSM1=second_LON_LAT(1);
second_XOBSM1=second_LON_LAT(2);

if second_min==100
  fprintf(fid5,'No conjugate OBS position!\n');
else
  fprintf(fid5,'the conjugate OBS location is :%10.5f %10.5f %8.5f\n',...
  second_YOBSM1,second_XOBSM1,second_min);
end

fclose(fid4);
fclose(fid5);
fclose(fid6);

f=figure('name','The Relocated  OBS Position','NumberTitle','off');
DELR=DELR';
%level=0.0:0.01:1.8;
level=[0 0.05 0.1 0.2 0.4 0.8 1.6 3 5];
num_xtick=(east(M)-east(1))/4;
num_ytick=(north(L)-north(1))/4;
axis off
x_tick=east(1):num_xtick:east(M);
[xx,xnum]=size(x_tick);
for i=1:xnum
xlabel(i)={num2str(round(x_tick(i)))};
end
```

```
y_tick=north(1):num_ytick:north(L);
[xx,ynum]=size(y_tick);
for j=1:ynum
   ylabel(j)={num2str(round(y_tick(j)))};
end

hold on
axes('YLim',[north(1) north(L)],'Ytick',y_tick,...
   'YTickmode','manual','YTickLabel',ylabel,...
   'YTickLabelMode','manual',...
   'XLim',[east(1) east(M)],'Xtick',x_tick,...
   'XTickmode','manual','XTickLabel',xlabel,...
   'XTickLabelMode','manual')
hold on

axis square;
hold on

[hh,hc]=contour(east,north,DELR,level);

hold on
plot(XOBSM,YOBSM,'r+')

hold on
plot(XOBSM,YOBSM,'rO')

if second_YOBSM > north(1) & second_YOBSM < north(L)...
      & second_XOBSM > east(1) & second_XOBSM < east(M)
hold on
plot(second_XOBSM,second_YOBSM,'m+')

hold on
plot(second_XOBSM,second_YOBSM,'gO')
end
hold on
plot(East,North,'b*')

label=0.01:0.04:0.2;
hold on
clabel(hh,level)
%clabel(hh,'manual');

hold on
title('Graph of the relocated OBS')
```

```
for i=1:N
  if north_east(i,1) > north(1) & north_east(i,1) < north(L)...
       & north_east(i,2) > east(1) & north_east(i,2)...
       < east(M)
    hold on
    plot(north_east(i,2),north_east(i,1),'g+')
    plot(north_east(i,2),north_east(i,1),'gO')
  end
end
```

Subroutine "utm.m":

```
function lat_lon=utm(north,east,CM)
%This function transfer the UTM coordinats into Latitude and longitude
A=6378206.4;
RECIPF=294.97898;
k0=0.9996;
RADDEG=57.29577951;
fe=500000.0;
F=1.0/RECIPF;
B=A-A*F;
E1=(A*A-B*B)/(A*A);
E2=(A*A-B*B)/(B*B);
degrad=1.7453292519945e-2;
DELM=100.0;

%Arc length constants:
A0=1.-0.25*E1-0.046875*E1*E1-0.01953125*E1^3.0-175.0/16384.*E1^4.0;
A2=0.375*(E1+0.25*E1*E1+0.1171875*E1^3.0-455.0/4096.0*E1^4.0);
A4=0.05859375*(E1*E1+0.75*E1^3.0-77.0/128.0*E1^4.0);
A6=35.0/3072.0*(E1^3.0-1.28125*E1^4.0);
A8=-315.0/131072.0*E1^4.0;

lat_lon(1:2)=0;
raddeg=1.0/degrad;
phift=footpoint1(north);
phift=phift*degrad;
%y=north/k0;
x=(east-fe)/k0;
t=tan(phift);
m=A*(1-E1)/(1-E1*sin(phift)^2.0)^1.5;
n1=A/sqrt(1-E1*sin(phift)^2.0);
n=E2*cos(phift)^2.0;
t1=-t*x/m*x/n1/2.0+t*x/m*x/n1*x/n1*x/n1/24.0*(5.0+3.0*t*t+n+4.0*n*n...
   +9.0*n*t*t);
```

```
t2=t*x/m*x/n1*x/n1*x/n1*x/n1*x/n1/720.0*(61.0-90.0*t*t+46.0*n+...
   45.0*t^4.0-252.0*t*t*n+3.0*n*n+100.0*n^3.0-66.0*t*t*n*n-...
   90.0*t^4.0*n+88.0*n^4.0+225.0*t^4.0*n*n+84.0*t*t*n^3.0-...
   192.0*t*t*n^4.0);
t3=t*x/m*x/n1*x/n1*x/n1*x/n1*x/n1*x/n1*x/n1/40320.0*(1385.0+...
   3633.0*t*t+4095.0*t^4+1575.0*t^6.0);
lat_lon(1)=(phift+t1-t2+t3)*raddeg;

t1=x/n1-x/n1*x/n1*x/n1/6.0*(1.0+2.0*t*t+n);
t2=5.0+6.0*n+28.0*t*t-3.0*n*n+8.0*t*t*n+24.0*t^4.0-4.0*n^3.0+...
   4.0*t*t*n*n+24.0*t*t*n^3.0;
t3=61.0+662.0*t*t+1320.0*t^4.0+720.0*t^6.0;
lat_lon(2)=CM+(t1+x/n1*x/n1*x/n1*x/n1*x/n1/120.0*t2-...
   x/n1*x/n1*x/n1*x/n1*x/n1*x/n1*x/n1/5040.0*t3)/cos(phift)*raddeg;
```

Subroutine "true_depth.m":

```
function cor_depth=true_depth(cal_depth)
%this fucntion calculate the corrected depth
%based on the calculated depth assuming signals travel at 1500m/s
%syntax: input a measured depth,output a true depth

global water

depth=cal_depth/1500.0;
Tsum=0;
Dsum=0;
i=0;
while Tsum < depth
   i=i+1;
   if i>120
      break
   end
   AD=water(i+1,1)-water(i,1);
   Dsum=Dsum+AD;
   AT=AD/water(i,2);
   Tsum=Tsum+AT;
end

cor_depth=Dsum-AD*(Tsum-depth)/AT;
```

Subroutine "medarc1.m":

```
function get_medarc=medarc1(phi)
A=6378206.4;
```

```
RECIPF=294.97898;
k0=0.9996;
RADDEG=57.29577951;
fe=500000.0;
F=1.0/RECIPF;
B=A-A*F;
E1=(A*A-B*B)/(A*A);
E2=(A*A-B*B)/(B*B);
degrad=1.7453292519945e-2;

%Arc length constants:
A0=1.-0.25*E1-0.046875*E1*E1-0.01953125*E1^3.0-175.0/16384.*E1^4.0;
A2=0.375*(E1+0.25*E1*E1+0.1171875*E1^3.0-455.0/4096.0*E1^4.0);
A4=0.05859375*(E1*E1+0.75*E1^3.0-77.0/128.0*E1^4.0);
A6=35.0/3072.0*(E1^3.0-1.28125*E1^4.0);
A8=-315.0/131072.0*E1^4.0;

b=A0*phi-A2*sin(2*phi)+A4*sin(4*phi)-A6*sin(6*phi)+A8*sin(8*phi);
get_medarc=A*b;
```

Subroutine "latlon_utm.m":

```
function get_utm=latlon_utm(lat,lon,CM)
%This function transfer latitude and Longitude into UTM coordinates
global A A0 A2 A4 A6 A8 B E1 E2
A=6378206.4;
RECIPF=294.97898;
F=1.0/RECIPF;
B=A-A*F;
E1=(A*A-B*B)/(A*A);
E2=(A*A-B*B)/(B*B);
get_utm(1:2)=0;
phi=lat/57.29577951;
v=E1*sin(phi)^2.0;
n=A/sqrt(1.0-v);
t=tan(phi)^2.0;
delta=(lon-CM)/57.29577951;
n2=E2*cos(phi)^2.0;
k0=0.9996;
s0=medarc1(phi);

t1=delta*delta/2.0*sin(phi)*cos(phi);
t2=delta^4.0/24.0*sin(phi)*cos(phi)^3.0*(5.0-t+9.0*n2+4.0*n2*n2);
t3=61.0-58.0*t+t*t+270.0*n2-330.0*t*n2+445.0*n2*n2+324.0*n2^3.0...
   -680.0*n2*n2*t+88.0*n2^4.0-600.0*n2^3.0*t-192.0*n2^4.0*t;
```

```
t4=1385.0-3111.0*t+543.0*t*t-t^3.0;
get_utm(1)=k0*s0+k0*n*(t1+t2+delta^6.0/720.0*sin(phi)*...
   cos(phi)^5.0*t3+delta^8.0/40320.0*sin(phi)*...
   cos(phi)^7.0*t4);

t1=delta*cos(phi)+(delta*cos(phi))^3.0/6.0*(1-t+n2);
t2=5.0-18.0*t+t*t+14.0*n2-58.0*t*n2+13.0*n2*n2+4.0*n2^3.0-...
   64.0*n2*n2*t-24.0*n2^3.0*t;
t3=(61.0-479.0*t+179*t*t-t^3.0)/5040.0;
get_utm(2)=500000.0+k0*n*(t1+(delta*cos(phi))^5.0/120.0*t2+...
   (delta*cos(phi))^7.0*t3);
```

Subroutine "latlon.m":

```
function get_utm=latlon(lat,lon,CM)
%This function transfer latitude and Longitude into UTM coordinates
%format long A
%format long B
A=6378206.4;
RECIPF=294.97898;
K0=0.9996;
RADDEG=57.29577951;
FE=500000.0;
F=1.0/RECIPF;
B=A-A*F;
E1=(A*A-B*B)/(A*A);
E2=(A*A-B*B)/(B*B);
degrad=1.7453292519945e-2;


%Arc length constants:
A0=1.-0.25*E1-0.046875*E1*E1-0.01953125*E1^3.0-175.0/16384.*E1^4.0;
A2=0.375*(E1+0.25*E1*E1+0.1171875*E1^3.0-455.0/4096.0*E1^4.0);
A4=0.05859375*(E1*E1+0.75*E1^3.0-77.0/128.0*E1^4.0);
A6=35.0/3072.0*(E1^3.0-1.28125*E1^4.0);
A8=-315.0/131072.0*E1^4.0;

get_utm(1:2)=0;
phi=lat/57.29577951;
v=E1*sin(phi)^2.0;
n=A/sqrt(1.0-v);
t=tan(phi)^2.0;
delta=(lon-CM)/57.29577951;
n2=E2*cos(phi)^2.0;
```

```
k0=0.9996;
s0=medarc1(phi);

t1=delta*delta/2.0*sin(phi)*cos(phi);
t2=delta^4.0/24.0*sin(phi)*cos(phi)^3.0*(5.0-t+9.0*n2+4.0*n2*n2);
t3=61.0-58.0*t+t*t+270.0*n2-330.0*t*n2+445.0*n2*n2+324.0*n2^3.0...
   -680.0*n2*n2*t+88.0*n2^4.0-600.0*n2^3.0*t-192.0*n2^4.0*t;
t4=1385.0-3111.0*t+543.0*t*t-t^3.0;
get_utm(1)=k0*s0+k0*n*(t1+t2+delta^6.0/720.0*sin(phi)*...
   cos(phi)^5.0*t3+delta^8.0/40320.0*sin(phi)*...
   cos(phi)^7.0*t4);

t1=delta*cos(phi)+(delta*cos(phi))^3.0/6.0*(1-t+n2);
t2=5.0-18.0*t+t*t+14.0*n2-58.0*t*n2+13.0*n2*n2+4.0*n2^3.0-...
   64.0*n2*n2*t-24.0*n2^3.0*t;
t3=(61.0-479.0*t+179*t*t-t^3.0)/5040.0;
get_utm(2)=500000.0+k0*n*(t1+(delta*cos(phi))^5.0/120.0*t2+...
   (delta*cos(phi))^7.0*t3);
```

Subroutine "get_range.m":

```
function cor_range=get_range(AQ,water_layer,...
   lowerdepth,upperdepth)
%this fucntion calculate the corrected range
global water

Xsum=0;
Tsum=0;
Dsum=upperdepth;
cor_range(1:2)=0;
j=water_layer-1;
if j<1
   j=1;
end
VP=water(j,2)*AQ;
AD=water(j+1,1)-upperdepth;
if VP >= 1.0
   VP=1.0-0.1e-09;
end
AT=AD/((sqrt((1.0-VP)*(1.0+VP)))*water(j,2));
AX=AT*water(j,2)*VP;
Xsum=Xsum+AX;
Tsum=Tsum+AT;
Dsum=Dsum+AD;

if Dsum <= lowerdepth
```

```
    ja=water_layer+20;
    for i=water_layer:ja
      VP=water(i,2)*AQ;
      AD=water(i+1,1)-water(i,1);
      if VP >= 1.0
        VP=1.0-0.1e-09;
      end
      AT=AD/((sqrt((1.0-VP)*(1.0+VP)))*water(i,2));
      AX=AT*water(i,2)*VP;
      Xsum=Xsum+AX;
      Tsum=Tsum+AT;
      Dsum=Dsum+AD;
      if Dsum > lowerdepth
        break
      end
    end
  end
  FRAC=(Dsum-lowerdepth)/AD;
  cor_range(1)=Tsum-AT*FRAC;
  cor_range(2)=Xsum-AX*FRAC;
```

Subroutine "get_distance.m":

```
  function cor_distance=get_distance...
    (QQ,Vm,dsb,water_seabed,d_depth,...
    time_dif,low_depth,up_depth)
  %this fucntion calculate the corrected distance

  global water
  %format long cor_distance
  %format long QQ

  for j=1:2
    QCA=QQ(j);
    bb=get_range(QCA,water_seabed,low_depth,up_depth);
    if j==2 & bb(1) < time_dif
      DDIST=time_dif*Vm;
      DD1=dsb-d_depth;
      DDEL=DDIST*DDIST-DD1*DD1;
      if DDEL <= 0.0          %right at the top of OBS
        DDEL=0.00001;
      end
      cor_distance=sqrt(DDEL);
      return
```

```
    else
      if j==1 & bb(1) > time_dif
        while bb(1) > time_dif
          QQ(1)=QQ(1)+(QQ(1)-QQ(2))/10.0;
          QCA=QQ(1);
          bb=get_range(QCA,water_seabed,low_depth,up_depth);
        end
      else
      end
    end
    BDC(j)=bb(2);
    BTC(j)=bb(1);
  end

  for i=1:100
    QQ(3)=(QQ(1)+QQ(2))/2.0;
    QCA=QQ(3);
    bb=get_range(QCA,water_seabed,low_depth,up_depth);
    BDC(3)=bb(2);
    BTC(3)=bb(1);
    if bb(1) > time_dif
      QQ(2)=QQ(3);
      BDC(2)=BDC(3);
      BTC(2)=BTC(3);
    else
      QQ(1)=QQ(3);
      BDC(1)=BDC(3);
      BTC(1)=BTC(3);
    end
    if (BTC(2)-BTC(1)) < 0.002
      break
    end
    if abs(QQ(1)-QQ(2))/QQ(1) < 0.2e-05
      break
    end
  end
  cor_distance=BDC(1)+(BDC(2)-BDC(1))*...
    ((time_dif-BTC(1))/(BTC(2)-BTC(1)));
```

Subroutine "footpoint1.m":

```
function get_footpoint=footpoint1(north)
% Calculate the foot point Latitude
%global k0 degrad
degrad=1.7453292519945e-2;
```

```
k0=0.9996;

latft=fix(north*90.0/10000000.0)+1.0;
phi=(latft-1.0)*degrad;
arc=medarc1(phi)*k0;
while north < arc
  latft=latft-1.0;
  phi=latft*degrad;
  arc=medarc1(phi)*k0;
end
latft=latft-1.0;
phift=latft;
phi=latft*degrad;
arc=medarc1(phi)*k0;
latft=latft+1.0;
phi=latft*degrad;
arc2=medarc1(phi)*k0;
phift=phift+(north-arc)/(arc2-arc);
phi=phift*degrad;
arc3=medarc1(phi)*k0;
get_footpoint=phift+(north-arc3)/(arc2-arc);
```

APPENDIX C

EQUIVALENT OFFSET PRE-STACK TIME MIGRATION (EOM) FOR SMART LINE2

C.1 Introduction

This report introduces the technical issues of equivalent offset pre-stack time migration (EOM). The data set includes short sections along LITHOPROBE line 881a and BGR 8911 (the German Federal Agency of Geosciences and Natural Resources), provided by Bedford Institute of Oceanography. The objective of pre-stack migration is to improve the image of the large dipping reflections across the outer continental slope and rise. The technique "Equivalent Offset pre-stack time Migration (EOM)" is fully described by Bancroft et al. (1998) and Bancroft (1998). The Claritas software used for this project is provided by the Institute of Geological and Nuclear Sciences, New Zealand. Conventional seismic data processing techniques, such as scaling, filtering and CMP sorting are required prior to EOM, and conventional NMO and stacking are also required after EOM. The techniques prior to and after EOM are not discussed in the report. The results of EOM are compared with migrated sections by dip-moveout (DMO) correction followed by post-stack migration and conventional pre-stack time migration—finite difference migration. The technical issues of DMO correction, post-stack migration and finite different pre-stack time migration are not introduced since they are described in many literatures (e.g. Deregowski and Rocca, 1981; Hale, 1984; Yilmaz, 2001).

C.2 Essentials of EOM

C.2.1 Kirchhoff Pre-Stack Time Migration Theory

EOM is based on Kirchhoff pre-stack time migration. In Kirchhoff migration theory, a subsurface model consists of scatterpoints that scatter energy from any source to all receivers. An organized arrangement of scatterpoints produces coherent reflections while disorganized scatterpoints will not create coherent reflections. The objective of pre-stack migration is to collect all of the scattered energy and relocate it to the position of the scatterpoints. Kirchhoff pre-stack time migration assumes each scatterpoint as an output location, and then sums the appropriate energy from all available input traces.

C.2.2 Cheops Pyramid and Common Scatterpoint Gathers

Kirchhoff time migration assumes straight raypaths from the source (S, Figure C.1) to the scatterpoint, and from the scatterpoint to the receiver (R, Figure C.1).

The traveltime $t(x, h)$ from source to scatterpoint and from scatterpoint to receiver is given by the following equation (Bancroft et al. 1998):

$$t = \sqrt{\frac{t_0^2}{4} + \frac{(x+h)^2}{V_{mig}}} + \sqrt{\frac{t_0^2}{4} + \frac{(x-h)^2}{V_{mig}}} \qquad (1)$$

Where t is the total traveltime from source to scaterpoint and to receiver; x is the location of the source-receiver mid-point relative to the scatterpoint located at x=0; z_0 is the depth of the scatterpoint; $t_0 = t(x = 0, h = 0)$ is the two-way zero-offset time computed from the average velocity V_{ave} as $t_0 = \frac{2z_0}{V_{ave}}$; V_{mig} is the migration velocity, which is approximated

by the RMS velocity $V_{rms} = \sqrt{\frac{1}{t_0}\int_0^{t_0} V_{ins}^{\,2}\,dt}$ at t_0. V_{ins} is instantaneous velocity at specific point and $V_{ave} = \frac{1}{t_0}\int_0^{t_0} V_{ins}(t)dt$.

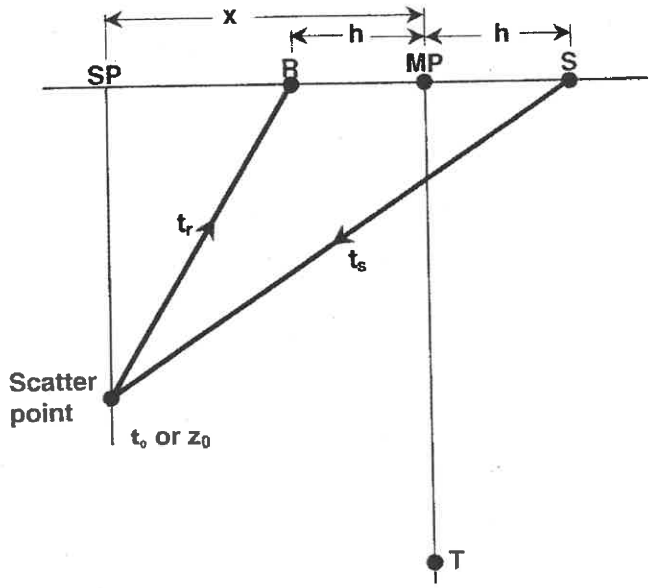

Figure C.1. Geometry of Kirchhoff pre-stack time migration with source (S) and receiver (R). The total traveltime T is the sum of source to scatterpoint time (t_s) and scatterpoint to receiver time (t_r). x is the location of the source-receiver mid-point (MP) relative to the scatterpoint (SP) located at x=0; h is half the source-receiver offset. After Bancroft et al. (1998).

The energy from one scatterpoint lies on a traveltime surface (Figure C.2a), known as Cheops pyramid. A CMP gather that is located at the scatterpoint ($x = 0$) intersects Cheops pyramid on a hyperbolic path (Figure C.2a) and allows conventional NMO correction. The intersections of all other CMP gathers ($x \neq 0$) have non-hyperbolic paths and energy will be mis-positioned with conventional NMO correction and stacking.

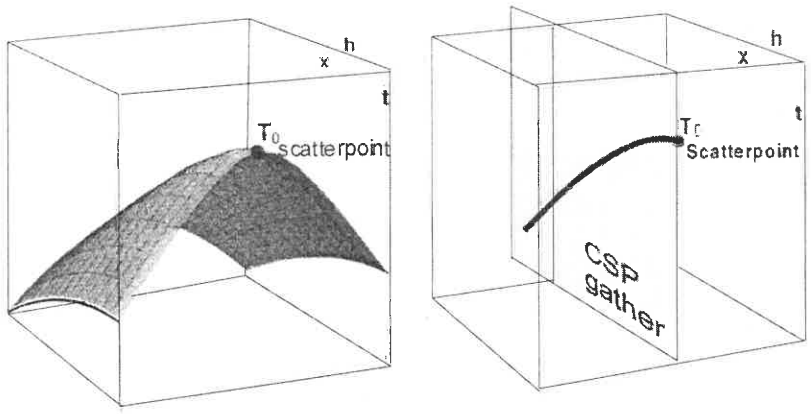

(a) (b)

Figure C.2. (a) Cheops pyramid—the traveltime surface $t(x, h)$ for one scatterpoint. (b) The CSP (Common ScatterPoint) gather formed by collapsing the Cheops pyramid to hyperbola in the $x = 0$ plane. After Bancroft (1998).

C.2.3 Equivalent Offset

The equivalent offset is defined by converting the double square equation (1) into an equivalent single square root format. This is accomplished by defining a new source and receiver collocated at the equivalent offset position E, as illustrated in Figure C.3.

The equivalent offset $\boldsymbol{h}_e$ is chosen to maintain the same traveltime as the original path, i.e.

$$2\sqrt{\frac{t_0^2}{4}+\frac{h_e^2}{V_{mig}^2}}=\sqrt{\frac{t_0^2}{4}+\frac{(x+h)^2}{V_{mig}}}+\sqrt{\frac{t_0^2}{4}+\frac{(x-h)^2}{V_{mig}}} \tag{2}$$

The equivalent offset $\boldsymbol{h}_e$ can be solved from equation (2) as follows (Bancroft et al. 1998):

$$h_e^2 = x^2 + h^2 - (\frac{2xh}{tV_{mig}})^2 \tag{3}$$

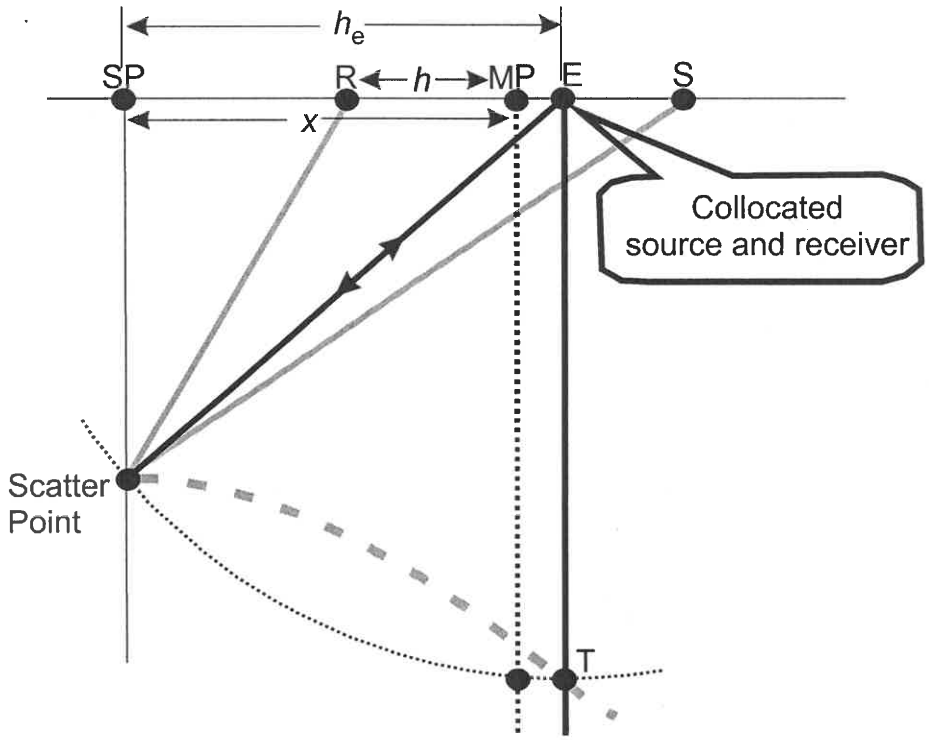

Figure C.3. Equivalent offset $\boldsymbol{h_e}$ is defined as the offset from the surface position of the scatterpoint to a collocated source-receiver having the same total traveltime as the original source-receiver. Scatter energy from all source-receiver pairs lies along the hyperbola at their equivalent offset. Other features refer to Figure C.1.

The equivalent offset equals a quadratic sum of the distance of CMP gathers relative to the scatter point (x^2), the source-receiver half offset (h^2), and a cross term of distance, time and velocity. By using the equivalent offset, the data in the CMP plane can be mapped onto a common scatter point (CSP) gather plane. The cross term allows the formation of the CSP gather without a prior DMO correction.

C.2.4 Mapping Data to CSP Gather by Equivalent Offset

Migration is accomplished by reformulation of conventional CMP gathers into CSP gathers, where energy is relocated to the hyperbolae of individual scatter points of the

subsurface. By using the equivalent offset defined by the single square equation (3), data samples in CMP gathers are mapped directly to CSP gathers at constant time.

Consider one input trace in the CMP gather where the values of x and h are constant in equation (3). Figure C.4 shows that only a portion of the input trace beyond time t_α contributes to one CSP gather, and that the data are distributed over offsets from $\boldsymbol{h}_{e\alpha}$ to $\boldsymbol{h}_{e\omega}$.

The first usable sample t_α comes from a scatterpoint located at the surface ($x = 0$, $t = 0$) and is computed from

$$t_\alpha = \frac{2x}{V_0} \tag{4}$$

Where V_0 is the average velocity at the surface. The equivalent offset $\boldsymbol{h}_{e\alpha}$ is given for t_α by

$$h_{e\alpha} = x \tag{5}$$

The remaining portion of input trace is spread over a range of offset to a maximum equivalent offset $\boldsymbol{h}_{e\omega}$ given by

$$h_{e\omega}{}^2 = x^2 + h^2 \tag{6}$$

which is the asymptotic limit of the equivalent offset $\boldsymbol{h}_e$ as t tends to large values. The cross term in equation (3) causes the input trace to be spread over a range of offset as identified in Figure C.4.

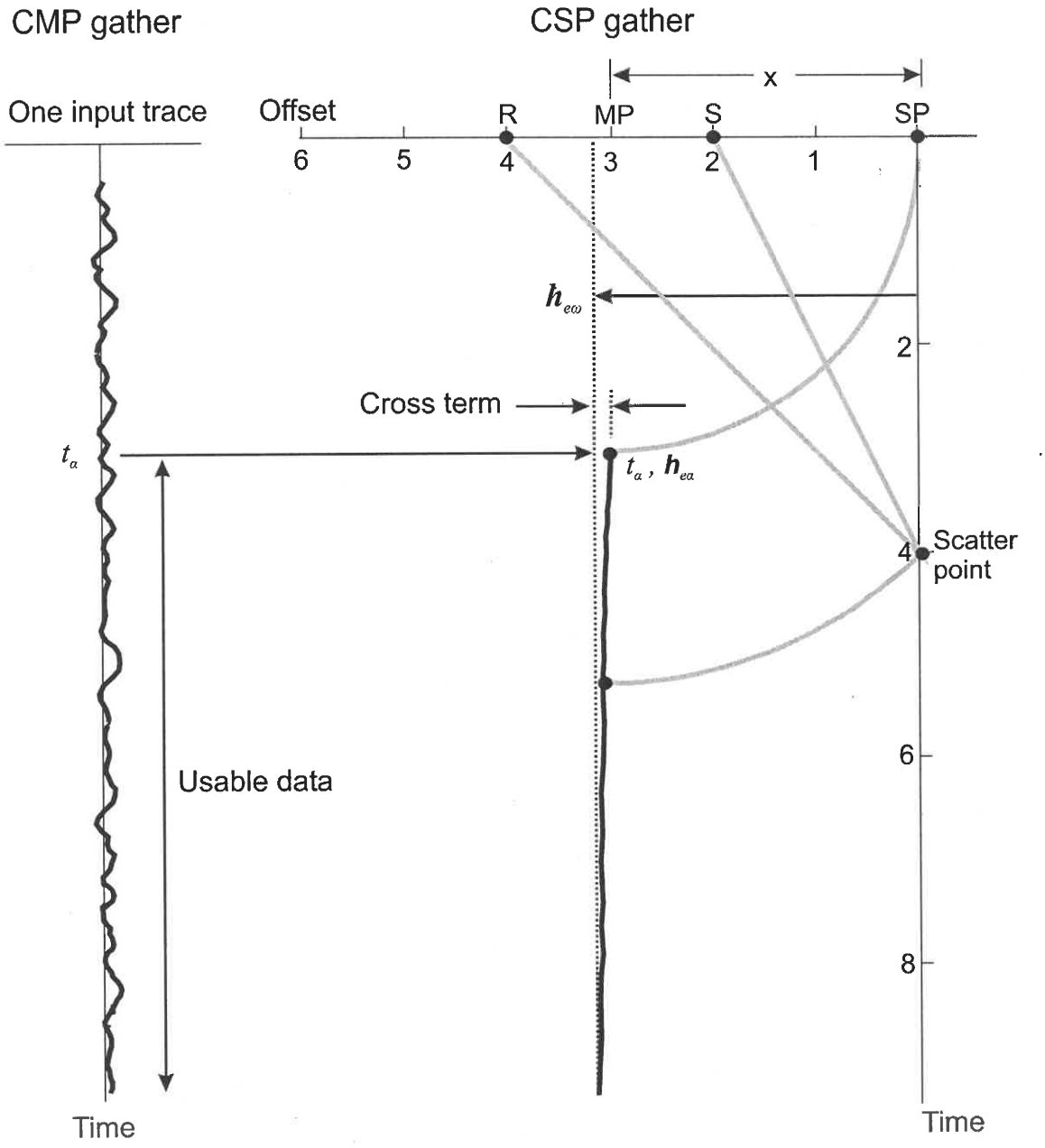

Figure C.4. Schematic diagram showing data from a single input trace mapped to a range of equivalent offset in a CSP gather. The first usable sample on a trace occurs at time t_α that maps to equivalent offset $\boldsymbol{h}_{e\alpha}$. With increasing time, the equivalent offset becomes asymptotic to $\boldsymbol{h}_{e\omega}$, due to the cross term of time and velocity in equation (3). Arcs indicate the scatterpoints from which energy is scattered. Other features refer to Figure C.1.

Migration aperture is defined to be the radius of maximum offset within which reflection energy on a hyperbola is focused into a scatter point. All input traces within the migration aperture, regardless of the source or receiver location, may contribute to form a CSP gather. Many CMP gathers may be used to create one CSP gather, and one CMP gather may contribute samples to many CSP gathers. A two-sided CSP gather is formed by transferring the signs of midpoint location to the equivalent offset.

A CSP gather is similar to a CMP gather as they both define the subsurface location and their traces are sorted by offsets. However, the maximum offset of CMP gathers is defined by the acquisition geometry, while the maximum offset of CSP gathers is the migration aperture, which is defined by processor. Therefore, the maximum offset of CSP gathers is not limited by the acquisition geometry.

C.2.5 Kirchhoff NMO and Stacking

When the data in the CMP gathers are mapped to CSP gathers using equivalent offset, NMO and stacking technique are used to focus the scattered energy to the scatterpoint. This is basically similar to conventional CMP stacking and therefore is not discussed in this report.

C.3 Processing Sequence for Profile 88-1A, SP 3700-4356

C.3.1 Input data

Input data are CMP gathers sorted from shot records.

CMP range: 9829-13944

CMP spacing: 13.333 m*

Trace time range: 0-12000 ms **

CMP fold: 30

Note:

*the multiple decimal digits are necessary because Claritas requires an integer number of shot to CMP ration.

**CMP traces must begin with 0 ms at the surface of datum because the "first usable sample t_a" for each input trace (discussed in 2.4) comes from a scatterpoint located at the surface ($x = 0$, $t = 0$), and mapping samples to CSP gathers are relative to t_a. In order to migrate samples to the correct location, all the input data have to be at the true depth (depth migration) or time (time migration).

C.3.2 Input Parameters for EOM

This section describes how to choose appropriate parameters for EOM with consideration of technical requirement and memory size. The detailed technical consideration is complementary to the basic concepts of pre-stack migration which is discussed in the previous session "Essentials of EOM". The input parameters are:

CMP_START: 9829 (CMP number corresponding to first CSP gather)

CMP_END:13944 (CMP number corresponding to last CSP gather)

CMP_DX:13.333 (distance between CMP gather)

MAXEO: 5023.2 m (pre-stack migration aperture: radius of maximum equivalent offset)

CSPFOLD: 180 (expected fold for CSP gather)

CSP_DX:133 m (distance between CSP gather)

ANGLE: 45 (maximum migration dip)

MAX_VEL:4500 m/s (maximum migration velocity)

SDEFILE: home/wuyue/prestackmig/support/velocities/pass1.nmo (time-velocity file)

FIRSTCSP: 9829 (first CSP corresponding to first CMP)

CSPINCR: 10 (CSP number increment)

GRID: vertical interpolation

The first three fields CMP_START, CMP_END and CMP_DX are parameters for the input data, and therefore are not discussed in this report. The remaining fields and relevant technical issues are discussed below with consideration of the most important parameters first.

C.3.2.1 Migration Aperture (MAXEO)

Pre-stack migration aperture is defined to be the radius of maximum migration offset. It refers to the distance of the farthest CMP gather or trace that will contribute data to a particular CSP gather.

Pre-stack migration aperture can be estimated in two ways: 1) estimate from the stacked section by measuring the horizontal extent of individual hyperbolae of interest (e.g., Figure C.5), and 2) guess an initial migration aperture value if a stacked section is not available and see if the hyperbolae in the resultant CSP gather are complete (well developed). Increase the migration aperture if the hyperbolae are truncated at far offsets (e.g., Figure C.6a), or decrease it if there are no useful signals at far offsets.

For this data set, migration aperture is set to 5023.2 m, which is equal to the distance between the shot and the farthest hydrophone. The resultant CSP gather has fully determined hyperbolae (Figure C.6b). If computation efficiency permits, it is better to increase this parameter to twice this value because the hyperbolae (marked by an arrow in Figure C.5) still demonstrate weak energy outside of the migration aperture. This is also indicated by the hyperbolae in Figure C.6b (ca. 9-10 s) that are truncated at far offsets.

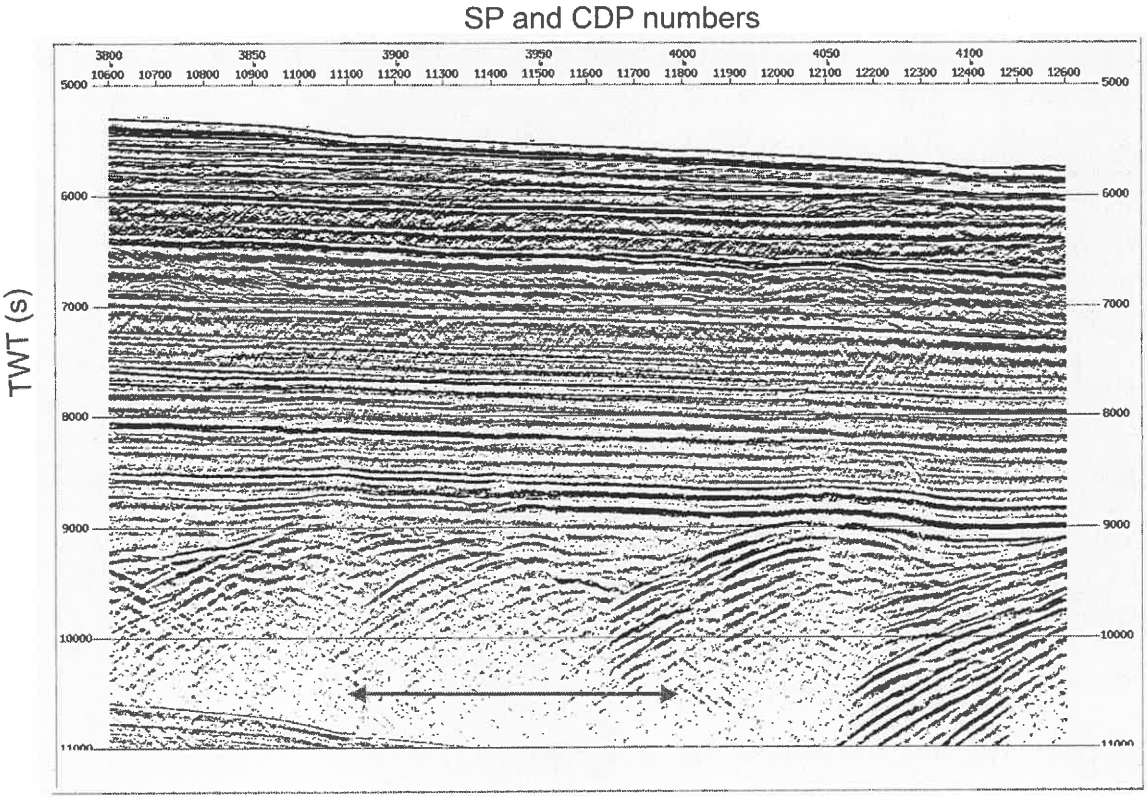

Figure C.5. An unmigrated time section between SP 3800-4100 from a conventional CMP stack. The arrow in lower part (within the basement) indicates the horizontal extent for a single hyperbola of about 10400 m across.

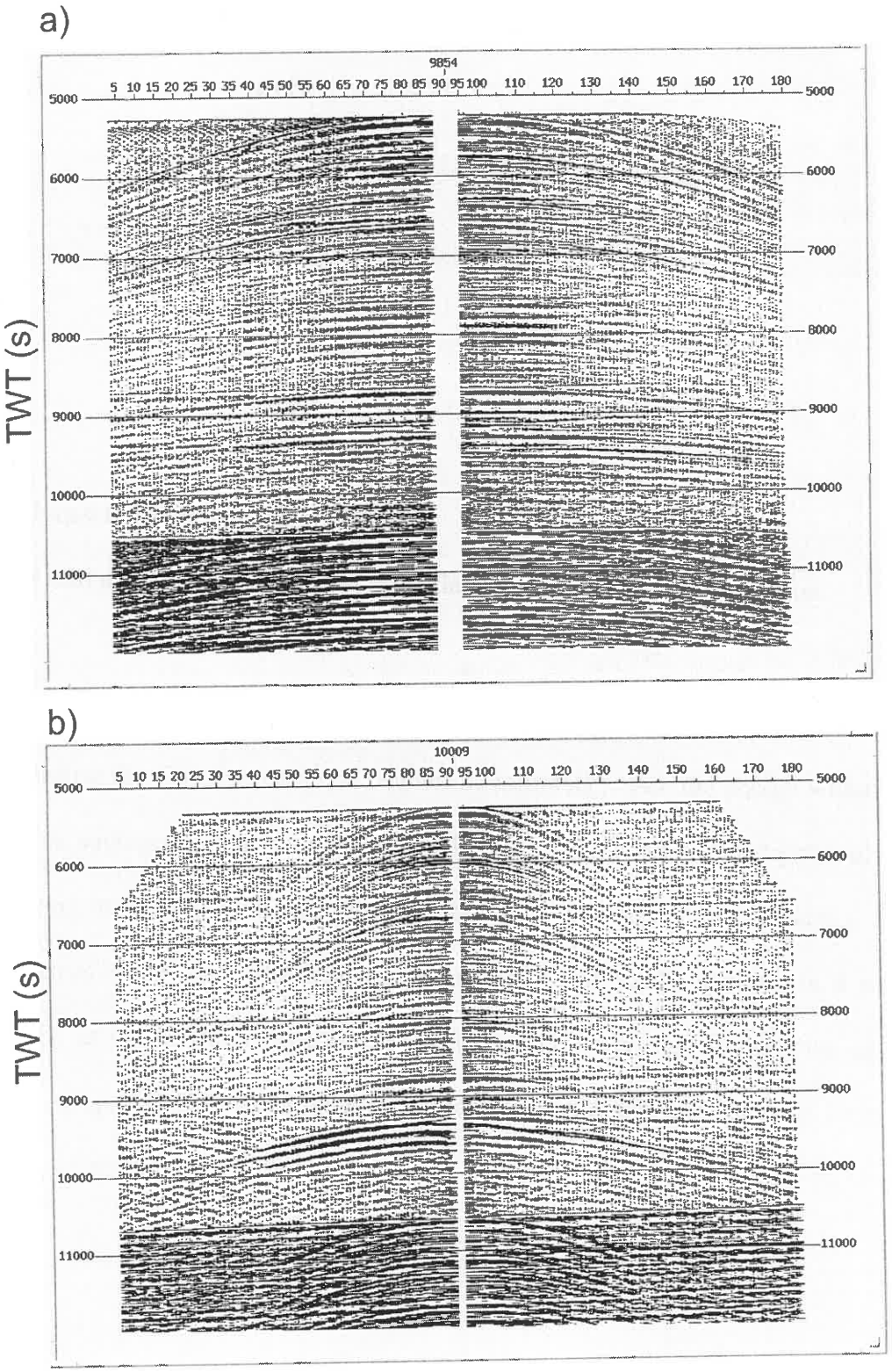

Figure C.6. a) A CSP gather with migration aperture set to be 2500 m. Note that hyperbolae are truncated at far offsets (trace 1 and 180). b) A CSP gather with migration aperture set to be 5023.2 m. Most hyperbolae are fully determined.

C.3.2.2 Expected Fold (CSPFOLD)

The CSP fold number is associated with spatial aliasing and vertical resolution.

Diffraction energy from a scatterpoint will map to a hyperbola on a CSP gather (Figure C.7). Because the CSP trace interval can not be infinitely small, the energy within a bin width δh is averaged when many traces are binned. This is equivalent to convolving a bin-centered trace with a boxcar filter of width δt, a process that attenuates higher frequencies at steep dip. The larger a bin width, δh, is used (resulting in a smaller CSPFOLD, as the migration aperture is constant), the more high frequencies are lost. Therefore, a sparser CSP trace interval acts a natural anti-aliasing filter for large dips (Bancroft, 1996; Bancroft, 1998).

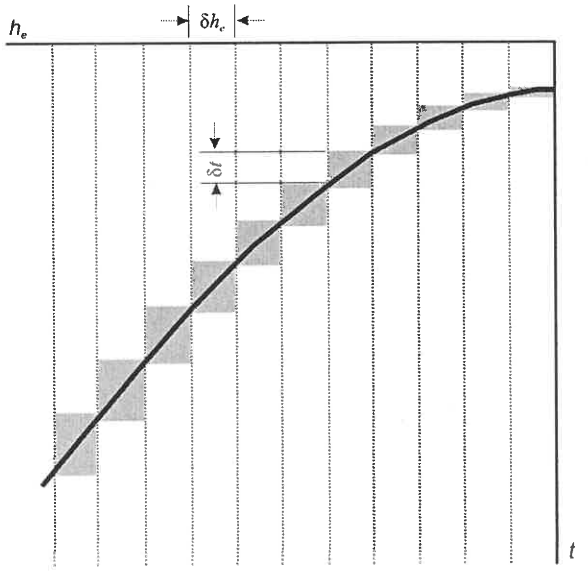

Figure C.7. Samples within a CSP bin width δh are averaged into one sample when data are reformatted into CSP gathers. For a hyperbolic event, this is equivalent to a boxcar filter with dip-dependent width δt. This filter has similar properties to a temporal filter in attenuating high frequencies for steep dips.

Based on the theory of 2-D Fourier transform (Yilmaz, 2001), decreasing the trace interval is also an efficient way to avoid spatial aliasing. Therefore, aliasing is not important in reformulation of CSP gathers since either decreasing or increasing the CSP fold avoids spatial aliasing. Spatial aliasing is also less important in the CSPs as we do not usually do any multichannel processing on them, except for NMO correction and stacking in the focusing process. In that case, the NMO correction should flatten the diffraction events in the CSP gathers and therefore spatial aliasing will not be a problem.

However, a small CSP fold (i.e. a larger CSP trace interval) reduces the vertical resolution (signal sharpness) due to the loss of high frequency component. To preserve the high frequencies as much as possible, folds of 30, 60, 90 and 180 are tried to choose an appropriate fold number. The resultant CSP gathers (Figure C.8) indicate that the hyperbolae are hardly seen in CSP gathers of lower folds, e.g. 30 fold and 60 fold, while the hyperbolae in the higher fold gathers, e.g. 90 fold and 180 fold, are clearer and well developed. More important is that only low frequency components show up in the lower fold CSP gathers while higher frequencies stand out in the higher fold CSP gathers. Their corresponding frequency spectra are shown in Figure C.9. The frequency spectra in sections c) and d) have higher amplitudes between 30-100 Hz, compared to the frequency spectra in sections a) and b) with relatively lower amplitudes between 30-100 Hz. This indicates that the high frequency component is enhanced for the high-fold CSP gathers. Furthermore, the frequency component for a) and b) is dominated by lower frequencies while sections c) and d) have more balanced low and high frequency components.

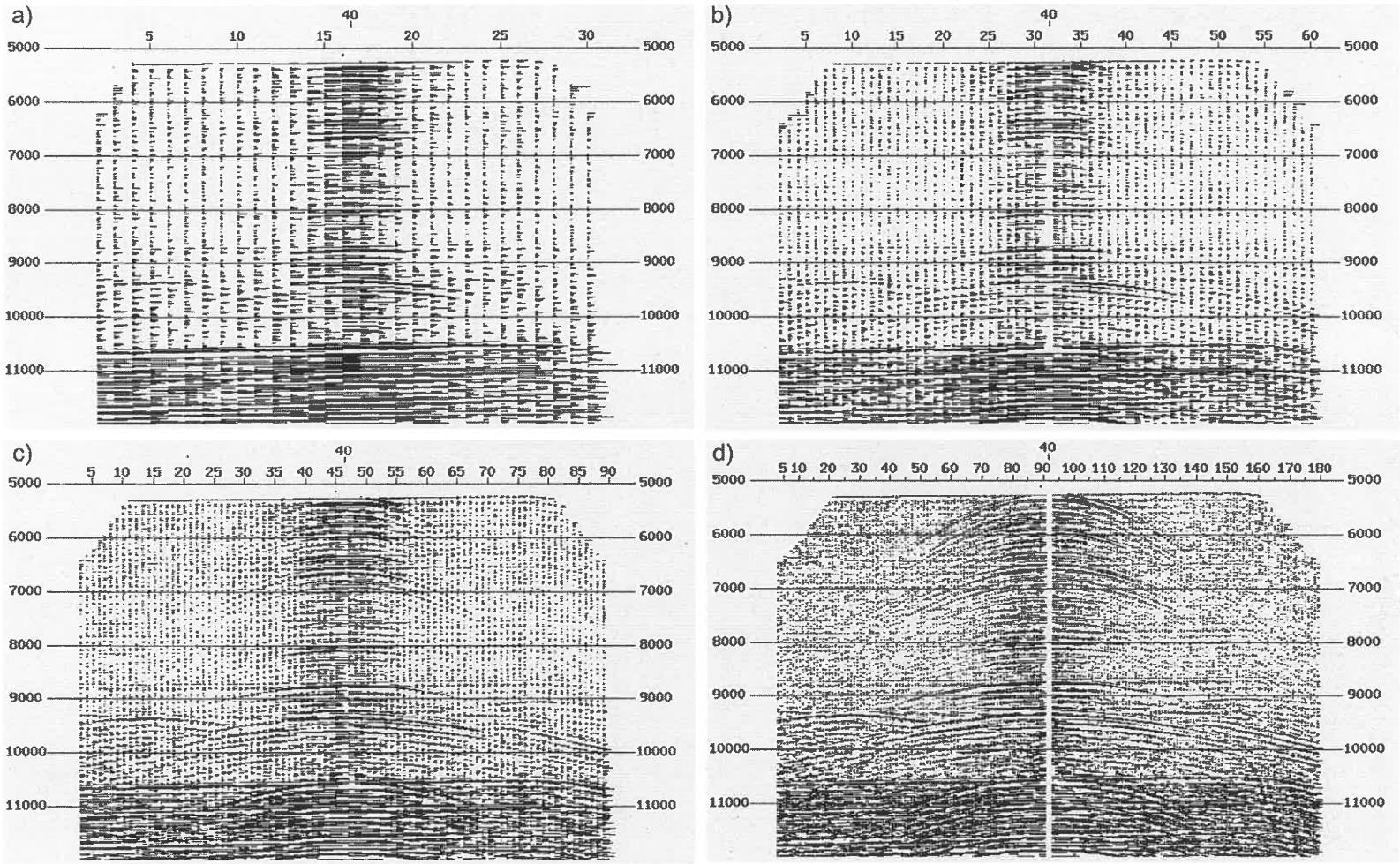

Figure C.8. Examples of CSP gathers with different folds: a) 30 fold, b) 60 fold, c) 90 fold and d) 180 fold. Low frequency components dominate in the lower fold CSP gathers while higher frequencies are observed in the higher fold CSP gathers.

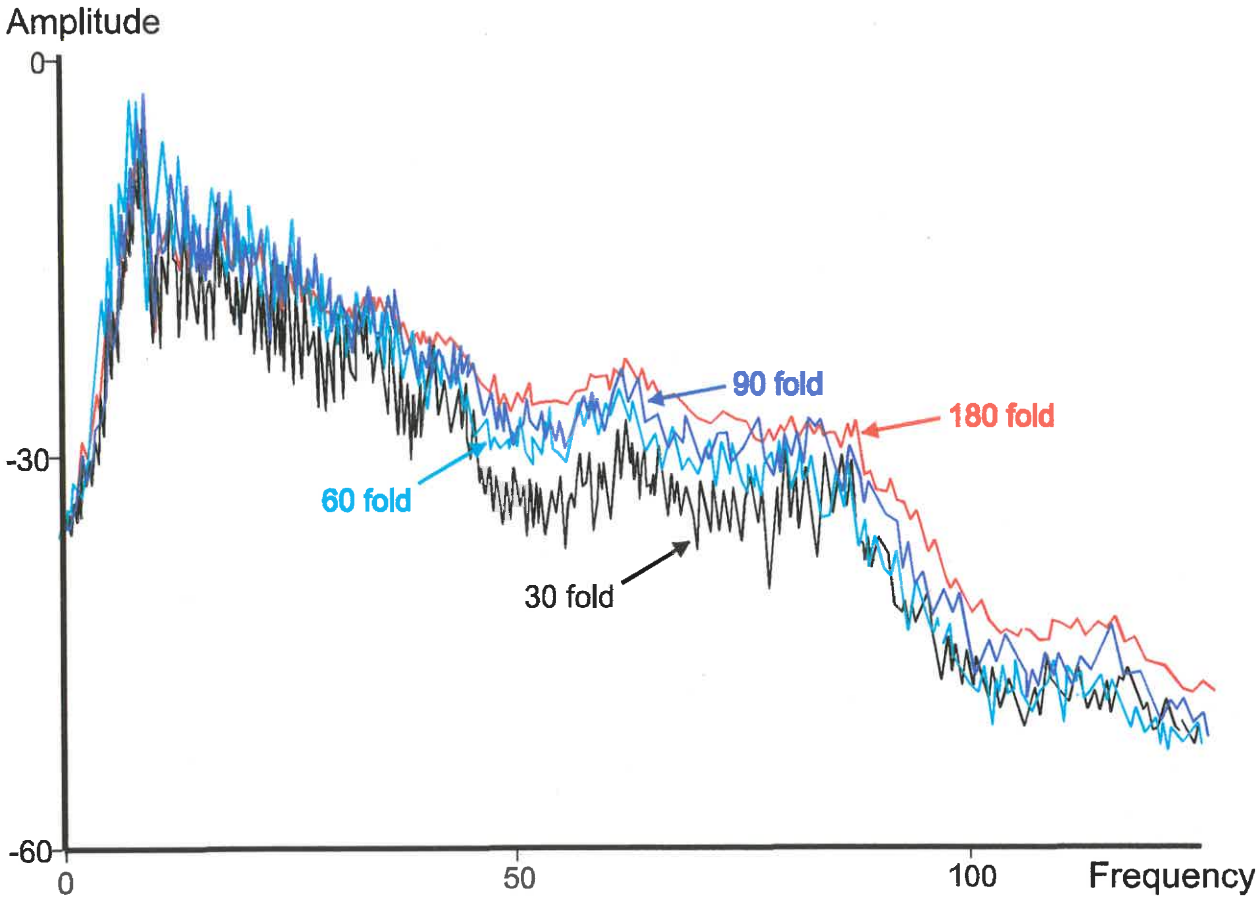

Figure C.9. Frequency spectra corresponding to CSP gathers a), b), c) and d) in Figure C.8 shown as black, cyan, blue and red, respectively. The frequency spectra amplitude between 30-100 Hz increases as CSP fold increases.

To preserve high frequency component as much as possible, a high CSP fold is preferable. Figure C.10 shows a 1440-fold CSP gather with more high frequencies preserved (note: the frequency component between 40-80 Hz has almost the same amplitude as low frequencies between 5-40 Hz). However, if the CSP fold is too high, the CSP trace interval will be so fine that there will not be enough data to fill all the CSP traces. In addition, increasing the CSP fold will inevitably reduce the total number of CSP gathers for each single migration due to limited memory and therefore CSP spacing (discussed in session 3.3) will be unacceptably sparse. In a sense of preserving frequency component as much as possible, as well as computational efficiency, the CSPFOLD is set to be 180 for this data set.

C.3.2.3 CSP Spacing (CSP_DX)

CSP spacing is mainly an issue of computation memory, though it is also an issue of horizontal resolution.

EOM requires a large amount of memory while the maximum memory is currently 2 Gigabyte on our Linux computer (Fox) running Claritas. Thus, the CSP spacing needs to be carefully calculated. If the trace length is 12 s with 3001 samples, each CSP gather requires 3001 sample × 4 bytes × 180 traces = 2.17 Megabytes. With 2 Gigabyte of memory, we can fit about 800 CSPs, without considering memory required by other fields discussed in the following sections and memory required by the system and other programs. As the trace length is set to 12 s and the CSPFOLD is 180, the CSP_DX can

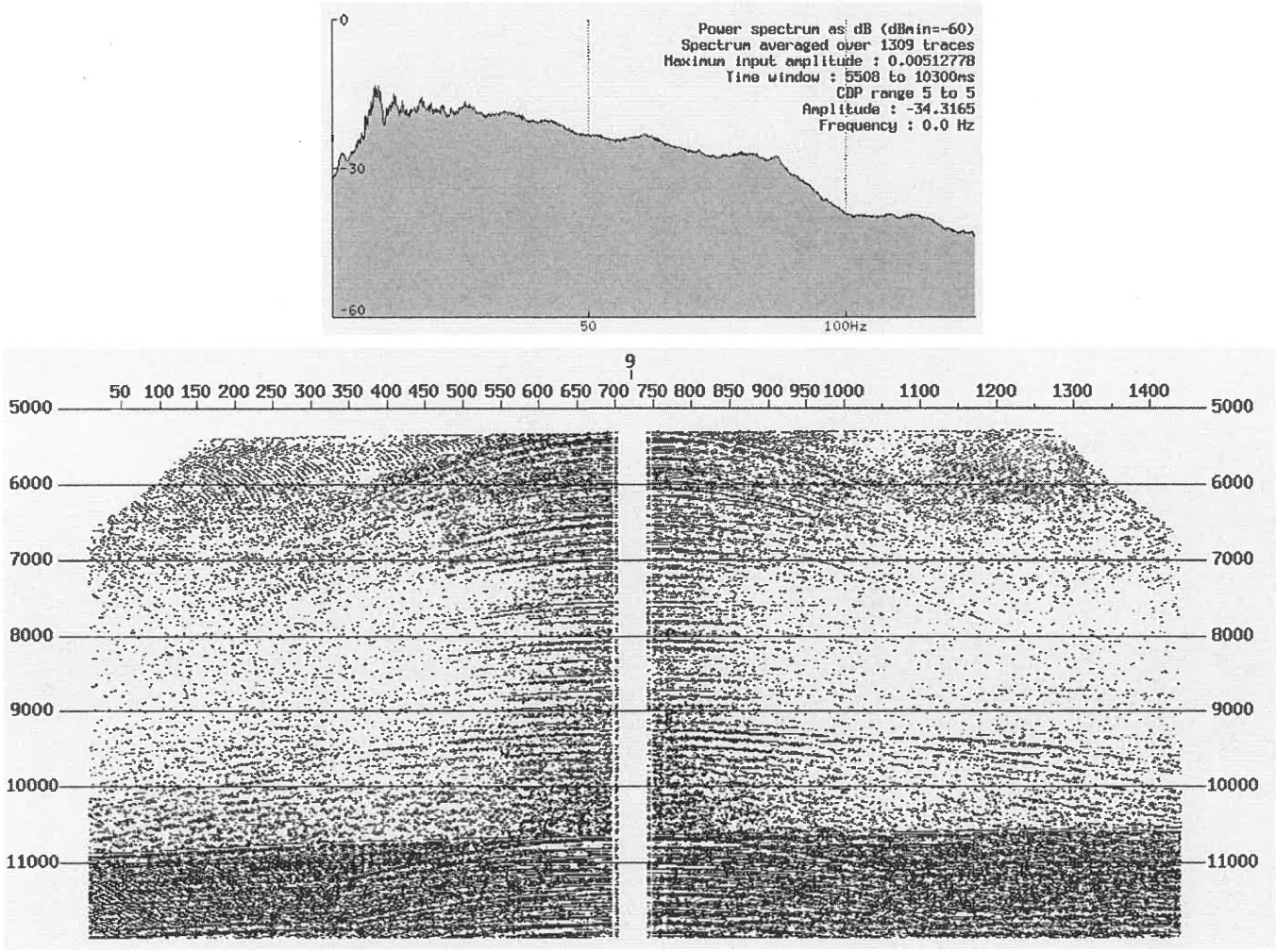

Figure C.10. A CSP gather with 1440 fold (bottom) and its frequency spectrum (top). Note: the frequency components between 40-80 Hz have almost same amplitude as low frequencies between 5- 40 Hz.

not be smaller than 130 m. I used 133 m (roughly 10 times the CMP spacing) for this parameter.

Is 133 m CSP spacing small enough for expected horizontal resolution? Assume the dominant frequency at 9.0 s TWT (basement) to be around 20 Hz, the velocity for the basement 5000 m/s (based on OBS data), then the Fresnel radius r can be computed by (Yilmaz, 2001):

$$r = \frac{v}{2}\sqrt{\frac{t_0}{f}} = 1118 \text{ m}$$

where t_0 is the two way travel time at the reflector; v is the interval velocity at t_0; and f is the dominant frequency at or below the depth (time) 9.0 s TWT. The horizontal resolution is twice the Fresnel radius and therefore much larger than the CSP spacing (133 m) used in EOM.

If the CSP spacing (CSP_DX) needs to be finer than 133 m, then either the CSPFOLD or the data trace length has to be reduced. Reduction of these two fields can save a noticeable amount of memory. Adjusting the other fields (described in the following sections) also helps to save memory, but their contribution is less noticeable. In most cases, however, the trace length will not be a choice because the total depth of interest (trace length) is predetermined. Therefore, reducing CSPFOLD (a sparse CSP trace interval) will be the only choice, but this will attenuate high frequency components and damage the vertical resolution.

C.3.2.4 Maximum Migration Dip (ANGLE)

I used 45 degree for maximum migration dip. Maximum migration dip is chosen to preserve the dips of interest in the input data but to suppress very steeply dipping coherent noise. Diffraction hyperbolae are truncated beyond the specified maximum dip; therefore, dip events steeper than the maximum dip angle will be suppressed. The 45 degree dip was chosen because I knew the largest dip reflector is about 40 degrees (Wu et al. in press) and this is shown in the stacked section (lower right, Figure C.5).

Increasing the maximum dip angle may be able to preserve steeper dips of interest; however, this will take more computational time and memory, since it is related to aperture as follows (Yilmaz, 2001):

$$d_x = \frac{v^2 t}{4} \frac{\Delta t}{\Delta x} \tag{7}$$

Where: d_x is the horizontal displacement during migration; $\frac{\Delta t}{\Delta x}$ is the dip on the unmigrated time section; v is migration velocity; and t is the travel time.

Equation (7) shows that the larger the maximum allowable dip, the larger the displacement. The combination of maximum aperture and the maximum dip limit determines the actual effective aperture width used in migration. Therefore the maximum dip angle must be carefully chosen so that the steep dips of interest are preserved but allow to reduce the computation memory and time.

C.3.2.5 Maximum Migration Velocity (MAX_VEL)

Maximum migration velocity is chosen as 5 km/s. MAX_VEL is used to determine how far the trace will migrate from the CMP position. A trace at location x will contribute to CSP gathers at locations between (x - a) and (x + a), where a = 0.5 × MAX_VEL × tracelength. This can be derived from equation (4) as V_{mig} is replaced by maximum velocity (MAX_VEL) and t_α replaced by the total trace length. Hence greater MAX_VEL requires more memory to store a larger number of CSP gathers.

C.3.2.6 Time-Velocity File for Migration (SDEFILE)

The time and velocity dependent cross term in equation (3) requires a velocity estimate to form CSP gathers. The time-velocity file for migration is the NMO velocity function, similar to NMO velocity from conventional velocity analysis.

The time-velocity file can be obtained in two ways. The most efficient way is to conduct a conventional velocity analysis of CMP gathers by picking the velocity from semblance and hyperbolic scanning techniques. The other way, in case no velocity analysis has been conducted, is to construct a crude velocity file by semblance picking of shot gathers and then form a few CSP gathers at selected locations. After a few CSP gathers have been formed, a more accurate velocity model may be estimated from the CSP gathers by applying conventional velocity analysis to the CSP gathers. The refined velocity file can be used to reform the selected CSP gathers and then repeat the velocity analysis. After a suitable input velocity is found, the entire set of CSP gathers can be formed, after which velocity analysis may again be applied to determine the optimum velocity.

Since CMP velocity analysis was conducted before EOM, the initial CMP velocity function is used by EOM to form CSP gathers. After the CSP gathers are formed, a velocity analysis is applied to the CSP gathers. The refined velocity is put back in EOM to reform the CSP gathers. This can be repeated until a suitable velocity is reached. In practice, only one iteration is required because: 1) the initial velocity has been refined by a few iterations of velocity analysis of CMP gathers, 2) velocity converges rapidly in the CSP gathers indicated by the velocity semblance (e.g., Figure C.11) and also shown by Bancroft and Geiger (1996), and 3) the hyperbolae in the CSP gathers (e.g. Figure C.6 lower panel) are already migrated (i.e. data points are at the right position) and they are two-sided. Therefore, the resultant velocity is a better representation of the true velocity.

The CMP velocity function can not be entered directly as the initial velocity model to form CSP gathers because the CSP spacing (CSP_DX) can not be as fine as the CMP spacing due to memory restrictions (discussed above). In our case, the CSP spacing has to be more than ten times sparser than the CMP spacing. Therefore, the CSP number can not be the same as CMP number of the input data, and the NMO velocity from analyzing CMP gathers can not be used directly by EOM. However, by manipulating the parameters of FIRST_CSP and CSPINCR, the CSP numbering can be made roughly the same as the CMP numbering. This is described in the following session 3.2.8.

Figure C.12 shows a refined velocity model from velocity analysis of CSP gathers (upper panel) compared to the NMO velocity model from CMP gathers (lower panel). The

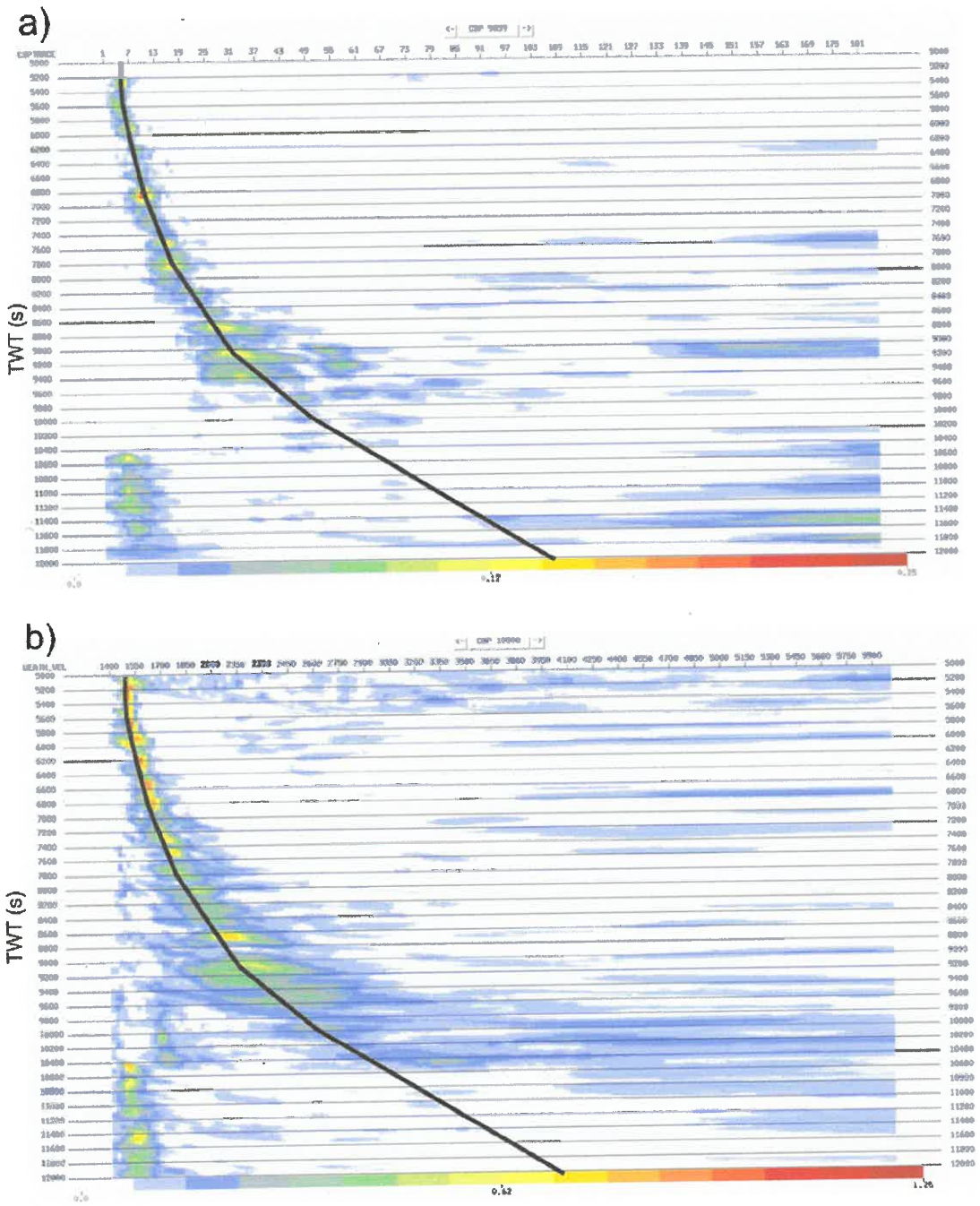

Figure C.11. a) An example of velocity semblance of CSP gather 9859, compared to velocity semblance of CMP gathers shown in b). The CSP gather has a more focused velocity semblance compared to the semblance from CMP gather. The lines through the velocity semblance are the picked velocity profiles.

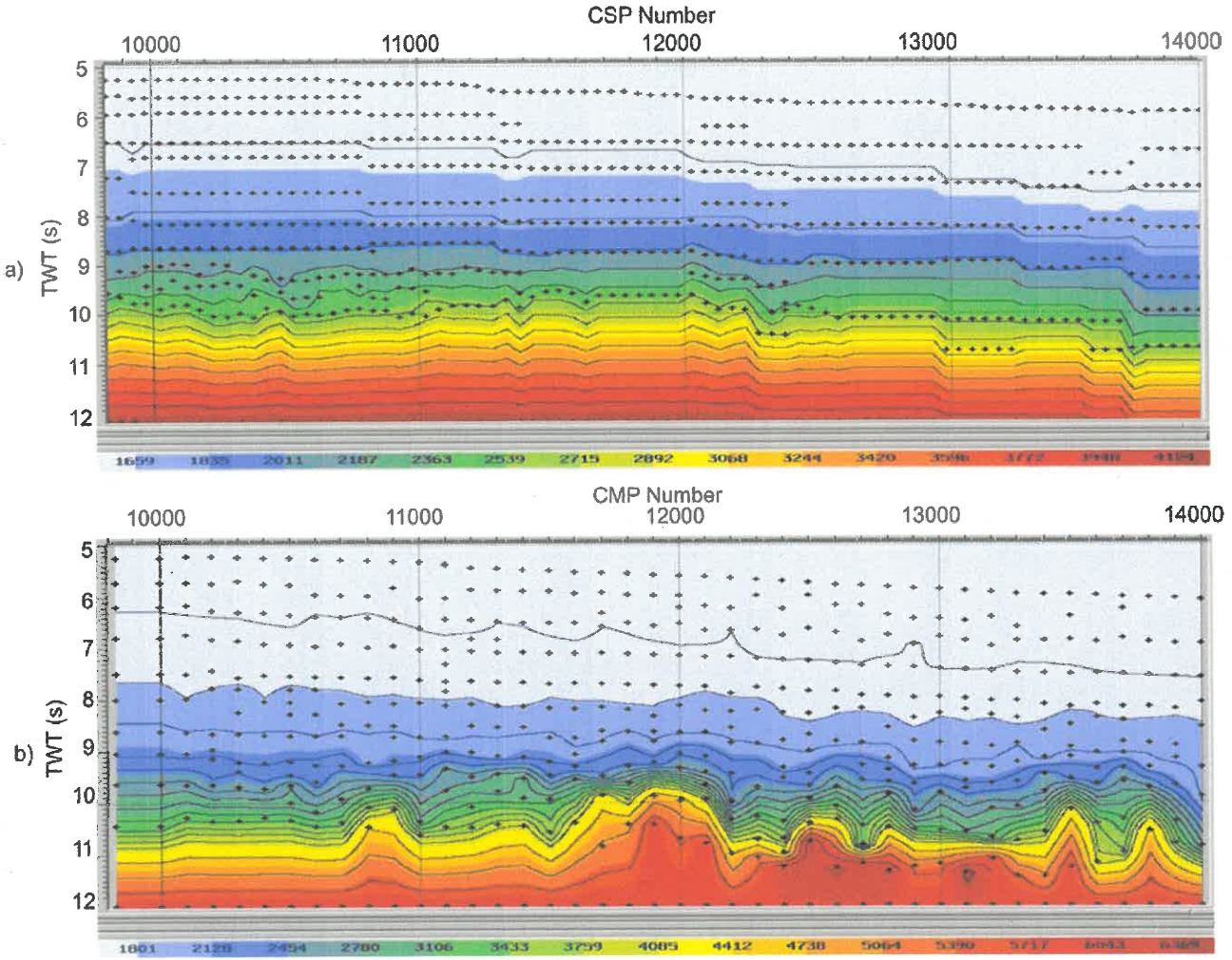

Figure C.12. NMO velocity models from velocity analysis of CSP gather (top) and CMP gathers (bottom).

a) Velocity scan analysis in CMP gathers

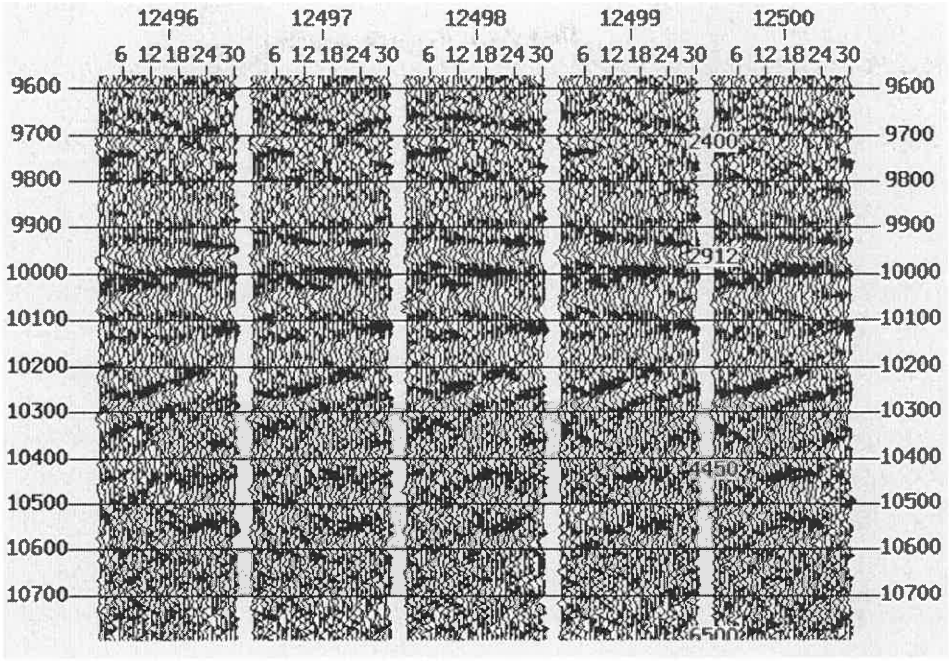

b) Velocity scan analysis in a CSP gather

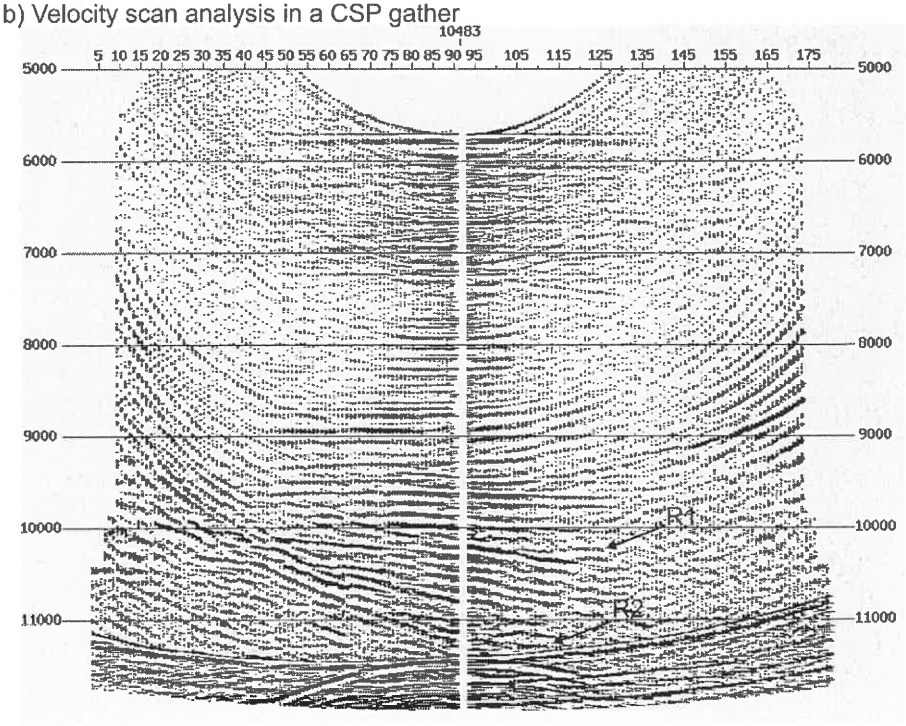

Figure C.13. Velocity scanning in CMP gathers (upper) and in a CSP gather (lower). The reflections from 10.0- 10.7 s (upper panel), which are related to the dipping reflectors in the stacked section (shown in Figure C.1, around CMP 12500), will roughly line up by choosing an appropriate velocities. However, similar dipping reflections show up in CSP gather (roughly 10-11 s, lower panel) are still dipping and will not be flattened by any velocity because they are two-sided. Reflections R1 and R2 are mentioned in text.

sediment velocities for these two models are almost same, with a difference of ± 10-50 m/s. However there is a noticeable difference in velocity below about 9 s (basement). The major difference is that the velocity from the CSP gathers is smooth while the velocity is rugged in the CMP velocity semblance. The difference is caused by the velocity scanning technique illustrated in Figure C.13.

In Figure C.13, the reflections in CMP gathers from 10.0- 10.7 s (upper panel) are related to the dipping reflectors in the stacked section (shown in Figure C.5, around CMP 12500). By using the velocity scan technique, these reflections will roughly line up by choosing appropriate velocities. This may over- or under-correct the dipping reflections. However, similar dipping reflections showing up in the CSP gather (roughly 10-11 s, lower panel) are still dipping and will not be flattened regardless of velocity because they are two-sided. Trying to flatten these dipping reflections will loose their coherence in the stacked section (e.g., Figure C.14). What I did in this situation is to line up the reflections above these reflections and some horizontal reflection components within or below the dipping package if there are some, for instance R1 and R2 (lower panel). If there are no such reflections, I just let velocity grade down to the bottom of the velocity model. The different approaches of velocity scanning analysis led to different velocity models in Figure C.12.

The subsurface structure is sensitive to the input velocity function. Figure C.15 shows two EOM migrated sections: one is produced by using the velocity model from velocity analysis of CSP gathers (Figure C.12, top) as input velocity function and NMO correction and stacking, and the other created by using the velocity model from CMP gather based

velocity analysis (Figure C.12, bottom) as input velocity function and NMO correction and stacking. Figure C.15 indicates that the more rugged velocity function will distort the geometry of subsurface structure and loose signal coherence (e.g. Figure C.15, bottom).

In conclusion, the velocity model (Figure C.12, bottom) based on CMP gather analysis is used as the initial velocity function to create CSP gathers. Then, a velocity analysis is applied to the CSP gathers to create a refined velocity model (Figure C.12, top). The refined velocity function is then used to recreate the CSP gathers. This process can be repeated if necessary.

C.3.2.7 FIRST_CSP

9829. It is the first CSP corresponding to first CMP 9829. This is an arbitrary number.

C.3.2.8 CSPINCR

CSPINCR is the increment of the CSP gather. It is normally one but it could be an arbitrary number. It is mentioned above that the CSP numbering in most cases is different from the CMP numbering. However, by manipulating the parameters of FIRST_CSP and CSPINCR, the CSP numbering can be made roughly the same as the CMP numbering. Note that the input data CMP spacing is 13.333 m and the finest CSP spacing (CSP_DX) is 130 m, which is about 10 times the CMP spacing. To match the CSP numbering with the CMP numbering, let the FIRST_CSP number be exactly the same as the first CMP number (9829), put the CSP spacing (CSP_DX) to be 133.33 m, which is 10 times 13.333 m of the CMP spacing, and then put the CSPINCR to be 10. The resultant CSP gathers

will have the same numbers as input CMP gathers although the CSP gathers are not continuously numbered.

Manipulating the parameters of FIRST_CSP and CSPINCR as well as the input data CMP_START, can also produce a finer CSP spacing using the following steps: 1) let CSP_DX be 133.33 (10×13.33) and CSPINCR be 10, do 10 runs increasing FIRSTCSP for each run and outputting each run to a new file. So FIRSTCSP will be 9829, 9830, …, 9838, for the successive runs. The files can be all read into a new single file in a new job and then sorted to construct a section with 13.333 m trace spacing (Note, however, that this is very time consuming and may only be useful for selected regions to detail structure of particular importance).

C.3.2.9 GRID

This field is used for vertical interpolation of velocities with time.

C.3.3 CSP Stacking

The resultant CSP gathers can be stacked by using the conventional NMO correction and stacking. The velocity file from velocity analysis of CSP gathers can be directly used to stack the CSP gathers. Other conventional techniques, like post-stack deconvolution and time variant filtering and scaling are also applied to the data. These are exactly the same as done in post-stack migration and therefore are not discussed further.

CSP stacking is also sensitive to the stacking velocity. The impact of different velocity functions on CSP stacking is shown in Figure C.15. The refined velocity from CSP gathers based velocity analysis is recommended.

The CSP gathers formed by EOM are already migrated. Stacking the CSP gathers results in a migrated section and there is no need to conduct post-stacking migration anymore.

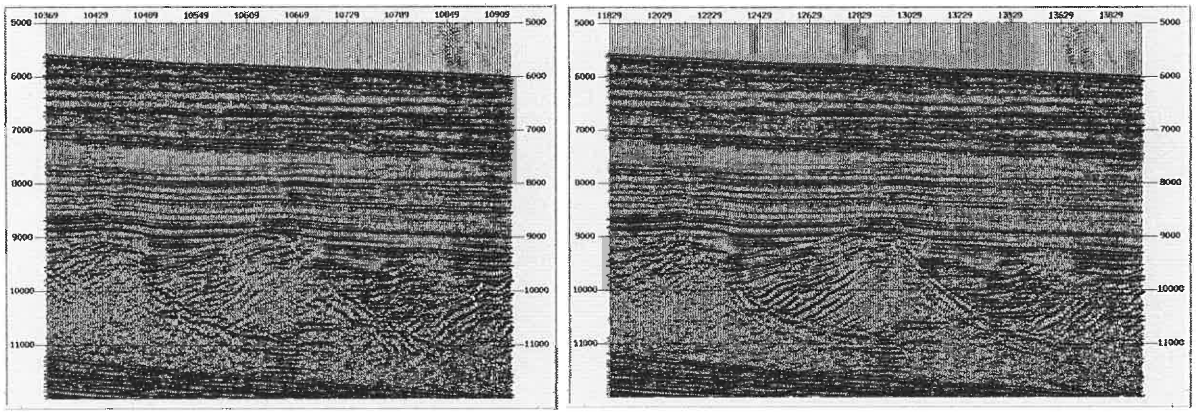

Figure C.14. (Left) An example of loosing coherence of the dipping reflections when the corresponding hyperbolae (between R1 and R2 shown in Figure C.13) in the CSP gathers are over-corrected. CSP spacing is 150 m. (Right) A comparison of the same section with the hyperbolae in the CSP gathers not over-corrected. CSP spacing is 133.3 m.

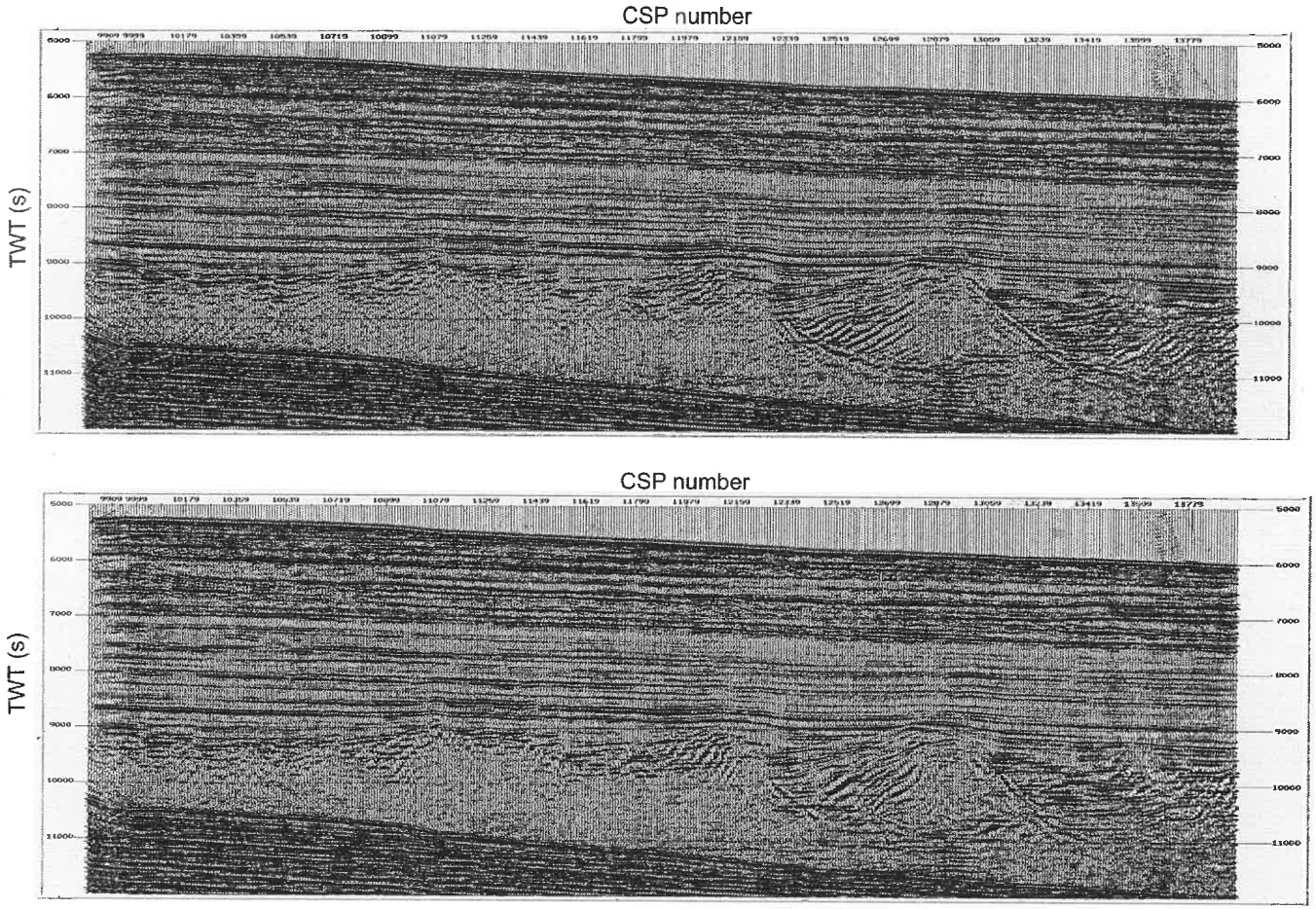

Figure C.15. (Top) An EOM migrated section by using the velocity model in Figure C.12a as input velocity function and NMO correction and stacking. (Bottom) An EOM migrated section by using the velocity model in Figure C.12b as input velocity function and NMO correction and stacking. Note the distortion of the fault and the dipping reflection between CSP 12339-12699, which is caused by the rugged velocity model, while the same features in the top section are more coherent and smooth. CSP spacing is 133 m for both sections.

C.3.4 References

Bancroft, J. C., 1996. Natural antialiasing in equivalent offset prestack migration: 66 th Annual Internat. Mtg., Soc. Expl. Geophys., Expanded Abstracts, 1465-1466.

Bancroft, J. C., Geiger, H. D., and Margrave, G. F., 1998. The equivalent offset method of prestack time migration: *Geophysics*, Vol.63, No. 6, 2042-2053.

Bancroft, J.C.,1998. A practical understanding of Pre- and Poststack Migration—Volume 2 (Prestack). Society of Exploration Geophysicists Course Note Series no. 9.

Deregowski, S. M., and Rocca, F., 1981. Geometrical optics and wave theory of constant offset sections in layered media: *Geophys. Prosp.*, 29, no. 3, 374-406.

Hale, D., 1984. Dip-moveout by Fourier transform: *Geophysics*, 49, no. 6, 741-757.

Yilmaz, Ö.Z., 2001. *Seismic data analysis: processing, inversion, and interpretation of seismic data,* second edition, SEG publication.

APPENDIX D

PROCESSING REPORT OF MULTI-CHANNEL SEISMIC DATA ALONG SMART-2—USING STANDARD PRE-STACK MIGRATION TECHNIQUES

D.1 Introduction

This report introduces the re-processing of the multi-channel seismic data along SMART-2 using conventional techniques. The data set includes short sections across the salt diapiric slope area and the faulted basement blocks seaward of the salt structure along MCS line 88-1a, and the entire BGR (the German Federal Agency of Geosciences and Natural Resources) line 8911. The main techniques include post-stack finite difference (FD) time migration, dip-moveout correction (DMO) followed by post-stack FD time migration, and prestack FD time migration. The principles of these techniques are not discussed in details since they are conventional tools and are well described in the literature (e.g. Deregowski and Rocca, 1981; Hale, 1984; Yilmaz, 2001).

D.2 Highly Faulted Basement and Diapiric Slope Sections

D.2.1 Input Data

D.2.1.1 Raw Data

Highly faulted basement and diapiric slope sections are short sections along 88-1a (Keen et al., 1991). The raw data for the entire 88-1a were downloaded from tapes at Bedford Institute of Oceanography (BIO). There are a total of 2411 shots, ranging from shot points (SP) 2062-4472. Each shot record is stored as a single file. Trace length is 24532 ms and sample interval is 4 ms. The streamer is 4800 m long with 180 receiver groups. Other detailed information is described in the geometry setup in section 2.2.

D.2.1.2 Data Reformatting

Raw data records are in a format of SEG-D 8021. The raw data were converted to SEG-Y format by the following scripts:

```
---------------------------------------------------------------
#!/bin/bash
# convert all SEG-D files to SEGY files in a directory
for i in `ls *.segd`;
do
#       file $i
        echo working on $i
        segdstdout_new $i > `basename $i .segd`.sgy
done
---------------------------------------------------------------
```

Note:
(1) The following shots are not able to be read due to an error in format: 2164, 2296, 2396, 2585, 2702, 2955, 2986, 3089, 3303, 3401, 3402, 3741, 4129, and 4286.
(2) The following are noisy shots: 4028, 4121, 4122, 4123, 4125, 4126, and 4127.

Each shot record file is named by the shot number, for example the data file for shot 3700 is named as 881Asp3700; however, the shot number information is not set in the header of the SEGY files. The following script is used to insert the shot number from the file name as "recordnum" in the header:

```
---------------------------------------------------------------
#!/bin/bash
#
# Script to use SU to add the shot numbers to the headers of the segy files
# in this directory.
for filename in `ls *.sgy`;
do
        OUTFILE=../881a_new/$filename
        SHOTNUM=`echo $filename | sed s/881Asp// | sed s/.sgy//`
        segyread tape=$filename endian=1 conv=0 | \
        segyhdrs | \
        sushw key=fldr a=$SHOTNUM | \
        segywrite tape=$OUTFILE endian=0
done
---------------------------------------------------------------
```

D.2.1.3 Data Redundancy

The brute stack indicates that SP 4014-4129 is a repeat of SP 4130-4245. Note: the data redundancy indicates that 116 shots of data are lost at the seaward end.

D.2.2 Geometry Setup

The geometry setup is based on the acquisition report of 88-1a (available at: http://gsca.nrcan.gc.ca/pubprod/fgp/reports/88f.pdf).

The coordinate origin is set to the last channel (180) of receivers at the onset. The acquisition geometry is shown below:

Line name/number: 881a
Comment: project for prestack time migration

Number of channels: 180
Offset of Channel 1: 250.000
Last trace offset: 5050.000
Streamer depth: 7.620

Shot spacing:80.000
CDP spacing:13.333

Shot ID and distance:2062 5050.000
CDP ID and distance:1001 2525.000
First and last shots in profile:2062 4472

Coordinate origin:0.000 0.000
SEG-Y Coordinate scalar: decimeters
SEG-Y height scalar: decimeters
SEG-Y Coordinate type: seconds of arc
Length units: Meters

Note: the distance for the first shot (2062) is equal to the maximum offset. The distance of the first CDP (1001) is half of the maximum offset.

The geometry file is modified due to: (1) the SP to CDP ratio (i.e. the ratio of SP interval to CDP interval) is not an integer (≈6.000015), which is not acceptable to the processing software, and (2) the inconsistency between the streamer length (4800 m) in the acquisition report and that calculated from group interval times channel number, which is (180-1)*26.667 ≈ 4773.93 m. A slight modification was made to the SP interval and CDP interval below so that the SP/CDP ratio is exactly equal to 6.

Line name/number: 881a
Comment: project for pre-stack time migration

Number of channels: 180
Offset of Channel 1: 250.000
Last trace offset: 5023.214
Streamer depth: 14

Shot spacing: 79.998
CDP spacing: 13.333

Shot ID and distance: 2062 5023.214
CDP ID and distance: 1001 2511.607
First and last shots in profile: 2062 4472

Coordinate origin: 0.000 0.000
SEG-Y Coordinate scalar: decimeters
SEG-Y height scalar: decimeters
SEG-Y Coordinate type: seconds of arc
Length units: Meters

D.2.3 Pre-stack Processing Sequence

D.2.3.1 Bandpass Filtering

A minimum phase Butterworth bandpass filter of 7-15-50-70 with an amplitude scheme of 0.5-0.95-0.95-0.5, respectively, was applied to the shot records. Figure D.1 shows the frequency spectra before and after filtering.

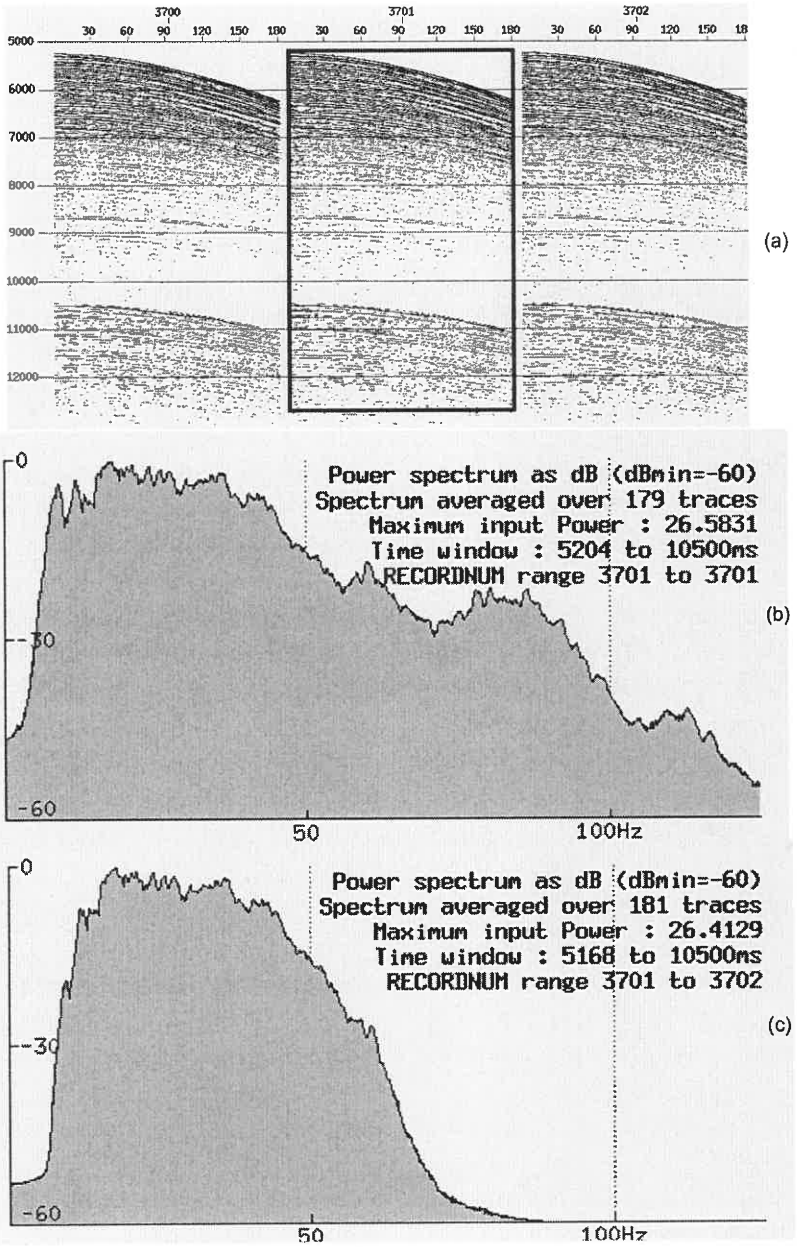

Figure D.1. (a) Raw data for shots 3700-3702, (b) the frequency spectrum for shot 3701 and (c) the frequency spectrum after Butterworth filtering (7-15-50-70).

D.2.3.2 Amplitude Recovery

Amplitude recovery consists of spherical divergence correction and a user-specified scaling function. The amplitude loss due to spherical divergence can be split into losses along offset direction and time (depth) direction. In order to recover amplitude loss due to

offset variation, offset is assigned to each channel based on the acquisition geometry (offset = 250 + 26.67 × channel number). A stacking velocity file is required for amplitude correction along the time-axis. The stacking velocity from previous processing (by Western Geophysical) was used as follows:

Time	Velocity	Time	Velocity	Time	Velocity	Time	Velocity
0	1460	5200	1460	5960	1525	6280	1580
6760	1650	7720	1800	8440	2005	8680	2075
9000	2160	9320	2330	9880	2675	10280	3060
11160	3760	12000	3958	14000	4751	16000	5268

Units: Time (ms); Velocity (m/s).

A user-specified scalar of 1db/s was also applied to the shot records because the lower part of the shots still presents weaker amplitude than upper part after spherical divergence correction. The combined correction of spherical divergence and user-specified scaling function is shown in Figure D.2.

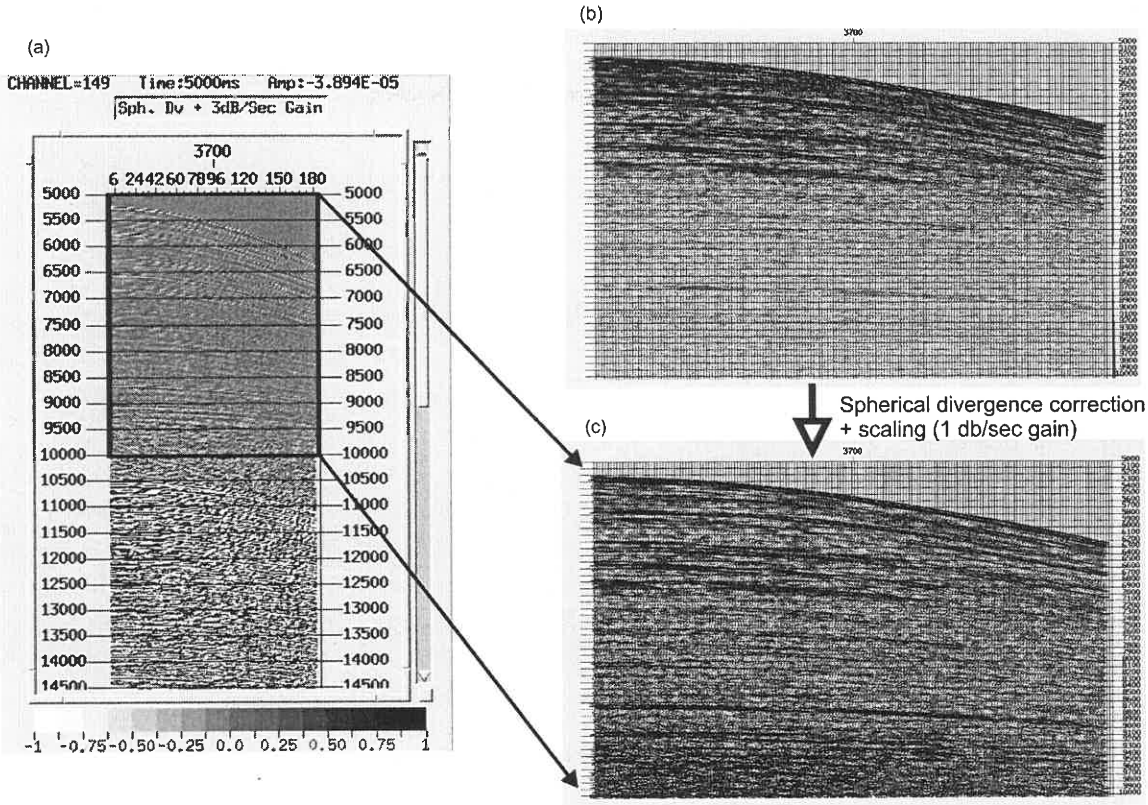

Figure D.2. (a) Amplitude recovery of shot record of 3700 after spherical divergence correction and scaling at gain of 1db per second. A blow-up for 5-10 s is shown on the lower-right panel (b) and the raw data section is displayed on the right-upper panel (c).

D.2.3.3 Prestack Deconvolution

A prestack deconvolution filter used in previous processing of this line was applied to the shots to improve the temporal resolution and to compress the signal reverberation. The filter operator length is 200 ms and the gap 12 ms, with 0.1% of white noise. The deconvolved and undeconvolved shots and their autocorrelograms are compared in Figure D.3.

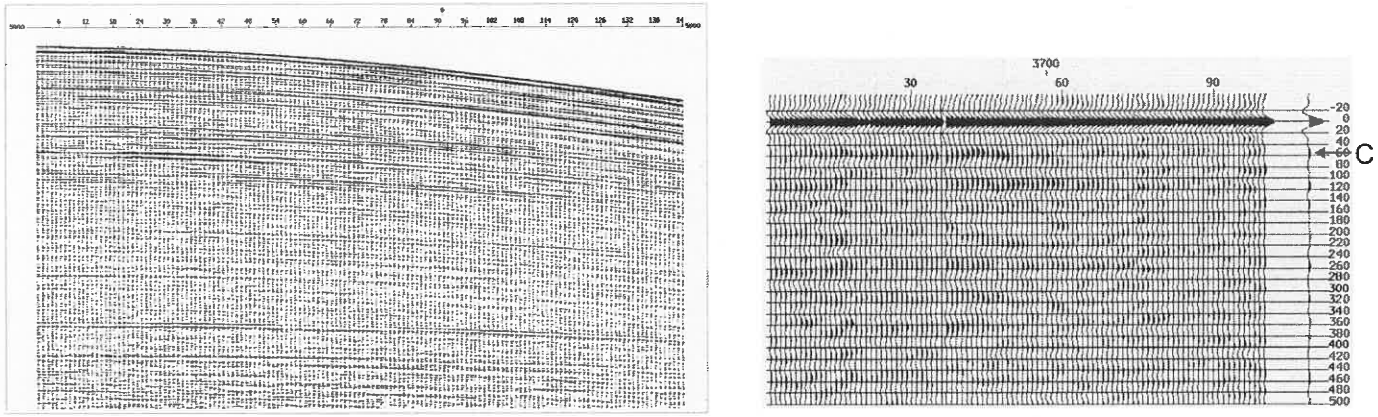

Figure D.3. The undeconvolved (a) and deconvolved record (b) for shot 3700. The autocorrelograms for undeconvolved and deconvolved shot 3700 are shown on the right side. Note the difference at reflections A and B in (b) compared to (a), as well as the reverberation (e.g. C) for the undeconvolved data compared to its counterpart for the deconvolved data.

D.2.3.4 CDP Sorting

Shots are sorted into CDP gathers according the geometry described in section 2.2.

D.2.3.5 Water Bottom Multiple Removal

A parabolic radon transform was used to model the water bottom multiple reflections in order to remove from the input data. The input data for this technique should be NMO-corrected. The following is a complete processing flow for demultipling:

DISCREAD
NMO
SUPERGATH
REORDER
SETLATTR
PRT_DEMULT
REORDER
SUPERGATH
SETLASTTR
NMO
DISCWRITE

The functions for these modules are described as follows:

DISCREAD reads in the CMP data.

The first **NMO** applies forward NMO correction to the CMP data. The velocity function used for NMO correction is the stacking velocity derived by the previous processing.

The first **SUPERGATH** sorts the input data into super gathers by combining every six 30-fold CMP gathers into one 180-fold super gather (the main parameter field: COUNT=6). This is to avoid possible aliasing due to undersampling in the CMP gather domain. Note: the reason for that a specific number of six CMP gathers are combined into one supergather is that the SP/CMP ratio is six (i.e. the shot spacing is 80 m and CMP spacing is 26.667 m). That is to say, for every adjacent six CMP gathers, all traces have different offsets. When the traces of the adjacent six CMP gathers are sorted into one gather, the resultant supergather will have six times the number of traces with different offsets than a single CMP gather, and the trace interval in the supergather is six times finer, compared to the CMP trace spacing.

The first **REORDER** reorders the traces in the super gathers in order of increasing offset.

The first **SETLASTTR** marks the last trace of the super gathers.

PRT_DEMULT models the multiple reflections and output signal or optionally subtract noise from data. The input is first split into modelled and unmodelled components. The modeled data are further split into signal and noise which refers to multiples in this case. The unmodelled component is usually uncorrelated background noise. The main parameters include:

MODE: Marine

OFFSETS: 250 5023.2 26.666 13.333 (start, end, increment and bin-size for the offsets)

FOLD: 180 (fold of super gather)

HMAX: 5023.2 (far offset)

MODEL_MS:-400 1000 (moveout limits at HMAX to be modeled)

NOISE_MS:100 800 (moveout limits at HMAX for the noise)

OUTPUT: subtract noise

The second **REORDER** reorders the traces in the demultipled super gathers by offset.

The second **SUPERGATH** sorts the demultipled super gathers back into CMP gathers.

The second **SETLASTTR** sets the last trace of the demultipled CMP gathers.

The second **NMO** applies inverse NMO correction to the demultipled CMP data.

DISCWRITE outputs the resultant data.

Figure D.4 shows the result of water bottom multiple removal in CMP domain.

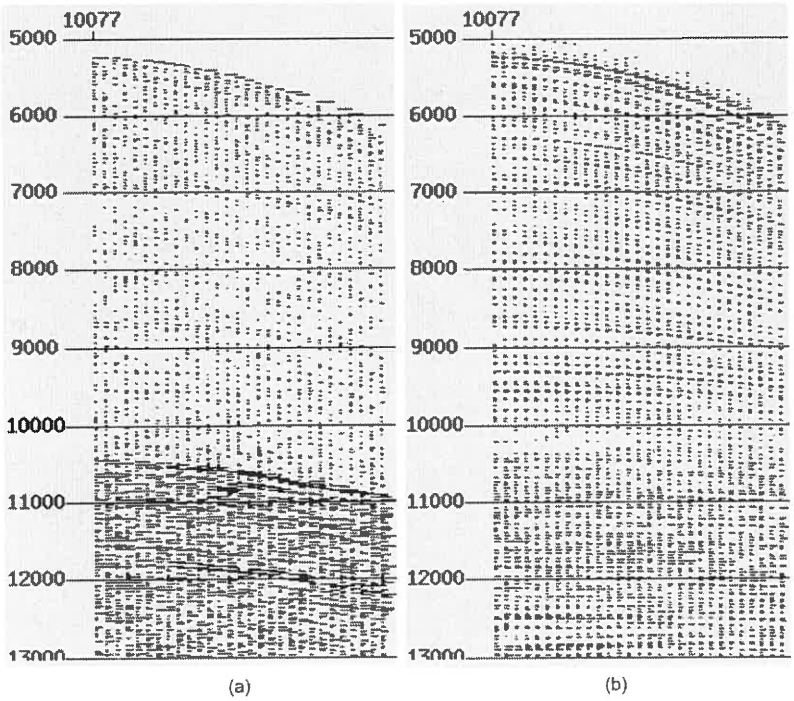

Figure D.4. Water bottom multiple removal by parabolic radon transform for CMP 10077. (a) is the CMP gathe10077 without water bottom removal. (b) is the same CMP gather after water bottom multiple removal.

D.2.3.6 Velocity Analysis

Velocity analysis includes two steps. The first step is to calculate the velocity semblance from the CMP data and produce a velocity file by picking the maximum semblance at every 100 CMPs. The second step is to refine the velocity profile by applying a constant velocity analysis (CVA) to the CMP gathers. This step was repeated after the refined stacking velocity was used to do DMO and prestack time migration, which will be introduced in the following sections 2.3.7 and 2.5.2.2. An example of picking velocity semblance and constant velocity analysis is demonstrated in the Appendix C. The detailed process is not included since this is a commonly used technique.

D.2.3.7 Dip-Moveout Correction (DMO)

The refined velocity from the velocity analysis mentioned in section 2.3.6 was used to do DMO. The following are the processing flow of DMO:

DSORT_OFF
NMO
SETHEADER
SETLASTTR
DMO_DX
NMO
GENSORT
DISCWRITE

DSORT_OFF sorts the CMP gathers into common offset gathers. The input parameters include:

DISCFILE: sp3700-4356.cdp (name of the input seismic data)

BINVALS: -4970:-330/160 (offset bin start, end and increment, in meter)

BINSIZE: 80 (half of the increment)

BINVAL_HDR: spare1. spare1 is the trace header keyname. BINVAL_HDR is specified as spare1 in that we sort the data into common offset panels and want to save the value of the bins without changing the original offset in the trace header.

The first **NMO** applies forward NMO correction to the offset gathers, using a stacking velocity file previously determined by conventional velocity analysis.

SETHEADER defines the trace header. Input field TRACE_HDRS: offset=spare1, in correspondence with the field of BINVAL_HDR in module **DSORT_OFF**.

SETLASTTR is used to mark the last trace in each CMP gather.

DMO_DX applies dip moveout correction to offset gathers in the time domain. **DMO_FK** has the same function but it works in the FK domain and takes more time. The input fields include:

CDPRANGE: 9829 13944 (the first and last CMP to process)

CDP_DX: 13.333 (CMP spacing, in meter)

N_OFFMIX: 1 (number of offsets to mix)

OFFMAX:-4970 (maximum offset that will be present)

The second **NMO** applies inverse NMO correction to the common offset gathers following the DMO correction.

GENSORT sorts the offset gathers back into CMP gathers.

DISCWRITE saves the resultant CMP gathers.

To accomplish a DMO correction, the entire processing flow needs to run more than once. The first run is to do DMO using the stacking velocity file from the initial velocity analysis. DMO corrected CMP gathers were created after the first run of DMO. A more accurate velocity model was estimated from the DMO corrected CMP data by repeating the conventional velocity analysis. This process can be repeated if the velocity semblance of the resultant CMP gathers is not well focused. The improved velocity was then put into the flow to redo the DMO correction.

D.2.4 Stacking

The CMPs are stacked using the final stacking velocity from velocity analysis.

D.2.5 Post-stack Processing Sequence

D.2.5.1 Deconvolution after Stack

A predictive deconvolution filter was applied to the stacked section to further improve the temporal resolution and to compress the signal reverberation. The operator length is

300 ms and the gap 60 ms, with 0.1% of white noise. The deconvolved and undeconvolved stack and their autocorrelograms are compared in Figure D.5.

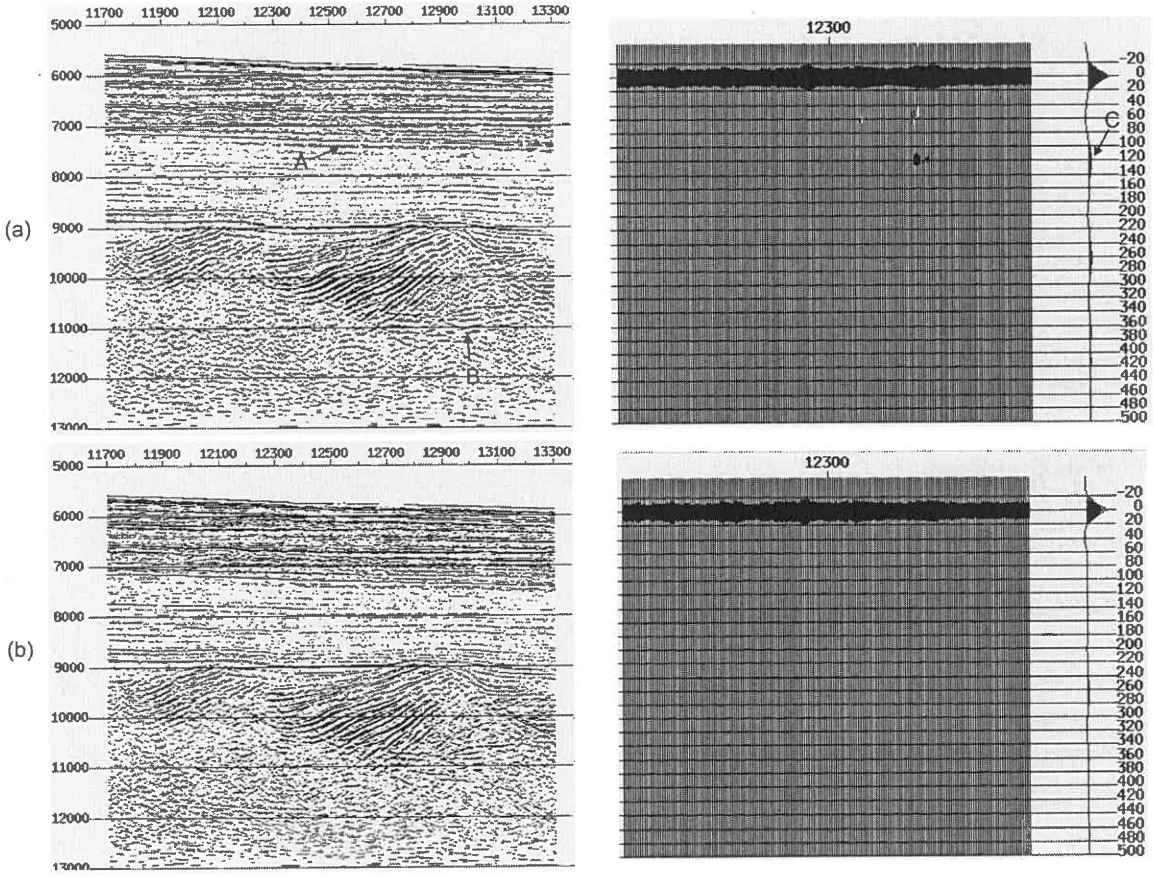

Figure D.5. (a) A stack without post-stack deconvolution and (b) the same stack with post-stack deconvolution.The autocorrelograms for undeconvolved and deconvolved stacks are shown on the left. Note the difference at A and B in (a), as well as the reverberation (e.g. C) for the undeconvolved stack, compared to the same locations in (b).

D.2.5.2 Migration

Due to the variable lateral structure across this region, a 2-D migration algorithm—finite difference (FD) migration was used for this section. Post-stack and prestack FD migrations were carried out for comparison. Interval velocities constrained by OBS data or converted from stack RMS velocities were used to demonstrate the difference.

D.2.5.2.1 Post-Stack Migration

DMO correction is a pre-stack partial migration (Bancroft 1998; Yilmaz, 2001). Post-stack migration is used to complete the migration. For comparison, post-stack migration is also applied to the stacked section without DMO correction. Post-stack migration consists of the following modules:

DISCREAD
NMO
STACK
ZEROMUTE
FDMIG
ZEROMUTE
DISCWRITE

DISCREAD reads in the CMP data.

NMO applies forward NMO correction to the CMP data using the refined stack velocity model after DMO correction.

STACK creates a stack.

The two **ZEROMUTE** modules apply migration muting prior and after migration.

FDMIG is a FD time migration routine in X-T domain. The important input fields include:

NTRACES: 4116 (number of traces to be migrated)

DX: 13.333 (distance between CMP traces, in meter)

WINSIZE: 20 ms (depth step size)

VELFILE: dmo-cva-int.nmo (velocity file)*

SCALER: 1.0 (multiply the velocity in VELFILE by this amount)

* Note: the velocity is the interval velocity converted from stacking velocity. In order to obtain a reasonable interval velocity model, the following steps were conducted: (1) remove the extreme velocity points, (2) remove velocity points which are closer than 200 ms because these points and the extreme velocity points in (1) will create areal interval velocities, and (3) the stacking velocity model is smoothed before being converted to interval velocity.

DISCWRITE outputs the migrated section.

D.2.5.2.2 Prestack Time Migration

The following are the modules used for FD pre-stack time migration:

DSORT_OFF
NMO
SETHEADER
SETLASTTR
FDMIG
GENSORT
NMO*
DISCWRITE*
NMO*
STACK

DISCWRITE

Note: * marked modules are optional only if interim CMP gathers need to be output.

The descriptions for modules **DSORT_OFF, NMO, SETHEADER, SETLASTTR, GENSORT,** and **DISCWRITE** are same as described in section 2.3.7. **STACK** and **FDMIG** is described in section 2.5.2.1. The usage and parameterization of FDMIG is also exactly same as described in section 2.5.2.1. The difference from the processing flow in section 2.5.2.1, however, is that FD prestack time migration is now put before stack, rather than after stack. The stacking velocity improved by DMO correction described in section 2.3.7 was used in the prestack migration. After prestack time migration, a new round of velocity analysis is applied to interim CMP gathers to refine the stacking velocity. The refined stacking velocity was then converted to interval velocity, which would be used to do prestack migration again.

D.2.5.3 Water Bottom Top Muting

A top mute was applied to the migrated section to mute at time above the first break of the water bottom.

D.2.5.4 Time Variant Filtering

To further remove artifacts of migration, a set of four time-variant zero-phase Butterworth bandpass filters (TVF) was applied to each section. The set of filters for the faulted basement section (SP 3700-4356) is shown as follows:

Time-on unit: ms	Time-off unit: ms	Frequency-1 (low-end)	Frequency-2 (low-cut-off)	Frequency-3 (high-cut-off)	Frequency-4 (high-end)
5000	7000	5	8	60	70
7000	9000	5	8	50	60
9000	11000	5	8	40	50
11000	15000	5	8	30	40

Note: water depth 5000-6000 ms.

The set of filters for the diapiric slope section (SP 3232-3680) are slightly different from faulted basement section due to shallower seafloor. The filters are shown as follows:

Time-on unit: ms	Time-off unit: ms	Frequency-1 (low-end)	Frequency-2 (low-cut-off)	Frequency-3 (high-cut-off)	Frequency-4 (high-end)
4000	5000	5	8	70	80
5000	9000	5	8	60	70
9000	11000	5	8	40	60
11000	14000	5	8	30	50

Note: water depth 4000-5000 ms.

The effect of the TVF is demonstrated in Figure D.6. The low-frequency noise (e.g. A, Figure D.6a) is largely removed and the basement faults (e.g. B, Figure D.6b) are better imaged.

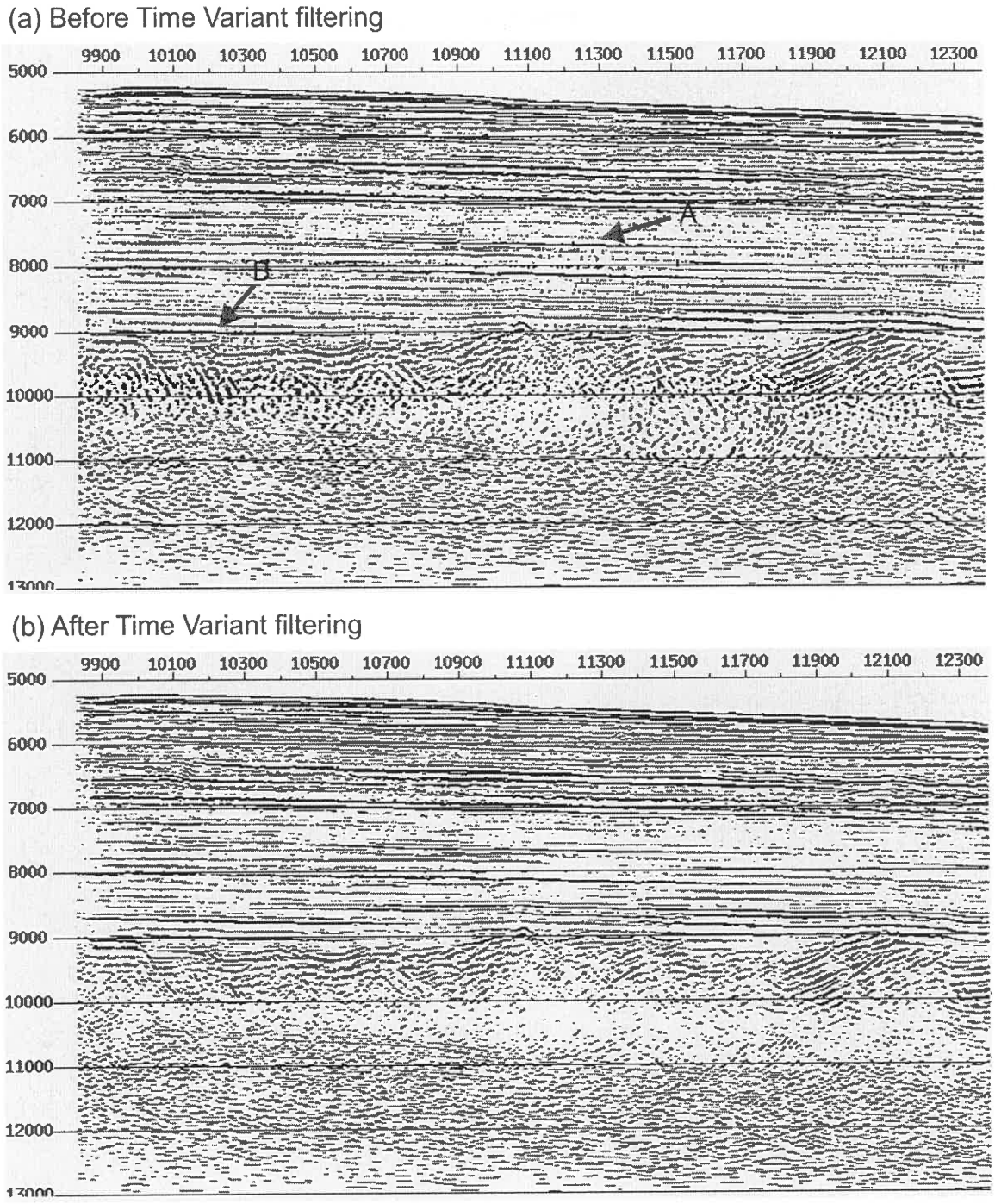

Figure D.6. A comparison of stack section before (a) and after time-variant filtering (b).Two sections are part of stack of the faulted basement blocks. The low-frequency noise in section (e.g. A) is largely cleared out. The basement faults (e.g. B) are better imaged.

D.2.6 Migrated Sections

The highly faulted basement section is the seaward end of 88-1a, including SP 3700-4356. The diapiric slope section includes SP 3232-3680. The processing flow for these two sections is generally the same. The resulting migrated sections are shown below.

D.2.6.1 Highly Faulted Basement Section (SP 3700-4356)

The migrated sections of post-stack time migration, DMO corrected section followed by post-stack migration, and pre-stack time migration are shown respectively in Figures D.7-D.9. FD time migration was used for pre- and post- stack migrations.

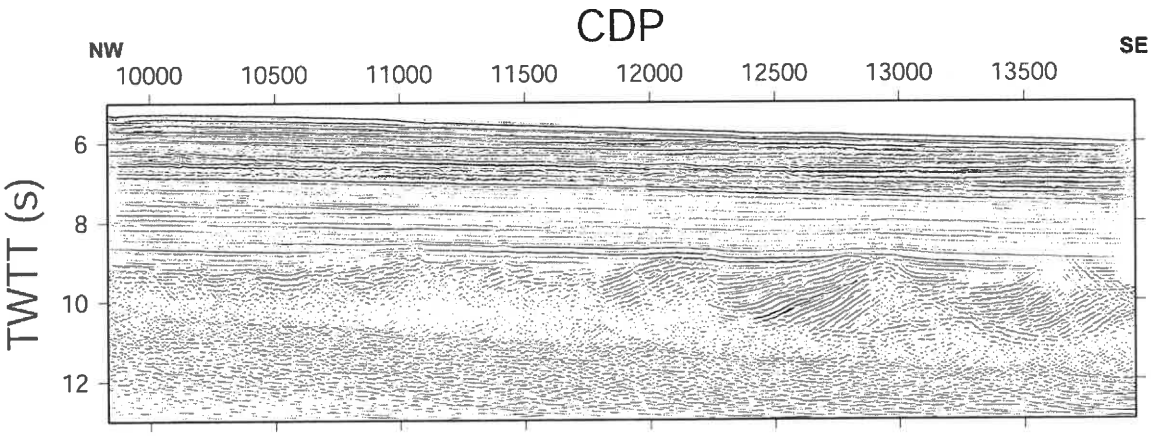

Figure D.7. Post-stack migrated time section of the faulted basement section. The velocity constrained by refraction data is used for migrations. The processing sequence is described in the text. Water bottom multiple is largely removed but some remnant energy is still visible. A set of four time-variant filters have been applied to different time windows as discussed in text.

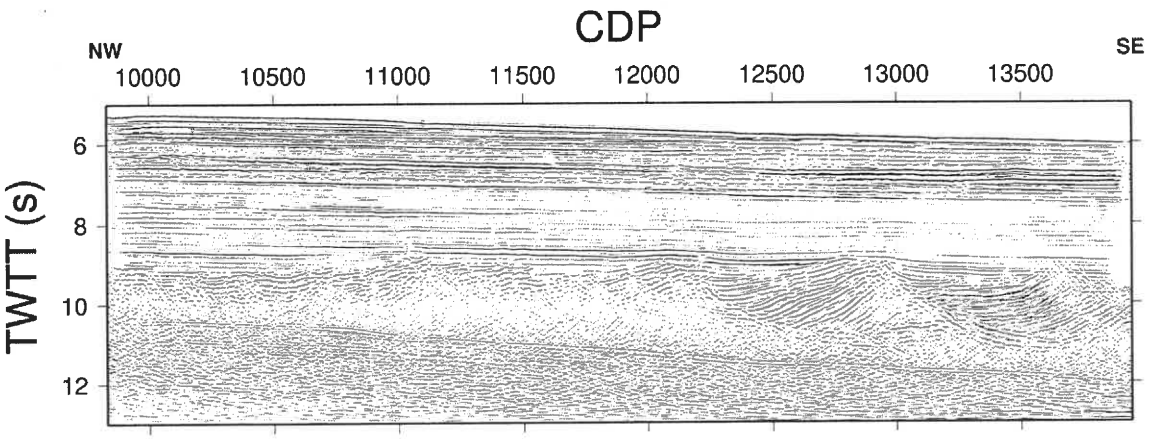

Figure D.8. Post-stack migrated time section after DMO correction for the faulted basement section. DMO is applied before post-stack migartion. Other features refer to Figure D.7.

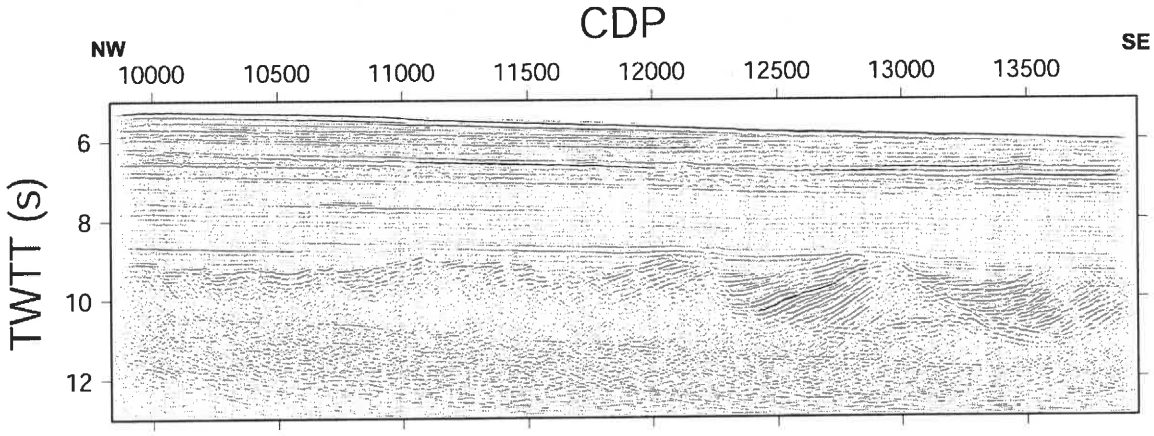

Figure D.9. Pre-stack migrated time section for the faulted basement section. Other features refer to Figure D.7.

D.2.6.2 Diapiric Slope Section (SP 3232-3680)

Figures D.10-D.15 show the migrated sections of post-stack time migration, DMO corrected section followed by post-stack migration, and prestack time migration, respectively. The processing flow is same as that of the faulted basement structure. Interval velocities, constrained by refraction data or converted from stacking velocities, are used for post-stack migrations. The corresponding post-stack migrated sections for various velocity funtcions are shown for the purpose of comparison in Figures D.10-D.13. The shape and structure of salt are only slightly different from each other due to different migration velocity.

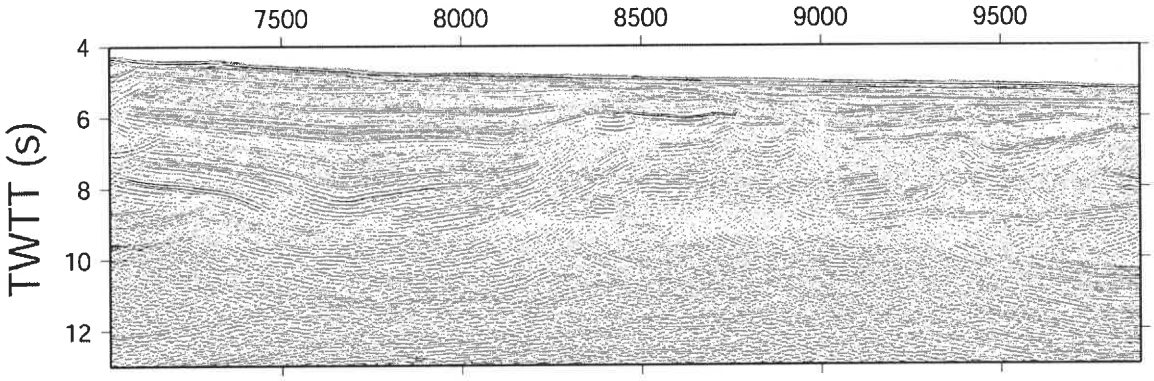

Figure D.10. Post-stack migrated time section of the diapiric slope area. The interval velocity converted from stacking velocity is used for migrations. Water bottom multiple is removed. A set of four time-variant filters have been applied to different time windows as discussed the in text. Automatic gain control is applied to the data.

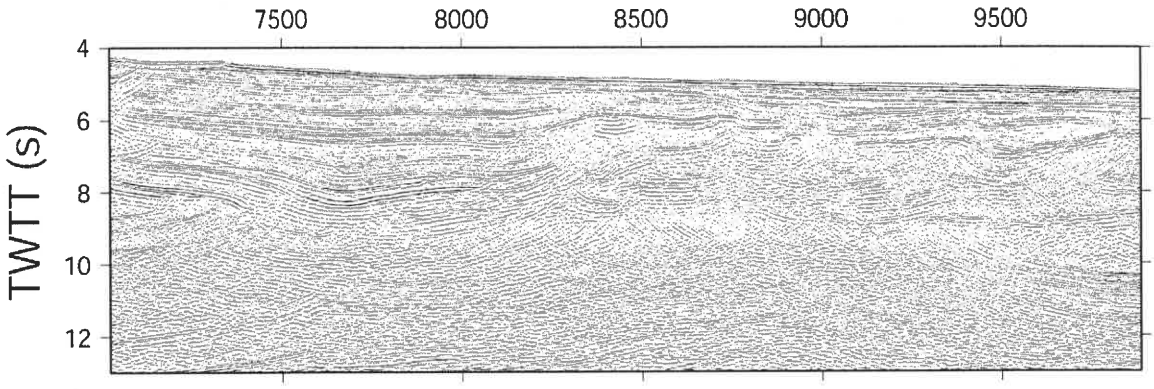

Figure D.11. Post-stack migrated time section for the diapiric slope area. Interval velocity converted from the stacking velocity of equivalent offset gathers (see Appendix C) is used for the migartions. Other features refer to Figure D.10.

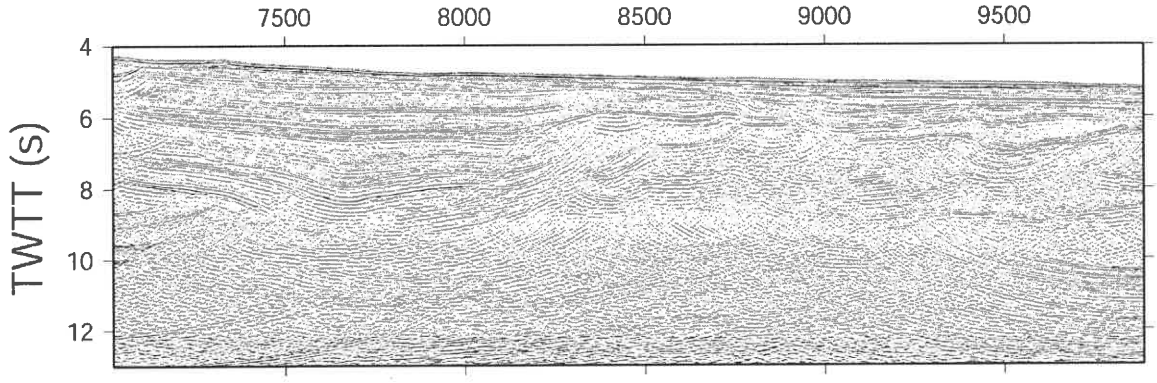

Figure D.12. Post-stack migrated time section for the diapiric slope area. The interval velocity constrained by the seismic refraction data is used for the migartions. Other features refer to Figure D.10.

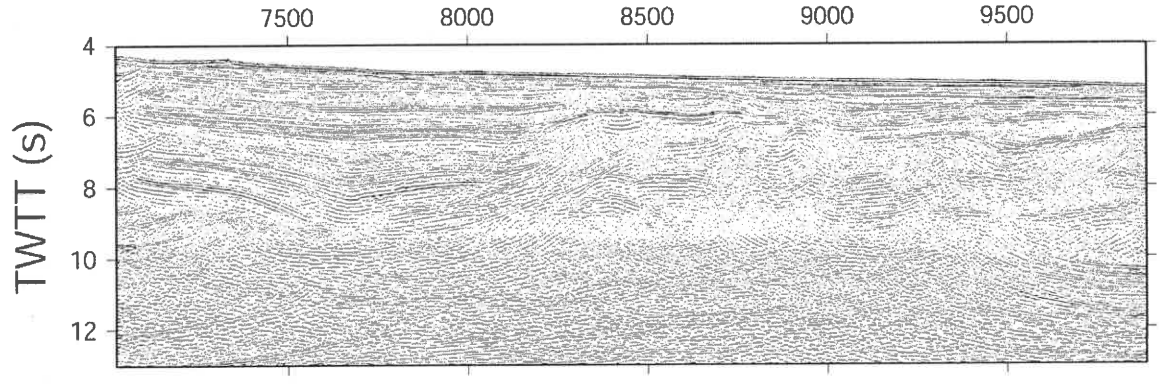

Figure D.13. Post-stack migrated time section for the diapiric slope area. The interval velocity converted from previous stacking velociy (used by WesternGeophysical) is used for the migartions. Other features refer to Figure D.10.

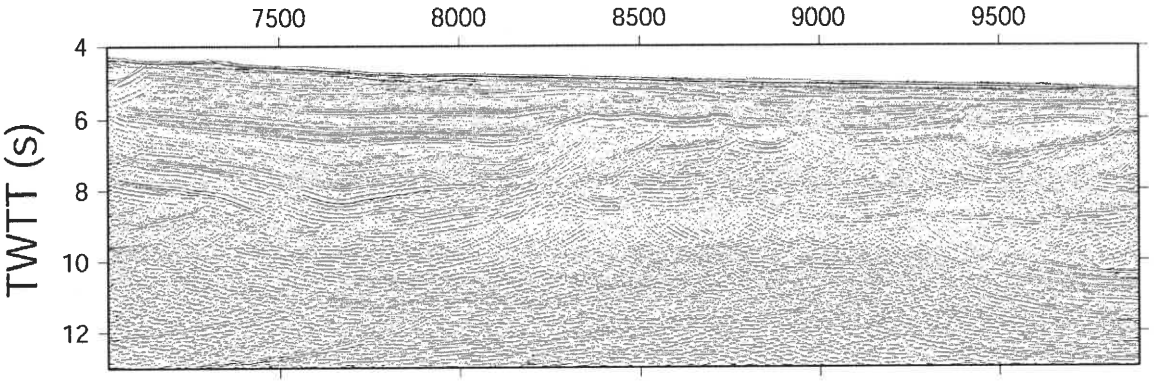

Figure D.14. Post-stack migrated time section after DMO correction for the diapiric slope area. DMO is applied before post-stack migration. Other features refer to Figure D.10.

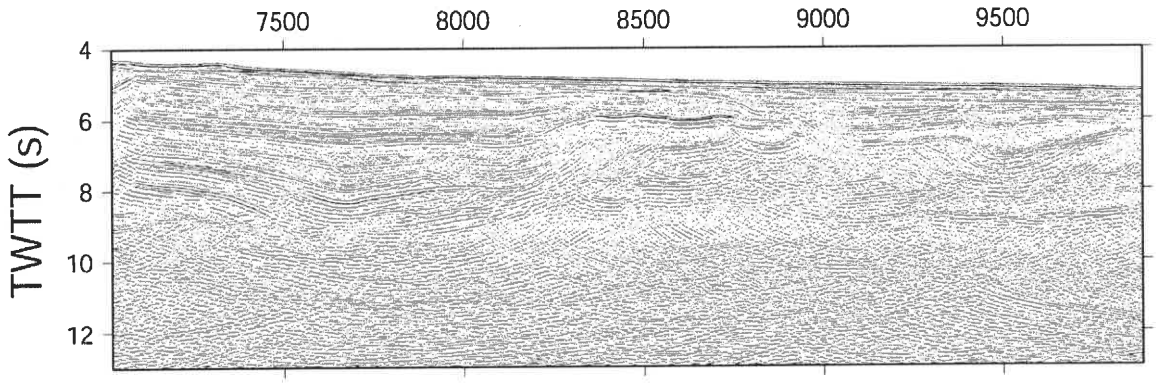

Figure D.15. Pre-stack migrated time section for the diapiric slope area. Interval velocity constrained by the seismic refraction data is used for the migrations. Other features refer to Figure D.10.

D.3 BGR 8911

D.3.1 Input Data

Raw shot data were downloaded from tapes at BIO in 2004. The raw data have been reformatted from SEGD to SEGY. There are 2799 shots, ranging from SP 101 at the seaward end to SP 2899 at the landward end. The shooting interval is about 50 m (about 19 seconds a shot at survey speed of 5 knots). There are 60 live channels with a 50-m spacing along a 3000m streamer. Trace length is 16000 ms and sample interval 4 ms. Detailed information is described in the geometry setup in the following section.

D.3.2 Geometry Setup

The geometry setup is based on the acquisition geometry. The coordinate origin is set to the first channel (1) of receiver at the onset. The acquisition geometry is shown below:

Line name/number: 8911
Comment: project for prestack time migration

Number of channels: 60
Offset of Channel 1: 314000
Last trace offset: 190.000
Streamer depth: 6-14

Shot spacing: 50.000
CDP spacing: 25.000

Shot ID and distance: 101 3140.000
CDP ID and distance: 101 1570.000
First and last shots in profile: 101 2899

Coordinate origin: 0.000 0.000
SEG-Y Coordinate scalar: meters
SEG-Y height scalar: meters
SEG-Y Coordinate type: seconds of arc
Length units: Meters

D.3.3 Pre-Stack Processing

D.3.3.1 Amplitude Recovery

Amplitude recovery is same as described in section 2.3.2.

First, offset is assigned to each channel of shot data based on the acquisition geometry (offset = 190 +50*(60-channel number). A semi-empirical velocity function was used for amplitude correction along time-axis. A stacking velocity profile from the previous processor was used first as follows:

Time	Velocity	Time	Velocity	Time	Velocity	Time	Velocity
0	1470	5127	1490	5605	1520	6029	1550
6602	1645	7698	2560	9223	2860	10053	3535
12511	4130	15252	4925				

Units: Time (ms); Velocity (m/s).

The amplitude is recovered very well (Figure D.16b). In order to increase the visibility of the late arrival times, a user-specified scalar of 2db was also applied to the shot records after spherical divergence correction. The combined effect of spherical divergence correction and user-specified scalar is shown in Figure D.16c.

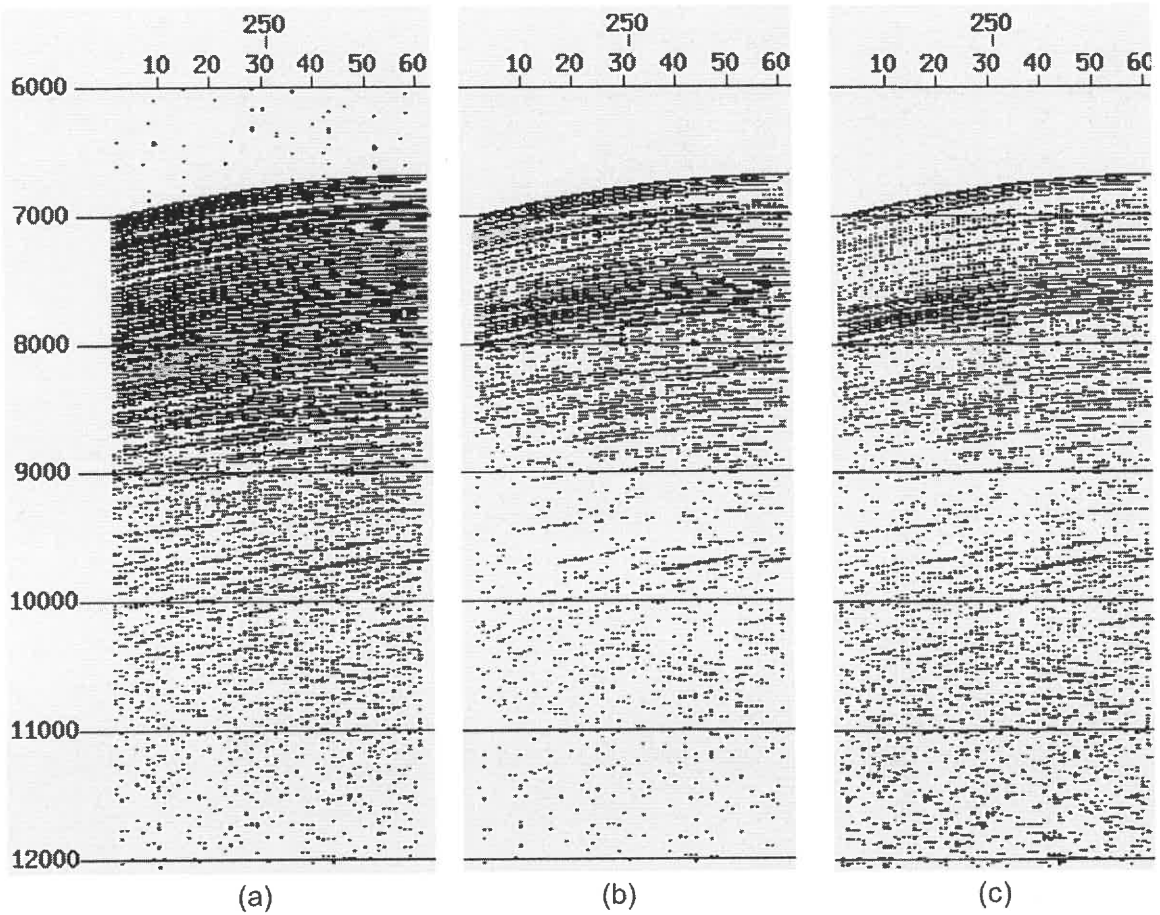

Figure D.16. Amplitude recovery of shot record of 250 after spherical divergence correction: (a) the raw shot record; (b) amplitude recovery using the RMS velocity; and (c) the amplitude recovery after a user-defined scalar (2db/second).

D.3.3.2 FK Muting

FK muting was applied to remove side scattering and steep linear reflections in the shots (A, Figure D.17a).

An FK analysis was conducted first and a muting filter was determined from the FK spectrum (Figure D.17c). This filter was applied to the shot records at time range: 10.0-11.0-9.5-11.5 (start-time, end-time, on-taper and off-taper, respectively; units in seconds). This FK filter successfully removed the side scatterings (Figure D.17b).

D.3.3.3 Bandpass Filtering

Figure D.18a shows that the raw shot data contain high-amplitude low-frequency noise in the lower part of the trace. A minimum phase Butterworth bandpass filter was applied to the shot records at 7-15-40-60 with an amplitude scheme of 0.5-1.0-0.95-0.5, respectively. The effect of this filter is shown in Figure D.18b.

D.3.3.4 Prestack Deconvolution

A prestack deconvolution filter was applied to the shots to improve the temporal resolution and to compress the signal reverberation. The operator length is 300 ms and the gap 16 ms, with 0.1% of white noise. The deconvolved and undeconvolved shots and their autocorrelograms are compared in Figure D.19.

D.3.3.5 CDP Sorting

Shots are sorted into CDP gathers.

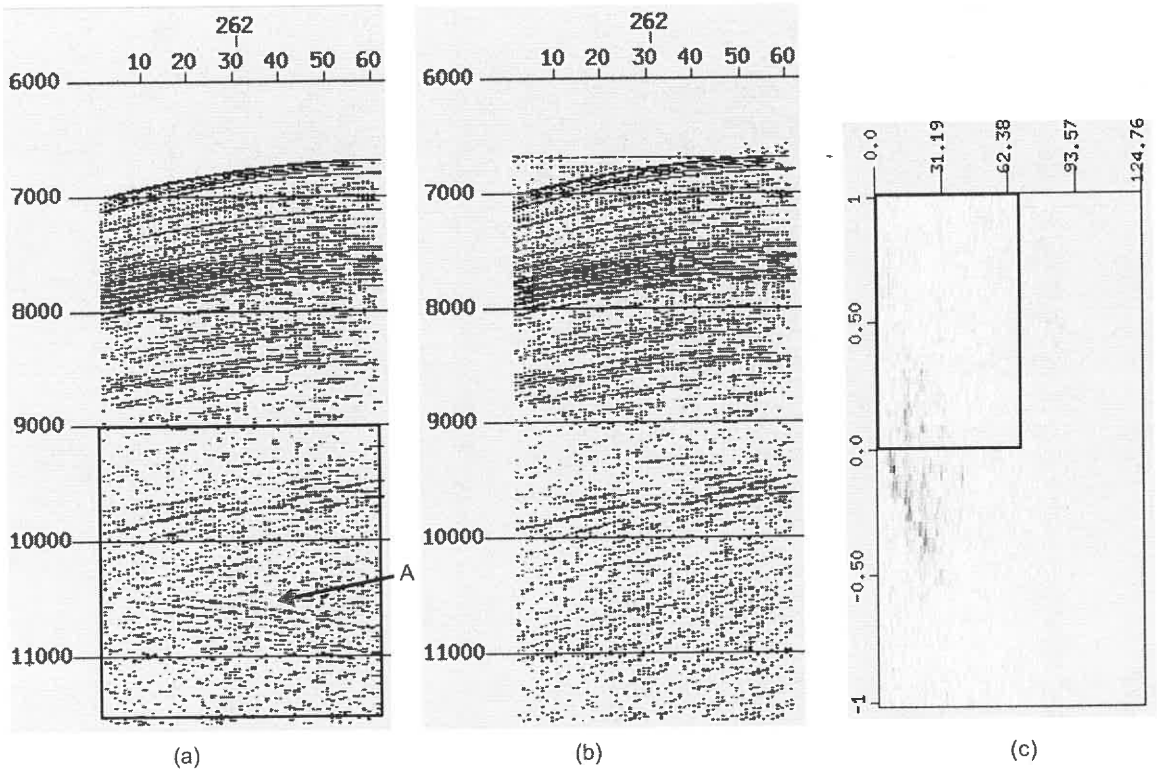

Figure D.17. FK muting of the raw shot record. The raw data (section a) show side-reflection or linear reflection in the lower part of the shots (e.g. A in section a). These reflections are removed (section b) by using the FK filter defined in section (c). Section (c) is the FK spectrum of shot data in the rectangular region of section (a). The FK filter defined by the rectangle in section (c) was applied to the shot records at time range: 10.0-11.0-9.5-11.5 (start-time, end-time, on-taper and off-taper, respectively; units in seconds).

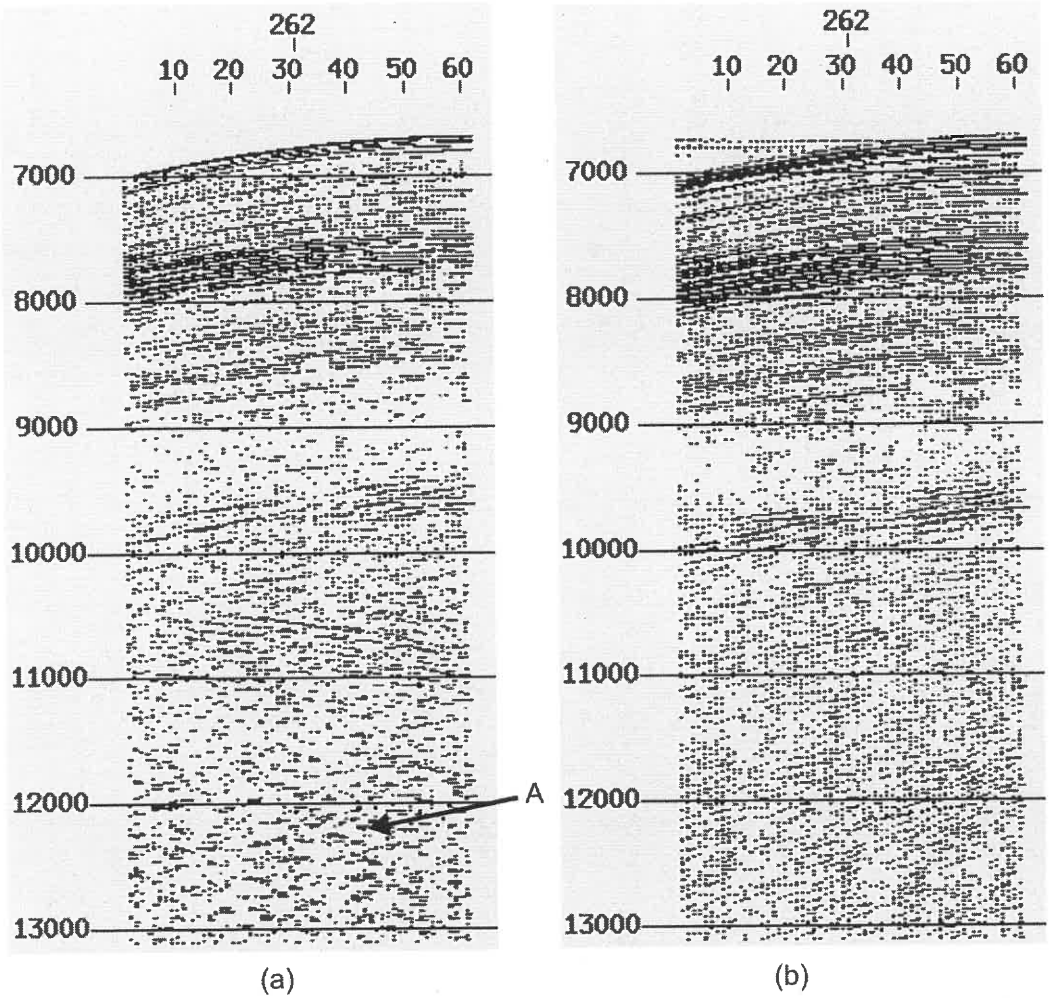

Figure D.18. Section (a) shows the high-amplitude low-frequncy noise at late arrival times (e.g. A). A minimum phase Butterworth bandpass filter 7-15-40-60 with an amplitude scheme of 0.5-1.0-0.95-0.5, respectively, was applied to the data. Section (b) demonstrates the effect of this filter. FK muting was applied to data as described in Figure D.17.

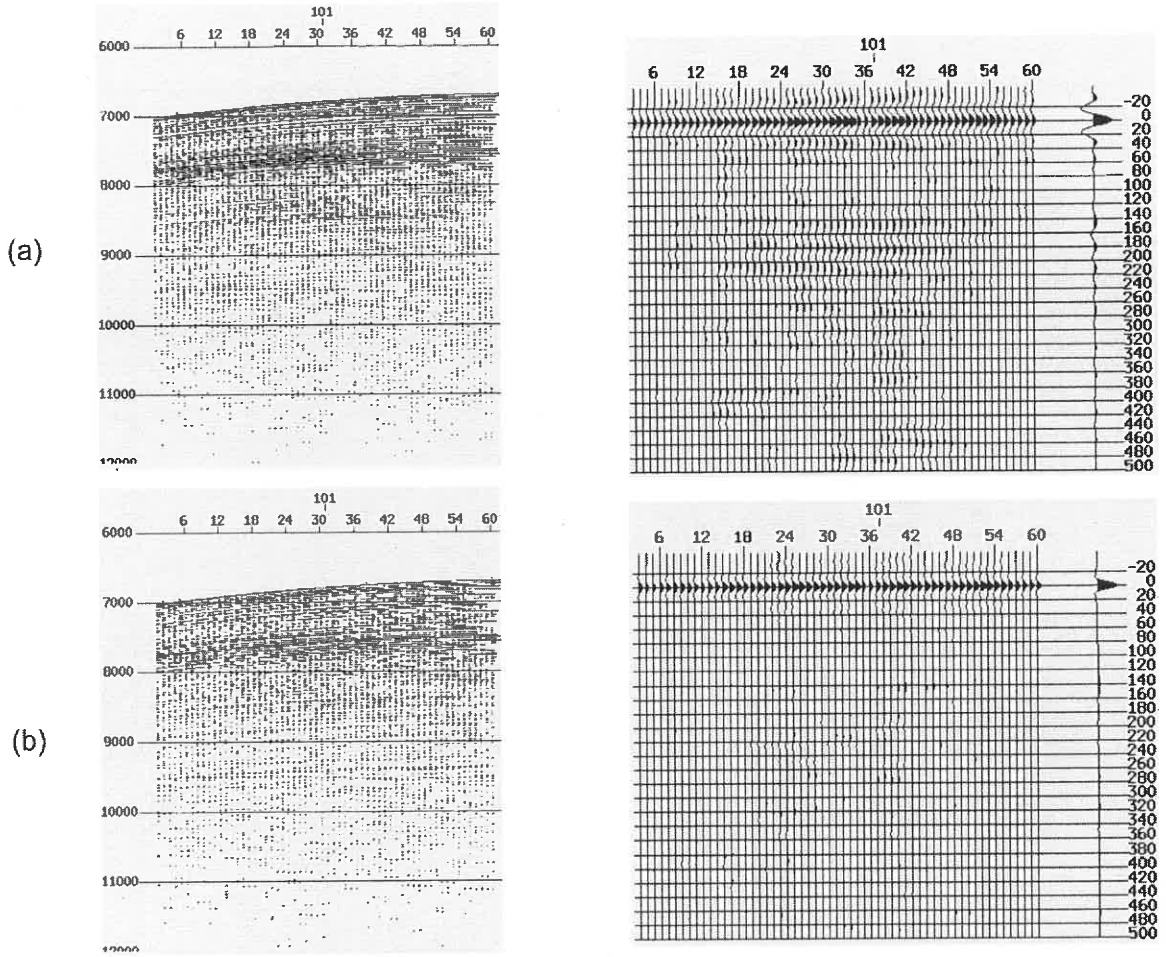

Figure D.19. The undeconvolved (a) and deconvolved record (b) for shot 101.The autocorrelograms for undeconvolved and deconvolved shot 101 are shown on the left. Note the reverberation in autocorrelogram of the undeconvolved data which is smoothed in the autocorrelogram of the deconvolved data.

D.3.4 Velocity Analysis, Stacking, Pre-Stack and Post-stack Migration

Velocity analysis, stacking pre-stack and post-stack migration are similar to description in sections 2.3.6, 2.4 and 2.5. The following are two approaches that were not included in the previous processing.

D.3.4.1 FK Muting

Artifacts of horizontal strips were created in the migrated sections, mostly between CDP 101-2700. To remove these artifacts, an FK muting filter is designed and applied to the migrated section in a similar way as described in section 3.3.2 and shown in Figure D.17. In this case, a nearly vertical narrow window was chosen to derive the FK filter. The filter is described as follows:

```
---------------------------------------------------------------
MUTE
PRIMARY KEY : INLINE
SECONDARY KEY : CDP
INTERPOLATION KEY : Interpolate/End
XV-zoom Xmin=-1.0000e+00 Xmax=1.0000e+00 Ymin=0.000000e+00
Ymax=1.2451e+02 Nx=256 Ny=256 XVIEW output at Thu Apr 20 22:04:42 2006
|Pkey    | Skey1|time1  | Skey2|time2  | Skey3|time3  | Skey4|time4. |
 INSIDE
 0        -0.02   15.99   -0.03   22.75   -0.03   29.05   0.02    29.05
          0.01    19.59   0       16.44   -0.02   15.77
---------------------------------------------------------------
```

Note: The FK filter is generally used for CMP or shot gathers. In order to make this filter work for a stack section, the following modules and their parameters have to be set up:

SETHEADER

TRACE_HDRS: inline=1

SETLASTTR

PKEY: inline

The effect of the FK muting is demonstrated in Figure D.20. The FK muting filter was only applied to the data below the basement surface.

D.3.4.2 Water Bottom Multiple Muting

The water bottom appears below the depth (time) of interest which does not require the water bottom removal. A simple bottom mute was applied to mute the water bottom multiples

D.3.5 Migrated Time Sections

The migration method is same as described in section 2.5.2.2. The velocity model constrained by the OBS data was used to do migration. The migrated sections of pre-stack time migration, post-stack time migration and DMO corrected section followed by post-stack migration and are shown respectively in Figures D.21-D.23.

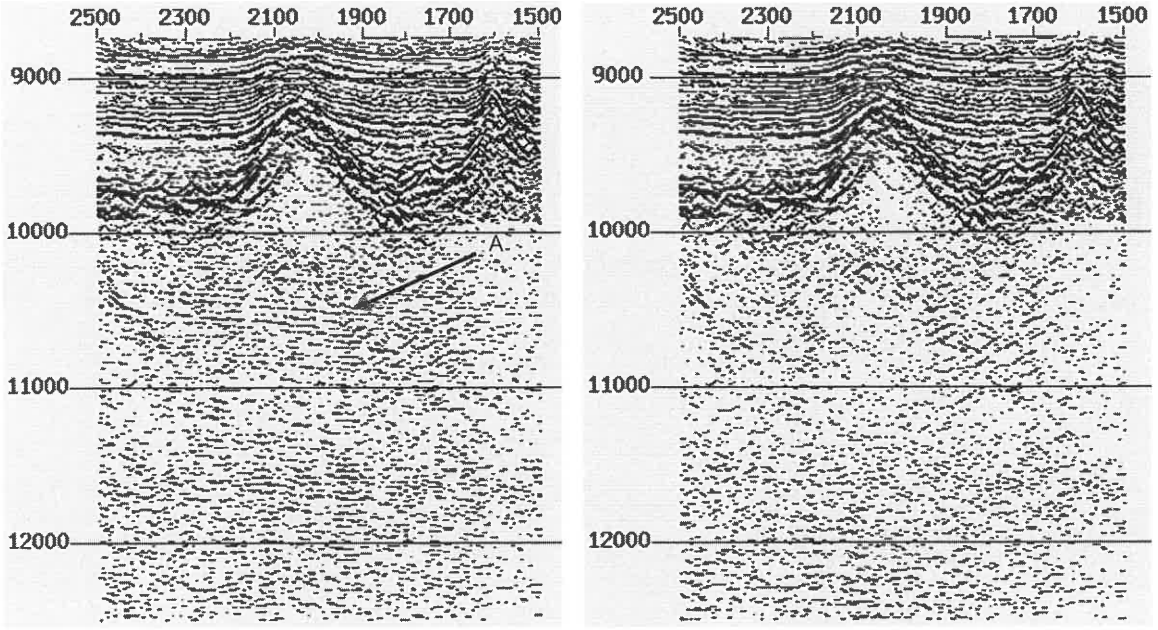

Figure D.20. FK muting of the stack section. The migrated stack section (a) show almost horizontal linear artifacts below the basement surface (e.g. A). An FK filter is designed in a similar way as shown in Figure D.7. This filter was only applied to the data below the basement surface. Section (b) illustrates the effect of this FK filter.

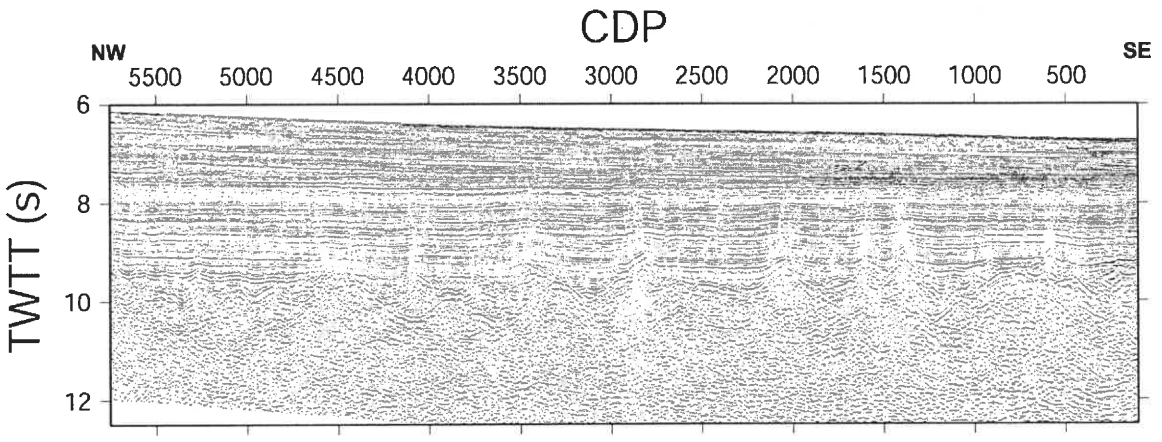

Figure D.21. Pre-stack migrated time section of BGR 8911.The velocity for migration is the velocity model constrained by seismic refraction data. The processing sequence is described in the text. A set of four time-variant filters have been applied to different time window discussed in text.

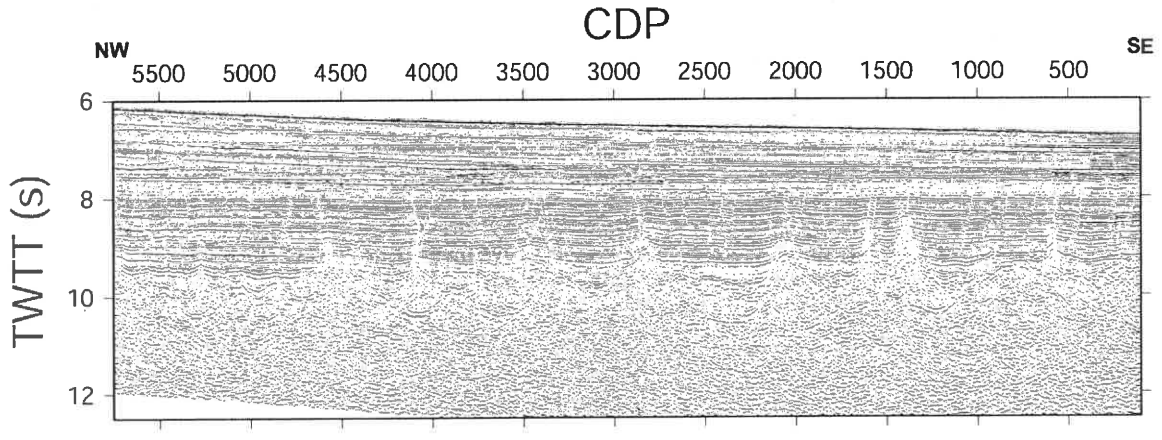

Figure D.22. Post-stack migrated time section of BGR 8911.The velocity for migration is the velocity model constrained by seismic refraction data. The processing sequence is described in the text. A set of four time-variant filters have been applied to different time window discussed in text.

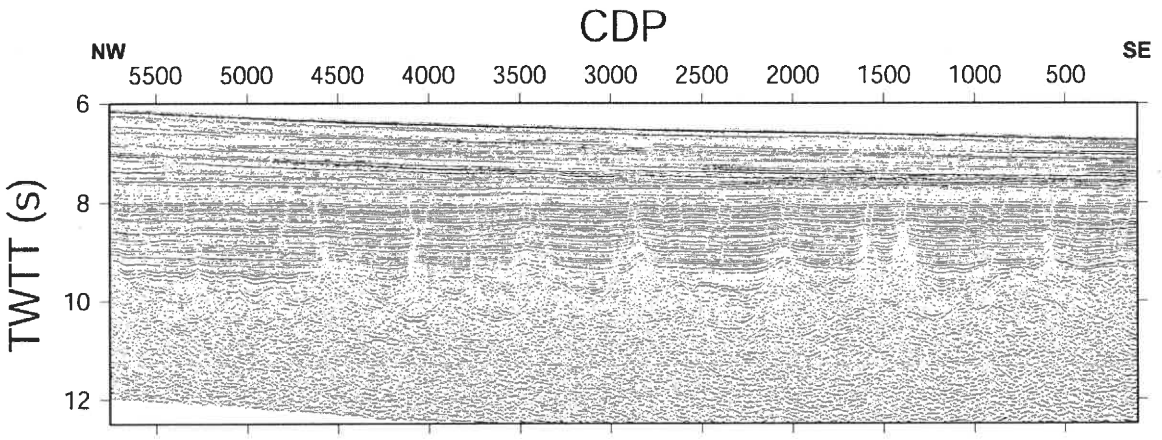

Figure D.23. Post-stack migrated time section of BGR 8911 after DMO correction. The velocity for migration is the velocity model constrained by seismic refraction data. The processing sequence is described in the text. A set of four time-variant filters have been applied to different time window discussed in text.

D.3.6 References

Bancroft, J. C., 1996. Natural antialiasing in equivalent offset prestack migration: 66 th Annual Internat. Mtg., Soc. Expl. Geophys., Expanded Abstracts, 1465-1466.

Bancroft, J. C., Geiger, H. D., and Margrave, G. F., 1998. The equivalent offset method of prestack time migration: *Geophysics*, Vol.63, No. 6, 2042-2053.

Bancroft, J.C.,1998. A practical understanding of Pre- and Poststack Migration—Volume 2 (Prestack). Society of Exploration Geophysicists Course Note Series no. 9.

Deregowski, S. M., and Rocca, F., 1981. Geometrical optics and wave theory of constant offset sections in layered media: *Geophys. Prosp.*, 29, no. 3, 374-406.

Hale, D., 1984. Dip-moveout by Fourier transform: *Geophysics*, 49, no. 6, 741-757.

Yilmaz, Ö.Z., 2001. *Seismic data analysis: processing, inversion, and interpretation of seismic data,* second edition, SEG publication.

APPENDIX E

COPYRIGHT PERMISSIONS

Chapter 2 has been published in Geophysical Journal International in volume 166 (2), page 878-906, in 2006. The copyright permission is issued from the publisher as follows:

From: Byers Sally [mailto:Sally.Byers@oxon.blackwellpublishing.com] On Behalf Of Journals Rights
Sent: August 8, 2007, 5:48
To: wuyue@phys.ocean.dal.ca
Subject: RE: copyright for published paper in GJI

Dear Yue Wu,

Thank you for your email request. Permission is granted for you to use the material below for your thesis, subject to the usual acknowledgements and on the understanding that you will reapply for permission if you wish to distribute or publish your thesis commercially.

With best wishes,
Sally

Sally Byers
Permissions Assistant
Wiley-Blackwell Publishing Ltd.
PO Box 805
9600 Garsington Road
Oxford OX4 2DQ, UK
Tel.01865 476149
Fax. 01865 471149

Dear Sir/Madam,

I am preparing my Ph.D. thesis for submission to the Faculty of Graduate Studies at Dalhousie University, Canada. I am asking for your permission to include the following published paper as one chapter in my thesis:

Wu, Y., Louden, K.E., Funck, T., Jackson, H.R., and Dehler, S.A., 2006. Crustal Structure of the central Nova Scotia margin off Eastern Canada, *Geophys. J. Inter.* 166 (2), 878-906.

Yours truly,
Yue Wu